Advanced planar pixel technology developments for ATLAS upgrade phase 2

Dmytro Hohov

université PARIS-SACLAY

NNT : 2019SACLS334

Thèse de doctorat

UNIVERSITÉ PARIS SUD
Comprendre le monde, construire l'avenir

Advanced planar pixel technology developments for ATLAS upgrade phase 2

Thèse de doctorat de l'Université Paris-Saclay
préparée à l'Université Paris-Sud

École doctorale n°576 Particules, Hadrons, Énergie, Noyau, Instrumentation, Imagerie, Cosmos et Simulation (PHENIICS)

Spécialité de doctorat: Physique des particules

Thèse présentée et soutenue à Orsay, le 01 Octobre 2019, par

Dmytro Hohov

Composition du Jury :

Fabien Cavalier Directeur de recherche (LAL)	Président
Giovanni Calderini Directeur de recherche (LPNHE)	Rapporteur
Fares Djama Ingénieur de recherche (CPPM)	Rapporteur
Sergey Barsuk Directeur de recherche (LAL)	Examinateur
Maxim Titov Directeur de recherche (IRFU/CEA)	Examinateur
Abdenour Lounis Maître de Conférence H-C. (LAL)	Directeur de thèse
Oleg Bezshyyko Professeur (TSNUK)	Invité

"What I **Cannot Create**, I Do Not Understand"

Richard Feynman,
last note on his blackboard in 1988.

Synthèse en français

Le travail de thèse, consacré aux développements de la technologie avancée de pixel (Silicium), est réalisé dans le cadre de la collaboration ATLAS au CERN. La collaboration vise la découverte et l'investigation des particules élémentaires constituant la matière dans l'univers. L'expérience ATLAS est située dans le Grand collisionneur de hadrons (LHC), qui a été conçu comme un instrument permettant de créer et de visualiser les particules et de mesurer ensuite leurs propriétés. En 2012, le projet LHC a connu un succès remarquable avec la découverte du boson de Higgs, une particule prédite par le modèle standard. Cependant, le projet n'est pas terminé et il vise à aller plus loin dans la recherche d'une nouvelle physique et à réaliser des mesures de haute précision en repoussant les limites de la technologie actuelle afin d'étendre le potentiel de découverte du LHC.

Pour cette raison, la phase de haute luminosité du grand collisionneur de hadrons (HL-LHC) est envisagée. Dans le contexte du HL-LHC, il est prévu d'augmenter la luminosité instantanée du faisceau jusqu'à $7{,}5\times10^{34}$ $cm^{-2}s^{-1}$ pour les collisions proton-proton à une énergie de collision de 14 TeV au centre de masse. Il en résulte une occupation accrue des détecteurs et une dose de rayonnement intégrée très élevé. Ces valeurs vont bien au-delà des paramètres de conception du trajectographe interne d'ATLAS actuel. Cela signifie que le trajectographe interne ne sera pas en mesure d'agir dans le cadre d'une telle augmentation du taux d'empilement et de rayonnement. Pour conserver les mêmes performances du détecteur interne d'ATLAS, le trajectographe actuel sera remplacé par un nouveau entièrement en silicium, appelé Inner Tracker (ITK), basé sur des détecteurs à pistes et à pixels dotés de capteurs avancés et de nouvelles technologies de lecture électronique. Les détecteurs au silicium sont les seuls types de détecteurs capables d'être efficaces et de survivre dans des conditions difficiles prévus pour HL-LHC.

Le travail décrit dans la présente thèse concerne principalement le développement de nouveaux détecteurs à silicium pour la mise à niveau d'ATLAS ITk afin de maintenir et, dans la plupart des cas, d'améliorer les performances du détecteur dans l'environnement hostile pendant l'opération du HL-LHC.

La thèse commence par une introduction, le **Chapitre 1**, qui trace le contexte général et donne un bref résumé du contenu des chapitres suivants. Le **Chapitre 2** donne un aperçu de la machine LHC avec ses principales expériences et objectifs physiques. Ce chapitre présente le détecteur ATLAS composé d'une série de sous-détecteurs concentriques autour du point d'interaction. Plus près du point d'interaction, il contient le détecteur interne (*Inner Detector*) placé dans un champ magnétique de solénoïde de 2 T, pour mesurer les trajectoires des particules chargées et leur impulsion; puis les calorimètres électromagnétiques et hadroniques (*Electromagnetic and Hadronic Calorimeters*) pour les mesures d'énergie des particules et le spectromètre à muons (*Muon Spectrometer*) pour mesurer les particules rapides non absorbées dans le calorimètre. Toutes ces parties avec des paramètres liés aux performances, ainsi qu'un déclencheur et des systèmes DAQ sont bien décrits dans cette partie de la thèse.

Le **Chapitre 3** présente les motivations et les projets de mise à jour pour la phase HL-LHC ; on y décrit le projet ITK, le futur trajectographe interne d'ATLAS, qui sera installé lors du troisième long arrêt (LS-3) du LHC entre 2024 et 2025. Les défis expérimentaux et les exigences du détecteur pour la phase de mise à niveau sont brièvement décrits. Les principales innovations et conceptions du trajectographe sont présentées (voir la Figure 1), incluant les nouveaux développements portant sur les détecteurs de pixels au silicium notamment la technologie des capteurs 3D et planaires *n-in-p* ainsi qu'une nouvelle puce de lecture frontale conçue dans la technologie CMOS 65 nm. Les détecteurs pixels sont dotés d'une épaisseur plus fine, de bords actifs et possèdent une taille plus petite pour augmenter la granularité du système interne. Toutes ces innovations visent aussi à accroître la tolérance aux rayonnements, à améliorer le débit de données et à réduire l'occupation des détecteurs.

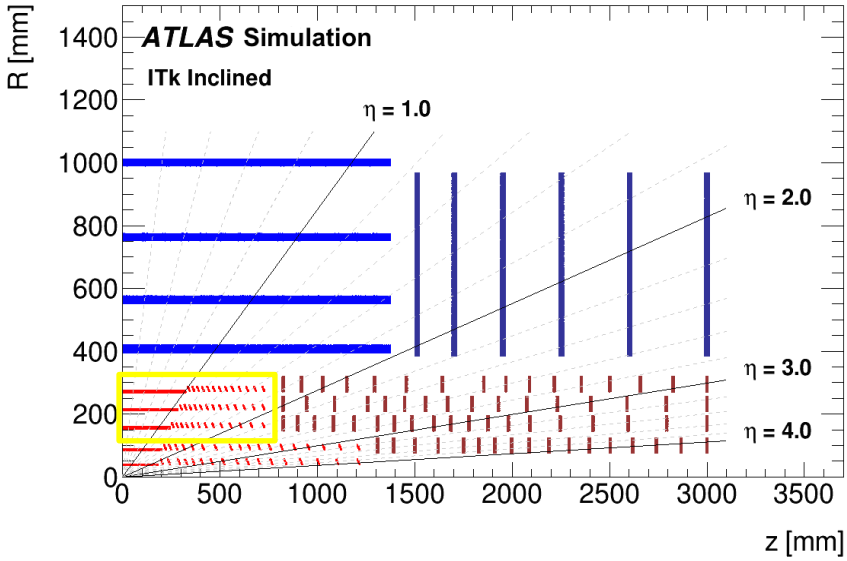

Figure 1 – Schéma général du détecteur ITk pour la Phase II ATLAS du HL-LHC [47]. Les éléments actifs en micro-pistes du barrel et des bouchons sont en bleu. Les capteurs Pixel du barrel sont en rouge et ceux des anneaux bouchons sont en rouge ocre. Les trois couches du baril externe « Outer Barrel » sont surlignées en jaune.

La validation des différentes options technologiques du détecteur pixel ont été étudiées, comme leur puissance d'alimentation, la séquence de lecture des évènements ainsi que les performances à froid de l'électronique. La séquence de construction des modules et les procédures d'assemblage sont particulièrement importantes pour la construction de l'ensemble du trajectomètre ITk. C'est pour cette raison que la collaboration ATLAS a lancé le programme ~~du~~ de démonstrateur, notamment un prototype de longeron utilisé pour tester les différents composants. Les procédures d'assemblage sont également décrites dans cette section. Plusieurs ressources techniques et humaines sont engagées dans ce programme qui prend une importance singulière car il permet de définir l'infrastructure nécessaire expérimentale au LAL, un des trois laboratoires du cluster Parisien engagés pour la construction de l'ITk. Une partie du chapitre est centrée sur la description du banc de tests, les mesures et les résultats de caractérisation des capteurs du démonstrateur.

Ce chapitre se termine sur une description de ma contribution à l'accomplissement des tâches relatives au démonstrateur ATLAS-barrel, qui comprennent la caractérisation électrique du capteur sur la probe station, le collage et assemblage du module, les tests visuels et la calibration

des RTDs (jauges de température résistives) présentes dans les modules thermiques dans la chambre climatique. Les 24 modules thermiques et 5 modules électriques ont été assemblés, ensuite validés suivant les tests habituels des détecteurs silicium, à savoir les *mesures I-V* et le balayage de source radioactive avant l'envoi au CERN pour l'installation sur le démonstrateur final (voir Figure 2).

Figure 2 – Photographie du démonstrateur thermique en longueur réelle avec les modules de chauffage thermique assemblés au cluster de Paris et installés sur la section inclinée.

Le **Chapitre 4** constitue la part de bibliographie sur l'interaction rayonnement matière, la physique des semi-conducteurs, les bases du fonctionnement des détecteurs de position au silicium, la méthode permettant la caractérisation de ces détecteurs aussi bien que les effets des dommages au irradiations sur leurs performances ainsi que les méthodes pour en réduire les effets.

Après une introduction aux mécanismes d'interaction des particules avec la matière, la théorie des semiconducteurs est décrite ainsi que les principes permettant l'utilisation de ces détecteurs semiconducteurs en physique des particules. La structure fondamentale d'un détecteur pixel est constitué d'une junction p-n formé lors du contact deux parties dopées *n* et *p*. A cause de la différence de concentration des porteurs mobiles libres, il s'opère un mouvement de ces porteurs: c'est le courant de diffusion. Ceci crée une zone d'espace de charges qui génère un champ électrique qui agit à travers la jonction. A cause du phénomène de recombinaison des électrons et trous, cette zone présente un déficit en porteurs mobiles. Cet aspect est très important pour la détection des particules, car cette zone représente le volume sensible du détecteur. En appliquant une tension inverse, il est possible d'étendre cette zone jusqu'aux limites physique du détecteur appelée tension inverse de désertion totale. Avec le courant de fuite *I,* la valeur *V* de la tension inverse de désertion totale sont des paramètres du détecteur au silicium déterminés par les mesures I(V) et C(V). Ces techniques de caractérisation des détecteurs silicium sont présentées dans ce chapitre ainsi que le banc de test utilisé pour la campagne de tests au laboratoire.

Dans le chapitre suivant, le but du travail s'est orienté sur les principes fonctionnels des senseurs pixel et les technologies innovantes qui visent à améliorer leurs performances et leur radio-tolérance. La première partie du **Chapitre 5**, donne une vue générale des technologies des capteurs silicium: les planaires, les 3D et CMOS qui équiperont le trajectographe ITk. Les pixels

planaires avec les structures auxiliaires typiques (voir Figure 3) sont décrits dans cette section, ce qui permet de mieux comprendre les arguments présentés dans la suite.

Le travail présenté ici concerne les pixels planaires produits par la fonderie ADVACAM lesquels ont été développés par le groupe de MPI Munich en collaboration avec le LAL et caractérisés dans cette thèse; ceux-ci sont décrits dans le détail notamment la version “bords-fins” et “ bords actifs”.

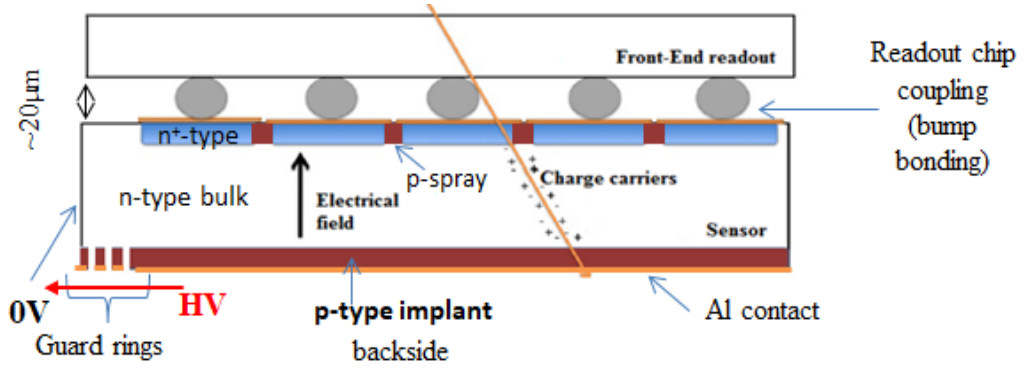

Figure 3 – Vue schématique du détecteur pixel hybride d’ATLAS. Le circuit de lecture est interconnecté au détecteur pixel avec des billes de soudure d’un diamètre de 20 à 30 µm.

La dernière partie du chapitre est dédiée à la simulation TCAD, pour lequel le groupe du LAL a contribué; ceci a permis d’optimiser les paramètres du processus de fabrication qui ont permis une meilleure robustesse notamment à la tension de claquage, à la concentration du dopage p-spray existant entre deux implants pixel n, assurant une meilleure isolation inter-implants, même après l’irradiation.

Afin d’améliorer l’accord entre les données et la simulation, les profils de dopage des senseurs silicium ont été remesurés vu que ces données ne sont pas été fournies avec précision par le fondeur. La mesure du profile des dopants actifs des substrats de silicium apportent des informations utiles qui permettent de définir les stratégies pour réduire les effets des irradiations. Une nouvelle méthode a été développée: la méthode Transmission Line Matrix (TLM). Le principe de la méthode ainsi les résultats obtenus comparés avec d’autres techniques sont présentées dans ce chapitre.

L’étape importante dans la phase R&D des nouveaux détecteurs pixels est leur caractérisation ainsi que les tests qui déterminent la façon dont ils fonctionneront dans des conditions similaires à leur environnement futur. A ce titre les zones sensibles des détecteurs sont exposées à des particules de hautes énergies et leurs réponses sont extraites dans diverses conditions d’opération. Le **Chapitre 6** est centré sur l’étude des performances du design de capteurs innovants pour le futur trajectographe ITk avec des faisceaux tests relativistes. Les installations au CERN et à DESY mettant à disposition des faisceaux tests de caractérisation des modules pixels sont décrites dans ce chapitre. Le banc de mesures expérimental et le télescope sont, détaillés avec les exigences délicates de refroidissement nécessaires pour les modules soumis aux radiations. La prise de données, la reconstruction et le processus d’analyse sont aussi expliqués.

La deuxième partie de cette section contient les résultats en terme d'efficacité de traces et de performance de reconstruction obtenues sur les capteurs conçus, précédemment décrits dans ce mémoire. Les modules pixels, compatibles avec la puce de lecture FE-I4, incluant les designs innovants de bords actifs minces, sont mesurés dans le faisceau test. Les capteurs de performance selon les deux designs et avec différentes épaisseurs de 50 µm, 100 µm et 150 µm avant et après irradiation de 1-2×10^{15} n_{eq}/cm^2 ont été évalués. La résolution spatiale des capteurs a également été estimée. L'efficacité de traces globale et locale par pixel a été calculée pour chaque design de capteur pour les traces de particules d'incidence normale et inclinée.

Ces mesures ont validé le concept d bords actifs en montrant l'efficacité non nulle à travers la région séparant le dernier pixel du bord physique du détecteur (voir Figure 4). Cette fonctionnalité donne à ce design un avantage dans le choix des capteurs du détecteur pixels ITk.

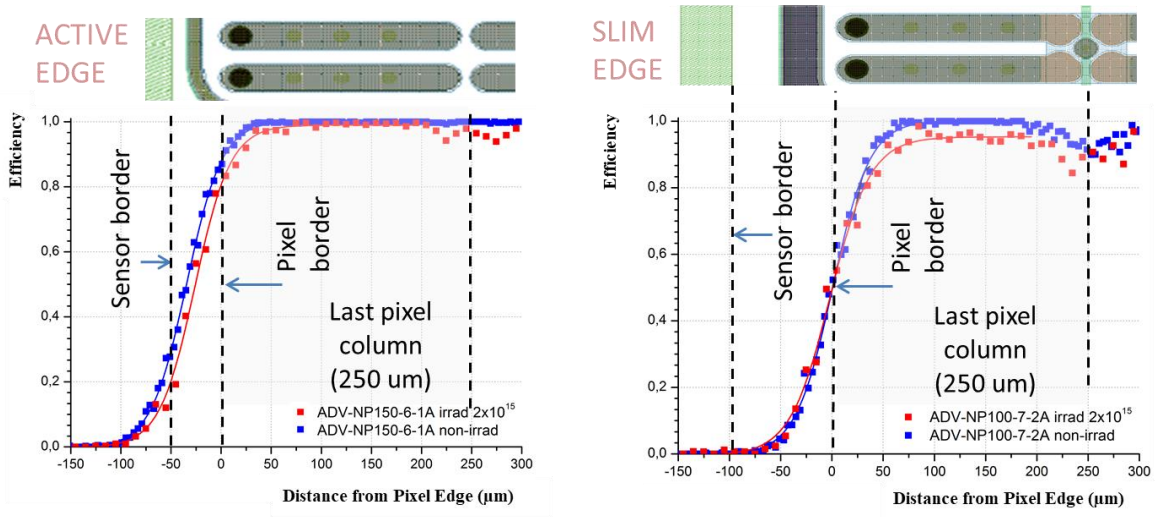

Figure 4 – Efficacité de trace sur le bord du capteur de 150 µm d'épaisseur (a) avec 50 µm de bord actif et (b) 100 µm d'épaisseur avec le design de bord mince de 100 µm bord large, avant et après irradiation. La cellule pixel à une cellule FE-I4 de 50×250 μm^2 et l'efficacité de trace est évaluée comme fonction de la distance de la dernière colonne pixels au bord de la région.

Le **Chapitre 7** donne plus de détails sur l'électronique front end du détecteur pixel. Le design type de l'électronique, les procédures de réglage, utilisées pour optimiser les conditions d'acquisition DAQ, sont expliquées au début de ce chapitre. L'architecture de la récente puce RD53A pour la lecture des pixels ITk est également présentée. Une attention particulière est accordée aux "ring oscillators", un élément incorporé dans la périphérie de la puce, pour lequel le LAL a fourni une contribution importante dans le cadre de la collaboration CERN RD53.

Dans ce chapitre, les mesures effectuées pour caractériser la tenue aux radiations de la puce sont décrites. Le comportement de la fréquence des anneaux d'oscillateurs "ring oscillators" a été déterminé en fonction de la température, de la tension d'alimentation et de l'exposition aux radiations et les résultats sont présentés ici. Le point important de ces mesures était de vérifier la capacité des "ring oscillators", à évaluer la dose de radiations absorbée. Compte tenu des résultats (voir Figure 5) du comportement linéaire, il semble possible avec pré-calibration d'utiliser les "ring oscillators" comme moniteur de radiation et de sonde de température. En plus,

ayant plusieurs ‘saveurs’ de “ring oscillators”, les mesures de dose peuvent être affinées pour atteindre une grande précision.

L’efficacité de la nouvelle génération de détecteurs pixel, avec une granularité de 50×50 µm^2 des capteurs planaires, a été évaluée sur le faisceau test avant et après irradiation. L’efficacité des différentes électroniques analogiques frontales ont été comparées. Les leçons de ces tests seront utilisées pour le design du circuit de lecture final.

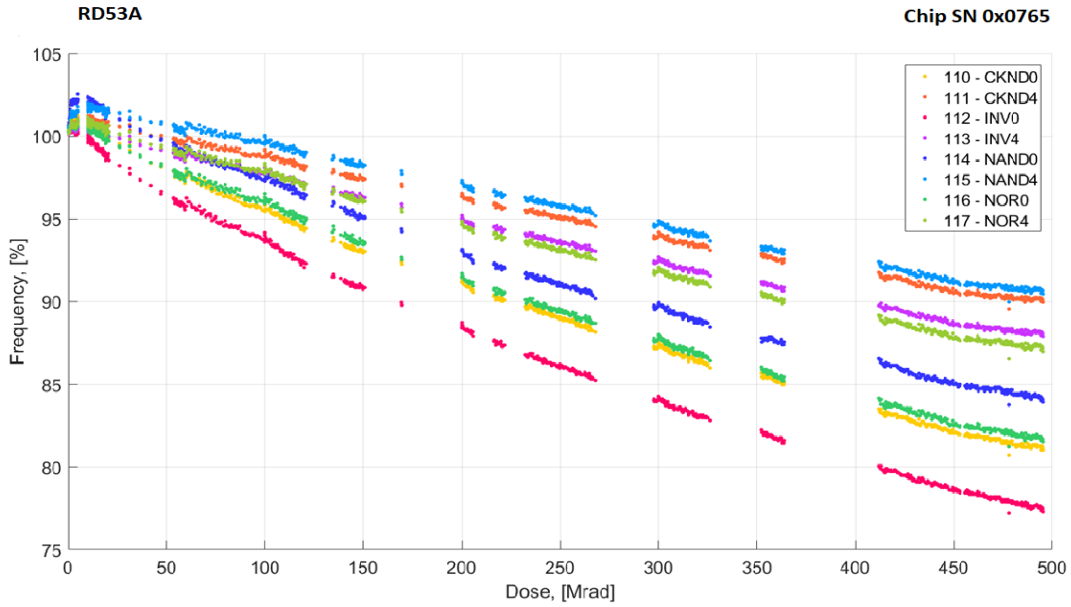

Figure 5 – Le comportement de la fréquence du “ring oscillators” en fonction de la dose de radiation jusqu’à 500 MRad. La dépendance de la fréquence dans la dose de radiation est quasi linéaire. En appliquant un ajustement linéaire aux résultats, un coefficient de réduction de fréquence pour toutes les ‘saveurs’ des “ring oscillators” a été obtenu : *0.167±0.015* [MHz/Mrad].

Le **Chapitre 8** couvre une partie conséquente de cette thèse, centrée sur le développement d’un outil supplémentaire pour la caractérisation des modules pixel. Le banc laser multitâches a été construit au LAL pour les études de performance des détecteurs pixels prototypes. Le principe consiste à utiliser un laser infrarouge de 1060 nm, monté au-dessus d’une table de translation micrométrique, dont le faisceau permet d’exciter une petite zone du capteur, de l’ordre de 20 µm en générant une charge similaire à celle déposée dans le substrat par une particule chargée au minimum d’ionisation.

La présence d’un tel instrument, compact, abordable et robuste pour la caractérisation des détecteurs pixel silicium est souhaitée car elle permet la possibilité de tests in situ des détecteurs pixels, préalable aux tests en faisceau de particules. Le banc de test, basé sur le laser infrarouge, permet une injection de charge, avec une grande précision, dans le capteur pixel silicium et du fait des propriétés de la lumière laser, il reproduit le dépôt de charge des particules de haute énergie. La position et l’aire d’injection de charge, de même que la quantité de charge injectée, sont bien connues et peuvent être ajustées avec précision. Avec cet outil, il est possible d’étudier les effets de bord qui apparaissent sur un pixel ou le capteur. Le taux des fréquences laser peut être régulé jusqu’à 1 MHz, ce qui permet d’obtenir une grande gamme d’injection de charge dans un temps assez court.

Ce chapitre donne le schéma détaillé du banc de tests (voir Figure 6) et décrit le programme de contrôle/commande, développé sous LabVIEW ainsi que le système d'acquisition de données et la procédure d'ajustement du banc de tests. En particulier, les éléments optiques et mécaniques, nécessaires à la construction du banc de tests, sont rapportés dans cette section. Les composants du banc de tests sont montrés dans la Figure 7.

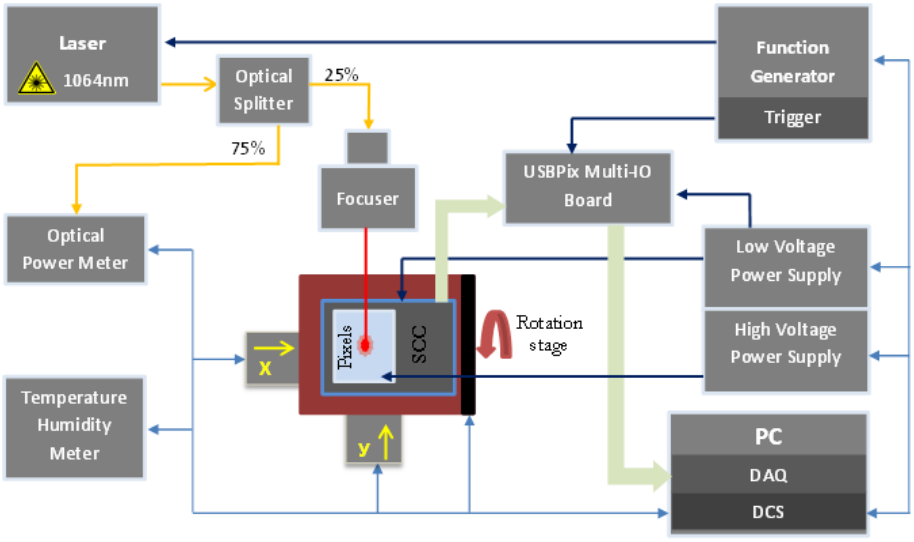

Figure 6 – Schéma de principe du banc de tests laser développé au laboratoire.

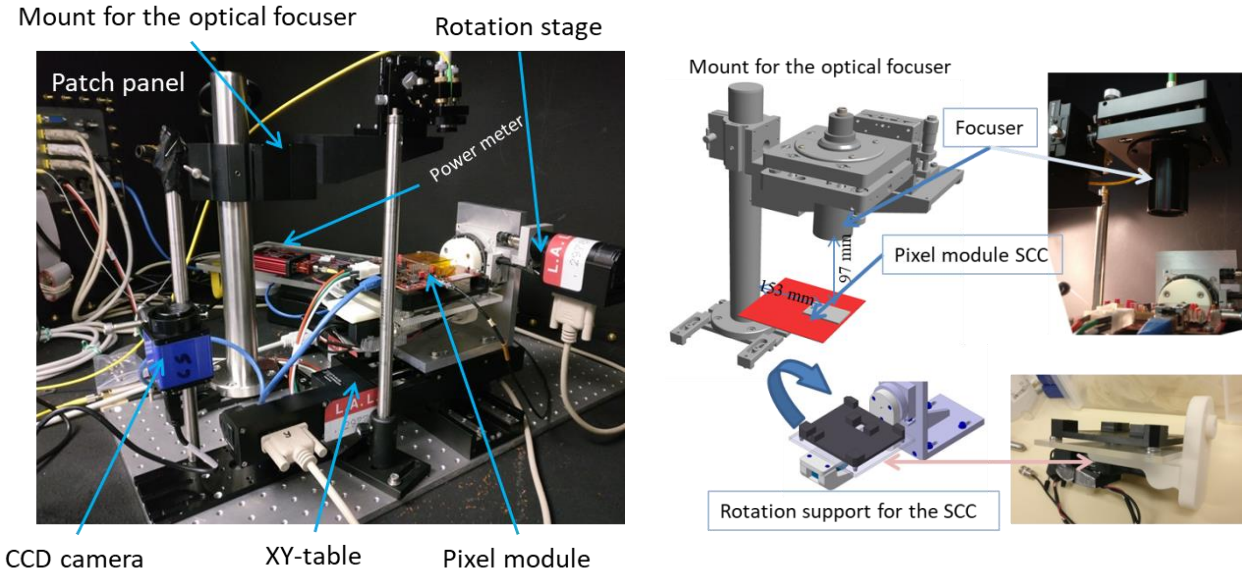

Figure 7 – a) Photo en salle blanche du banc de test laser. La carte SCC avec le module pixel, attachée au dispositif de rotation et l'ensemble monté sur la table de translation X-Y. Le portique à colonne maintient la focale. La caméra CCD bleue est fixée au même niveau que le module pixel pour la caractérisation faisceau. b) Embase et support du système de focalisation optique. La carte SCC et la distance du module à la lentille et au portique sont montrées. Embase et dispositif de maintien, en impression 3D plastique, de la carte SCC avec module pixel et scintillateur PMT.

Les balayages laser sur le module pixel FE-I4 et les ouvertures de la couche de métallisation arrière du capteur ont été effectués. Les exemples de balayages avec diagrammes de traces et

distribution de ToT (« Time over Threshold ») ainsi que les ToT de calibration de charge sont montrés en fin de chapitre.

Ce banc de tests peut aussi être utilisé avec des sources radioactives pour fournir des informations complémentaires au balayage laser. Dans ce but, la source est placée sur une potence aluminium (montrée sur la Figure 8) avec une plaque Plexiglas et un support plastique pour le positionnement de la source au-dessus du capteur pixel. Le système est déclenché en lecture par un scintillateur PMT placé sous le module, comme le montre la Figure 7(b).

Les mesures avec source sont effectuées avec une source béta Sr-90 pour les modules pixel FE-I4 non irradiés. Les résultats sont présentés en Figure 8 (b).

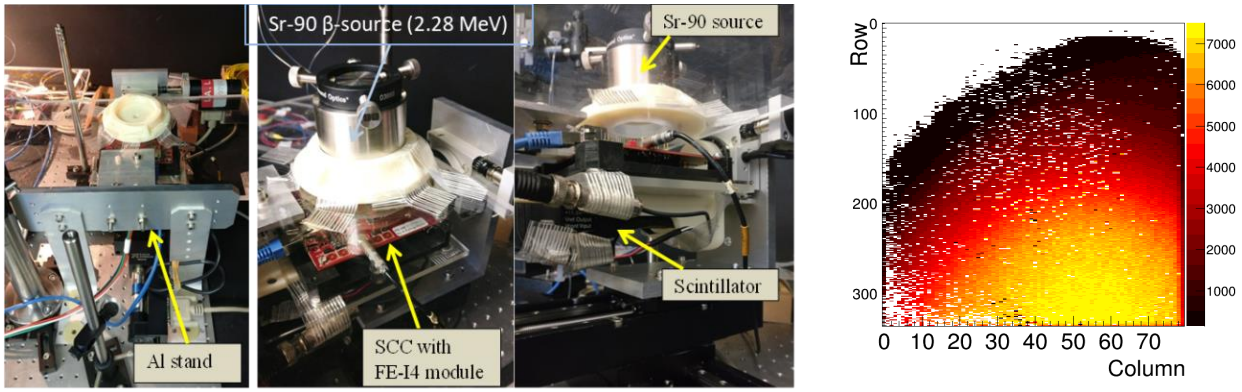

Figure 8 – a) Banc de tests des mesures avec source et un module pixel en cours de test. Le module est placé entre la source, qui émet les particules, et le scintillateur qui déclenche la lecture. La potence aluminium est installée en plus du montage laser pour supporter la source radioactive dédiée aux mesures avec source. b) carte en deux dimensions des traces enregistrées pendant le balayage source avec un déclencheur externe. La source est placée en position au-dessus de l'angle de la matrice pixels.

Un tel banc de test laser sera d'une grande aide dans la caractérisation du détecteur pixel, en complément aux faisceaux test. Dans le futur, ce banc de test sera équipé avec un nouveau système d'acquisition DAQ permettant la lecture des modules pixel ITk. Ensuite, ce banc de test sera intégré à d'autres instruments comme la station sous pointes pour encore améliorer les capacités de tests internes au LAL dédiées aux détecteurs pixel.

En fin, le **Chapitre 9** représente la section des conclusions, résumant les principaux résultats décrits dans cette thèse et aussi donne un aperçu des activités futures en vue de la finalisation de la construction du détecteur de pixels pour la future phase du projet ATLAS ITk.

Content

Chapter 1

Introduction

Throughout history, humanity aspires to understand the nature of the surrounding world and its own existence. People seek for explanations, theories, doctrines and beliefs in order to answer the demands of the curious mind, which are justified as an expression of human's innate philosophical spirit. A vivid example of the questions we ask ourselves could be a title of the painting by French artist Paul Gauguin: "*D'où venons-nous? Que sommes-nous? Où allons-nous?"*. These famous Gauguin's questions in the language of Particle Physics can be transformed into: What is matter made of? What is the origin of matter? What is the dark matter that fills the Universe? How does the Universe evolve and what is its future? Those are precisely the questions which physicists at CERN (European Organization for Nuclear Research), the largest particle physics laboratory in the world, try to tackle.

Through many experiments over the past century, it was found that everything in the Universe is made from a few basic building blocks called fundamental particles, governed by four fundamental forces. Our best understanding of how these particles and three of the forces are related to each other is encapsulated in the Standard Model (SM) of particle physics, developed in the early 1970s. This theory has successfully explained almost all experimental results and precisely predicted a wide variety of phenomena. On the 4th of July 2012, the discovery of the long-sought Higgs bosons, foreseen in the frame of the SM, was announced by the ATLAS and CMS collaborations at CERN. This finding completed the puzzle, endorsed CERN's pivotal role in the development of the Standard Model and was the beginning of the new era of search for more fundamental and general theory, making more accurate measurement of the properties in the SM and exploring new physics beyond the Standard Model (BSM). It should also be emphasized that many of these and future discoveries in particle physics would not be possible without parallel developments in accelerator and particle detection techniques.

The particle detection systems are the cornerstone of the experimental studies in the modern nuclear and high energy physics (HEP). Most state of the art experiments require the development of increasingly sophisticated detectors of ionizing radiation: X-ray, gamma radiation, particle beams, cosmic rays, etc. Moreover, the detector technologies are also widely used in astrophysics, cosmology, medical physics, radiation protection and security applications. In principle, detectors could be divided into several types according to their purposes: *spectrometers* and *calorimeters* can measure the deposited energy of ionizing particles; detectors, capable to determine the position of interaction point, are called *position sensitive detectors*, which, if they are able to record a whole path of the charged particle through the detector, are called *tracking detectors* or *trackers*; to record the fact of interaction of the ionizing radiation with matter the *radiation counters* are used; and *timing detectors* are able at an acceptable level to determine the time of particle registration. However, the modern detectors

used in HEP typically consists of several types of sub-detectors forming a single sophisticated detection complex.

The progress in the development of high spatial and time resolution detectors usually entails a breakthrough in particle physics. In 1968, Georges Charpak (Nobel Prize 1992) invented and improved the multi-wire proportional chamber (MWPC). He revolutionised particle detection, this new detector technique allowed to record millions of particle tracks each second with hundreds μm resolution. This was the beginning of the electronic era in particle detection, which led to important discoveries in particle physics including the charm quark (1974, SLAC and Brookhaven), the W and Z bosons (1983, CERN) and top quark (1995, Fermilab).

Nowadays, thanks to the development of semiconductor device technology, the MWPCs have been supplanted by silicon micro-strip and pixel detectors. They provide fast readout with high channel density of about 10 000 channels per cm^2, with less than 10 μm spatial resolution. Almost all the detector systems for large modern HEP experiments are equipped or going to be upgraded with pixel detectors in the innermost layers, as they are only devices capable to cope with a high occupancy and the harsh radiation environment close to the interaction point.

In the context of the High Luminosity phase of the Large Hadron Collider (HL-LHC), envisaged to start in 2026, it's planned to increase the instantaneous beam luminosity up to $7{,}5 \cdot 10^{34}$ $cm^{-2}s^{-1}$ at collision energy of 14 TeV in the center of mass to achieve the high-precision results in the project tasks. The resulting increase in occupancy levels and integrated radiation doses go beyond the design values for the current ATLAS tracker. Due to this the replacement of the tracker system is foreseen with new fully silicon tracker, called Inner Tracker (ITk) based on micro-strip and pixel detectors with advanced sensors and readout electronics technologies.

The work described in the present thesis is mainly concerned with the development of novel silicon pixel detectors for the ATLAS ITk upgrade to maintain and in most cases to improve the detector performance in the hostile environment during the HL-LHC operation.

The thesis opens with an introduction, **Chapter 1**, drawing the general context of this work and gives a short summary of the content of the next chapters of the present work.

Chapter 2 gives an overview of the LHC machine and the ATLAS detector with a detailed description of the designs and performance-related parameters.

Chapter 3: The motivation and plans for the HL-LHC upgrade of the accelerator and of the ATLAS detector are presented. The experimental challenges and the detector requirements for the upgrade phases as well as innovative technological ideas for the ITK Upgrade are discussed. The chapter ends with the description of my contribution to completing tasks to verify technological solutions in the frame of ATLAS Outer Barrel Demonstrator Project

Chapter 4: After the introduction of the mechanisms of particles interaction with matter, the semiconductors, their main properties and their application as particle detectors are given. Then the methods for the detector characterization in the clean room environment with the results are

presented. At the end of the chapter, the radiation damage in silicon sensors and its impact on the detector performance are discussed.

Chapter 5: The ideas of hybrid pixel detectors with an overview of sensor technologies are presented in the beginning of this chapter. The innovations in planar pixel sensor design for the ITk are discussed. A TCAD simulation work on the sensor design optimization, increasing the pixel robustness in terms of breakdown voltage, and its results are given. A new method for the active doping profile measurements, called a TLM method, to improve radiation hardness of silicon pixel sensors is discussed, and my contribution in these measurements is presented.

Chapter 6: The study of efficiency performance with relativistic particle beams of innovative sensor designs for the ITk is given in this part of the work. The facilities and the existing setup for a test beam characterization are described. The data taking, reconstruction and analysis processes are explained and the results with the comparison of different sensor designs are presented.

Chapter 7: The operating principles of the front-end pixel detector electronics and its tuning are explained in the beginning of this chapter. The details about a novel RD53A chip for the ITk upgrade are then described. The frequency of ring oscillators embedded in the chip has been studied depending on a radiation dose and other working conditions. The efficiency of new pixel detector generation with the 50×50 μm^2 granular planar sensor has been evaluated at the test beam before and after irradiation.

Chapter 8 presents the test bench setup based on an infrared laser for the pixel module characterization, which has been developed during the thesis work in the clean room conditions in the lab. This chapter describes the setup construction, the principle of testing method, the control software, the adjustment procedure and the results of the performed tests with the FE-I4 pixel module.

Finally, **Chapter 9** represents a general conclusion section, summarizing the main results described in this thesis work. It also includes a short outlook of future activities.

Chapter 2

The description of the LHC and the ATLAS experiments

Contents

The Large Hadron Collider (LHC) [2] is the world's largest and most powerful particle accelerator to date. The beam characteristics of the LHC allow the creation of the unique conditions at the collision point which may help physicists to find and test new theories of particle and high-energy physics.

The collider complex is located at CERN (*le Conseil Européen pour la Recherche Nucléaire*, the European Organisation for Nuclear Research) near Geneva, straddling the border between France and Switzerland. CERN was founded in 1954 in order to ensure collaboration among European States in nuclear research of a pure scientific and fundamental character, the Organization shall have no concern with work for military requirements and the results of its experimental and theoretical work shall be published or otherwise made generally available [1]. Now CERN has 23 member states and approximately 2500 scientific, technical, and administrative staff members, and about 12 000 visiting scientists.

This chapter will describe the LHC accelerator complex and the ATLAS experiment at CERN, as well as the ATLAS detector and its components.

2.1. The Large Hadron Collider complex

The Large Hadron Collider was built in 2008 and installed in the tunnel of the former Large Electron Positron (LEP) circular collider that operated from 1989 until 2000. The tunnel is 26.7 km long and located 45 m to 170 m underground. The first LHC proton-proton collision was recorded on 23 November 2009. The LHC has two beam pipes to accelerate the beams in opposite directions to provide collisions of protons with a centre-of-mass energy of $\sqrt{s} = 14$ TeV at a nominal designed instantaneous luminosity of 10^{34} $cm^{-2}s^{-1}$ (see 2.2). Also the LHC is designed to accelerate lead ions up to $\sqrt{s} = 1.15$ *P*eV with a luminosity of $10^{27} cm^{-2}s^{-1}$.

The injection of particles into the collider is done by the previously existing accelerator infrastructure; the complex layout is shown in Figure 2.1. Protons begin their journey in an ion source, from a simple bottle of hydrogen gas. Using an electric field one can strip away electrons from hydrogen atoms to yield protons, which are then injected into Linac 2, the first accelerator in the chain, where they are accelerated to the energy of 50 MeV. Then the beam reaches the Proton Synchrotron Booster (PSB), which accelerates the beam to 1.4 GeV. Later, the beam enters the Proton Synchrotron (PS), where protons reach energy of 25 GeV. After this, protons are sent to the Super Proton Synchrotron (SPS) which pushes them to 450 GeV. And finally the SPS beam fills the LHC with about 2808 bunches, each containing about 10^{11} protons and separated by 25 ns gap. It takes a bit more than 4 minutes to fill each LHC ring, and 20 minutes to reach protons the maximum energy.

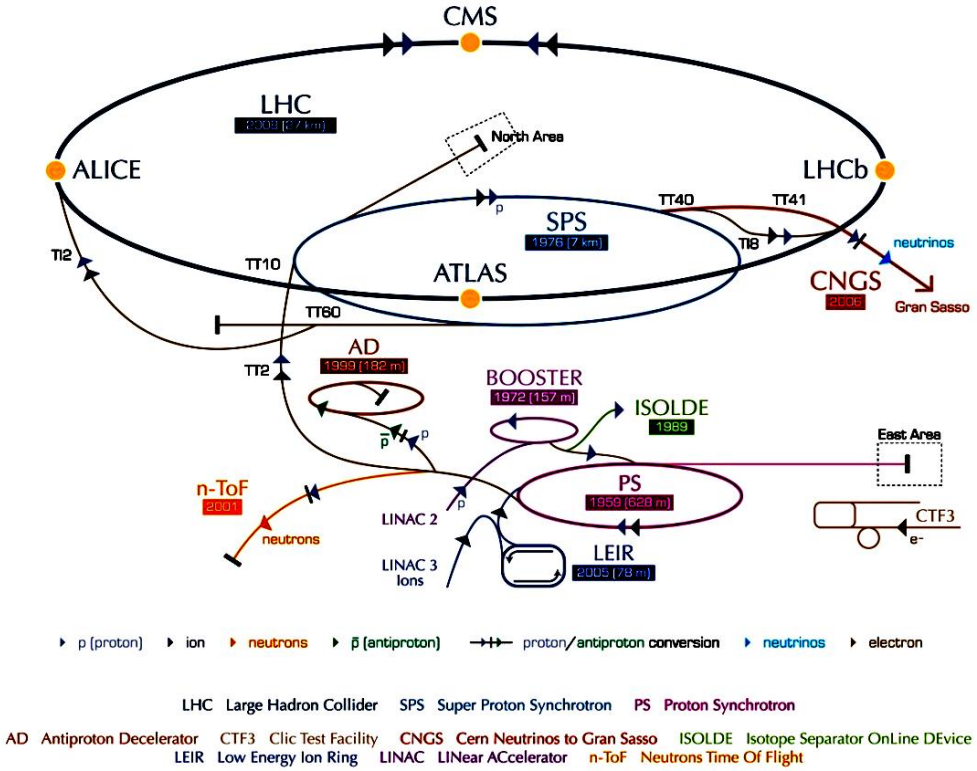

Figure 2.1 – The LHC ring shown in dark grey line and the smaller machines used in a chain to help boost the particles to their final energies. Besides the main experiments the complex includes the *Antiproton Decelerator*, the *Online Isotope Mass Separator* (ISOLDE) facility, the *Compact Linear Collider* test area, as well as the *neutron time-of-flight facility* (nTOF) and it previously fed the CERN *Neutrinos to Gran Sasso* (CNGS) project [3].

For heavy ion applications, the lead ions for the LHC are created by vaporization of pure solid Lead-208 and subsequent ionization of the vapour to become a plasma. Then the ions are extracted from the plasma and accelerated in Linac 3 to enter the Low Energy Ion Ring (LEIR). LEIR transforms the long pulses from Linac 3 into four bunches, containing 2.2×10^8 lead ions and accelerates them from 4.2 MeV to 72 MeV. Eventually the lead ions follow the same way as the protons to arrive the maximum energy.

The two beams are brought into collision at four Interaction Points (IPs), surrounded by the detectors for the main experiments: **A L**arge **I**on **C**ollider **E**xperiment (ALICE) [5], **A T**oroidal **L**HC **A**pparatu**s** (ATLAS) [6] **C**ompact **M**uon **S**olenoid (CMS) [7] and **L**arge **H**adron **C**ollider **b**eauty (LHCb) [8]. The ALICE is dedicated to investigate the properties of quark-gluon plasma (QGP) in heavy ion collisions. The LHCb experiment aims to study heavy flavour physics and Charge conjugation and Parity symmetry violation (CP violation) in the b and c hadron decays. ATLAS and CMS are general purpose experiments used multipurpose detectors based on different and complementary technologies to investigate the properties of SM and search for new physics.

The LHC ring is made of eight 545 m-long straight sections and eight 2.45 km-long arcs. The straight sections are used as experimental or utility insertions [28]. The two of them serve only as experimental insertions and other two are experimental insertions with injection systems. There is a straight section, which contains two RF (Radio Frequency) cavity systems. Two insertions have beam collimation systems dedicated to clean a halo. And another straight section holds the beam dumping system to fast-extract the circulating beam in a loss-free way. The arcs contain the special magnet structures composed of combination of dipole, quadrupole and other multipoles magnets. In total the LHC ring is made of 1232 dipole magnets, each weighing 35 tons and 15 meters long. The dipoles are made of copper stabilized NbTi Rutherford cables, which become superconductive at a temperature below 10 K. The magnets are used to generate a powerful magnetic field of 8.33 T nominally to allow the beam to take tight turns. This magnetic field is produced by passing 12 kA of current through the superconducting magnets, cooled down in superfluid helium at 1.9 K.

Along with bending, the beam must be focused to suppress its divergence and prevent the subsequent loss of the beam on the pipe wall with disastrous consequences. In the LHC this is achieved by using of 392 quadrupole magnets, 3 m long. The four magnetic poles of the magnet arranged symmetrically around the beam pipe to focus the particle beam either horizontally or vertically, depending on the type: “F quadrupoles” (which are horizontally focusing and defocusing vertically) and “D quadrupoles” (on the contrary vertically focusing but horizontally defocusing). In addition, there are eight sets of so called "inner triplet" magnets in the LHC. They serve to focus the particle beams before they collide. The size of bunches passes from 200 μm to 16 μm at the each of four IPs to achieve high luminosity collisions.

The instantaneous luminosity is a crucial parameter, that characterizes the number of collisions in a collider and given by the beam intensity *I* over collision area *A*:

$$\mathfrak{L} = \frac{I}{A} = \frac{N^2}{A} n_b f \tag{2.1}$$

where N is the number of particles per bunch, n_b is the number of bunches in a train and f is the revolution frequency.

For the transverse Gaussian beam profiles it can be expressed [11]:

$$\mathfrak{L} = f \frac{r}{4\pi} \frac{N_1 N_2}{\sigma_x \sigma_y} n_b f \tag{2.2}$$

where N_i – number of particles in i bunch, σ_x and σ_y characterize the root mean square (RMS) of transverse beam sizes in the horizontal and vertical direction. And r is a geometric factor, which takes into account the non-zero crossing angle and the length of the bunch.

The number of events, for a given physics process N_{exp}, is the product of the cross-section of interest σ_{exp} and the time integral over the instantaneous luminosity:

$$N_{\text{exp}} = \sigma_{\text{exp}} \times \int \mathfrak{L}(t) dt \tag{2.3}$$

The time integral over the instantaneous luminosity is called the integrated luminosity and given in units of cm^{-2}:

$$L = \int \mathfrak{L}(t) dt \tag{2.4}$$

In Figure 2.2, the total integrated luminosity recorded by the ATLAS detector in last three years is shown.

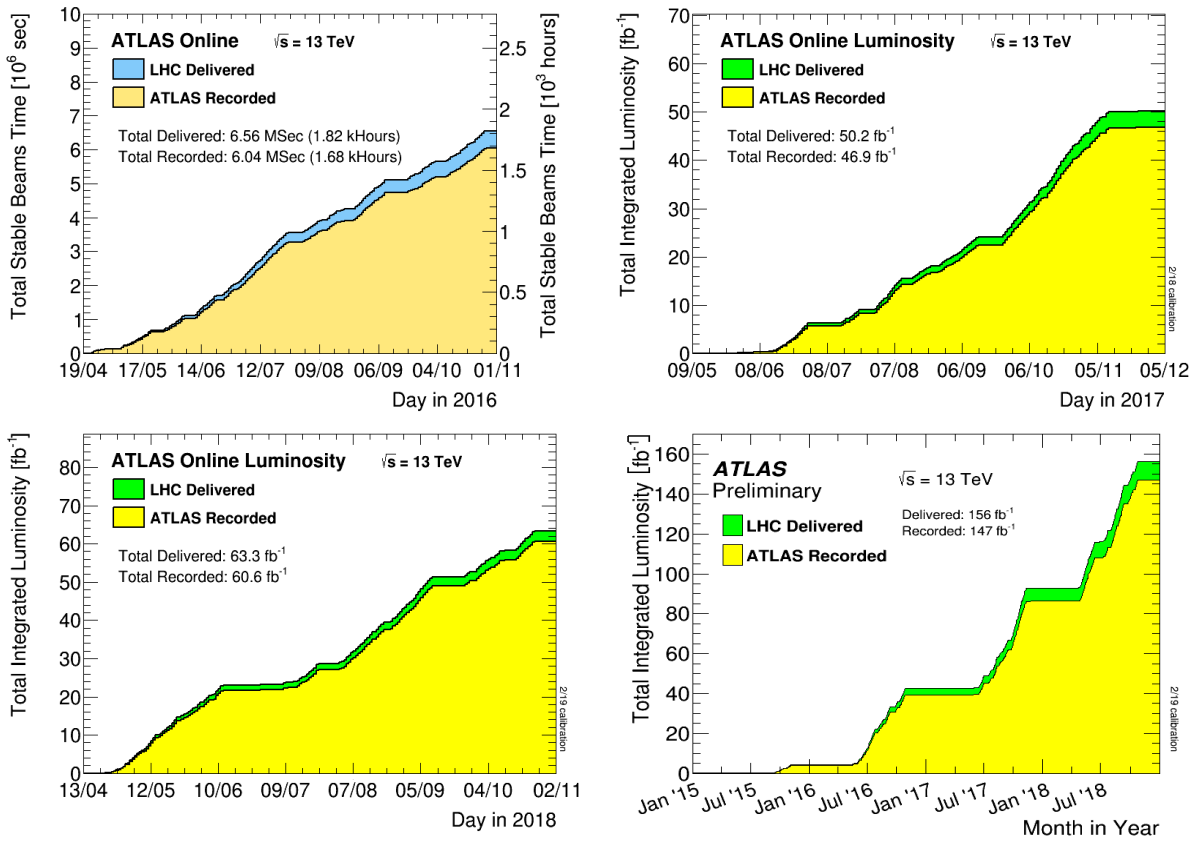

Figure 2.2 - Cumulative luminosity versus time delivered to ATLAS (green) and recorded by ATLAS (yellow) during stable beams for pp collisions at 13 TeV energy in LHC Run-2. Plots from [9].

There is another important parameter related to the instantaneous luminosity, called pile-up, which is essentially the number of pp interactions per bunch crossing. Its magnitude changes over time, as the luminosity evolves:

$$\mu(t) = \frac{\mathfrak{L}(t)\sigma_{inelastic}}{n_b f} \tag{2.5}$$

where $\sigma_{inelastic}$ is the inelastic cross-section for pp collisions, f =11.245 kHz is the revolution frequency for the LHC.

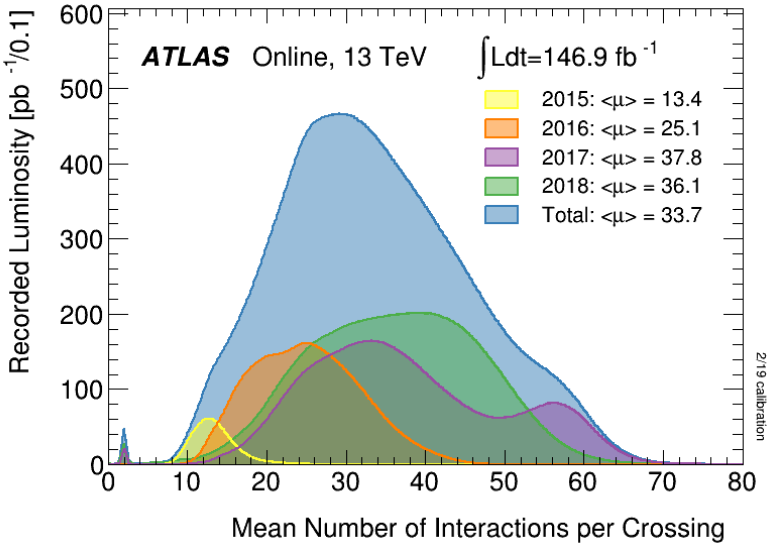

Figure 2.3 - Number of Interactions per Crossing. $\sqrt{s}$ = 13 TeV data from 2015 -- 2018. [10]

The pile-up events are usually soft interactions which constitute a background to the interested for the analysis interactions. The pile-up significantly increases the complexity of the topology of each recorded collision and decrease the resolution of the event reconstruction. The mean numbers of interactions per bunch crossing for each year ATLAS datasets starting from 2015 are presented in Figure 2.3.

2.2 The ATLAS Experiment and its physics goals

The ATLAS experiment [11] was set up at the LHC to identify and measure a wide range of various particles produced in proton-proton collisions. The motivation of the experiment was mainly driven by the search of the Higgs boson and other possible SM extensions at the TeV energy scale. The Higgs boson was indeed discovered in July 2012 [12] with a mass of 125.5±0.2 (stat) ±0.6 (sys) GeV [13] and then based on data recorded by the ATLAS experiment at the LHC at $\sqrt{s}$ =13 TeV, shown in Figure 2.4, the mass is measured to be 124.98±0.19(stat)±0.21(sys) GeV [14].

After the Higgs boson discovery, which undeniably was an important and a successful result of the efforts made to find technological solutions to build the ATLAS detector, the main objectives of the experiment are the precise measurement of the properties of the Higgs boson, in particular, mass, decay width, branching fraction in a variety of channels: $H \to \gamma\gamma$, $H \to ZZ^* \to 4$ leptons, $H \to b\bar{b}$, $H \to \tau^+\tau^-$, $H \to W^+W^-$ and other rare decays.

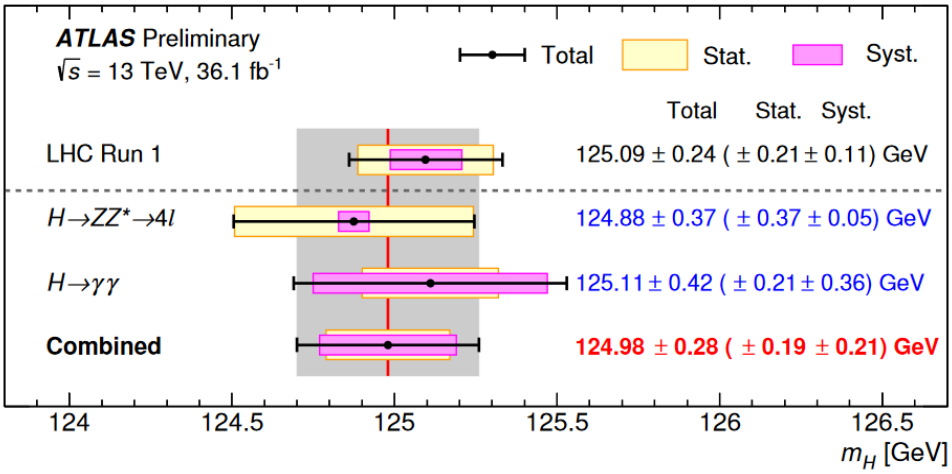

Figure 2.4 - Summary of the Higgs boson mass measurements from the individual and combined analyses, compared to the combined Run-1 measurement by ATLAS and CMS.
Plot is taken from Ref. [15]

Also the ATLAS experiment is orientated towards search of Beyond the Standard Model (BSM) particles. It may provide the answer for the mysterious dark matter and energy of the Universe, the matter-antimatter asymmetry problem, extra dimensions of space and the supersymmetric partner particles.

2.3. The ATLAS detector

One of two general-purpose detectors, located at the interaction points of the LHC ring, ATLAS is designed to detect a large variety of particles originating from $p-p$ collisions, and provide precisely measurements of their properties. It is approximately 44 m long and 25 m tall, and lies in a cavern 100 m below ground. The 7000-tonne ATLAS detector is the largest volume particle detector ever constructed.

The ATLAS detector is composed of three subdetector systems, which structured as barrels which fit inside each other, as shown in Figure 2.5. From the inner to the outer part these systems are: the Inner Detector (ID) [16,17], the Electromagnetic (ECAL) [18,19] and Hadronic Calorimeter (HCAL) [18,20] and the Muon Spectrometer (MS) [21]. All these subdetector-parts of ATLAS will be explained in the next sections.

2.3.1. Coordinate system

The ATLAS detector uses right-handed system centred on the nominal IP at the geometrical centre of the detector. The x-axis points towards the middle of the accelerator ring, y-axis is directed upwards and z-axis is parallel to the beam line. The x-y plane is referred to as the transverse plane and often described in cylindrical coordinates (Z, φ, θ) as shown in Figure 2.5. Z -axis points along the beam line. The azimuthal angle φ is an angle around the beam, measured from the x-axis. The polar angle θ is defined as the angle from the positive Z -axis to the transverse plane.

The polar angle is often convenient to specify in terms of pseudorapidity, defined as

$$\eta = -\ln[\tan\left(\frac{\theta}{2}\right)] \tag{2.6}$$

Pseudorapidity is used to describe the angle a particle exiting the IP relative to the beam axis within the detector. When it happens perpendicularly to the beam line the pseudorapidity $\eta = 0$, and $\eta = \infty$ when the particle moves in the direction of the beam line.

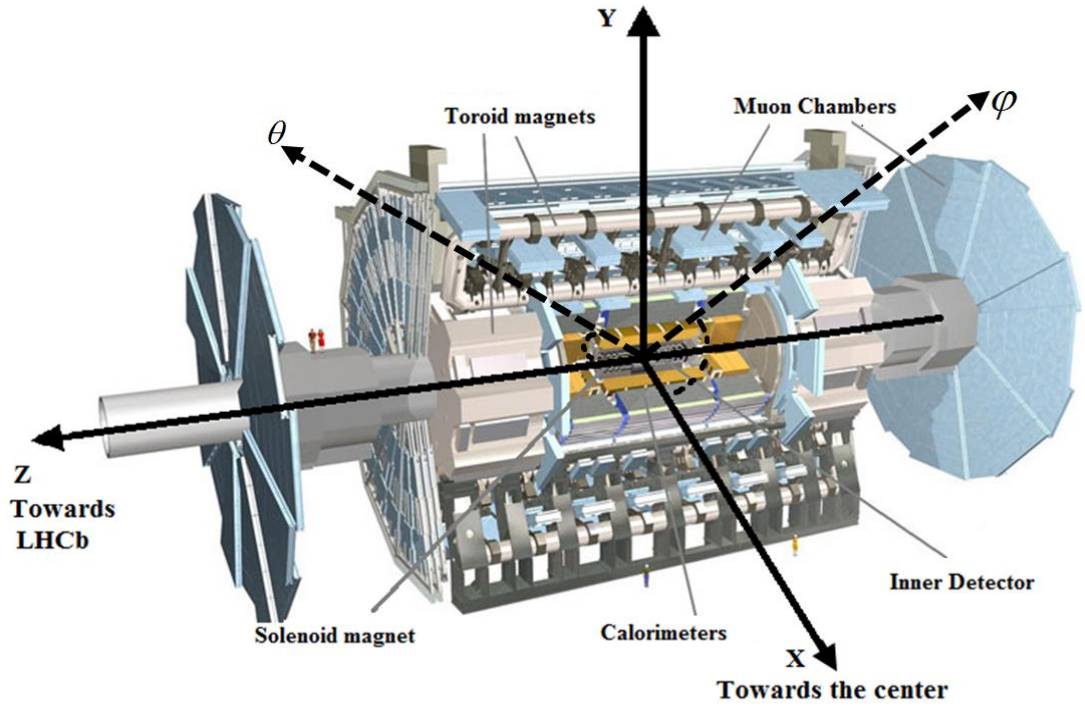

Figure 2.5. - Schematic view of the ATLAS detector with all main sub-detectors and magnetic systems. Also this illustration shows the ATLAS coordinate system.

The ATLAS detector covers almost all the 4π solid angle surrounding the IP. The muon spectrometer covers in range of $|\eta| < 2.7$, the HCAL provides coverage up to $|\eta| < 4.9$ and the ECAL reaches $|\eta| < 3.2$. The original ID had coverage of $|\eta| < 2.5$ but after the IBL insertion it was extended up to $|\eta| < 3.0$.

2.3.2 The Inner Detector

The ATLAS Inner Detector (ID) is the first sub-detector that particles encounter exiting the collision point. The ID measures the trajectory of charged particles as they traverse the detector, typically it provides 36 tracking points per track. It is placed in a 2 T magnetic field of the central solenoid to identify the sign of particles charge, measure their momentum and reconstruct the short-lived particles by their decay products. In order to make high-precision measurements, the ID has been designed with low material budget to reduce the particle deflection by multiple scattering, with fine detector granularity to be able to distinguish tracks in high pile-up. After the initial alignment, a transverse impact parameter resolution of $22.1 \pm 0.9\ \mu m$ and a relative

momentum resolution $\frac{\sigma(p_T)}{p_T} \simeq (4.83 \pm 0.16) \times 10^{-4} \, p_T(GeV)$ have been measured for high momentum tracks [23].

The ID is placed within a cylinder with a length of 7 m and 2.3 m diameter and structurally composed of parallel central barrel layers and end-cap wheels or disks at both ends of the barrel, as shown in Figure 2.7, 2.8. From the centre out, the ID consists of three tracking systems: the Pixel Detector, the Semi-Conductor Tracker (SCT) and the Transition Radiation Tracker (TRT), as shown collectively in Figure 2.6 and 2.7.

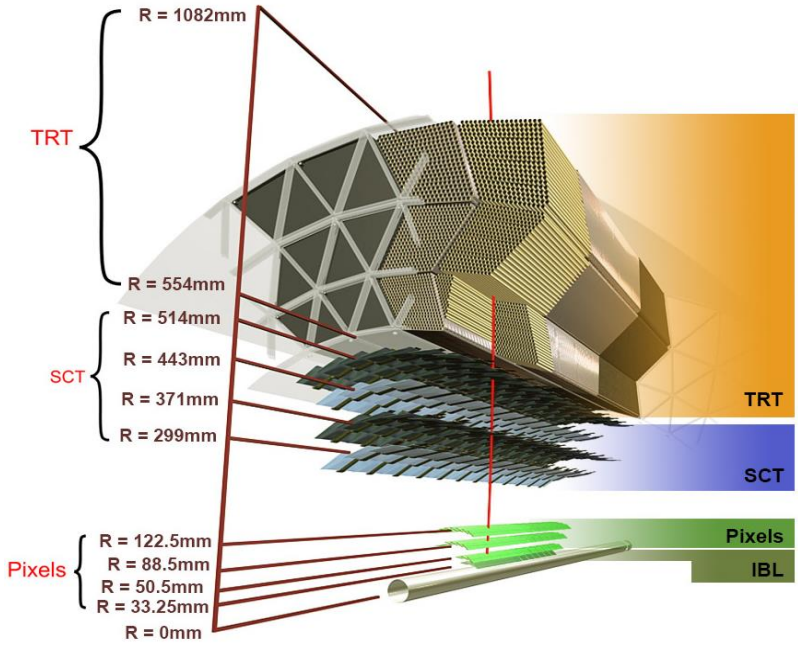

Figure 2.6 – A detailed layout of the Inner Detector barrel layers.[22]

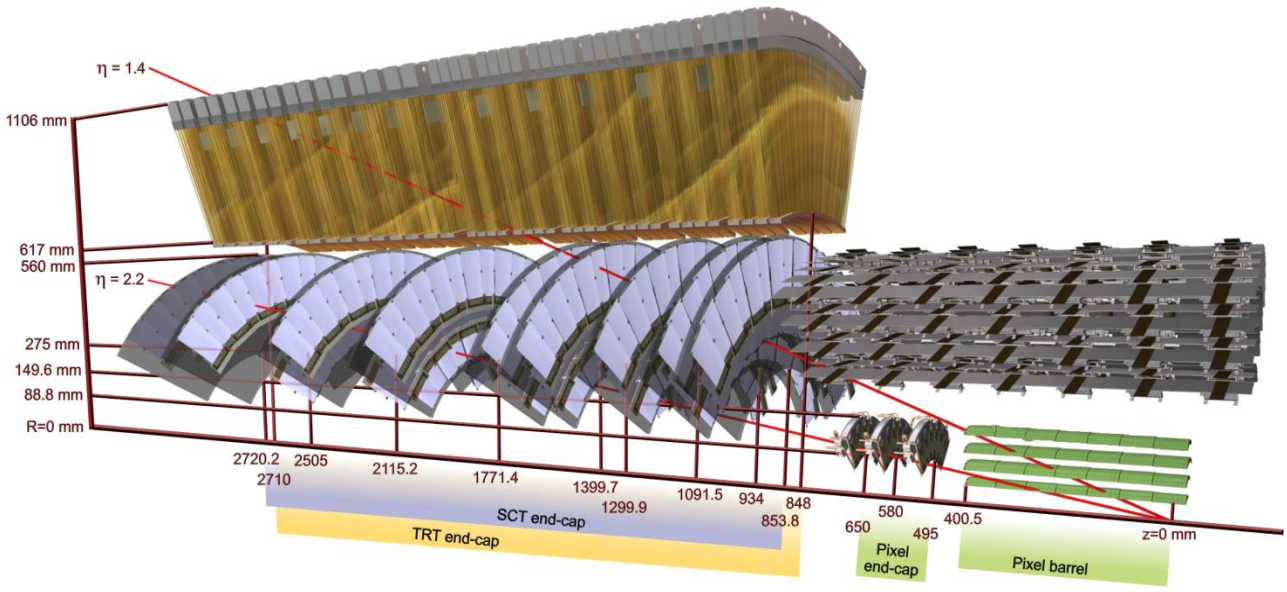

Figure 2.7 – Schematics showing the end-caps of the different layers of the Inner Detector.

Before the first layer of the ID there is the 0.8 mm thick beryllium beam pipe, starting at a radius of 29 mm, which contains an ultra-high vacuum for beam propagation. The choice of beryllium as a wall material is due to the desire to reduce particle showering and multiple scattering.

2.3.2.1 The Pixel Detector

The Pixel Detector [24] is the most close to the interaction point (IP) the part of the ATLAS detector and serves to provide high granularity track points to allow as high as possible tracking and vertexing performances. By reconstructing and extrapolating particle tracks back towards the IP, it can be determined if the particle originated from close to the primary vertex of the interaction, or if it was originated from displaced or secondary vertices that are product of particles that have a longer lifetime. In this case 'long-lived' is on the order of picoseconds, which is enough time for a particle to travel a few mm. To be able to distinguish these vertices, the resolution of the pixel detector should be as small as possible in fact it has a position resolution of 10 μm in the $r-\varphi$ plane and 115 μm along Z .

The Pixel Detector is constructed from four barrel layers, including the Insertable B-Layer (IBL) added in 2014 (more details about upgrade Phase 0 in the section 3.2) and six end-cap discs, three on either side (Figure 2.8). Each of the barrel layers is placed at 33.25 mm, 50.5 mm, 88.5 mm and 122.5 mm from the IP respectively (Figure 2.6).

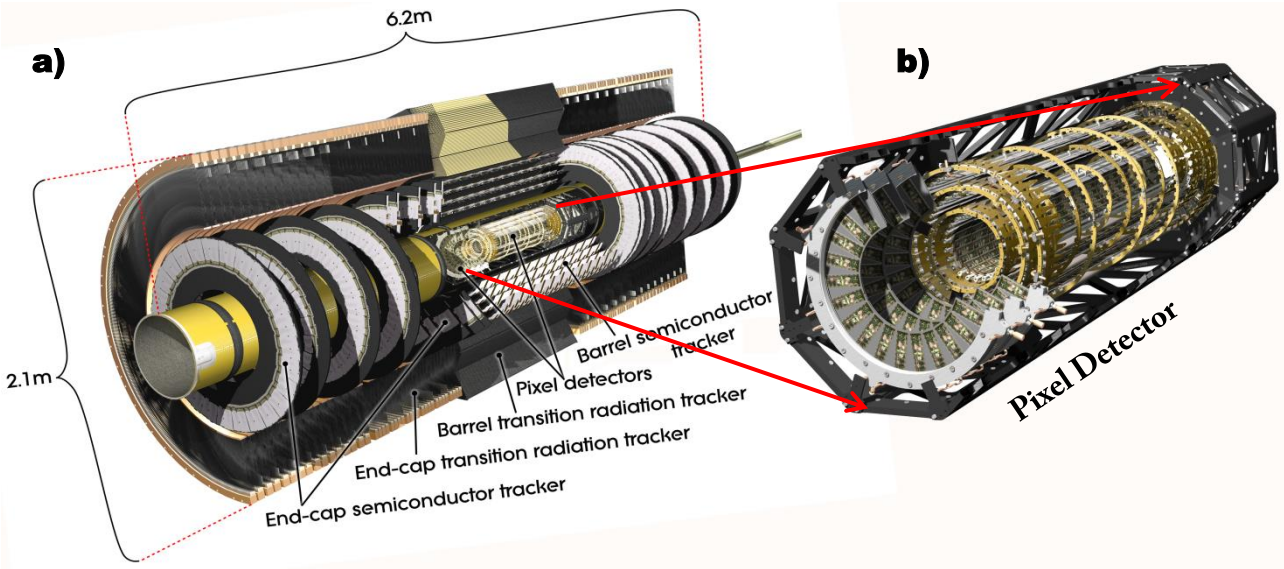

Figure 2.8 – a) Schematic view of the Inner Detector for experiment ATLAS. b) The ATLAS pixel sub-detector. Image courtesy of the ATLAS Experiment at CERN, http://atlas.ch.

In general, the three original layers of the PD consist of 1744 modules (Figure 2.9) of 2 by 6 cm size. Each module contains 16 FE-I3 [25] readout chips flip chipped to a 250 μm thick silicon sensor. The MCC is the Module Control Chip which controls the front end readout card. In general, the function of the MCC is to distribute the command signals to the attached FEs and to collect the data signals from these in order to merge them into one common module data stream. This electrical data stream will be converted then into optical signals.

The sensor has 47232 pixels arranged in 144 columns and 328 rows. The standard pixel size is 50 x 400 μm^2. The IBL layer is equipped with a new FE-I4 [26] readout chips, which has an increased pixel matrix (80 columns by 336 rows) compared to the FE-I3 chip and decreased

pixel cell size to 50 x 250 μm^2, which improves the resolution along the beam direction. As sensors the IBL exploits 200 μm thick planar sensors and 230 μm thick 3D sensors [27] for the outermost four modules. All the barrel modules are overlapped on their mechanical supports in order to achieve hermetic coverage. For the IBL layer it is not possible to obtain the full geometrical coverage in Z-axis as the PD does, because there is not enough space for overlapping [53]. In total the PD comprised of over 92 million channels and covers more than 1.7 m^2 area.

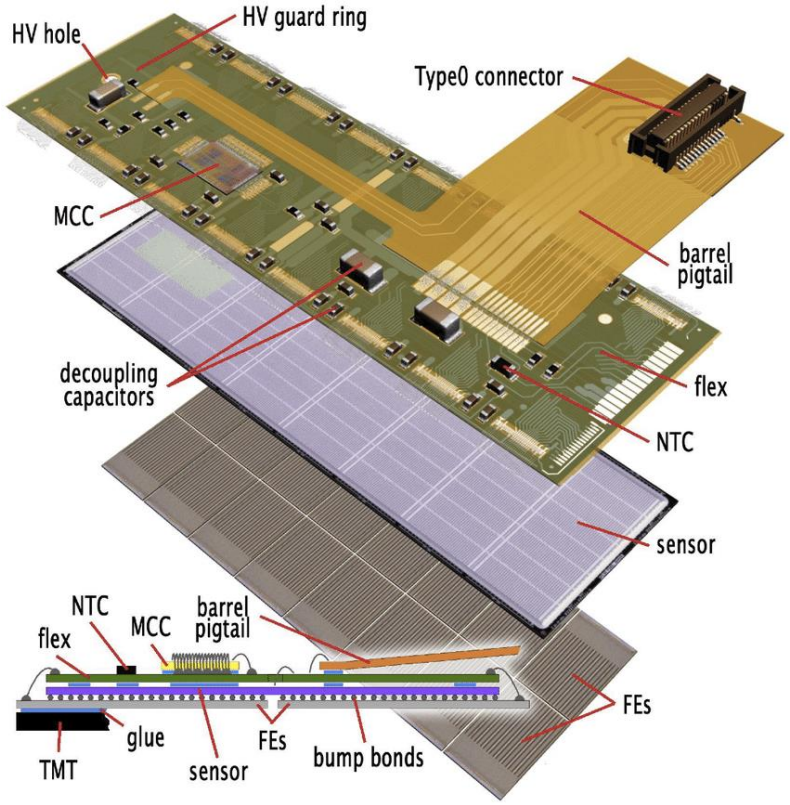

Figure 2.9 - An ATLAS Barrel Pixel Module. The hybrid structure consists of sixteen frontend (FE) chips, the silicon sensor tile, the flex and the barrel pigtail [28].

2.3.2.2 The Semi-Conductor Tracker

The middle layer of the ID is the Semi-Conductor Tracker (SCT) [29], which is made of 4088 double-sided silicon strip modules. Each side is mounted back-to-back and rotated to an angle of 40 mrad relatively to one another, providing possibility to measure position of the tracks in two dimensions. The sensor contains 1536 active strips of 123.2 mm length with 80 μm pitch. It gives a spatial resolution of 17 μm in the direction transverse to the strips ($r-\varphi$) and 580 μm in Z direction.

The silicon microstrip sensors are produced in a single side process. The chosen technique for the sensors and their readout is low cost and simpler in manufacturing and assembly. This makes the silicon microstrips particularly suitable to cover large surfaces at outer radii.

The SCT comprises 61 m^2 of silicon microstrip detectors with 6.2 million readout channels arranged into 4 cylindrical barrel layers and 18 planar endcap discs, providing a minimum of four space points for tracking.

2.3.2.3 Transition Radiation Tracker

The Transition Radiation Tracker (TRT) [30, 31] is the largest and the outermost part of the ID. It has a volume of 12 m^3 and consists of one barrel layer with axial drift tubes and two end-caps with radial drift tubes. The barrel is composed of about 50000 straws, each is 144 cm long and divided in two at the centre in order to reduce the occupancy and read out at each end. The end-caps contain 320000 radial straws of 39 cm long, with the readout at the outer radius. Each straw is 4 mm in diameter and contains in the centre a 0.03 mm diameter gold-plated tungsten wire, giving a fast response and good mechanical properties. Inside, the straws are filled with the a gas mixture of 70% Xe, 27% CO_2 and 3% O_2 and hold a potential difference of 1530 V with respect to the straw wall. Such TRT configuration provides a spatial resolution of 130 μm in φ.

Transition radiation (TR) occurs when an ultra-relativistic charged particle passes through the interface of the material with different dielectric constants. The TRT provides not only 36 additional space points for the track reconstruction, but additional information on the particle type that flew through the detector, allow to distinguish between electrons and hadrons, such as pions. The probability of emitting a TR photon is a function of the Lorentz factor - γ. At a fixed momentum, electrons will emit more transition radiation photons than charged hadrons. The number of TR photons detected in the TRT provides separation between electrons and charged hadrons.

2.3.3 The Calorimeter

The ATLAS Calorimeter system [32],[35] provides measurements of the energy of electromagnetic (EM) and hadronic showers, by stopping hadrons, electrons and photons forcing them to deposit all of their energy within the detector volume. It is also possible to measure the position of particle shower development.

The ATLAS calorimeters, as shown in Figure 2.10, consists of the Electro Magnetic Calorimeter (ECAL) covering the region $|\eta|< 3.2$, and the Hadronic Calorimeter (HCAL) barrels covering $|\eta|< 1.7$, end-caps covering $1.5 <|\eta|< 3.2$, and forward calorimeters covering $3.1 <|\eta|< 4.9$.
Both ECAL and HCAL are known as “sampling calorimeters”, it means that the calorimeter is composed of an absorbent layer to cause showering and an active layer for readout; these layers alternate until there has been sufficient material to measure the total energy of the charged or neutral particle. Compared to a homogeneous design, a sampling calorimeter has a better spatial resolution, but this is at the cost of the energy resolution.

2.3.3.1 Electro Magnetic calorimeter

The ATLAS Electro Magnetic Calorimeter (ECAL) [35] uses interleaved lead absorbers and layer of liquid argon (LAr) operated at a temperature of 87 K. The ECAL alternating sampling is done with layers of 2.1 mm gaps filled by LAr with readout electrodes in the middle, and lead absorber plates, typically 2 mm thick, all shaped in an “accordion geometry” as illustrated in Figure 2.11. The calorimeter has a barrel of 6.4 m long and 53 cm thick and two endcap parts of 2.077 m radius and 0.632 m thickness housed in three cryostats. It has 110,000 readout channels. When a particle crosses the LAr, an output signal, proportional to its energy, is created by the

drift of ionization electrons under high voltage. LAr has the advantage of a very good intrinsic linear energy response and radiation tolerance.

The design energy resolution is parametrized by:

$$\frac{\sigma_E}{E} = \frac{10\%}{\sqrt{E}} \oplus \frac{170MeV}{E} \oplus 0.7\% \tag{2.7}$$

where the energy E is expressed in GeV [34].

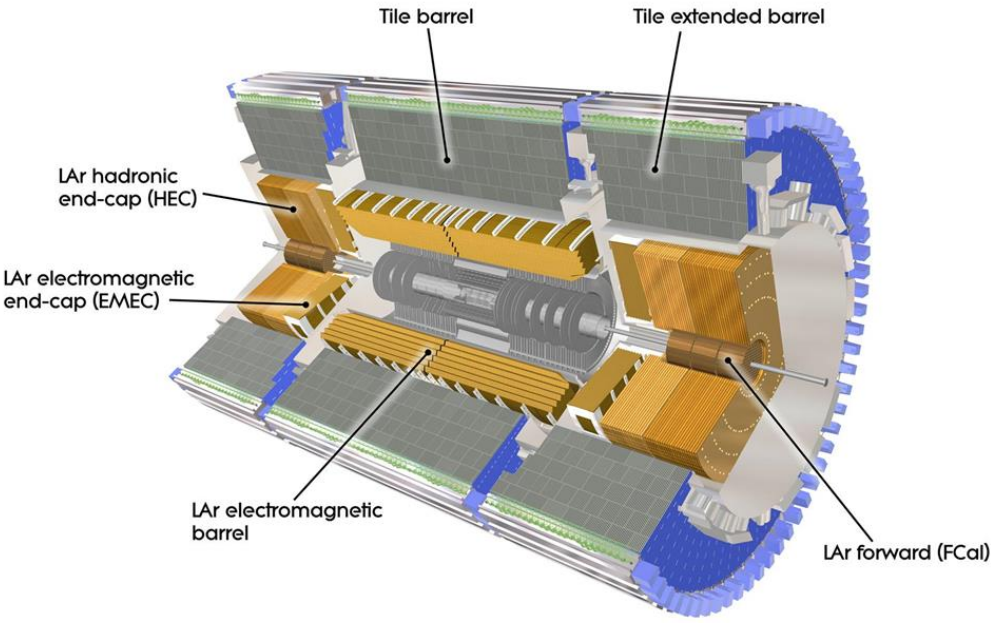

Figure 2.10 - Schematics of ATLAS calorimeters.

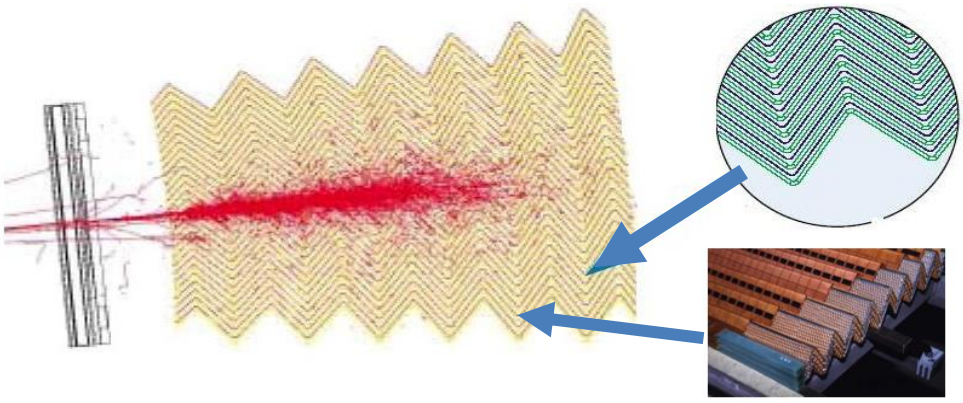

Figure 2.11 – The accordion geometry.

2.3.3.2 The Hadronic Calorimeter

The Hadronic Calorimeter (HCAL) [36] is functioned to stop and measure the energy of the particles, producing hadronic showers. The hadronic showers are much larger than EM ones, consequently the HCAL needs to be much bigger. The HCAL barrel part is divided into three sections: the fixed central barrel and two identical moveable extended barrels. The central barrel is composed of 64 wedges, each 5.6 m long and weighing 20 000 kg. Two extended barrels as well divided into 64 wedges, 2.6 m in length and 9600 kg in weight. The hadronic end-caps are made of copper and tungsten absorbers with LAr active layers. The end caps consist of two wheels of thickness 0.8 m and 1.0 m with radius 2.09 m.

The HCAL, also known as the Tile Calorimeter (TileCAL), is built of alternating iron tiles of 14 mm as absorbers and 3 mm plastic scintillating material coupled to optical fibers and read out by photomultipliers (PMTs). The charged particles create ultraviolet (UV) light, when they pass through the scintillators. This UV light is shifted in wavelength to visible light by a fibre, then collected and measured in two separate photomultiplier tubes on both sides of the scintillating tiles. In total, TileCal has approximately 5000 cells and 10 000 channels [40].

The required energy resolution of the hadronic calorimeters is [34]:

$$\frac{\sigma_E}{E} = \frac{52.9\%}{\sqrt{E}} \oplus 5.7\% \tag{2.8}$$

where the energy E is expressed in GeV.

2.3.4 The Muon Spectrometer

The Muon Spectrometer (MS) [38] surrounds the Calorimeter and it is the outermost system in the ATLAS detector. The MS is designed to detect the charged particles exiting the calorimeter, mostly muons, hence the name of the detector. Muons are about 207 times heavier than electron and due to this muons do not emit as much bremsstrahlung. This allows muons of a given energy to penetrate even dense materials far deeply and escape the detector volume.

The MS is responsible for the enormous size of the ATLAS detector. It has a large size to measures the muon tracks in the magnetic field. Also by measuring the track curvature the momentum of the muons can be determined. The magnetic field, created by a huge 8-coils superconducting barrel toroid and two end-cap toroids, is not uniform. The bending power - $I_B = \int Bdl$, depends on the muon initial direction, on its momentum and its charge. The magnetic field provides for typical bending powers of 3 T·m in the barrel and 6 T·m in the end-cap regions. [56].

There are four different detector technologies implemented in the different part of the MS as shown in Figure 2.12. In the barrel region ($\eta < 1$), the positions of the muons are measured in Monitored Drift Tubes (MDTs) [41] and Resistive Plate Chambers (RPCs) [43] arranged in three cylindrical layers around the beam axis. In the transition and end-cap regions $\eta < 2.7$, Thin Gap Chambers (TGCs) [44] and Cathode Strip Chambers (CSCs) [42] plus two disks per side of MDTs are used.

TGCs (440 000 channels) and RPCs (380 000 channels) are used for triggering and second coordinate measurement in the ends and in central part of detector respectively.

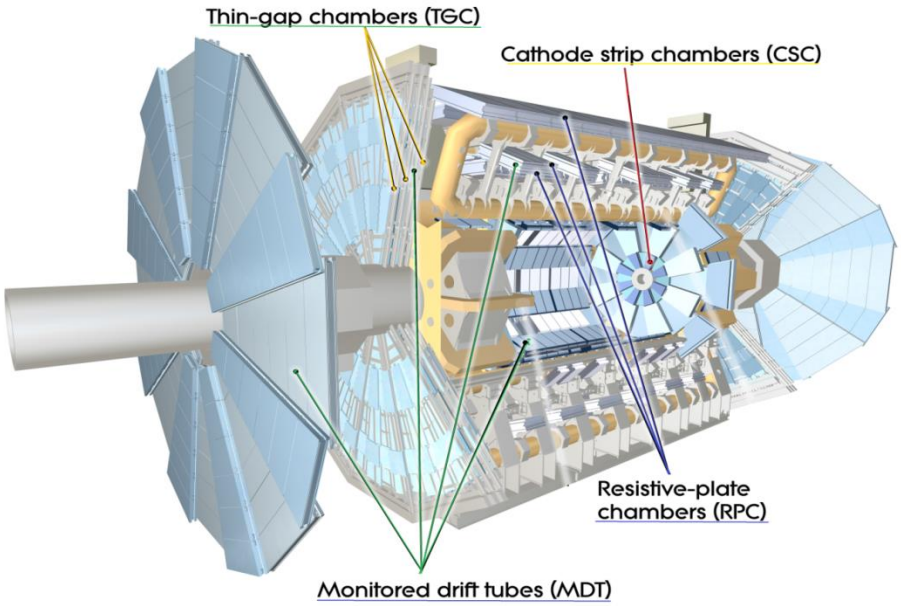

Figure 2.12 - Four different technologies are used in the ATLAS muon subsystem.

MDTs are represented by 1171 drift chambers with 354 240 tubes of 3 cm in diameter and 0.85 – 6.5 m long. They are used for the precision measurement of the curved track coordinates. It provides a single-wire resolution of about 80 μm.

CSCs are high granularity multi-wire proportional chambers with cathode strip. They are used close to the beam axis in forward direction, where the muon flux is higher, and in the innermost plane to withstand the demanding rate and background conditions. They provide spatial resolution up to 60 μm and high counting rate capability.

2.3.5. Triggering system and DAQ

In order to process an enormous volume of data from the ATLAS detector within nanosecond timescales, the trigger system [45] is used to reduce an event rate and to select only interesting for physics events fast and efficient. The data acquisition (DAQ) system is collecting the output data from the detectors, putting them into a coherent format and structure and then transporting only selected by trigger system events to permanent storage, where the data is available for further offline analysis.

The ATLAS trigger system represented in Figure 2.13 has three components: the Level-1 trigger (L1), the High Level Trigger (HLT) and Event filter.

The Level-1 is a fully hardware trigger, constructed with custom-made electronics, works on a subset of information from the calorimeter and muon detectors. The Level-1 trigger reduces within a time frame of 2.5 μs the data rate from 40 MHz to less than 100 kHz by selecting interesting events passing a set of criteria.

The HLT is a software based trigger, which is using over 20 000 CPUs to refine the analysis of the Level-1 trigger. It conducts a very detailed analysis either by performing overall examination of the whole event for selected layers of the detector (for example calorimeters, trackers, muon detectors), or, by utilizing the data in smaller and isolated regions of the detector. About 1 kHz events per second are selected by the HLT analysis and are fully assembled into an event record. And finally the Event Filter process perform code algorithms and further filter the events decreasing the data rate down to roughly 400 Hz. In Run-1 the ATLAS trigger system had separate Level-2 and Event Filter computer clusters. For Run-2, the system has been merged into a single event processing HLT farm, which reduces the complexity and allows for dynamic resource sharing between algorithms [33]. The new arrangement reduces code and algorithm duplication and results in a more flexible HLT. The average output rate of the HLT has been increased from 400 Hz to 1 kHz, as imposed by data storage constraints [33].

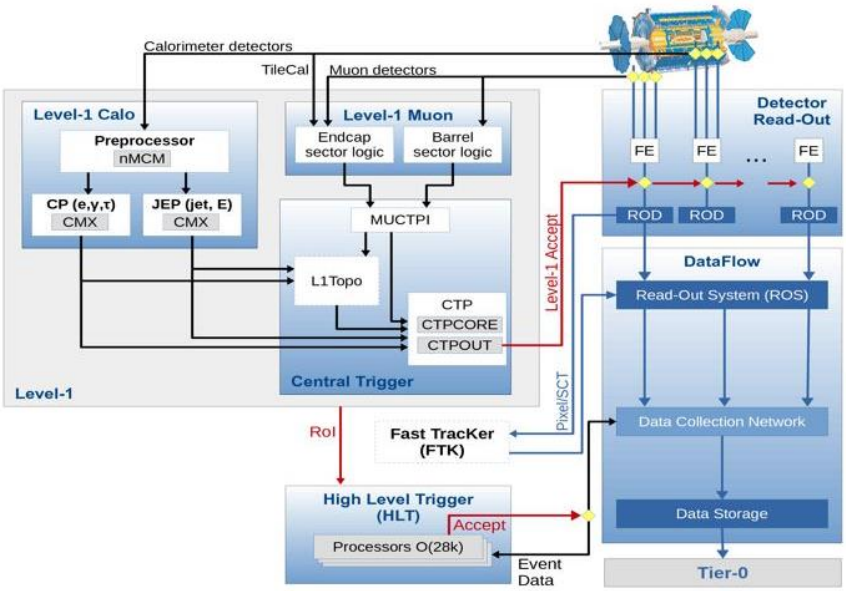

Figure 2.13 – ATLAS Trigger/DAQ system.

Chapter 3

Towards the HL-LHC and the ATLAS detector upgrade

Contents

The LHC, extending its discovery potential, has scheduled several upgrades of the accelerator complex to increase the luminosity and the collision energy. In the end the LHC will become the High-Luminosity-LHC (HL-LHC) to produce $4000\ fb^{-1}$ of integrated luminosity; this is about 10 times more data than is going to be collected during LHC's Runs combined. The HL-LHC will deliver proton-proton collisions at the energy up to $14\ TeV$ in the center of mass with the instantaneous beam luminosity up to $7.5\times10^{34}\ cm^{-2}s^{-1}$ [46].

The upgrades will substantially increase the statistics to achieve the high-precision studies of SM processes and searches for new physics BSM. But at the same time they will cause higher occupancy and increased radiation damage within the detector modules. To cope with the harsher running conditions and to maintain or even improve the actual performance and, eventually, to profit from the increased luminosity at the HL-LHC, the ATLAS detector will be upgraded. One of the most important improvements will be a complete replacement of the ID with a new all-silicon Inner Tracker (ITk) [47] [48].

This chapter gives an overview of the main requirements and planned upgrades of the ATLAS detector focusing mainly on the Inner Detector. The main improvements in pixel detector technologies during the IBL Phase-0 upgrade as well as an innovative Inner Tracker (ITk) layout and pixel sensors and electronics R&D progress to fulfill the requirements for the Phase-2 ATLAS upgrade are described in section 3.2 and 3.3 respectively. The Outer Barrel Demonstrator project as a preparation step to the ITk construction is presented in section 3.4. In the section 3.5 my contribution to the Demonstrator project is given.

3.1 Motivation for the HL-LHC

After the Higgs boson discovery [12] which is certainly a great success for the ATLAS and CMS experiments, as well as for the LHC project as a whole, the LHC programme is far from over. The measured properties of the Higgs boson are going to be refined with the analysis of more data, improved with higher statistics, which could be achieved by increasing the luminosity an important parameter of the collider defined by (2.2). The increase of the luminosity will lead to higher collision rate giving an opportunity to explore some expected rare processes with small cross sections, as well as to increase the sensitivity to new physics searches. Therefore the LHC evolution to the High Luminosity phase is foreseen.

The aim of this new phase, called HL-LHC, is to provide a substantial increase of the instantaneous luminosity up to $5-7.5\times10^{34}\,cm^{-2}s^{-1}$ and to collect a total integrated luminosity of $4000\ fb^{-1}$ with an average of $200-300\ fb^{-1}$ per year to exploit the further discovery potential of the machine in a reasonable operation time of 10-12 years. The HL-LHC will offer us the opportunities to precisely measure the Higgs coupling using as many Higgs production and decay channels as possible. It will allow the exploration of Higgs potential by studying Higgs-boson pair production. Also, better track parameter resolution, which is expected with the detector upgrades, will lead to better mass resolution in the results of physics analysis. The running time of the LHC towards the HL-LHC is divided into several data taking periods, called runs, by long shutdowns for accelerator and detector maintenance and upgrades in the periods of 2013-2014 for LS-1, 2019-2020 for LS-2 and 2024-2026 for LS-3, as illustrated in Figure 3.1.

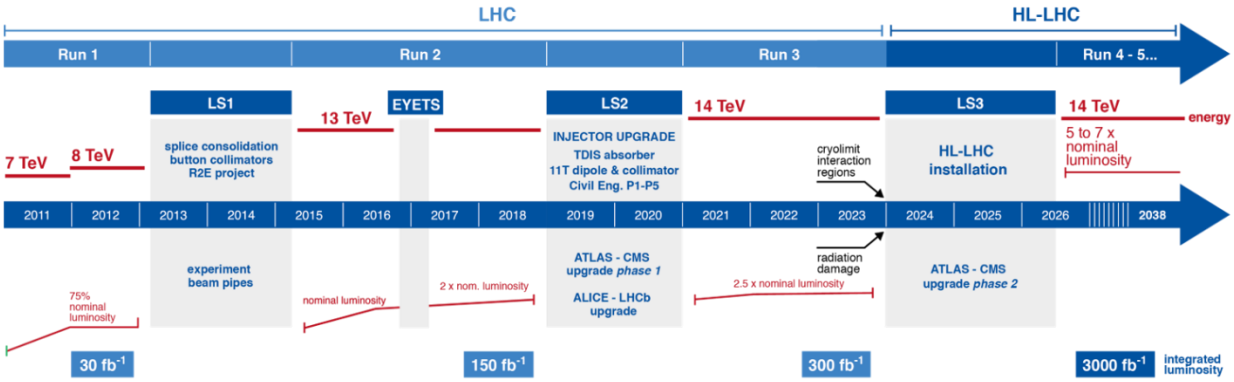

Figure 3.1 – The LHC baseline plan for the upcoming decade in terms of collision energy (upper line) and luminosity (lower lines). [50]

The LHC started its operation in 2011 at a reduced $\sqrt{s}$ =7 TeV and then continue at $\sqrt{s}$ =8 TeV until the first shutdown period, known as LS-1. The LS-1 was used to make the consolidation of the electrical splices between the superconducting magnets (and many other consolidation actions) in order to prepare the machine for the operation at $\sqrt{s}$ =13 TeV. After LS-1 the LHC was able to reach the nominal design luminosity of 1×10^{34} $cm^{-2}s^{-1}$ and even to double it during Run-2 (2015-2018). Throughout LS-1 the Insertable B-Layer (IBL) [53] was inserted in the pixel detector as the innermost additional layer. More details on the IBL upgrade is discussed in the next section 3.2.

The second long shutdown (LS-2) is focused on a preparation of the injectors and collimators for the LHC. The current Linac 2 is going to be replaced with the more powerful proton linear accelerator Linac 4, as well as the Proton Synchrotron Booster output energy is planned to

increase. During LS-2 the ATLAS detector will be changed in the outer parts. Among the main upgrades to the detector systems are those to the Liquid Argon (LAr) calorimeter electronics and the replacement of the inner stations of the endcap muon system of the MS with a New Small Wheel (NSW) detector to improve the muon Level-1 trigger system to reduce the overall data-taking rate. Also, to handle luminosities well beyond the nominal values, a new hardware-based Fast Tracker (FTK) is being added to process data from the silicon tracking detectors in the ID, aiming to reconstruct charged particle tracks within a latency that is short enough for the tracks to be used at the start of the High-Level Trigger (HLT) processing [53].

After the Run-3 of data taking at $\sqrt{s}$ =14 TeV, scheduled from 2021 to 2023, the final long shutdown (LS-3) is foreseen before starting the HL-LHC phase. To maintain the instantaneous luminosity about seven times higher than the nominal value, many systems of the LHC machine like cryogenic system, some RF cavities, inner triplet magnets to provide much focused and dense beam at the collision points, will be upgraded.

At the same time, the ATLAS detector will undergo major changes, because of increased workload and radiation degradation of the detector systems. The higher event rates and event sizes will be a challenge for the trigger and data acquisition (DAQ) systems, which will require a significant expansion of their capacity. For the muon system, a complete replacement of the readout electronics is foreseen, together with additional upgrades of the trigger systems, which will allow the implementation of a track trigger improving the ATLAS triggering capabilities. The calorimeters will receive new front-and back-end electronics, as these are subject to significant radiation exposure and have to meet the increased radiation tolerance requirement for higher background. The ID will be replaced by a new all-silicon tracker, called Inner Tracker (ITk) (more details will be given in the section 3.3), with an extended geometrical acceptance up to $|\eta| = 4.0$, and based on a new layout featuring high granularity, improved material budget and increased radiation hardness.

3.2 IBL Upgrade Phase 0

During LS-1 the so-called Phase-0 upgrade of the ATLAS Detector was implemented. The Insertable B-Layer (IBL) was included in the Pixel detector as an additional pixel layer, the closest to the beam line, located at the radius of 3.325 cm. To perform such manipulation together with the IBL a new smaller beam pipe section employing an inner radius of 2.5 cm was inserted instead of the old beam pipe with radius of 2.9 cm.

Figure 3.2 - (a) Photograph of the ATLAS pixel layers and the beam pipe before the IBL insertion.

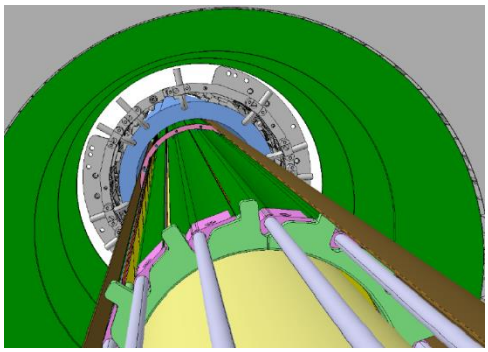

(b) Rendered image showing the location of the ATLAS Insertable b-Layer. Images are from [53]

The primary physics driver of the IBL upgrade was to enhance the lifetime tagging of b-flavoured hadrons. The new pixel layer provides high precision track measurements close to the IP, improving the track extrapolation back to the primary vertexes.
The IBL consists of 14 staves (mechanical support structure of the detector), each stave is CO_2 cooled and can contain 32 (16) single chip (double-chip) modules. Actually, an IBL stave has 12 modules (75%) of planar n-in-in sensors and 8 modules (25 %) of 3D silicon sensors, as illustrated in Figure 3.3. The details about different sensor technologies will be described in the Chapter 5.

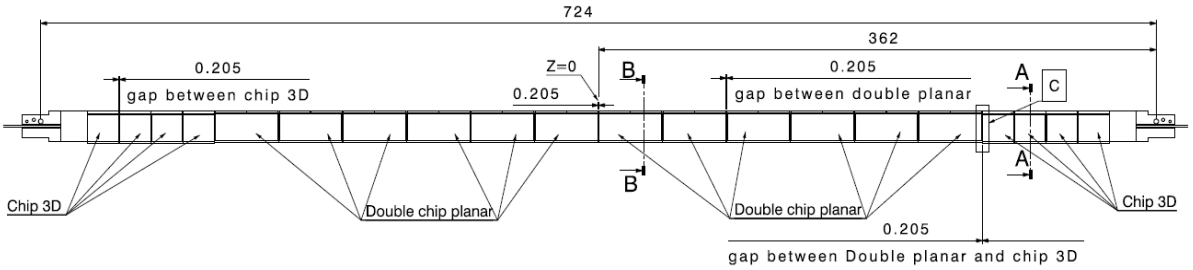

Figure 3.3 – Diagram of the IBL stave layout. 3D sensor modules are located in the high η region. The gaps between neighboring modules is fixed at 0.205 mm. [57]

The modules employ a newly designed readout chip, the FE-I4 [26], which features a larger area with a reduced pitch and improved radiation hardness than the former FE-I3 chip [25] used in the original pixel detector. The key characteristics are summarized in the Table 3.1. A new FE-I4 readout chip is designed in a 130 nm CMOS technology, presenting advantages in terms of digital logic density, power consumption and radiation hardness compared to the 0.25 µm CMOS technology used for the ATLAS pixel front-end chip. The FE-I4 is qualified to work up to 250 MRad of total ionising dose.

	FE-I3	FE-I4
Year	2003	2010
Feature size	250 nm	130 nm
Chip size	7.6×10.8 mm^2	20.2×18.8 mm^2
Active area	74%	89%
Size of pixel array	18×160 (2880)	80×336 (26880)
Pixel size	50×400 μm^2	50×250 μm^2
Number of transistors	3.5 M	87 M
Data rate	40 Mb/s	320 Mb/s
Wafer yield	80%	70%

Table 3.1 – Key features of FE-I3 and FE-I4 read-out chips.

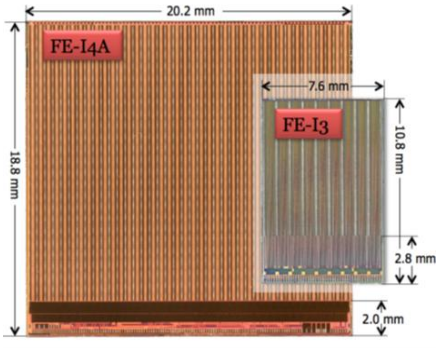

Figure 3.4 – The size comparison between FE-I3 and FE-I4 chips.

Each pixel cell contains an independent, free running amplification stage with adjustable shaping, followed by a discriminator with independently adjustable threshold. The FE-I4 keeps track of the time-over-threshold (ToT) of each discriminator with 4-bit resolution, in counts of an external supplied clock of 40 MHz frequency [58]. The larger chip area (Figure 3.4) and the higher active fraction of the footprint compared to the precedent chip were essential to build a compact layer with high geometric acceptance.

The silicon planar sensors were thinned to 200 µm and an inactive area at the sensor edges was visibly reduced due to the new design of a guard ring structure from 1100 µm to 200 µm, as

shown in Figure 3.5. The pixel pitch became smaller (50×250 μm^2) to decrease the occupancy and to improve the resolution in the longitudinal direction.

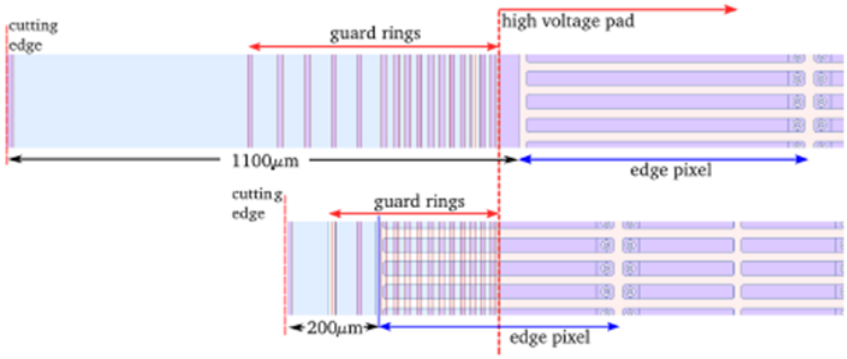

Figure 3.5 – Comparison of the cutting edge of the pixel sensor between the current pixel layer (top) and IBL layer (bottom).

The IBL installation was completed in spring 2014. The higher granularity of readout chip and sensor helps to maintain and improve the tracking and b-tagging efficiency to withstand the development of the fluence and the larger number of pile-up events expected for Run-2 and Run-3. Moreover, the IBL provides compensation for the expected degradation of the original pixel detector due to radiation damage. During the development and installation of the IBL layer many technical challenges were dealt, novel technologies and ideas were adopted to build pixel detectors, providing valuable experience for the future pixel detector developments. The FE-I4 readout chip was extensively used for new silicon sensor R&D for the ITk ATLAS upgrade. Moreover, it is using in many qualification and performance tests for the projects towards the ITk construction for the HL-LHC, like the pixel Outer Barrel Demonstrator project I have contributed to during my thesis work.

3.3 The ITk Phase-2 upgrade

As was discussed in the section 3.1 the evolution of the LHC to the HL-LHC is foreseen during the LS-3 from 2024 to 2026. The HL-LHC will present a unique challenge for the ATLAS detector and the tracking system specifically. The increased instantaneous luminosity up to $\mathfrak{L} = 7.5\times10^{34}$ $cm^{-2}s^{-1}$ will result in much higher detector occupancy, the number of pile-up events is expected to be 140-200 per beam crossing. This number is about five times higher than the pile-up value the ID was designed for, namely, 25 events at the nominal LHC luminosity. Moreover, the performance of the PD and the SCT will degrade with the increase in integrated radiation dose by approximately a factor of ten. The current Pixel detector was designed using radiation-hard sensors and electronics to withstand the radiation damage that is equivalent to an integrated luminosity of 400 fb^{-1}. Similarly, the Semi-Conductor Tracker (SCT) was designed and constructed to operate up to an integrated luminosity of 700 fb^{-1}. The IBL itself was designed for integrated luminosities equivalent to roughly 850 fb^{-1} [48]. Accordingly, to exploit fully the physics potential of the HL-LHC, maintaining an optimal tracking and b-tagging performance in the harsh environment up to 4000 fb^{-1} a replacement of the whole tracker with all-silicon new system will be necessary.

The design of the new tracking detector (ITk) assumes five layers of pixel detectors surrounded by four layers of strip detectors. The total silicon surface of the pixel detector will be about 13 m^2 and 160 m^2 for the strip detector in comparison with the current 1.7 m^2 and 60 m^2 for the PD and the SCT respectively. The five successive barrel pixel layers L0 to L4 will be placed at radii of 39 mm, 99 mm, 160 mm, 220 mm and 279 mm. The proximity to the collision point means that the pixel detector will be exposed to very large radiation levels over the full HL-LHC run period. Due to this, the ITk detector will be built in such a way, that it will be possible to replace the two innermost pixel layers after collected 2000 fb^{-1} of a total integrated luminosity. In this scenario, according to the radiation background simulations, performed for the ATLAS ITk using the FLUKA particle transport code [59] and the PYTHIA8 event generator [60], the predicted maximum 1 MeV neutron equivalent fluence for the innermost layer L0 is about $1.4 \times 10^{16} n_{eq} / cm^2$ and about $10^{15} n_{eq} / cm^2$ for the outermost layer (see Figure 3.6) including a safety factor of 1.5 [48].

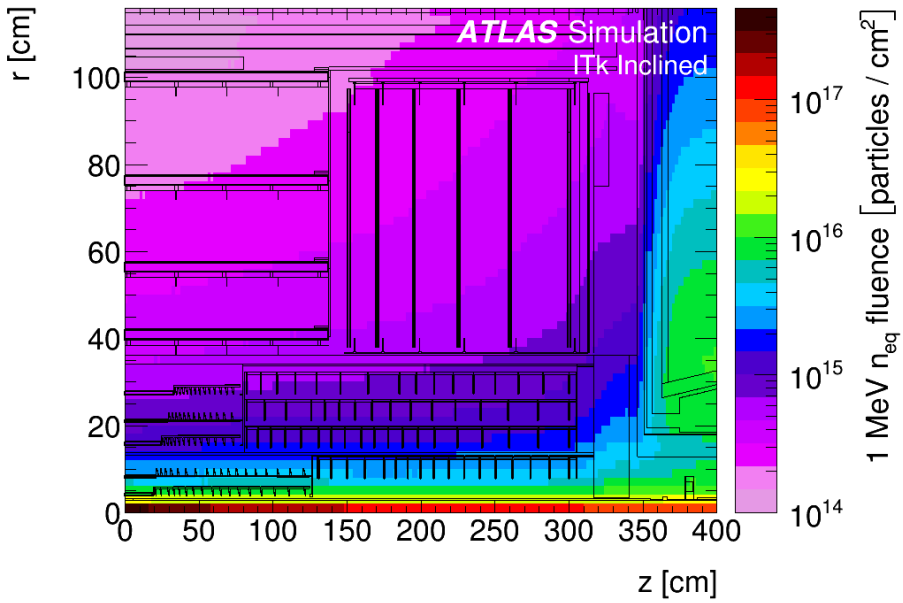

Figure 3.6 - The 1 MeV neutron equivalent fluence distributions for the ITk layout [48].

The final ITk layout, called "Inclined Layout", is shown in Figure 3.7. It opens up an extension of the tracking coverage to a pseudorapidity of $|\eta| = 4.0$ while maintaining excellent tracking efficiency and performance to fully exploit the physics potential of the HL-LHC. The combined Strip plus Pixel Detectors provide a total of 13 hits for $|\eta| < 2.7$, with the exception of the barrel/end-cap transition of the Strip Detector, where the hit count is 11 hits [47]. Such ITk performance is made possible by novel ideas implemented in its design.

3.3.1 The innovative design concepts for the ITk pixel detector

The design of the ITk benefits from the enormous amount of experience gained over more than two decades in the construction and operation of the existing inner tracking detector. The ITk will be based on the highly successful concept of "Hybrid Pixel Detector" developed for and implemented in the present ATLAS Pixel Detector and in the IBL. However, in view of the

harsh operational environment at HL-LHC the particular requirements for pixel detectors must be fulfilled, which is impossible without the development and implementation of new technical solutions.

The first innovation is the inclined barrel stave design, where the flat barrel stave is prolonged with a section with inclined modules. This concept minimises the amount of silicon needed as inclined modules have a larger angular coverage in this region. The second novel concept is the end-cap ring system instead of the typical end-caps to best facilitate the space constraints. The layers of pixel rings extend the coverage in z and allow routing of the service separately along each ring layer [47].

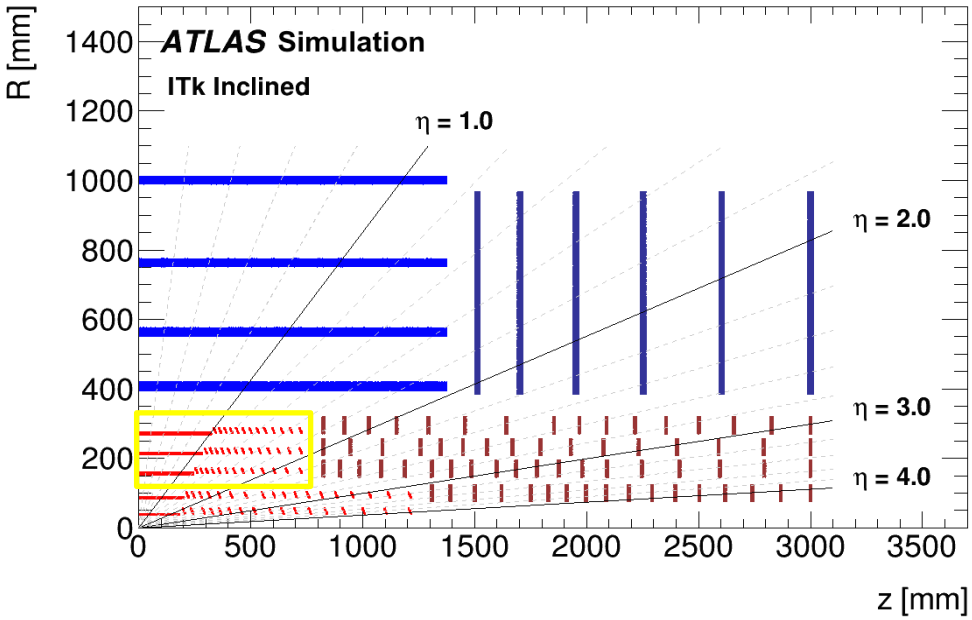

Figure 3.7 - Schematic layout of the ITk for the HL-LHC phase of ATLAS as presented in [47]. The active elements of the barrel and end-cap Strip Detector are shown in blue, for the Pixel Detector the sensors are shown in red for the barrel layers and in dark red for the end-cap rings. The outer barrel layers are highlighted by yellow.

Due to the high particle density at the HL-LHC the detector occupancy is going to be diminished by reducing the pixel cell size from $50 \times 250\ \mu m^2$ using in the IBL and $50 \times 400\ \mu m^2$ to either $50 \times 50\ \mu m^2$ or $25 \times 100\ \mu m^2$. For this reason the new more radiation tolerant and fast read-out chip with the cell size of $50 \times 50\ \mu m^2$ was developed using 65 nm CMOS technology. This chip is compatible with both $50 \times 50\ \mu m^2$ or $25 \times 100\ \mu m^2$ sensor pixel sizes. The first prototype, called RD53A [61], has been already tested and characterized, in particular the results on irradiation tests and from the test beams are presented in Chapter 7. The characteristics of the RD53A chip are summarized in Table 3.2 in comparison to the FE-I4 chip.

There are few sensor technologies chosen to instrument the pixel layers of the ITk. The 3D sensors will be used in the innermost layer in use single and double chip modules, as they are intrinsically more radiation tolerant than other available sensors. Also they operate at lower voltages, hence the power dissipation will be less. The remaining three layers will employ planar sensors formed quad and dual modules. For a potential cost reduction, CMOS sensors may be used to instrument the large area of the fifth barrel layer. More details on sensor technologies will be given in Chapter 5.

For the planar sensors which will be used in L1, L2, L3, L4, n^+-in-p technology is chosen. This technology represents a potentially cost-effective option compared to the present n^+-in-n planar sensors, because of the single-side processing. Moreover, n^+-in-p technology is more radiation hard as it will not undergo space charge sign inversion (SCSI) in the bulk as discussed in section 4.4.1.

	RD53A chip	**FE-I4 chip**
Technology	65 nm	130 nm
Size	20.1×11.9 mm^2 (50%)	20.2×19.0 mm^2
Pixel size	50×50 μm^2	50×250 μm^2
Pixel array	400×192 (50%)	80×336
Pixel capacitance	<100 fF (200 edge)	<500 fF (700 edge)
Hit rate	3 GHz cm^{-2}	400 MHz cm^{-2}
Trigger rate	1 MHz	200 kHz
Trigger latency	12.8 μs	6.4 μs
Current consumption	8 μA/pixel	20 μA/pixel
Radiation tolerance	0.5-1 Grad	300 Mrad
Minimum stable threshold	600 e^-	1500 e^-
Readout data rate	1.28 Gb/s	160 Mb/s

Table 3.2 - A subset of the specifications for the RD53A demonstrator readout chip. The final RD53B chip will be increased twice in size.

The next concept will be implemented in the ITk is the use of the sensors with reduced thickness from 200 μm and 250 μm (in the current ID) to 100 μm (L1) and 150 μm (L2, L3, L4). This option will reduce the material budget and consequently the multiple scattering within the tracking devices and improve the energy resolution of the calorimeters. The ITk design foresees no more than 2 radiation lengths X_0 (see formula (4.1)) in any direction up to $|\eta| = 6.0$, which is significant improvement compared to about $6\,X_0$ for the present detector including services. Furthermore, the reduced sensor thickness leads to an increased radiation tolerance. As discussed in section 4.5, the charge trapping has a great contribution in loss of pixel efficiency after irradiation. Reducing the sensor thickness we lower the probability for charge carrier trapping during the collection time. Also, the lower operational voltage for the thinner sensors results in reduced power dissipation. Another advantage concerns the reducing readout bandwidth requirements, since the inclined tracks will result in less number of pixels traversing the thinner sensors.

The backside implantation in n^+-in-p planar technology can be extended to the sensor borders to create a rectifying junction reducing the defects induced by the cutting. This helps to decrease a number of guard rings and thus to reduce an inactive area at the peripheries of the sensors. Moreover, since the electric field extends up to the side implantation, it makes sensor to be fully efficient up to physical edge. This design, called an active edge, is used to produce edgeless sensors with a reduced down to 50 μm distance between the last pixel implant and the sensor edge by FBK and ADVACAM companies. More details about the active edge technology will be given in the section 5.2.1.2, as well as, the results of the test beam measurements with the sensors of the active and slim edge design produced by ADVACAM are presented in section 6.4.

The active edge sensor design allows for high tracking efficiency and maximizes the geometrical acceptance of the detector, which is important for the inner layers in the ITk.

All these new approaches in pixel detector technologies are the result of generative R&D activities, simulations and experimental work. Many intensive test beam campaigns, to which I have contributed testing the sensors of active edge design, have been performed to evaluate the detector performance and choose better technology. Much work also needs to be done to implement these new concepts during the construction of the ITk. For this reason, the creation of the detector stave demonstrator is very important. It can help to test different system solutions in close to the real operation conditions and to verify the production and testing infrastructure at all stages of creation of working final stave prototype for the ITk. The demonstrator project and my contribution to this will be given in the next section.

3.4 The Outer Barrel Demonstrator project

The Pixel Outer Barrel Demonstrator project is a successful collaboration between many institutes, which was initiated to build and test the functional stave of the new pixel tracker, to test many integration steps and to prepare for the ITk construction phase. Moreover, the demonstrator project was an important preparatory step for the research institutions to organize the Market Survey, the procedure to qualify the pixel sensor foundries, which is now ongoing. Samples of single-chip and multi-chip sensors are being required to be produced by the participating companies and a campaign of measurements before and after irradiation is being organized to validate that the samples provided will be inside the ATLAS ITk specifications.

The outer barrel region of the Pixel Detector for the ITk, illustrated in Figure 3.7, comprises three sensing layers (Layer 2, Layer 3, and Layer 4) at different radii. Each layer featuring three sections: a central flat part where the pixel modules are parallel to the beam pipe and two tilted regions, one at either end. This is a new concept in the design; previously the inclined modules were not used in the ID. In the inclined region the normal of the active elements forms a 56^0 angle with respect to the beam axis. The proposed local support concept for this area of the detector relies on two main design elements: “cells” to achieve the desired thermal performance, and “longerons” to support the cells and achieve the necessary structural stiffness [47]. The longerons (see Figure 3.8) are made from a blend of high and ultra-high modulus fibres. And

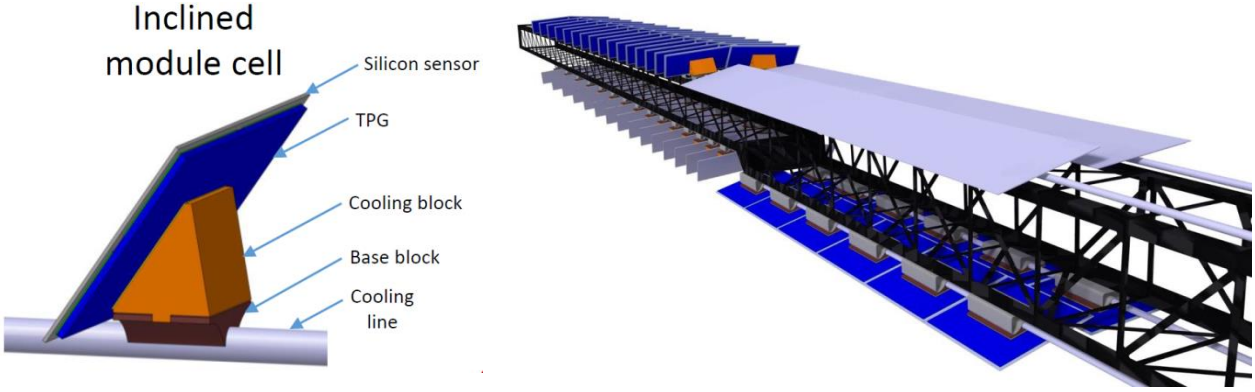

Figure 3.8 – Left: Schematic representation of a tilted module cell. Right: A typical longeron supporting four cooling lines.

each cell, either it is a flat or an inclined one, contains a silicon pixel module supported by a thermal pyrolytic graphite (TPG) plate, used as a heat spreader, which is glued to a cooling block made of a highly conductive, lightweight material such as aluminium-carbon fibre or graphite.

Also, the novelty of the ITk pixel detector is use of multi-chip modules. The stave will be equipped with inclined dual (two FE chips per one large area sensor) and flat quad (four FE chips per a sensor) modules. This is necessary to reduce the total amount of modules which is beneficial for both production and loading to the stave points of view.

Based on this, for each type of module cell, the special connection from the FE chips to the off-detector readout system must be developed, providing an efficient data and other control signals transferring, high and low voltage supplying, keeping a low material budget and showing high radiation tolerance. A serial powering (SP) scheme will be used for the ITk Pixel Detector. It will reduce the number of cables and the amount of inactive material in the tracker. For using this scheme the FE chip must be equipped with the special power regulators called ShuLDOs (a combination of the word shunt and the acronym for Low Drop Out regulator), which allow regulation of voltage on chip while drawing a constant current from an external power source. That also means constant power consumption during the operation, which prevents temperature fluctuations that would limit the mechanical stability of the detector. New elements are required to operate and monitor a serially powered detector, including a Detector Control System (DCS), constant current sources and front-end electronics with shunt regulators.

Many new concepts are planning to be implemented in the ITk, but before they all have to be proven and tested. The goal of the Demonstrator Project is to build several prototypes of the ITk pixel detector stave designed to investigate different aspects like: cell loading, mechanical integration, thermal performance, electrical and data transmission services. The list of the demonstrator prototypes with their description, which are anticipated in the frame of the project, is given:

- A short electrical prototype, to perform tests on the SP chain and readout scheme. It consists of a short support structure with one cooling line (CL) and 7 quad *electrical modules* (i.e. real pixel sensors wire-bonded to the real FE readout chip)
- A short thermal prototype, to study the average thermal properties of the system. It consists of a short support structure equipped with 7 silicon *heater modules (heaters)*. The heater modules (also called thermal) are designed as a cheap alternative to the real modules. Each module has the same size of an electrical module (either a “doublet" - corresponding to the size of an electrical module wire bonded to two readout chips - or a quad). The heater module has two lateral bus bars on its sides, which can be contacted in order to force a current to flow through the silicon from one side to the other, such that the dissipated thermal power due to Ohm's law (I^2R) is of similar size as the expected one dissipated by the front-end chip. The heater also includes several resistive temperature sensors which, once their resistance vs temperature R(T) response is calibrated, can be used to infer the module temperature by measuring the resistance and so to determine the temperature field inside the demonstrator barrel.
- A thermo-mechanical prototype: one full-scale longeron with 4 cooling lines (Figure 3.8), with services and cells (i.e. modules + support structure for integration) added in steps to study deformations.

- A long thermal prototype made of 1 full-scale longeron (1.6 m long) with one cooling line equipped with 46 cells loaded with heaters: 14 quad-size heaters (in the “flat" section of the longeron) and 32 doublet-size heaters in the “inclined" section, to evaluate the thermal performance changes along the cooling line.
- A full demonstrator (Figure 3.9): a full-scale longeron with four cooling lines, one fully equipped with electrical doublet and quad modules, and three fully equipped with thermal modules.

The Demonstrator program aims to assemble a fully-functional prototype implementing a system design and layout solution for the three outermost layers of the ITk Pixel Detector, including required infrastructure for testing the full system. Not all components will be in their final form,

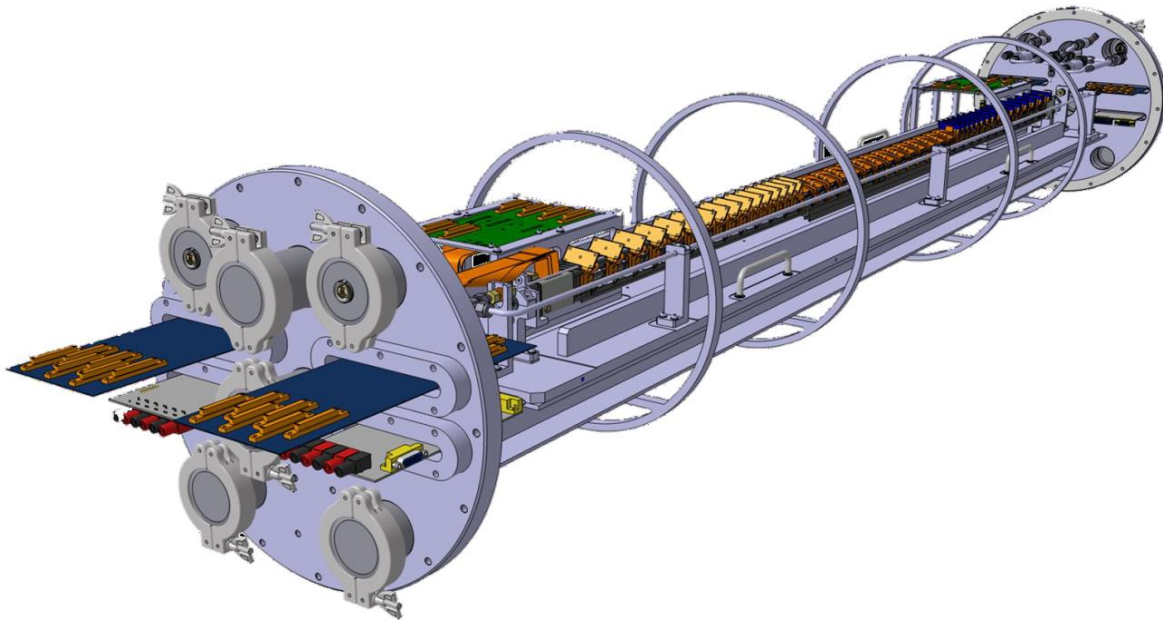

Figure 3.9 – A model picture of a full-scale demonstrator.

but still allow verifying and qualifying different concept and gaining experience in building and operating larger systems, and performing system tests with various prototypes. The final demonstrator will use as a readout electronics the already exist FE-I4 chip, the readout ASIC developed for the IBL pixel layer. This readout chip already includes a shunt regulator required for operation in a SP chain. In total the demonstrator will include about 120 FE-I4 chips that have to be tested and assembled. The demonstrator project brings together more than 20 institutions, including the three laboratories from the Paris area (LPNHE-Paris, LAL-Orsay, and CEA- Saclay) which work in synergy as a single “Paris cluster" for the final ITk module construction. A personal technical contribution on specific tasks related to this collective task will be detailed in the following paragraph.

3.5 Contribution to module assembly for the Demonstrator project

The contribution on the Demonstrator project efforts consists of producing 40 thermal and 5 electrical module assemblies for the long thermal and the full demonstrators being built at CERN. In this part, the following tasks will be described:

- Thermal and electrical modules assembly using the CERN jig tooling;
- Performing tests: visual inspection, the calibration of the resistive temperature detectors (RTD) with a probe station and in the climate chamber after the assembly and wire bonding process.

3.5.1 Resistive temperature detectors calibration

To build a full size thermal prototype of the ITk stave for studying its thermal properties and testing the performance of an innovative cooling system, the special silicon sensors are produced to be installed on the demonstrator to measure the temperature field and to fulfill a geometrical acceptance of the real sensors. Such silicon sensors, called heaters, are produced on 300 μm thick silicon wafers, as shown in Figure 3.10.

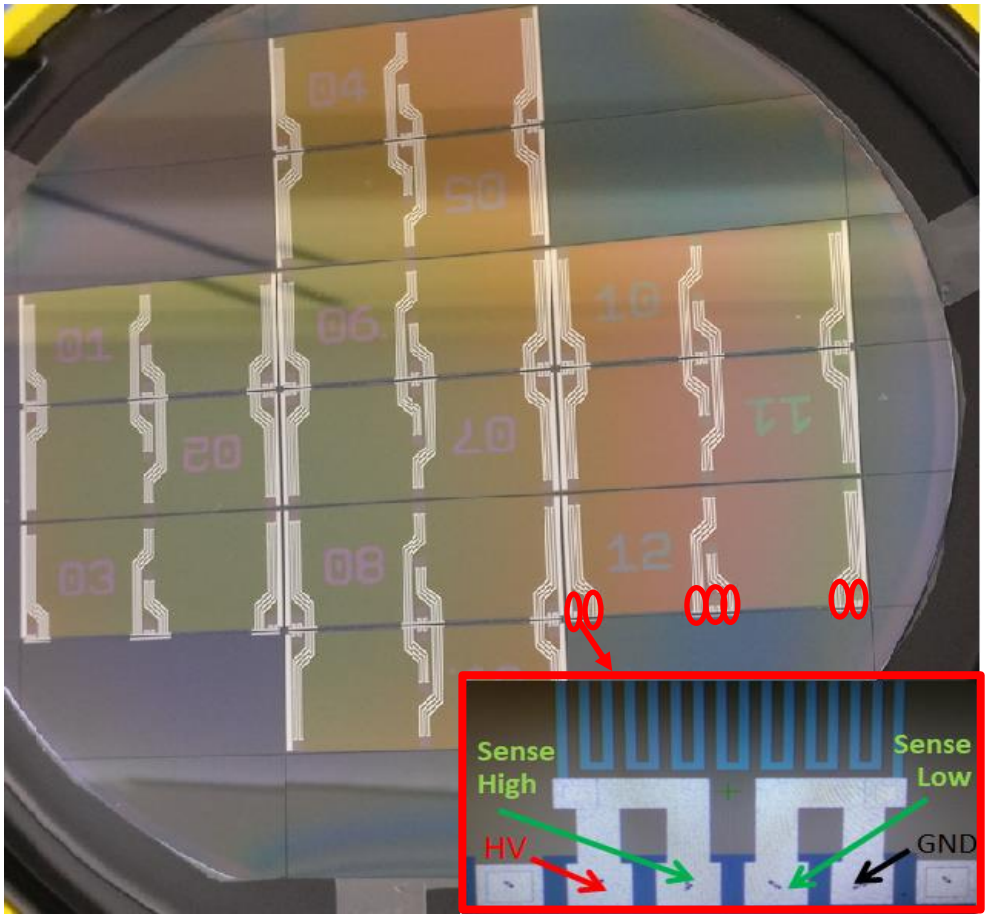

Figure 3.10 – Arrangement of the M2-size heater production in the 6" silicon wafer. Each of 12 heaters has 7 RTDs (thermal sensors) embedded. The small picture in the bottom right corner is a zoomed image of the wire bonding pads and illustrates the schematic of a four-point probe (Kelvin sensing) for RTDs measuring.

At the beginning of the heaters production process the metal layer is sputtered on a thermal oxide grown on the silicon substrate. Next, a second layer of oxide is deposited, and the metal coils are deposited and patterned to act as resistive temperature detectors (RTDs). The geometry and material of the individual RTDs has been designed to yield a nominal resistance in the kΩ range.

Subsequently, the metal coils are covered by a further passivation layer for protection. The last layer comprises the bus bars and RTD's tracks to connect the coils to a line of wire-bonding pads (see Figure 3.11). Each RTD is connected to four wire-bonding pads in order to perform four-wire measurements as shown in the bottom right corner of Figure 3.10. For a given RTD, the two external pads are used to supply the current, while the voltage drop is measured using the inner pair of pads.

The nominal size of the heater silicon die (41.30 x 19.30 mm^2) has been chosen to replicate the dual or "M2" hybrid pixel module based on FE-I4 front-end chips. The basic M2 heater features seven RTDs, the wire-bonding pads of which are located in the same edge of the heater. Bus bars cover the full length of each of the shorter edges of the rectangular device, while the fourth edge remains free to have to have an opportunity to place two heaters side-by-side along their free edges to obtain a device with dimensions equivalent to the quad or "M4" hybrid pixel module (i.e. 41.30 x 38.65 mm^2, including 50 μm separation between the two units).

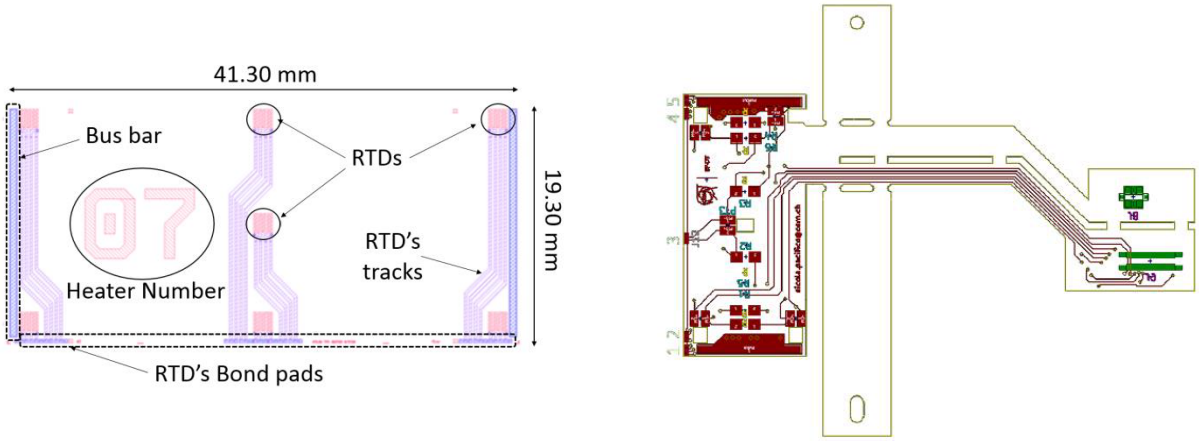

Figure 3.11 – (Left) Schematic representation of a dual (M2) heater, featuring bus bars and seven RTDs with their corresponding tracks and wire-bonding pads. (Right) The dual heater flex used to for the heater module assembly.

Upon the reception of heater wafers and electrical modules, prior their assembly and wire bonding the quality control has to be performed. The IV curves and CV curves of the electrical modules and heater sensors resistance-temperature (R-T) dependences have been measured in the cleanrooms using a SIGNATONE WaveLink 350 probe station (CAPTINOV platform at LAL) shown in Figure 3.13 and semiautomatic SUSS PA200 (at LPNHE).

Before the silicon heaters use in the various prototypes of the Outer Barrel demonstrator programme the heating element and RTDs of each individual must be calibrated. The purpose of such a calibration step is twofold:

- Determine the temperature coefficient of resistance (i.e. TCR or α) for the individual RTDs;
- Measure the resistance of the heating element at a reference temperature to estimate the heat dissipation of each individual device when connecting in a serial powering chain. Whenever possible, the TCR of the heating element shall be also measured.

The calibration step can be performed before or after the heater assembly process, resulting in two different procedures:

- The bare silicon heaters can be calibrated using a probe station with a temperature controlled chuck;

- Alternatively, an environmental chamber can be used to calibrate the finished heater/flex assembly, employing a dedicated test board to connect the heater flex to the required measuring equipment (these measurements are presented in the section 3.5.3).

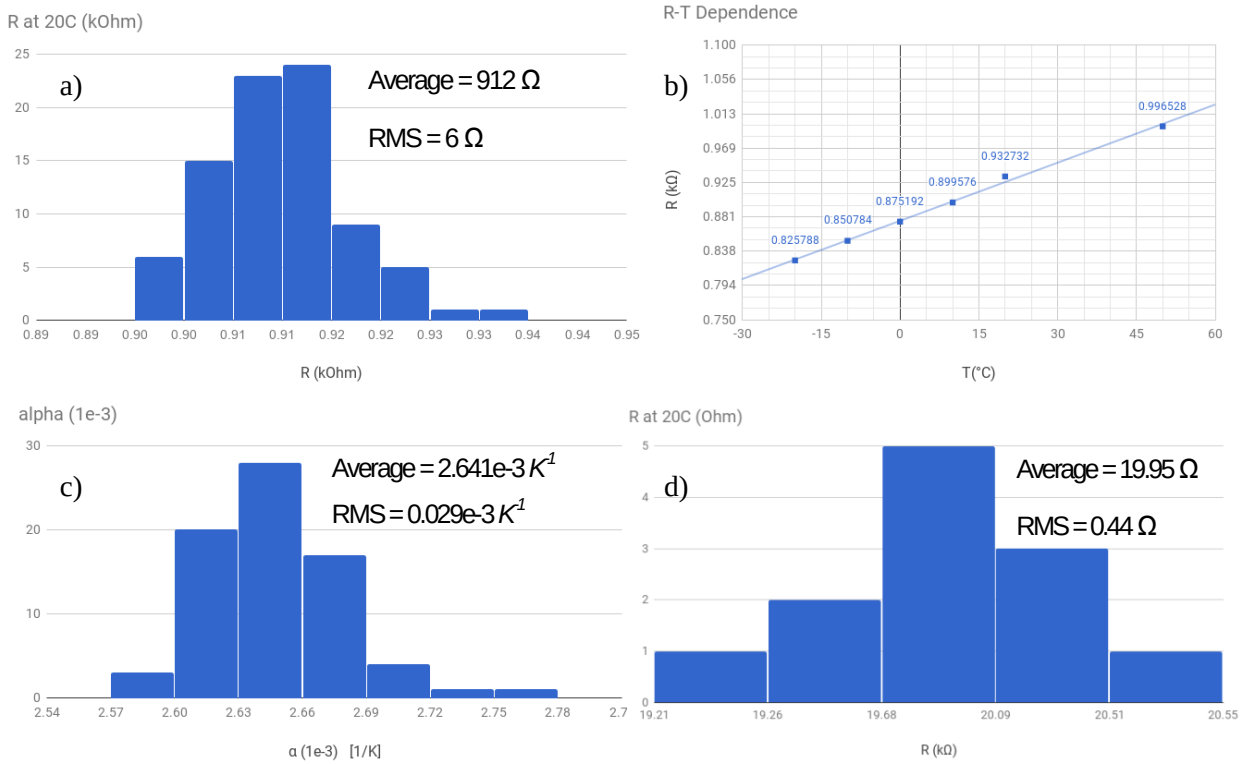

Figure 3.12 – An example of the results of the heaters measurements: a) The diagram of the resistance of each RTD on a wafer at 20˚C; b) Dependence of the resistance on temperature for a single RTD; c) The diagram of the distribution of temperature coefficient of resistance (α) of RTD on a wafer; d) The diagram of resistance of the heater elements at 20˚C. All results are in good agreement with numbers provided by manufacturer.

To perform the first type of calibration, the silicon heater is placed on the temperature-controlled chuck of the probe station. In order to measure the resistance of each individual RTD, four needles are put in contact with the corresponding four wire-bonding pads: a 100 μA fixed current is applied to the external pads, while an accurate multimeter or Source measure unit (SMU) is employed to read the voltage drop between the inner pair of pads (as shown in the right bottom corner of Figure 3.10) and then infer the resistance. The filtering functions of the measuring instrument should be used to avoid voltage fluctuations greater than 300 μOhm.

Taking into account the expected temperature operating range of the devices, this procedure is repeated for the six temperature points: -20˚C, -10˚C, 0˚C, 10˚C, 20˚C, 50˚C. In order to avoid condensation problems, the dew point in the test area shall be kept at least 10˚C below the heater (i.e. chuck) temperature, the dry air flushing to the measurement ambience must be provided.

In order to estimate the resistance of the heating element, six probe needles are put in contact with the power bus-bars and a current of 20 mA is applied.

The results (see Figure 3.12) and temperature-resistance data pairs are used to fill in a dedicated "calibration spreadsheet" provided by CERN. A separate spreadsheet is to be used for each wafer, storing the data of each heater or heater assembly in a different sheet. In addition to the heater identifiers, if the calibration takes place in after the gluing (described in the section 3.5.3), the spreadsheet shall also contain the corresponding flex and heater assembly identifiers for traceability purposes.

3.5.2 The heaters assembly process

The next step after calibration and the quality control measurements is the electrical connection of the thermal and electrical modules to the flex cables. The result of the assembly procedure for the electrical and thermal sensors is shown in Figure 3.14.

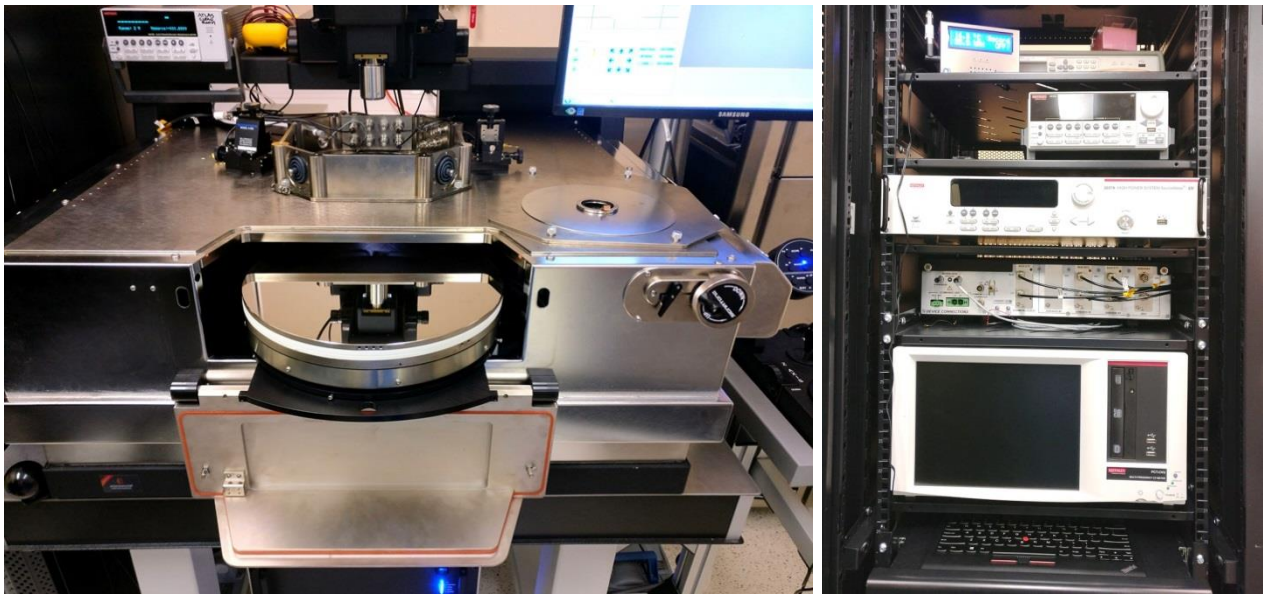

Figure 3.13 – (Left) A picture of the semiautomatic probe station with a temperature controlled chuck and with a possibility to measure large silicon wafers. (Right) Keithley Instruments DAQ system used to master a probe station and perform high precision electrical measurements. The equipment is a part of CAPTINOV platform, located in the clean room at LAL.

There are three types of heater flexes produced: a quad flex compatible with the M4 heaters, and two types of dual flex, referred as "left-side" and "right-side" dual heater flexes (shown in Figure 3.11), each featuring a different location for the pigtail. The heater flexes are manufactured using a standard three-layer, adhesive-less process. The purpose of these flexes, which must to be glued and wire-bonded to the heaters, is threefold:

(i) deliver the power to the heater via wire-bonding to the bus-bars;

(ii) connect five RTDs per heater to the external readout;

(iii) mimic the geometry of the module flexes for integration purposes.

Upon reception, the flexes have to be visual inspected using a microscope to check for any corrosion and the connector soldering. Also, they have to be cleaned with an ultrasonic bath of isopropanol at 50˚C and then warmed at 120˚C in a climate chamber for 12h.

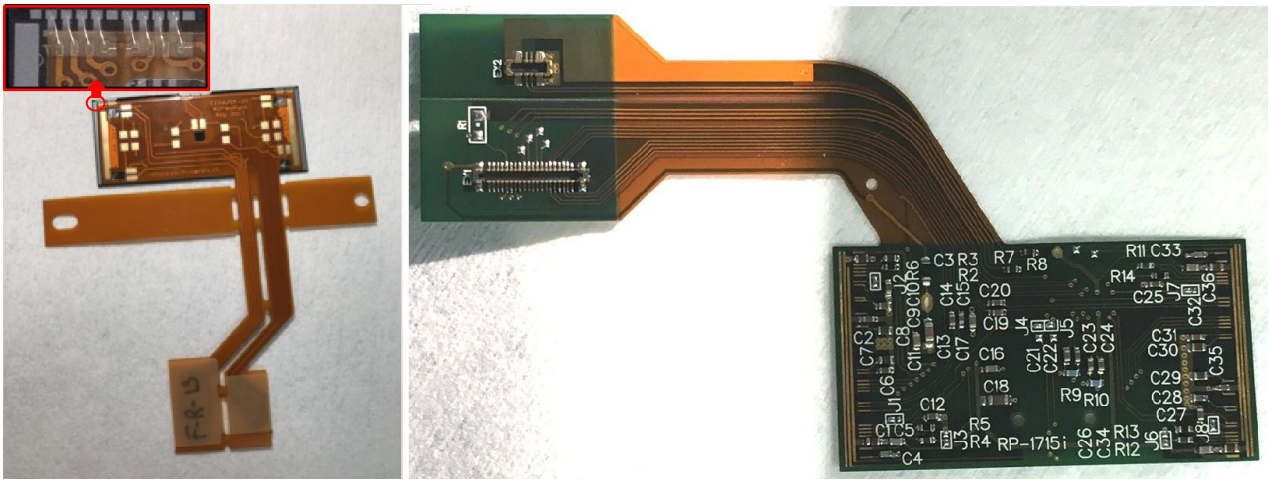

Figure 3.14 - (Left) A picture of a glued thermal module. On the top a zoomed image of the pads with performed wire bonding is presented. (Right) A picture of a glued electrical module.

The heater assembly process comprises two steps, namely:

- Gluing of the heater flex to the silicon heater, guaranteeing the correct relative position of both elements;

- Wire-bonding of the heater to the heater flexes to provide the necessary electrical connections to power the heating element and read the RTDs.

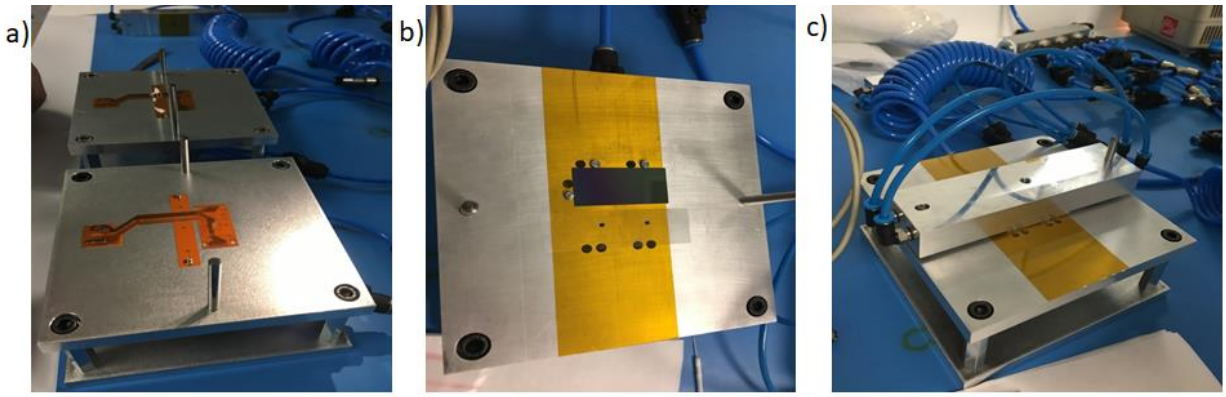

Figure 3.15 – a) An assembly jig to position the flexes; b) A jig to position silicon device (the dual heater is shown); and c) A bridge to transfer the sensor to the jig with a flex (picture shows the bridge in the final position during the curing process). In order to guarantee the correct alignment and relative position of the heater and the flex, the positioning jigs and the bridge employ a system of matching dowel pins.

The gluing step is take place in a clean room environment (preferably class 10 000 or better). To glue the heater to the heater flex, the dedicated tooling, designed at CERN is using. The tooling set comprises three different parts:

- A jig for positioning the silicon heater, shown Figure 3.15(b). Originally developed for the quad heaters, this jig can also be used for the dual heaters if two holes are covered with tape;
- A jig for positioning the heater flex, shown in Figure 3.15(a). A specific jig is required for each type of heater flex (quad, left-side and right-side dual);
- A bridge used to pick-up the silicon device from the heater positioning jig and transfer it to the flex positioning jig, as shown in Figure 3.15(c). The design of the pickup/transfer jig was originally developed for M4 heaters, but it can also be used for the dual heaters if two vacuum lines are disconnected temporarily.

In order to secure the position and transfer the various items, the different tools feature vacuum holes for suction. They are connected to a suitable vacuum pump though a common manifold using flexible pipes and fittings. The utilized glue UHU Endfest 300 to attach sensor to the flex has to be robust against environmental influences as a wide range of temperatures and a high level of irradiation.

Overall, the gluing of the heater is a three step process:

1. Position the heater flex (up-side-down) on the pre-cleaned with isopropanol corresponding jig, deposit the adhesive tape and the glue following the appropriate pattern and let it cure for five minutes;

2. Clean the silicon heater and locate on the corresponding jig;

3. Pick-up the silicon heater using the bridge, place it over the flex and complete the curing process. Place an appropriate mass over the pick-up bridge (200 g and 400 g for the dual and quad heaters respectively) and let the assembly cure for approximately 8 hours (the vacuum in the flex alignment jig and the pick-up bridge remains switched on for the entire duration of the curing cycle).

The flexes and the heater sensors must be weighted before and after assembly process. The weights are entered in a dedicated table. Up to four modules have been glued per day, since it was limited by the number of jigs available for gluing (two) and the curing time (7 - 8 hours) of the glue.

Once the gluing step has been completed, a unique identifier is used to trace each individual heater assembly and each assembly is placed in the corresponding transport box (Figure 3.16) to ship the modules to our colleagues in CEA Saclay for wire-bonding between the flexes and the pads on the heaters (for thermal modules) or on the front-end chips and the backside of the sensor for biasing (for electrical modules). The wire-bonding (see Figure 3.14) was performed in a clean room environment using a BondTec 56xx series wire-bonding machine, employing standard Al-wedge bonding. Then, as the last step, the quality of the bonds was verified with a pull-tester.

3.5.3 The assembly calibration

After bonding, we have performed a visual inspection of the modules to check the wire-bonding, the second calibration of the thermal heaters inside a CLIMATS climate chamber (LPNHE), and electrical tests (biasing, IV, source scans with a radioactive β-source) of the electrical modules.

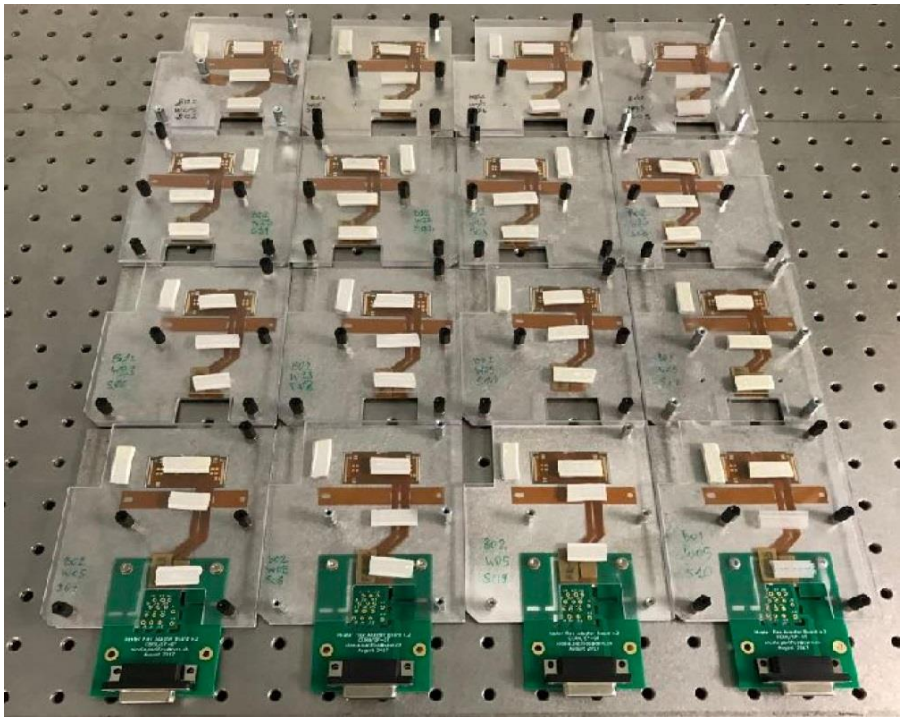

Figure 3.16 – The assemblies in the transport boxes. In the bottom line the assemblies are connected to the card to read-out used during the calibration in the climate chamber.

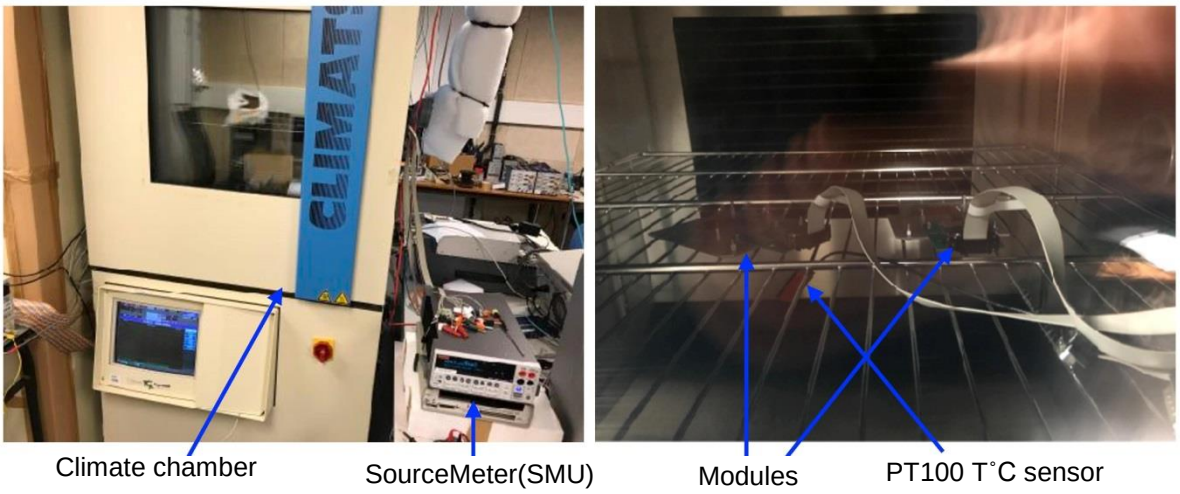

Figure 3.17 – The heater assemblies' calibration process using the CLIMATS climate chamber and SMU Keithley 2410 at LPNHE. (Right). A picture shows the modules placed inside a climate chamber for the measurements.

To perform calibration an assembly is attached with the pigtail of the heater flex to a purpose-built test card, which routes the signals from the data and power connectors to a single D-SUB 15 connector. Then the test card is connected to the SMU to measure the voltage drop. In this case, all the RTDs for a heater assembly are powered in series through the flex. The resistance for the heating element and each individual RTD is to be measured for the six reference

temperatures (the same to the ones that indicated in the section 3.5.1), storing the data in the corresponding spreadsheet.

These measurements were taken to re-test, in addition the 4-wires measurement with a probe station, the performance of the assembly as a whole.

The reference temperature for the calibration is measured in the vicinity of the heater: an additional PT100 was attached to the bottom of the heater assembly. The dew point in the climate chamber should be maintained at least 10˚C below the temperature of the assemblies at all times in order to avoid condensation problems.

Figure 3.18 – Picture of the long thermal demonstrator with the thermal doublet heater modules assembled in the Paris cluster and installed in the inclined section.

In total 24 thermal modules and 5 electric modules have been assembled, with an overall yield of 86%, improving over time as more experience was gained. The good modules have been shipped to CERN, where the wire-bonds have been encapsulated (potting), before the modules were “loaded" on their local supports to form a cell, and then the cells have been integrated in the long thermal and full demonstrator (shown in Figure 3.18) by the CERN team, which is also going to perform the final tests of the fully assembled prototypes.

Validation of new ideas, technological solutions, module construction and loading procedures, quality control and testing programs is very important for the ITk construction. This process involves a lot of technical resources and manpower. I have been participating in module testing and module assembly for the construction of a full scale thermal and electrical stave prototype for the ITk. To be loaded to the final demonstrator 24 thermal and 5 electric modules have been assembled and calibrated during this work. In the next chapter the focus of the work will be moved to the function principles of the pixel sensors and to the innovative technologies improving their performance and radiation hardness.

Chapter 4

Basics of Interaction of Radiation with Matter and Silicon Detector devices

Contents

In HEP experiments solid-state particle detectors are widely used. Compared to other types of detectors e.g. gaseous or liquid ones, the solid-state detectors have a high material density, rapid signal collection and produce large numbers of charge carriers which allow for good spatial and time resolution. This makes them favorable for using in high particle rate environments. However, solid-state detectors, e.g. silicon detectors, are susceptible to radiation damage and so research and development is required to improve the radiation hardness of these detectors.

In this chapter, after the introduction of the mechanisms of particles interaction with matter, the semiconductors, their main properties and application as particle detectors are given. Then the methods for the detector characterization in the clean room environment, the examples of the results of the electrical characterization measurements which I have done many times throughout my thesis work with various sensors structures are presented. At the end of the chapter, radiation damage in silicon sensors and its impact on the detector performance are discussed.

4.1 Radiation-Matter Interaction

Depending on charge, mass, energy and other parameters particles interact differently passing through the media. There are a variety of methods in which radiation interacts with atoms. In this section the interaction of light and heavy charged particles, as well as neutral particles and photons will be introduced.

4.1.1 Interaction of charged particles

There are several kinds of interactions for charged particles in matter. The primary method of interaction of the charged particles is via the electromagnetic interaction, which could be divided into two types. The first one is the energy losses on ionization and excitation of target atoms due to electromagnetic interactions with orbital electrons. This case is typical for both heavy and light charged particles. The second type of the electromagnetic interaction is when particles lose energy by radiation, which is very significant for high-energy light particles. When radiative energy loss is dominant, it is convenient to introduce a **radiation length**, which is is the distance in the material over which the charged particle losses its energy by a factor of e

$$E = E_0 e^{-\frac{x}{X_0}} \tag{4.1}$$

$$X_0^{-1} = \frac{4 \cdot Z^2 \cdot N_A \cdot \rho \cdot \alpha \cdot r_e^2}{A} \ln\left\{\frac{183}{\sqrt[3]{Z}}\right\} \tag{4.2}$$

where r_e is the classical electron radius, $\alpha = \frac{e^2}{2\varepsilon_0 hc}$ is the fine structure constant, N_A is Avogadro's constant, ρ is the mater density, Z and A (in g mol^{-1}) are the atomic number and atomic weight of the material.

4.1.1.1 Bremsstrahlung

Bremsstrahlung radiation is emitted when a charged particle is accelerated (decelerated) or deflected by interaction with the Coulomb field of another particle or the atomic nuclei. Decelerating in the mater, the particle is losing its energy by emitting photons in the Bremsstrahlung process.

The average loss of energy per distance caused by Bremsstrahlung can be calculated using (4.1):

$$\frac{dE}{dx} = -\frac{1}{X_0} E_0 e^{-\frac{x}{X_0}} = -\frac{E}{X_0} \tag{4.3}$$

The intensity of bremsstrahlung radiation is proportional to the square of the atomic number of the target, the energy of the bombarding particle and to the inverse square of the particle mass. It follows that light particles such as electrons and positrons bombarding targets of high atomic number are more efficient producers of bremsstrahlung radiation than heavier particles

4.1.1.2 Cherenkov radiation

Fast charged particles traveling in a dielectric medium with $n>1$ (n - refraction index) may create an electromagnetic radiation, which is called Cherenkov radiation. This only happens when the speed of the particle greater than the phase velocity of light in the particular medium, which is c/n. Cherenkov light emits a forward cone with a specific angle θ, depending on the velocity of the particle and the refractive index in the following way: $\cos\theta = \frac{1}{\beta n}$. Cherenkov radiation is extensively used to detect high-energy charged particles and cosmic rays.

4.1.1.3 Transition radiation

Transition radiation is a form of electromagnetic radiation emitted during the uniform motion of a charged particle in a spatially inhomogeneous media, such as a boundary between two media with different dielectric constants. It depends strongly on the relativistic γ factor of the particle which makes it usable for particle identification. Typically, the intensity of transition radiation is low, but using a multilayered dielectric radiator spaced in vacuum, may increase the radiation yield.

4.1.1.4 Interactions of heavy charged particles

For quantification of energy loss of heavy particles by atom ionization and excitation traversing the material, relativistic quantum mechanics gives the Bethe–Bloch formula which describes the mean rate of energy loss $-\left\langle \frac{dE}{dx} \right\rangle$ [64] or [65]:

$$-\left\langle \frac{dE}{dx} \right\rangle = Kz^2 \frac{Z}{A}\frac{1}{\beta^2}\left[\frac{1}{2}\ln\frac{2m_e c^2\beta^2\gamma^2 T_{\max}}{I^2} - \beta^2 - \frac{\delta(\beta\gamma)}{2}\right] \tag{4.4}$$

with $K = 4\pi N_A r_e^2 m_e c^2 = 0.307075$ [MeV g^{-1}cm^2];

$N_A = 6.022\times10^{23}$ [mol^{-1}] - Avogadro's number;

$r_e = \frac{e^2}{4\pi\varepsilon_0 m_e c^2} = 2.817$ [fm] - classical electron radius;

z - charge of incident particle;

Z - atomic number of the absorption medium;

A - atomic mass of the absorption medium;

$m_e c^2$ - rest energy of the electron;

β - velocity of the traversing particle in units of c (speed of light);

$\gamma = \frac{1}{\sqrt{1-\beta^2}}$ - Lorentz factor;

I - mean excitation energy [eV], 173 eV for silicon.

$T_{\max}$ - kinetic energy [MeV] describes the maximum kinetic energy that can be transferred to an electron by a hitting particle in a single collision;

$\delta(\beta\gamma)$ - Density effect correction to ionization loss. [65]

The (4.4) describes the mean rate of energy loss in the region $0.1 < \beta\gamma < 1000$, see Figure 4.1

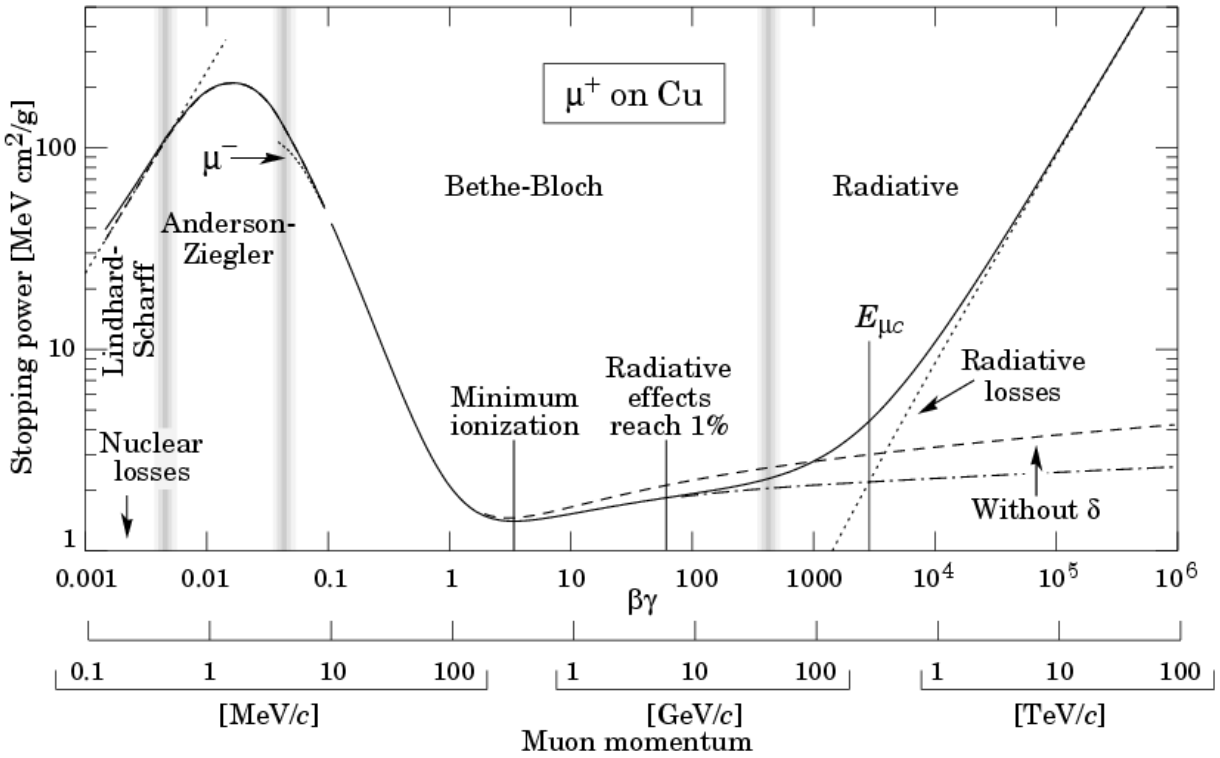

Figure 4.1 - Stopping power −dE/dx for positive muons in copper as a function of $\beta\gamma$, muon momentum [65].

Figure 4.1 shows of the mean energy loss given for muons in copper as a function of the incident particle momentum. The first part of the graph describes particles at momentum 0.1-100 MeV/c according to the non-relativistic description of energy and momentum.

The second part of the graph at momentum between 0.1-100 GeV describes the regime with lowest stopping power values for an incident particle, which determines the Minimal Ionizing Particles (MIP). MIPs are particles have mean energy loss rates close to the minimum, it happens at $\beta\gamma \approx 3.5$.

The mean energy losses for MIPs are about: $-\frac{1}{\rho}\frac{dE}{dx} \approx 1 \div 2 \frac{\text{MeV}}{\text{g cm}^{-2}}$

The third part of the graph describes the increasing energy loss mostly due to radiation of high energetic particles in the ultra-relativistic regime.

4.1.2 Photon interaction

There are three processes for interaction of photons with matter: the Photoelectric Effect, the Compton Effect and the electron pair production (see Figure 4.2). Depending on the photon energy and material properties, different processes take place in the interaction (see Figure 4.3).

Photoelectric effect

The photoelectric effect is the emission of electron from the bound state into a free one with energy $E_{e^-_{kin}}$ by a photon, when the energy of the photon E_γ is higher than the binding energy E_b

$$E_{e^-_{kin}} = E_\gamma - E_b \tag{4.5}$$

The photoelectric effect is the dominating interaction for photons with energy up to few tens of *keV*. Electrons emitted in this manner are called photoelectrons.

Compton scattering

Unlike the photoelectric effect, in the Compton scattering the photon is not completely absorbed, but it transfers a part of its energy to the recoiling electron and the photon can then continue to undergo additional interactions. It can occur for a free electron. In the Compton interaction both the photon and electron are scattered. With

$$E'_\gamma = \frac{E_\gamma}{1 + \frac{E_\gamma}{m_e c^2}(1 - \cos\Theta)} \tag{4.6}$$

in which E_γ and E'_γ is the energy of the photon before and after the scattering on an electron, the distribution of the scattering angle Θ can be determined.

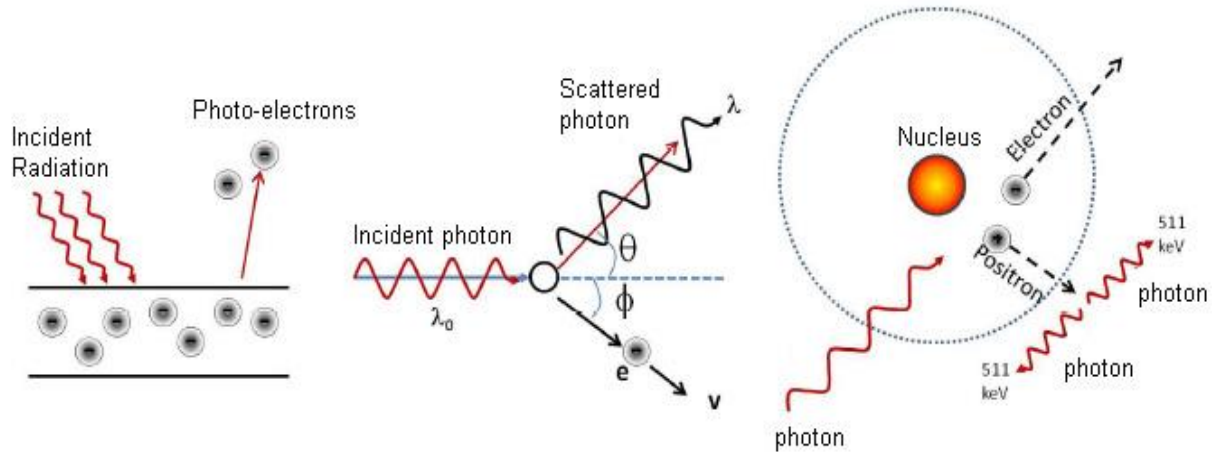

Figure 4.2 – Illustration of three photon interactions. (a) Photoelectric effect (b) Compton effect (c) Pairs production.

Pair production

When the energy of the incoming photon is high enough pair production becomes possible in the Coulomb field of atom. The minimum photon energy needed must be greater than the combined rest mass of electron and positron $2m_e = 1.022$ MeV .

To create the pair, the photon must have at least energy of:

$$E_{\gamma} = 2m_e(1 + \frac{m_e}{m_N}) \tag{4.7}$$

where m_N is the mass of the nucleus. Electron and positron take away the remaining energy in the form of kinetic energy. After a short period of time, the positron will annihilate with an electron in the bulk of the material producing two photons with energy of 511 keV.

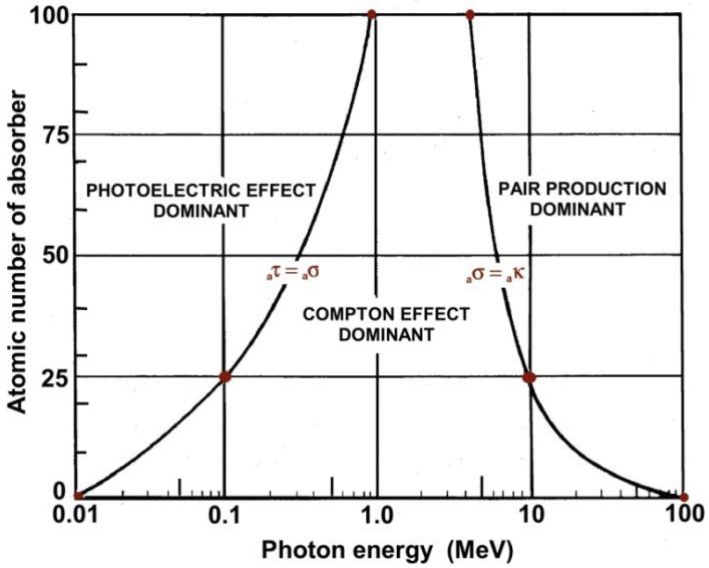

Figure 4.3 - Regions of the relative predominance of the three main forms of photon interaction with matter [62].

4.1.3 Interactions of neutral hadrons

Neutrons can scatter elastically and inelastic on atomic nuclei. In the first case the neutron transfers a part of its energy to the nuclei and if the neutron energy is high then a target light nuclei may recoil and in turn lead to ionization in the detector. Inelastic hadronic interactions may lead to hadronic showers in the detector where the secondary hadronic reaction products if energetic enough lead to subsequent hadronic interactions. In addition, various nuclear reactions, the importance of which depending on the neutron energy, may occur between neutrons and nuclei in the detector material.

Neutrinos can only interact weakly either by a charged-current or a neutral-current interaction. As the corresponding cross sections are small, very large detector masses are necessary to detect the secondary charged particles with reasonable efficiency.

4.2 Properties of semiconductors

Solid state materials are grouped into three types: metals, semiconductors and insulators, which are differ by their electronic band structure. The Figure 4.4 shows the relative position of the energy bands and their occupancy by electrons for each type of solid-state materials. Conductors have overlapped conduction and valence bands, thus the electron can freely move between them. Hence, metals are highly conductive, they cannot be used for the detection, since the additional ionization introduced by traversing particle will not be distinguishable given the background

current once the external voltage applied. Unlike conductors, insulators have a large region between the valence and conduction bands, called band-gap, typically, the gap width is greater than 9 eV. The use of insulators as a detection material is unacceptable too, since the charge freed by ionization will not be possible to collect, due to the huge electrical resistance.

Semiconductors also have a forbidden energy gap ($E_g = E_C - E_V$) between the valence (E_V) the conduction (E_C) bands, however the width of this gap is small enough to have interesting properties and to be used as a sensor material for the different detector systems. The band-gap for some widely used semiconductors: Ge – 0.7 eV, Si – 1.12 eV, diamond – 5.5 eV.

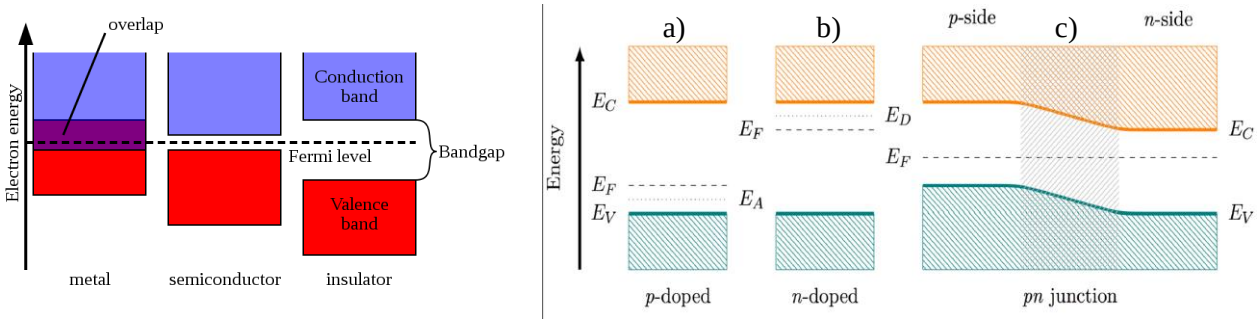

Figure 4.4 – (Left) Diagram showing the band structure for solid-state materials. (Right) Schematics of the energy levels in p-type (a) and n-type (b) silicon. Combining the differently types results in a p-n junction (c) with a balanced Fermi level in between the two segments. The new energy levels in the band-gap pull the Fermi energy towards the respective side.

In semiconductors the valence electrons are distributed between the conduction band and the valence band. The concentration in the conduction band is directly proportional to the width of the energy gap and is dependent on the temperature. At T = 0 K all electrons are bound in the valence band and a semiconductor behaves like an insulator. Due to its smaller energy gap, electrons from the valence band can be thermally excited and can overcome band-gap energy to reach the conduction band. Then, the electrons can move in the conduction band and the semiconductor can conduct electricity. Unbound electrons create vacancies, also called holes, in those positions, which behave like a positive charge that can also move in the lattice.

The resulting resistivity ρ of the semiconductor is given by the concentration of electrons in the conduction band n_e and holes in the valence band n_h, and their mobilities (μ_e and μ_h):

$$\rho = \frac{1}{e(n_e\mu_e + n_h\mu_h)} \tag{4.8}$$

To estimate the number of free charge carriers, for this case we can use the Fermi-Dirac distribution. The probability of the occupancy of a given electronic state E_e in the band levels can be expressed as:

$$F(E_e) = \frac{1}{1+\exp\dfrac{E_e - E_f}{k_B T}} \tag{4.9}$$

where k_B is Boltzmann's constant, T is the absolute temperature, E_f - the Fermi energy, the highest electron energy level at T = 0 K.

The number of free electrons n_e can be calculated by multiplying the density of states in the conduction band N(E) with the probability of their occupation given (4.9) [63]

$$n_e = \int_{E_C}^{\infty} N(E)F(E)dE \tag{4.10}$$

where E_C is energy of the lower bound of the conduction band. The density of states in the conduction band can be calculated as [63]

$$N(E)dE = 4\pi(\frac{2m_e}{h^2})^{2/3}E^{1/2}dE \tag{4.11}$$

where m_e is the effective mass of electrons. The Fermi level at room temperature is more than 10 k_BT below than E_C. Therefore the function (4.9) can be approximated by an exponential function in the conduction band:

$$F(E) \approx \exp(\frac{-(E-E_F)}{k_BT}) \tag{4.12}$$

Substituting (4.11) and (4.12) into (4.10) and integrating it, the concentration of free charge carriers can be obtained:

$$n_e = 2(\frac{2\pi m_e k_B T}{h^2})^{3/2}\exp(\frac{-(E_C-E_F)}{k_BT}) = N_C\exp(\frac{-(E_C-E_F)}{k_BT}) \tag{4.13}$$

$$n_h = 2(\frac{2\pi m_h k_B T}{h^2})^{3/2}\exp(\frac{-(E_F-E_V)}{k_BT}) = N_V\exp(\frac{-(E_F-E_V)}{k_BT}) \tag{4.14}$$

n_e and n_h are the concentration of free electrons and holes. The quantity N_C (N_V) is effective density of states in the conduction (valence) band.

In an **intrinsic** semiconductor, the concentration of electrons in the conduction band exactly equals the concentration of holes in the valence band. This indicates that the Fermi energy level, which is determined by the charge balance between the two bands, lies between the energies of the valence E_V and conduction E_C bands, in the middle of the band gap.

The product of (4.13) and (4.14) is independent of the Fermi level and as $n_e = n_h$ in the intrinsic semiconductor it can be used to calculate the intrinsic carrier concentration:

$$n_e n_p = {n_i}^2 = N_C N_V \exp(-\frac{E_g}{k_BT}) \tag{4.15}$$

At 300 K in silicon $n_i = 1.45\times10^{10}\ \mathrm{cm}^{-3}$.

By introducing impurities into the lattice, which called doping process (see next section), the electrical, optical and structural properties of semiconductor can be modified. The resulting semiconductor is called **extrinsic** or doped semiconductor.

4.2.1 Doping

In semiconductor device production, the intrinsic semiconductors are rarely used, because their low electrical conductivity. Therefore, to enhance their conductivity, the specific impurities (dopants) are intentionally introduced into pure semiconductors in a controlled way. Depending on a valence of added material, a greater density of electrons or holes can be produced. The

semiconductors with an excess of electrons in the conduction band are called **n-type**, and in case of majority of holes in the valence band they are called **p-type** semiconductors.

Considering silicon material, as the most common semiconductor in technology, which has an atom with four valence electrons, the silicon conductivity can be improved by doping with impurity elements either from group V or group III.

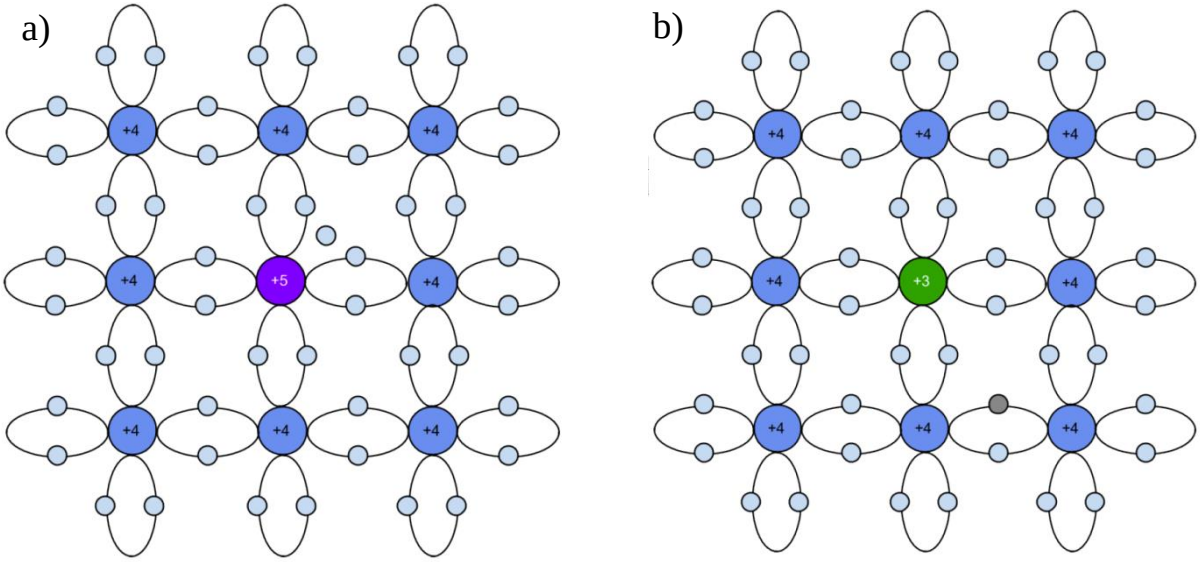

Figure 4.5 – A two-dimensional bond structure of a silicon crystal in n-type (a) and p-type (b) semiconductors.

The first case, as illustrated in Figure 4.5(a), when one silicon atom is replaced by a Phosphorus atom with five valence electrons. Only four are used for the formation of covalent bonds with neighboring atoms, while the fifth is not bound to a specific atom but is free for conduction. It should be stressed that the crystal as a whole remains neutral, since the charge of the free electron is compensated for by the excess charge of the arsenic nucleus bound in the crystal lattice [64]. The impurities, introducing the addition of free electrons, are called **donors** and are found in n-type silicon. In terms of the band theory, donors create additional energy levels E_D in the band-gap, close to the conduction band (see Figure 4.4). Since the levels E_D are close to the conduction band, as in case of Phosphorous dopants $E_C - E_D = 0.045\ [\text{eV}]$, these states can be ionised at room temperature and the electrons will be lifted to the conduction band.

On the other hand, if silicon atom is replaced by an atom with three valence electrons (as pictured in Figure 4.5(b)) e.g. Boron, one electron is missing in the covalent bonds and hole is thus created. This hole may be filled by an electron from a neighbouring atom, this can be interpreted as a hole jumping e.g. a movement of positive charge. The hole introducing dopant is called an **acceptor**. The introduction of additional holes is accompanied by the creation of an energy level E_A close to the valence band. For Boron in silicon the acceptor level lies $E_A - E_V = 0.045\ [\text{eV}]$ above the energy of the valence band. So electrons from the valence band can easily reach this level, leaving holes behind in the valence band.

The total atomic dopant concentration is possible to measure using such methods as Secondary Ions Mass Spectrometry (SIMS) [80]. But not all the deposited dopant atoms are electrically

active, only ones that manage to reside on a lattice place are active dopant and contribute to the electric current flow when a potential difference is applied to the semiconductor. To evaluate the electrically active doping concentration another methods like Hall Effect, Capacitance-Voltage (CV) or Transition Line Matrix (TLM) measurements (more details in the Ref [79]) are used.

4.2.2 p-n junction

For particle detection only pure silicon or a junction of n-type and p-type silicon is used. The so called p-n junction is formed in the interface between two opposite doped pieces of silicon. Due to the difference of the concentration of free charge carriers, there is diffusion current when the n-type and p-type semiconductors are brought into contact. Electrons and holes diffuse from the zones of high concentration to those of low concentration leaving behind positively and negatively charged ions respectively. So the previously electrically neutral n-type region charges up positively and in the p-type region the negative charge will be created. In thermal equilibrium diffusion and drift current are equal and cancel each other. For the junction with constant doping concentration of the both sides the potential inside the p-n junction can be expressed by Poisson equation:

$$\Delta\phi = -\frac{\rho}{\varepsilon_{Si}\varepsilon_0} = -\frac{e}{\varepsilon_{Si}\varepsilon_0}\left(N_A - N_D\right) \tag{4.16}$$

ε_{Si} - is the dielectric constant for Silicon and ε_{Si} = 11.75. The vacuum permittivity or electric constant ε_0 = 8.85×10^{-12} F/m. The charge density ρ is represented by elementary charge e and the acceptor and donor concentration in the respective regions N_A, N_D.

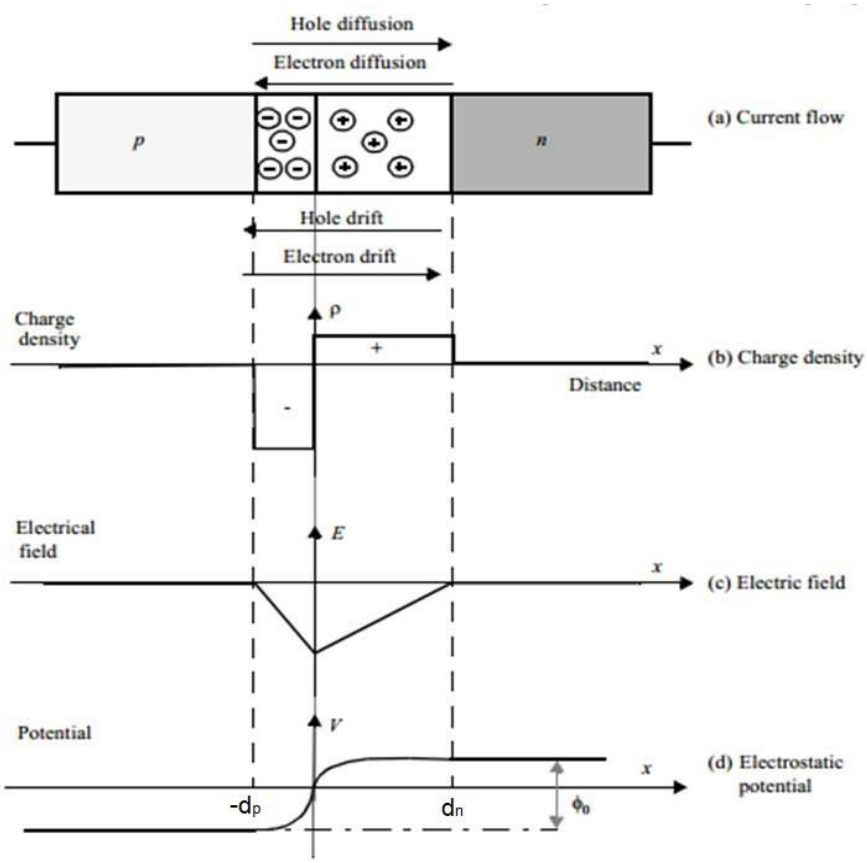

Figure 4.6 – An abrupt p-n junction in thermal equilibrium with zero voltage applied. The current flow (a), the charge density (b), the electric field (c) and electrostatic potential (d) are shown.

The space charge causes an electric field at the junction which acts against the diffusion until the electrical potential is reached, which prevents further diffusion of the charge carriers. This "built-in" voltage V_{bi} which corresponds to the electrical field in the junction can be expressed as:

$$V_{bi} = \frac{kT}{e}\ln\left(\frac{n_{0,n}p_{0,p}}{n_i}\right) \approx \frac{kT}{e}\ln\left(\frac{N_D N_A}{n_i^2}\right) \tag{4.17}$$

where $n_{0,n}$ is electron concentration in the n-type material, $p_{0,p}$ - is the hole concentration in the p-type and n_i - is the intrinsic concentration. The typical value of V_{bi} is about *0.7 V*.

The electric field in the p-n junction is obtained from the charge density using Gauss's law:

$$\frac{dE}{dx} = \frac{\rho}{\varepsilon_{Si}\varepsilon_0} \cong \frac{e}{\varepsilon_{Si}\varepsilon_0}(N_A - N_D) \tag{4.18}$$

As a result one finds that the electric field changes linearly with position *x* (as shown in Figure 4.6). The maximum electric field occurs at *x* = 0 and can be obtained by integrating from -d_p to 0 or by integrating from d_n to 0 yielding:

$$E_{\max}(x=0) = \frac{1}{\varepsilon_{Si}\varepsilon_0} eN_D d_n = \frac{1}{\varepsilon_{Si}\varepsilon_0} eN_A d_p \tag{4.19}$$

Both calculations must yield the same result since the dielectric constant is the same in both regions. The electric field has to be zero outside the depletion region since any field would cause the free carriers to move so that the associated charge eliminates that field. The fact that the electric field is zero on both ends of the depletion region also implies that the total positive charge per unit area in the depletion layer equals the total negative charge.
The equation (4.19) provides the relationship between d_n and d_p - the depletion widths in the n-type and p-type semiconductor:

$$N_D d_n = N_A d_p \tag{4.20}$$

This equation expresses the fact that the total positive charge in the n-type depletion region exactly balances the total negative charge in the p-type depletion region. The total depletion region width will be the sum of these components: $d = d_n + d_p$.
Using Maxwell equations and then relationship (4.20) the setting voltage in p-n junction can be written as:

$$\begin{aligned} V = -\int_{-d_p}^{d_n} E(x)dx = \frac{e}{2\varepsilon_{Si}\varepsilon_0}\left(N_A + N_D\right)d_n d_p = \\ = \frac{e}{2\varepsilon_{Si}\varepsilon_0}\frac{\left(N_A + N_D\right)N_D}{N_A}d_n^2 = \frac{e}{2\varepsilon_{Si}\varepsilon_0}\frac{\left(N_A + N_D\right)N_A}{N_D}d_p^2 \end{aligned} \tag{4.21}$$

And this obtained by (4.21) voltage is equal to the built-in voltage V_{bi}. So, we can express an electric field and the depletion width using V_{bi} given by (4.17):

$$E_{\max} = \sqrt{\frac{2e}{\varepsilon_{Si}\varepsilon_0}\frac{N_A N_D}{N_A + N_D}V_{bi}} \tag{4.22}$$

$$d = \sqrt{\frac{2\varepsilon_{Si}\varepsilon_0}{e}\frac{N_A + N_D}{N_A N_D}V_{bi}} \tag{4.23}$$

And for simplified case for asymmetric doping when one dopant type prevails over another, for example $N_A >> N_D$:

$$E_{\max} \approx \sqrt{\frac{2e}{\varepsilon_{Si}\varepsilon_0}N_D V_{bi}} \tag{4.24}$$

$$d \approx \sqrt{\frac{2\varepsilon_{Si}\varepsilon_0}{e}\frac{V_{bi}}{N_D}} \tag{4.25}$$

The electric field sweeps away any mobile charge carriers (electrons and holes) in the region around the boundary, so that a space-charge region is obtained in which the excess nuclear charge from the doping atoms is not neutralized by the movable carriers [64]. This space charge region depleted of free charge carriers close to the junction is called a depletion region or **depletion zone**.

The net flow of electrons and holes across the junction is zero. The application of an external electric field to the each side of the junction (as shown in Figure 4.7a) will produce a small current due to the net migration of the electrons and holes. It will modify the width of the depletion zone. If the positive terminal of the voltage source is connected to the p-type side (and negative pole to the n-type), it will result in a smaller width of depletion zone, such a connection is known as **forward bias** (Figure 4.7b). If the external voltage is applied in an opposite way, it is known as **reverse bias** (Figure 4.7c), then the depletion layer gets wider. In this case the width of depletion zone d_{dep} can be calculated using the following:

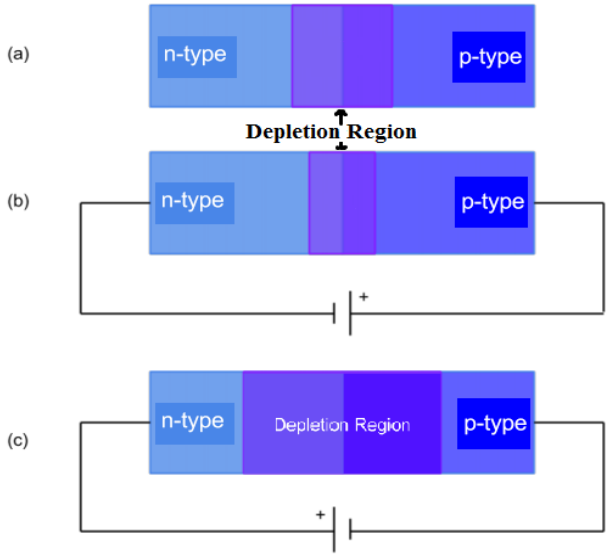

Figure 4.7 - Representation of the relative depletion regions for (a) an unbiased pn-junction, (b) a forward biased semiconductor and (c) a reverse biased semiconductor.

$$d_{dep} = \sqrt{\frac{2\varepsilon(V_b + V_{bi})}{e}}\left(\frac{1}{N_D} + \frac{1}{N_A}\right) \tag{4.26}$$

with V_b - external bias voltage, ε - is absolute permittivity of silicon, N_D and N_A - the donor and acceptor concentrations. The (4.26) can be simplified, because typically $V_b \gg V_{bi}$ and one doping is dominant in most applications.

$$d_{dep} \approx \sqrt{\frac{2\varepsilon V_b}{eN}} \tag{4.27}$$

where N represents the dopant concentration of the side of the junction with lower dopant level.

4.3 Introduction to Silicon detectors for High Energy Physics

The discussed in the previous section p-n junction can function as a sensitive volume for the particle registration in the silicon detectors. The operating principle of pixel sensors is based on a segmented p-n junction matrix.

Depletion Voltage

For high detection performance the sensitive volume i.e. the depletion region should be as large as possible. As we have seen in the previous section, formula (4.27), increasing the reverse bias voltage we can extend the depletion region over the entire sensor thickness. The case, when the depletion zone is only limited by the boundaries of semiconductor device is known as **full depletion**, and the minimum voltage needed for that is called **full depletion voltage**. For the unstructured diode the full depletion voltage is depended only on thickness d and the effective doping concentration N_{eff} and expressed as:

$$V_{dep} = (\frac{e \cdot d^2}{2\varepsilon\varepsilon_0})\left|N_{eff}\right| \tag{4.28}$$

But for the structured devices the depletion voltage can differ from (4.28). It can be determined from *IV* or *CV* measurements (see the section 4.4).

Capacitance

The pixel sensor capacitance is important for two reasons: it determines the electronic noise of the preamplifier [141] and influences the cross talk between pixels. The total capacitance has a few components: capacitance to the backside, the interpixel capacitance and other contributions (ground, bump-bonds, etc).

An inversed bias junction presents a charge built-up in either side of the depletion region, resulting to properties similar to a charged capacitor. If the bias voltage increases, the depletion region is enlarged and the capacitance is reduced. The value of capacitance per unit of pixel area is defined using the formula for parallel plate capacitor:

$$C = \frac{\varepsilon}{d} \cong \sqrt{\frac{e\varepsilon N}{2V}} \tag{4.29}$$

For a typical pixel cell on 300 μm thick silicon it gives about 7 fF.

An interpixel capacitance, the sum of capacitance to the neighbour pixels is proportional to the perimeter of pixels as well as to the gap between them. For example square pixel with 125 μm side and 20 μm gap between pixels gives about 60 fF.

Cross talk

Due to the capacitive coupling, a signal collected at one pixel can be induced at the neighbouring pixels. This effect is called cross talk. This leads to the increased fraction of multiple hits and has to be taking into account during the position reconstruction. To reduce the cross talk effect the interpixel capacitance must be as low as possible.

Leakage current

When the reverse bias voltage is applied to the p-n junction device, in the absence of particles or light there is a current flow, which called **leakage** or **dark current**. There are two main components of the free charge carrier's leakage into the depletion zone: one is minority carrier diffusion/drift near the edge of the depletion region; the other is due to electron-hole pair generation in the depletion region of the reverse-biased junction [66].

The resulting leakage current increases with the increase in the applied bias voltage. So far as the sensor is not yet depleted, the leakage current rises with the square-root of the voltage. As soon as full depletion is established the leakage current becomes almost constant, the only slow growth is due to the tunneling effects. This continues until the electrical potential somewhere in the device is high enough to gain electron sufficient kinetic energy to ionize further atoms. This process, known as avalanche, is characterized by exponential current increase and results in the **breakdown**, which may destroy the device.

The breakdown may be caused by three effects. First is the **tunneling mechanism**, which happens due to quantum mechanical tunneling of carriers through the bandgap. This is a dominant breakdown mechanism when both sides of a junction are very heavily doped. The **avalanche multiplication** appears when the electrical field at the p-n junction reaches too high values and the free charge carriers are strongly accelerated. The energy gained by electron between two sequential scatterings is enough to create new electron hole pair by ionization. This process leads to further generation electron-hole pairs, causing an avalanche of charge carriers. The last mechanism is caused by **thermal instabilities**. The temperature of the device during operation may increase, inducing thermal generation rate of free charge carriers and hence a higher leakage current. Higher current again causes an increased power dissipation of the device resulting in a positive feedback situation, evolving to very high currents and destroy of the device.

Since the leakage current is specified by the thermal generation rate of carriers which depends on temperature, it can be given for the temperature T as:

$$I_{leak}(T) = I_{leak}(T_{ref})\frac{T^2}{T_{ref}{}^2}\exp\left(\frac{-E_g}{2k_B}\left[\frac{1}{T}-\frac{1}{T_{ref}}\right]\right) \tag{4.30}$$

with $I_{leak}(T_{ref})$ is the current measured at T_{ref} . According to this formula, for the silicon sensors, the leakage current approximately doubles every 7˚C. It is very important, especially for the irradiated sensors, to cool down them operating the detector, in order to avoid *thermal runaway*.

Charge generation and signal formation

Ideally full depleted radiation detectors should have no charge in the absence of radiation and lots of charge when radiation comes. Of course there is a thermal generation causing the charge flow in the bulk material. That's why some pure semiconductor detectors are cooled to liquid nitrogen temperatures. The same motivation is in using the detectors with p-n junction, because the depletion zone is almost perfect for signal charge collection. The number of free charge

carriers in the full depleted sensitive volume of the semiconductor detector is very small, allowing for a lower noise contribution to the actual measured charge.

Any ionizing particle passing through a silicon sensor loses the energy in one of the interaction ways, described in the section 4.1, depending on its type. The transferred to the silicon lattice energy results in electron hole pairs creation. The energy required to create an electron-hole (e-h) pair in silicon at 300 K is 3.62 eV [67], so the expected number of e-h pairs per μm produced by an incident minimal ionizing particle MIP (see the section 4.1.1) is about 70 – 80 e^-. The created pairs will propagate under the effect of the electric field, established in the bulk by the applied reverse bias voltage; the electrons will drift to the n-type electrode and holes to the p-type electrode generating an additional current in the diode that can be measured using detection electronics.

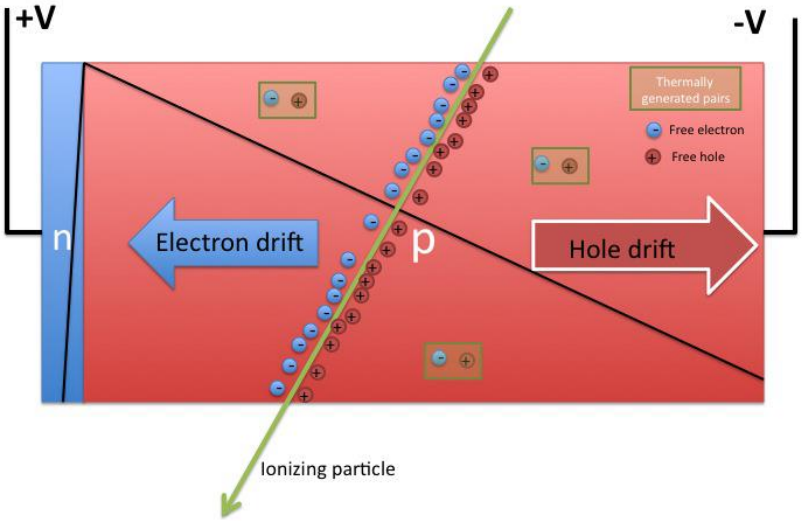

Figure 4.8 - Schematics of ionizing particle detection in a reverse biased diode. The free electron hole pairs produced by the particle energy loss drift in the electric field and produce a current in the diode. Thermally generated pairs (green boxes) are also generated in the depleted zone of the diode [68].

The drifts velocity of generated carriers depending on the electrical field E as:

$$v_{e,h}(E) = \mu_{e,h} E \tag{4.31}$$

where $\mu_{e,h}$ is mobility of electrons/holes. The mobility of the carriers is also influenced by the electric field in which they are drifting, so the saturation of their speed can happen.

The carriers' movement within the bulk induces a signal i on the collecting electrodes. This current continues until the free charge carriers recombine at their respective electrodes and can be calculated using the Shockley-Ramo theorem [69,70]:

$$i_{e,h} = eN(\vec{v}_{e,h}\vec{E}_w) \tag{4.32}$$

$\vec{E}_w$ is the weighting field. The weighting field depends only on the geometry of the electrodes and determines how the charge's motion couples to a specific electrode to induce a signal. It is derived from the weighting potential

$$\vec{E}_w = -\nabla \varphi_w \tag{4.33}$$

The weighting potential has to be obtained solving the Laplace equation $\Delta \varphi_w = 0$ with special boundary conditions in which the electrode for which the charge is calculated has voltage of 1 V and zero potential for all the other electrodes.

The total charge collected by the electrode we can obtain by integrating the induced current over the charge collection time. This principle is using to recover the charge using the ToT (Time over threshold) and the threshold settings on a discriminator in a read-out chip in the post-processing.

4.4 Silicon sensor electrical characterization

The electrical characterization of the sensors before being interconnected to the electronics is the most important phase of testing after their production. This procedure is based on two essential measurements: the current versus bias voltage and the capacitance versus bias voltage measurements, which are very powerful tools for sensor testing.

Current vs Voltage (IV) measurements allow for finding almost all possible problems in the sensor production process by a deviation from the expected shape. The current voltage characteristics help to determine the depletion voltage, the level of leakage current and the breakdown voltage of the device under test (DUT).

The current measured in the IV measurements is basically the leakage current. It represents the amount of charge per unit of time generated in reverse biased sensor, when no external excitation is provided. A current-voltage dependence of a reversely biased silicon sensor or a diode has a typical shape, shown in Figure 4.9, which represents the IV measurements of the simple diodes with the special guard ring structures. At the beginning of the IV characteristics, the current rises, as a square root of the voltage until the sensor is fully depleted. After this point we have a more or less stable current region, but then by further increasing in the bias voltage we reach breakdown which corresponds to the rapid current gain. It happens, because the electrical field within the detector becomes so high that structure starts operating in avalanche mode. As at the beginning the breakdown occurs in a certain region, the increase of the current starts smoothly, but if the voltage rising further, it results in hard breakdown, the current jumps by several orders of magnitude, which eventually destroys the detector. The potential value when this happens called the breakdown voltage. It is one of the important parameters of the sensors, which is determined by IV measurements and shows the maximum operational biasing voltage, which is possible to safely apply to the device. The early breakdown indicates some problems with the sensor structure. It can be defects in the structure or scratches on the surface, which cause charge injection when the space charge region reaches them.

For the highest sensitivity to a charge particle traversing the detector, the level leakage current is required to be a small as possible. By increasing the bias voltage we extend the depletion volume, and by this we increase the signal and reduce the electronic noise, which depends on the sensor capacitance. However maximum applied reverse bias is limited by the breakdown. That means that the breakdown voltage is required to be as high as possible comparing to the full depletion voltage to allow stable operation. In particular, for the irradiated sensors, which have a

lower performance caused by radiation damage, and to recover their efficiency the operating voltage is greatly increased.

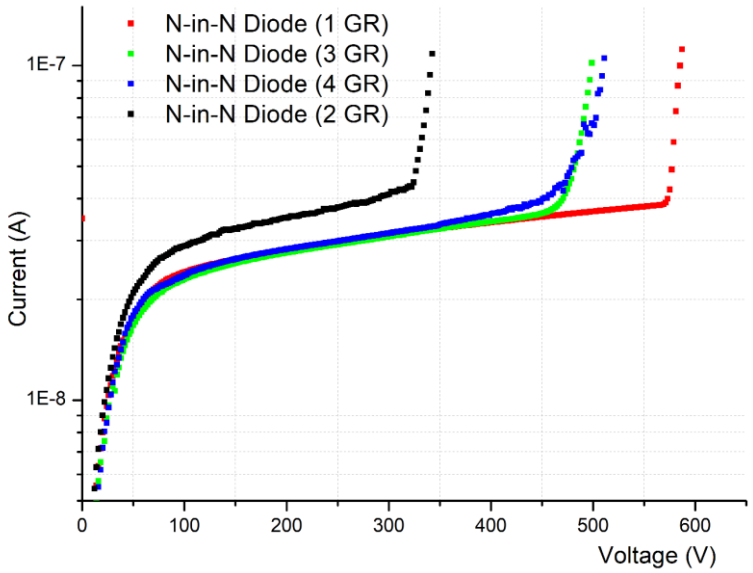

Figure 4.9 – The IV curves measured for the n-in-n diodes differ by the guard ring number.

To make possible the IV measurements of the sensors before the interconnection, the special biasing structure is implemented during the sensor production (section 5.2.1.1), which can keep all the pixels at the same potential to allow full sensor biasing. The IV measurements are performed in the clean room conditions in the light tight environment (in the dark box to avoid any ambient light entering). The current measuring is achieved using low impedance needles, while the biasing is performed through the copper conductive base chuck. The methodology used for the measurements is the voltage sweep technique is used, the applied to the detector reverse bias voltage is varied in steps of few volts and the current drawn through the device is measured at each step through tri-axial cables. The leakage current continuously fluctuates over a range at a given value of reverse bias, so an arrangement is made in the meter to average out all the fluctuating values of leakage current over few seconds.

Capacitance vs Voltage (CV) measurements are the second important sensor characterization process, which allows determining the full depletion voltage. In principle, as was discussed, the full depletion voltage could be determined from the IV measurement as a point when the leakage current does no longer increase. However, transition from the regime where the current is proportional to the square root of the voltage and the regime where the current is constant is not precisely measurable. The CV-measurements is more suitable, because the backside capacitance displays a stable plateau. The capacitance per unit area of a simple diode is calculated as two conductive plates separated by the depletion zone of width $W(V)$:

$$C(V) = \frac{\varepsilon_0 \varepsilon_{Si}}{W(V)} \approx \begin{cases} \sqrt{\dfrac{\varepsilon_0 \varepsilon_{Si} e N_D}{2V}} & \text{for } V < V_{depl} \\ \dfrac{\varepsilon_0 \varepsilon_{Si}}{d} & \text{for } V > V_{depl} \end{cases} \tag{4.34}$$

In the first case we have the growing of the depletion region and in the second case the depletion region is stable and equals d . The full depletion voltage can be determined by plotting $1/C^2$ vs V . In this view the curve rises constantly until it reaches a plateau and becomes a horizontal line. Both branches of the CV-curve have a linear behavior and can be fitted by a straight line. The intersection of these lines corresponds to a full depletion voltage, as shown in Figure 4.13.

The sensor capacitance is must be achieving small as it directly affects the noise and crosstalk. It is calculated from the measured amplitude and phase shift of the current signal in response to an AC measuring voltage with user selected frequency. The measurements are done with LCR meter using parallel equivalent circuit model, which is acceptable for the CR measurements. For this the detector is subjected to an AC voltage source coupled with DC bias voltages source to deplete the sensor. Detector capacitance is measured with the sweep of bias voltage. The meter measures the voltage across and the current through the DUT. From the ratio of these the meter can determine the magnitude of the impedance. The phase angle between the voltage and current is also measured in more advanced instruments; in combination with the impedance, the equivalent capacitance or inductance, and resistance, of the DUT can be calculated and displayed. The CV is carried at different operational frequencies AC (selectable test frequencies from about 100 Hz to 1 MHz. The frequency for the CV-measurements must be chosen carefully, especially for the irradiated sensors, which have more defects with less mobility free charge carriers and so the capacitance becomes bias independent at very high frequencies, because the contribution of the free charge carriers to the total capacitance in the bulk is small.

A wide variety of sensors and diodes structures has been electrically characterized during my thesis work. In the R&D phase it is very important to test sensor samples to evaluate a given sensor design or production. Usually these samples are of smaller size or simpler to reduce the cost of test production. The examples of sensors and diodes tested by me in the clean room at LAL are pictured in Figure 4.10. For the electrical characterization measurements I used two different setup based on probe stations: first is a manual one for more simple under test structure and a semi-automatic probe station, allowing to measure more advanced structures and it is shown in Figure 3.13.

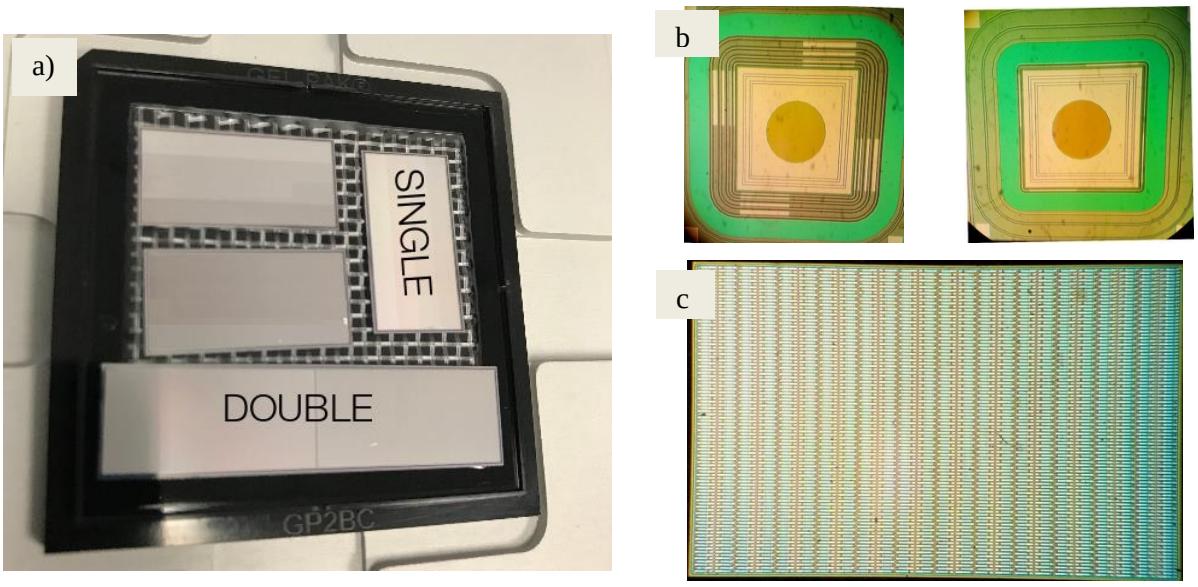

Figure 4.10 - a) Sensors compatible with the FE-I4 of a single and double size. b) The special designed n-in-n diodes with different guard ring structure. c) The n-in-p active edge sensors of 5×5 mm^2 size.

The measurements for the sensor electrical characterization are performed in the clean room environment. The clean room is special room designed and maintained in a way that there is no dust inside. The humidity and temperature are constantly monitored and controlled by special conditioning and filtering systems. The special clothes must be used to minimize the pollution from outside. Such conditions are necessary for detector development and testing.

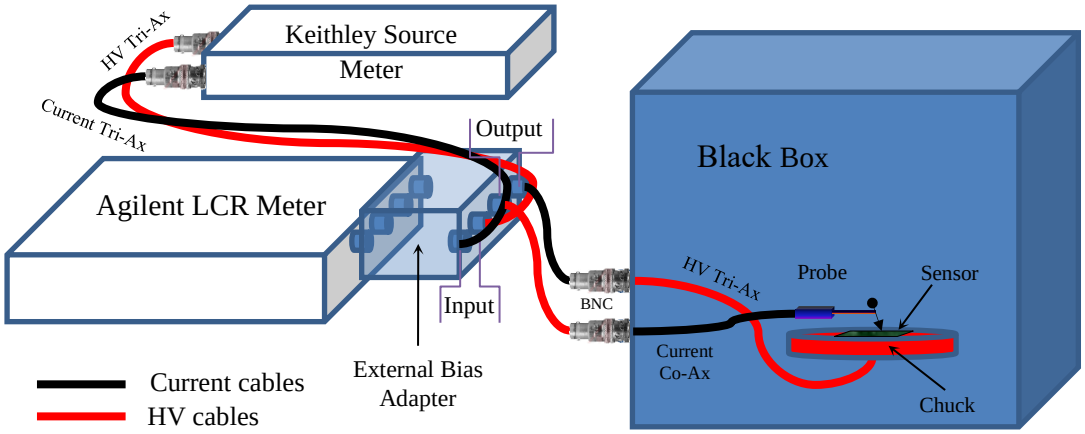

Figure 4.11 – The schematics of the setup for performing of the IV and CV-measurements. To switch between the measurement options the cabling connection configuration should be modified. The actual scheme is related to the CV-measurement option, for carrying out IV-measurements the LCR meter should be removed from the setup and Source Meter is connected directly to the black box patch panel to the respective terminals.

The typical setup for the sensor electrical characterization consists of a probe station, sensitive device meters (LCR meter and picoampere meter) and accurate power supplies. The scheme of the setup used for the IV and CV measurements with the connections is sketched in Figure 4.11. The heart of the installation is a probe station. It is placed in the black box and allows for precise electrical probing of the sensor structure. Through the low-impedance and good shielded cables the probes and the chuck of the probe station are connected to the relevant devices. To perform IV-measurements the Keithley source meter is used, which can measure current with 10pA accuracy and voltage while sweeping voltage. For the CV-measurement we should add an AC impedance meter, sometimes called an LCR meter. It measures AC impedance by supplying an AC voltage to the device. The current through the device and the voltage across the device are measured in a phase-locked manner that precisely identifies the phase angle between them. By knowing the amplitude and phase angle, it's possible to calculate inductance (L), capacitance (C) and resistance (R). The Agilent LCR meter doesn't have a built-in high voltage DC bias unit, which we need for the CV measurements of the silicon sensors; it can supply only voltage up to 40 V. For this the special bias coupling box is used. The bias box adds to the DC voltage supplied from Keithley, which may source up to 1000 V, the small (tens mV) AC voltage from the LCR meter. It connects by four terminals to AC impedance meter, by two terminals to the source meter that apply the high DC voltage for the sensor biasing, and two output terminals, which are connected to the probe station.

The manual probe station is shown in Figure 4.12. It has precise mechanical base, the microscope with three different magnifications and conductive copper chuck. To perform low

temperature measurements, the chuck can be cooled down by liquid cooling system which pumps the coolant through the pipes connected to the chuck. The setup is place in the black box, with the patch panel with needed connectors. The HV is applied using the HV tri-ax cables and the current measurements are performed via tri-axial and co-axial BNC cables connected to the low impedance probes: the simple one or the Kelvin type. The needles used in the setup have a different radius (from 0.2 μm to 5 μm) to contact tiny structures. The vacuum pump connected by pipes to the chuck is used to fix the samples on the chuck surface to prevent any movements during the measurements, which can lead to the scratches and probably destruction. The test setup must be adequately shielded, and has low parasitic capacitance probes, chuck and cables.

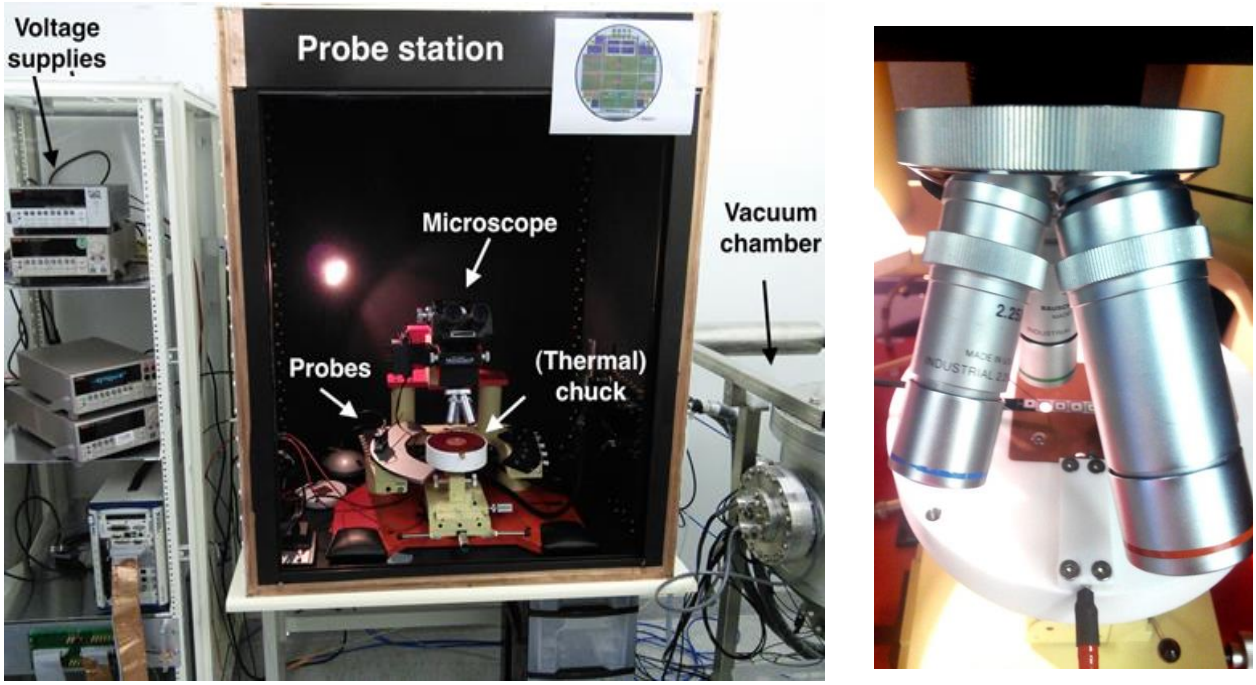

Figure 4.12 - Photo of the probe station in the clean room at LAL. The black box, containing the setup, and the rack with the measurement devices are shown.

Another setup, used for the wafer or sensors electrical characterization is a semi-automatic Signatone probe station with a large chuck (allows 6” wafer measurements) which can be cooled down by vortex cooling system up to -40^{o}C allowing the characterization of the irradiated sensor. Also it has a data acquisition system based on Keithley Parametric Curve Tracer configuration, which provide comprehensive device-level characterization and contains High Power System 2657A, providing up to 3 kV of biasing voltage, Source Meter 2636B and Multi-Frequency C-V Meter.

The DAQ system can be connected with the probe station in a master-slave configuration and behave as one integrated system. All the system is controlled by ACS Basic software [142], which manages external instruments through GPIB. ACS software (shown in Figure 4.13) is specifically tuned to take advantage of the performance capabilities of the instrumentation and includes several sample libraries for performing common device tests [142]. The software allows the user flexibility in configuring all of the measurement channels to create different tests with an adjustment of all required parameters.

The software allows creating the map of the wafer for automatic electrical measurements of periodically repeating structures on the test wafer. In this process the chuck can move automatically in the prescribed direction searching for the defined by user die, while the master software analyzes the picture from microscope and recognizes the dies on the wafer. Once the required die is found, the chuck stops moving in the horizontal plane and lifts up to make a contact between probes and wafer surface. When the contact is established the measurements are performed. The position of the contacting points on the tested structure can be set manually by entering the coordinates. The measured data can be treated with general analysis functions implemented in this software or be saved in file.

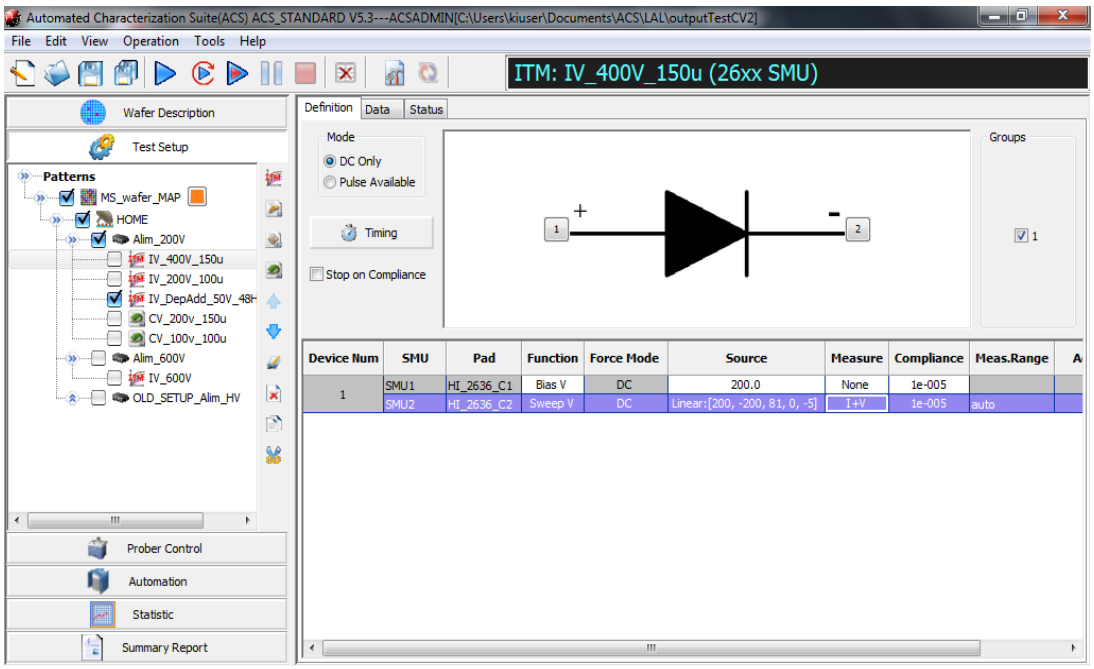

Figure 4.13 – Keithley Automated Characterization Suite (ACS) Software is shown, with the tests configuration tree on the left, in which the requirements for the different tests are saved.

The example of the results of the electrical characterization of the pixel sensor is shown in Figure 4.14. The IV-curve shows acceptable level of leakage current. The breakdown is not observable in the range up to 200 V, which was the minimal requirement for the under tested sensors. The measured CV-curve is fitted by linear function to calculate the full depletion voltage. The obtained value is 76 V which is far from the breakdown.

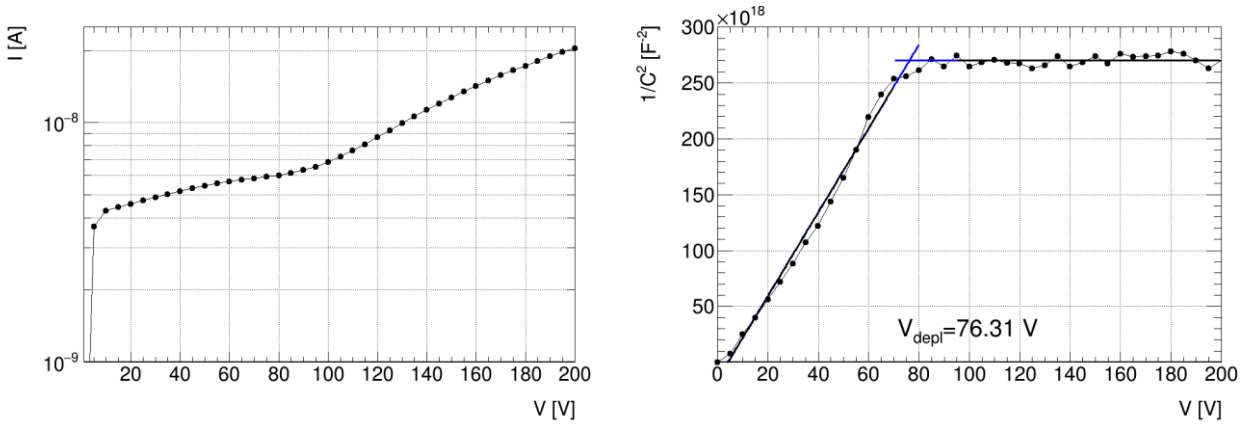

Figure 4.14 – The example of the results of IV measurements (left) and CV measurements (right).

4.5 Radiation damage in silicon

Silicon detectors are degraded by the exposure to radiation, their properties will change. This occurs due to two processes: **non-ionising** and **ionising** energy loss by particles interacting with the material [71]. Each effect leads to specific changes of detector properties and operation conditions. It is important to understand the radiation damage process and the effect they do in order to design sensors that are able to function efficiently in a regime of high occupancy and high radiation dose.

Non-Ionising Energy Loss (NIEL) occurs when the high energetic particle traversing the silicon sensor moves lattice atoms away from their normal position. This process produces the crystal imperfections which may be electrically active and hence change the electrical properties of the material [96]. Displacement damage occurs where an incident particle transfers enough energy, which is more than so-called displacement threshold energy (for Silicon it equals 12.9 eV) [73], to knock out the target atom from its normal lattice position to another position, creating behind a vacancy and an interstitial position (Frenkel pair) in the lattice. Such one-atom disorder in a crystalline lattice is called a point defect. If the transferred by incident particle energy is so high, that the displaced atom can itself cause further displacements, producing the cluster-like damage in quite large volumes with radius between 10 nm and 200 nm. Point defects in general introduce energy levels in the band gap close to mid-region, whose position can be measured by different spectroscopic methods. Experimentally, it is proven that these additional level defects are primarily acceptor level. Depends on the initial effective doping concentration N_{eff}, the radiation will reduce the N_{eff} for the n-type, and increase for p-type substrate.

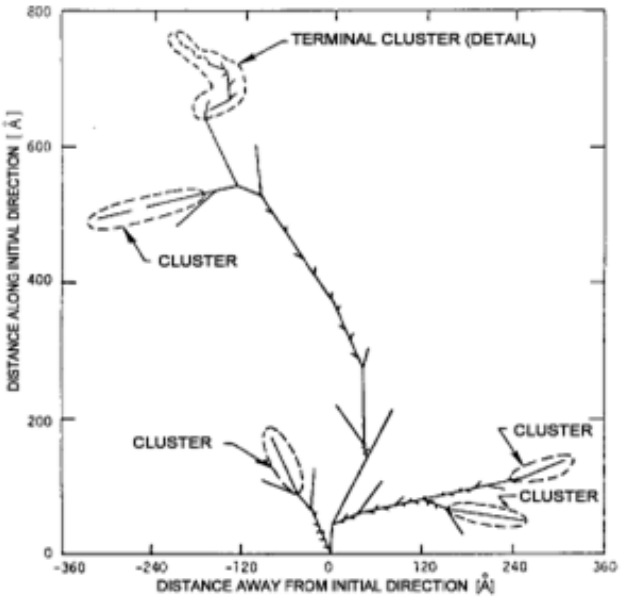

Figure 4.15 – Simulation of the development of clustered damage in silicon for the case that the energy transferred to the lattice site is more than 1000 times greater than the threshold energy for displacement.[74]

The primary defects, the vacancies and interstitials, are not stable; they are able to move through the lattice of the material. They can recombine if meet another defect or create secondary point defects. Such change of the amount of defects with time is called annealing, more details will be presented in the next section.

In contrast to ionization, which is a mechanism to produce the electrical signal in pixel detectors, the NIEL damage is caused by interaction of the incident particles with the lattice nuclei, which in most cases is not reversible. The amount of non-ionizing damage depends on the particle type, its momentum and interaction process. For example, charged particles interact via electromagnetic mechanism with atom nuclei that are partially screened by the electron cloud, so they produce more point defects than neutrons, which only feel the nuclear interaction and can produce more cluster defects. However, to be able to compare the damage caused by the

different type of particles, the radiation damage is scaled with NIEL and is usually expressed in 1 MeV neutron-equivalent by square centimeter (n_{eq}/cm^2). The displacement-damage by exposure to different particle types and energies can be calculated by scaling the flux of the incoming particles by the ratio between the NIEL for that particle and the NIEL for a 1 MeV neutron. This ration is defined as a hardness factor k . A large number of publications measuring the hardness factors for various types of particles are available in the literature. The measure of irradiation dose by particle fluence Φ of given type and energy can then be expressed in equivalent fluence Φ_{eq} of 1 MeV neutrons which would create the same damage:

$$\Phi_{eq} = k\Phi = k\int \Phi(E)dE \tag{4.35}$$

The experimental determination of the hardness factors is done via the normalization of the leakage current [138]. The irradiation facilities have the measured hardness factor for them, for example, the CERN-PS facility, provided 24 GeV protons, has a k = 0.62 [96].

Ionizing energy loss causes surface damage to the device. This usually occurs during irradiation by photons, X-rays or charged particles that generate pairs of electron-hole in the silicon oxide layer (SiO_2) grown on top of the Si bulk. The electrons generated by radiation diffuse faster out of the oxide layer, but the holes due to the lower mobility become trapped there, creating an accumulation of positive surface charge at the oxide and the bulk interface (see Figure 4.16). This sheet of positive charge attracts electrons reducing the charge collection and forming the layer of electrons which a conductive path between different pixel electrodes in sensors based on n-type pixels. This electrons layer increase crosstalk and would short all the pixels. Therefore, a p-spray layer with a low dose p-implant is used to compensate the accumulating electrons to keep the inter-pixel isolation at sufficient levels [75].

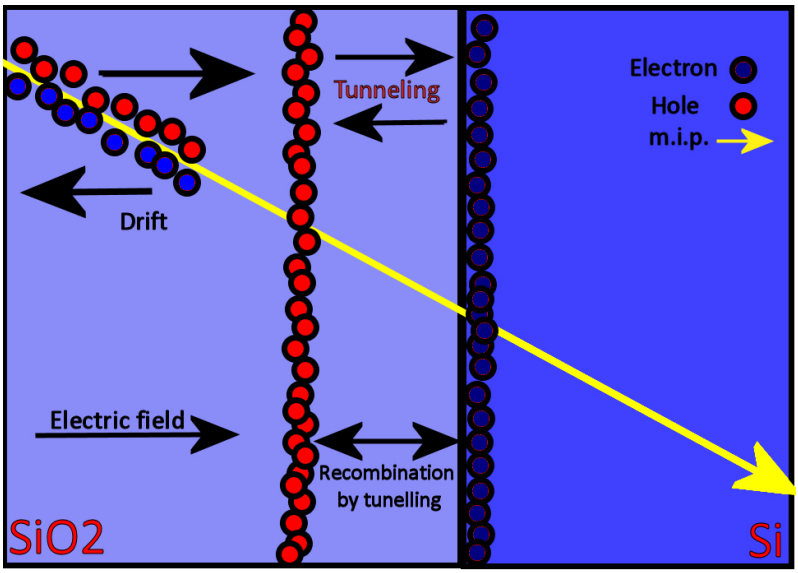

Figure 4.16 - Schematics of radiation damage effect at the silicon-silicon dioxide interface in silicon sensors [68].

The dose of ionizing energy loss radiation damage is usually expressed in *Rad*, representing 6.24×10^{10} MeV of ionizing energy deposition per kilogram of material [68].

4.5.1 Impact on sensor performance

The radiation effects lead to changes in the effective doping concentration that affects the electrical properties of the sensor: the depletion voltage, the leakage current. The vacancy of the displaced atoms created by the radiation damage can migrate in the lattice and becomes a trap for charge carriers, decreasing charge collection efficiency. The radiation-induced effects are usually reflects in two types depending on the volume where they produced: **bulk defects**, which are mainly caused by the Non-Ionizing Energy Loss and **surface defects**, which are caused by the Ionizing Energy Loss. The bulk defects caused by the displacement of crystal atoms, while the surface defects include all the effects in the SiO_2 region deposited on the sensor surface for protection, and in SiO_2-Si interface. Below the main irradiation effects in silicon sensors will be discussed, namely, they are:

- Increase of the leakage current;
- Change of the space charge in the depleted zone (increase of the full depletion voltage);
- Charge trapping

4.5.1.1 Implications of Bulk defects

Leakage current

As was discussed previously, the NIEL damage in the silicon bulk can result in energy levels forming in the band-gap. The electrons from these levels can be excited into the conduction band which contributes to the leakage current increase. In principle the NEIL defects act as **generation-recombination** centers. Some defects in lattice can capture charge carrier, leading to an increased recombination of electrons and holes after irradiation. The free carrier lifetime and drift length are reduced and hence the signal is decreased. The defects close to the middle of the band gap lead to increased thermal generation rates. The generation lifetime τ_g and the volume generation leakage current I_{leak} increase proportionally to the equivalent fuence Φ_{eq}:

$$\frac{1}{\tau_g} = \frac{1}{\tau_{g,\Phi_{eq}=0}} + k_\tau \Phi_{eq} \tag{4.36}$$

where k_τ -is the lifetime-related damage rate [96]. And the leakage current increases as:

$$\frac{I_{leak}}{V} = \frac{I_{leak,\Phi=0}}{V} + \alpha\Phi \tag{4.37}$$

The changes of leakage current ΔI_{leak} are material type independent and are generally proportional to the radiation dose Φ_{eq} and the total depleted sensor volume V:

$$\Delta I_{leak} = \alpha \Phi_{eq} V \tag{4.38}$$

where α is the proportionality factor for the current-related damage rate and it is related to the lifetime-related damage rate as:

$$\alpha = e n_i k_\tau \tag{4.39}$$

with n_i - intrinsic charge carrier concentration, so the current-related damage rate is depend on temperature. Considering this fact the increased after irradiation leakage current in the sensor results in constant heating and further leakage current increasing by generation and hence thermal runaway of the sensor more likely can happen.

Doping concentration

The bulk defects induced by irradiation mainly behave as acceptors and can change the initial effective doping concentration N_{eff}, which is the difference of all-donor like states and all-acceptor-like states:

$$\left|N_{eff}\right| = \left|N_d - N_a\right| \tag{4.40}$$

It can be experimentally determined using the full depletion voltage (the voltage needed to be applied to get a fully depleted sensor thickness d) using formula (4.28):

$$\left|N_{eff}\right| = \frac{2\varepsilon_0 \varepsilon_{Si} V_{depl}}{ed^2} \tag{4.41}$$

For a p-type material the effective doping will increase and consequently the full depletion voltage will also increase. The dependence of the depletion voltage on the example of the n-type 300 μm thick sensor on the absolute value of the effective doping concentration and irradiation fluence is shown in Figure 4.17.

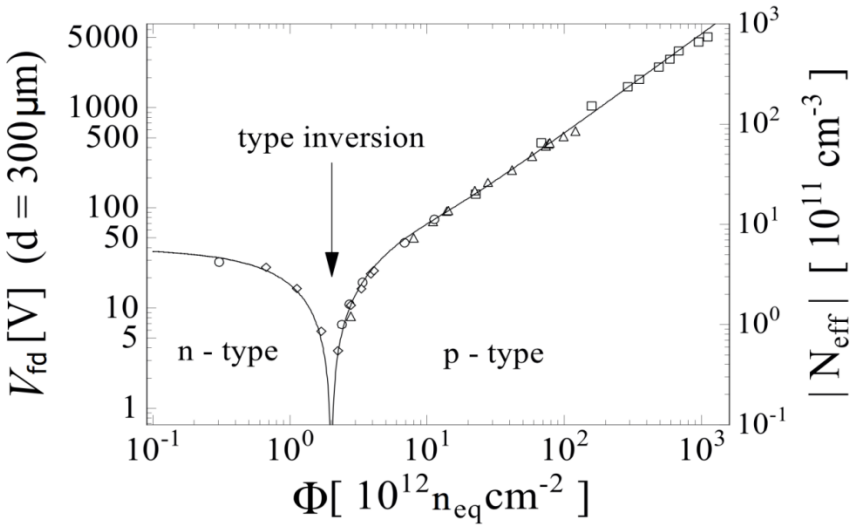

Figure 4.17 - Relationship between the depletion voltage, (left) and effective doping, N_{eff} , (right) as a function of the fluence for a 300 μm silicon detector [76].

As can be seen, for a semiconductor that was originally doped as n-type, the effective doping concentration will decrease until a point is reached where the number of acceptor sites cancels out the donors in the semiconductor. After this point the altering of the effective doping concentration results in a so-called **type inversion** or space charge sign inversion (**SCSI**), a change from an n-type to a p-type bulk material. For the present ATLAS n-in-n pixel sensors the SCSI is already happened at around 3×10^{13} n_{eq}/cm^2. Therefore, in the n-type material, the depletion voltage first drops and then increases after type inversion. Instead, in the p-type material, the depletion voltage always increases with fluence.

Trapping

Charged defects can act as trapping centres in the silicon bulk. They can hold charge carriers for a certain time (trapping) and then re-emit them (de-trapping). If the emission time is large with respect to the integration time (order of tens ns), the trapped charges do not contribute to the induced signal after being trapped, thus reducing the collected signal in the detector.

The length of a charge carrier drifts before being trapped L_{drift} is equal to the effective trapping time τ_{eff} multiplied by the drift velocity υ_{drift}:

$$L_{drift} = \tau_{eff} \upsilon_{drift} \tag{4.42}$$

The charge capture probability is the inverse of the effective trapping time constant τ_{eff} and is proportional to the effective radiation dose:

$$\frac{1}{\tau_{eff}} = \beta(t,T)\Phi_{eq} \tag{4.43}$$

where β - is referred to as trapping related damage constant that depends on the charge carrier type and also on the particle type (neutron or charge hadrons) used for the irradiation [77].

Using the trapping probability it can be concluded about the number trapped charge carriers over the collection time t_c, and consequently about the resulting collected charge Q, which also can be given as a function of irradiation fluence:

$$Q(\Phi_{eq}) \cong Q_0 \exp(\frac{-t_c}{\tau_{eff}}) = Q_0 \exp(-t_c \beta \Phi_{eq}) \tag{4.44}$$

where Q_0 is the full collected charge (i.e. the signal before irradiation).

At the fluences above 10^{15} n_{eq}/cm^2 the trapping time becomes less than 2 ns, meaning the L_{drift} less than 200 μm, which is a typical magnitude of the ATLAS pixel sensor thickness, so the trapping effect becomes dominant. It is the main limiting factor of radiation degradation of Charge Collection Efficiency (CCE) at the HL-LHC. CCE is a ratio of the collected charge Q to the collected charge Q_0 measured at full depletion before irradiation:

$$CCE = \frac{Q}{Q_0} \tag{4.45}$$

Annealing of defects

Radiation defects are not stable in time, they can move freely in the lattice reacting with other defects or impurities and recombining or forming new defect structures and even after irradiation the effective doping concentration $|N_{eff}|$ of a silicon sensor continues to change as a function of time and temperature. The effect is called annealing.

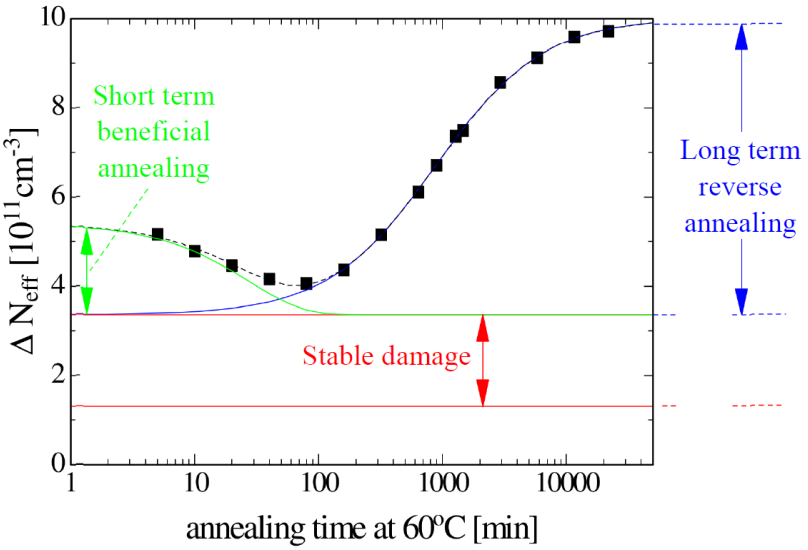

Figure 4.18 - Variation of the effective doping concentration as a function of time after annealing at 60^0C. On top of a stable damage effect (red), the beneficial annealing is shown in green and the reverse annealing in blue.[78]

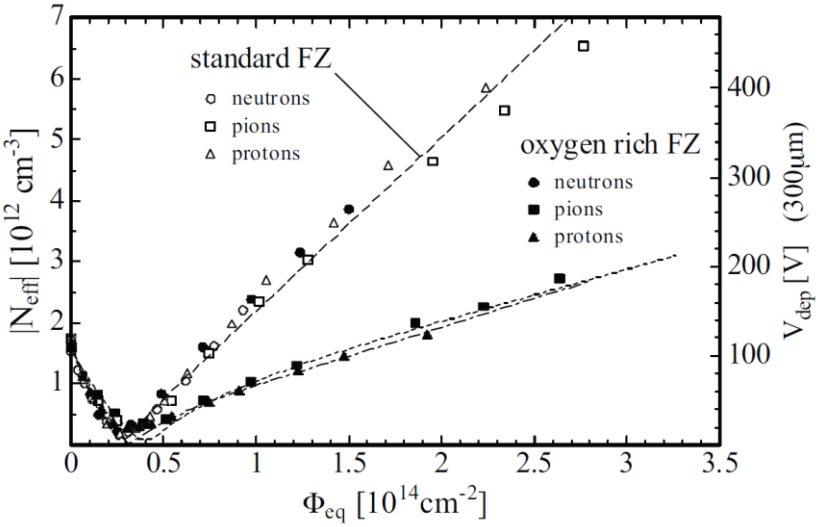

Figure 4.19 - Evolution of effective charge densities and full depletion voltage in standard and oxygenated silicon during irradiation with various hadrons. In oxygenated silicon the increase after type inversion induced by charged particles (pions, protons) is significantly lower [94].

The annealing is subject to three effects, which behavior is illustrated in Figure 4.18, and it is calculated as the sum of them according to the Hamburg model [78]:

$$\Delta N_{eff}(\Phi_{eq},t) = N_C(\Phi_{eq}) + N_A(\Phi_{eq},t) + N_Y(\Phi_{eq},t) \tag{4.46}$$

The first component N_C is time independent annealing, which stands for the stable damage in the crystal. The second term is related to so-called beneficial annealing described by the function N_A. This effect is observed on a short time scale after irradiation and characterizes by decaying acceptors causing decreasing of the depletion voltage in p-type material. The long term or reverse annealing is represented by a temperature dependent function N_Y. This process is slower and occurs at higher temperatures compared to the beneficial annealing. That's why during

storage or long time operations the sensors have to be maintained at temperatures lower than 0˚C to avoid a further degradation of their performance.

The radiation effects can be partially mitigated by changing the operational conditions (cooling, increasing bias voltage). Also, deliberate incorporation of impurities or defects (defect engineering) into the silicon bulk can affect the formation of radiation defects in the material, and thus minimize the influence of irradiation. For example, oxygen rich silicon material has been established to be radiation harder than standard silicon after irradiation with charged particles and photons (see Figure 4.19). It exhibits in a slower increase of depletion voltage with fluence. The radiation tolerance of silicon detectors can be also improved by device optimization, improving geometry and developing new technologies.

4.5.1.2 Implications of Surface defects

The surface of silicon pixel sensors is passivated by grown of several hundred nm layer of silicon oxide SiO_2. The radiation damage in the oxide layers consists of three components: the build-up of trapped charge in the oxide, an increase in the number of interface traps, and an increase in the number of bulk oxide traps [139]. The surface damage is caused by the total ionizing energy loss in the dielectric oxide layer and its interface with the silicon bulk. As the crystal structure of silicon oxide is highly irregular due to the growing process, the ionization is not fully reversible and may cause steady changes of the interface properties.

Most of electrons and holes created by the ionizing radiation in SiO_2 are recombining immediately. Electrons are very mobile and they will be collected by any positive electrode close by, in contrast to holes, which move slowly via complicated stochastic trap-hopping process and some of them may be trapped within the oxide, leading to a net positive charge. Others may move to the Si-SiO_2 interface, where they capture electrons and create an interface trap. As the lattice of Si and SiO_2 are not identical there are unpaired, positively charged dangling bonds at the interface forming the interface defects. Along with electron-hole generation process, some chemical bonds in SiO_2 may be broken by irradiation, and become electrically active defect, which serves as trap sites for carriers.

The positive oxide charge has an influence on the electric field in the silicon bulk close to the surface and induces a compensating electron accumulation layer in the n-type silicon and a depletion layer in p-type silicon. A further effect of radiation is the generation of interface states leading to a surface generation current when the space charge region reaches the surface.

Surface damage can be annealed at temperatures above 150^0C. Usually the controlled annealing with H+ ions diffused into the silicon is used to passivate the dangling bonds by forming Si-H bonds [140].

Understanding of radiation damage of silicon detectors is very important for the designing of highly radiation tolerant pixel sensors for the ATLAS ITk upgrade. We need to have the most accurate radiation damage model to perform the simulation work on sensor design optimization. This requires knowledge of the active doping profiles in the device as accurately as possible to access what happens to their electrical properties after irradiation. The development of such methods is essential for this type of study. During my thesis work I have been contributed to the development of a new in detector physics method for measuring the active doping profile of silicon sensors. The method and my contribution will be explained in the section 5.5.

Chapter 5

The pixel detector technology for the ITk upgrade

Contents

The pixel layers of the ATLAS ITk will be equipped with the hybrid pixel detectors. Two sensor technologies: planar and 3D have been chosen for these detectors. The different configurations of these sensors, their features and technological solutions, as well as monolithic sensors as a cost-effective option for the ITk are presented in the beginning of this chapter.

The active edge sensors provide a large fraction of sensor active area allows for high geometrical acceptance. The hit efficiency performance of these sensors, as a candidate to instrument the ITk pixel layers, has been studied during this thesis. The production technology and the different designs of the active edge sensors produced by ADVACAM are given in this chapter.

The TCAD simulation work on sensor design optimization, increasing the pixel robustness in terms of breakdown voltage has been done and the results are presented.

Also the new method to study the active doping profile within silicon sensors before and after irradiation has been developed, and my contribution and the first results obtained with this method are presented.

5.1 Pixel detector in particle physics

The notion of pixel in image processing applications is used in reference to the smallest perceptible element of an image or device and literally means a “picture element”. Using a large pixel array, it is possible to restore the entire image. This is a principle on which modern cameras are based. In HEP pixel detectors operate on the same idea, but they are optimized for radiation registration, giving the positional information of particle tracks.

The usage of pixelated structures in the two-dimensional positioning avoids ambiguities in the track reconstruction at high multiplicities. This is an advantage of pixels over double-sided strip detectors, which measure the real hit point along with the ghost-hits, which cannot be distinguished, as shown in Figure 5.1.

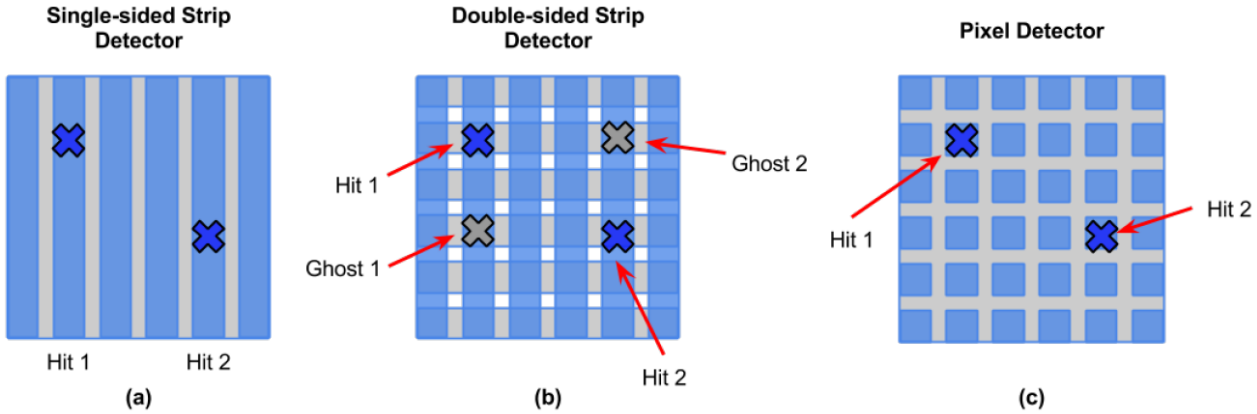

Figure 5.1 – Sketches of two hits on (a) a single-sided strip detector, (b) a double-sided strip detector and (c) a pixel detector. Ghost hits are illustrated in (b) due to the ambiguity of reconstructing multiple hits.[81]

5.2 Hybrid Pixel Detectors

The Hybrid Pixel Detectors (HPD) are composed of a sensitive part (sensor), where charge is generated by the passage of a particle, and a CMOS Application Specific Integrated Circuit (ASIC) for data readout and processing. They are completely separate entities, assembled by flip-chip process using bump-bond connections, as shown in Figure 5.2. The fact that those two parts are fabricated separately allows for their optimisation against radiation effects. Therefore, currently “hybrid detectors” is a state-of-art concept to instrument large scale pixel detectors operating at high particle rates in HEP experiments. This technology is of the fastest and the most radiation hard pixel detectors and is implemented in the present ATLAS Pixel Detector and for the IBL. Also, the hybrid detectors are a baseline choice for the ITk Upgrade.

The main challenge of hybrid detectors is the precise mechanical and electrical mating of sensors and readout chips, which characterized by complexity and very high cost. Since the integrated circuit cannot be produced large, the hybrid pixel modules can be made from multiple ASICs bumped to one sensor. Such module options are called dual-modules (two ASICs per a sensor) or quad-modules (four ASICs per a sensor) and will be used in the ITk.

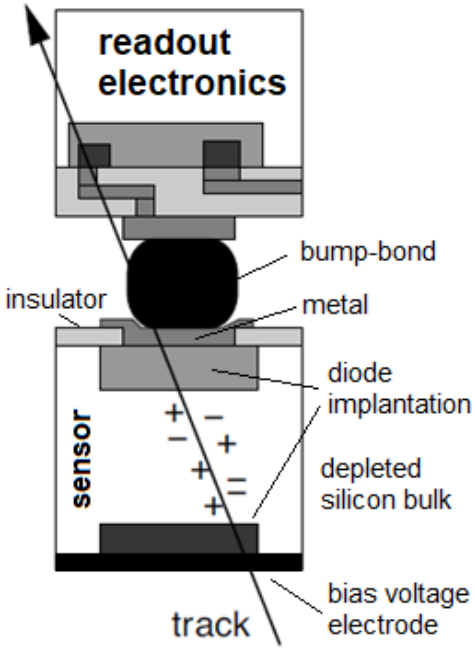

Figure 5.2 - Schematic view of a single pixel module cell in a hybrid pixel detector. A sensor and a readout chip interconnected via a solder bump ball of diameter around 20-30 μm.

5.2.1 Planar pixel sensor

The present ATLAS pixel detector is built with a planar silicon technology. This is a reasonable choice due to the relative ease of manufacturing and their high performance. For the same reason the planar sensors will be used in the ITk to instrument the outer pixel layers.
The planar pixel sensor consists of a matrix of small rectangular implantation defining the pixel cells on the top of a silicon wafer and a homogeneous opposite doped implant on a backside to form p-n junctions as shown in Figure 5.5.

Depending on the dopant type of implants and a sensor bulk there are four possible sensor configurations (see Figure 5.3): **n^+-in-n**, **n^+-in-p**, **p^+-in-p** and **p^+-in-n**. The two latest have p-type pixel implants that collect holes, which travel in silicon slower with respect to electrons due to the lower mobility, making charge collection time longer. This fact makes them less preferable for the role of radiation hard sensors, since such p^+-in-p and p^+-in-n sensors more affected by charge trapping after irradiation. For this reason only n^+-in-n, n^+-in-p, can be employed in the high radiation environment at the HL-LHC.

The sensor configurations n^+-in-n and n^+-in-p are differ in a bulk type. In case the sensor is built with n-type bulk, p-n junction is located on the backside and before irradiation the depletion starts from p-side and extends by increasing the bias voltage until the depleted region reaches the pixel implants, which are shorted together by the conductive bulk. In these conditions, the detector cannot be operated partially depleted. However, after the high radiation fluence, the n-type bulk is subject to SCSI (as was discussed in section 4.5.1), which is actually beneficial seeing the junction moves to the pixel side and the sensor can be operated even strongly under-depleted, as the depletion region is always at the collecting electrodes.

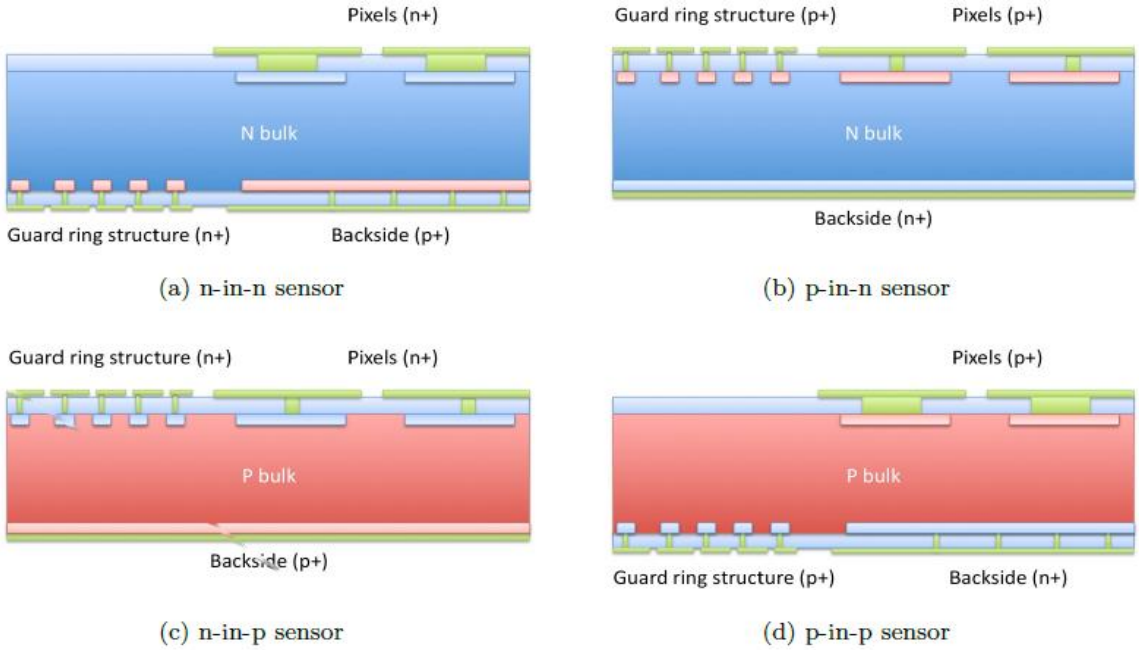

Figure 5.3 – Schematics of the possible pixel sensor implants and bulk configurations. ("+" indicates a higher concentration of dopants)

For the technology with the p-type bulk, the depletion region begins from the pixel implants and extends downward toward the backside. It enables the detector to operate at partial depletion.

The main p-n junction location defines the side where the guard rings (their purpose will be introduced in the next section) have to be built. Thus n+-in-n sensors require a complete double-sided wafer processing (as pictured in Figure 5.3a) which is more expensive than one-sided lithography, as in the case of n-in-p. Therefore sensors of n-in-p type configuration are cost-efficient (allows for cost reduction given) single sided processing suffices for fabrication while maintaining electron collection (n-type pixels).

During the initial LHC pixel development period (late 1990s) high ohmic p-type sensor wafers were not favoured, largely for reasons of historical development, and n^+-in-n planar pixel sensors have been used instead, requiring processing steps on both sides of the wafer [92]. The present ATLAS pixel planar sensors are used n^+-in-n technology, and consist of a 250 µm and 200 µm thick n-doped bulks. The bulk is made of oxygenated Float Zone (FZ) silicon for better resistance against charged particle radiation [93]. The sensor is highly doped with n^+ implants, defining the pixel cell, isolated with moderated p-spray. The p-spray is implanted in the center area between two pixels through an opening of the nitride layer. The backside is realized by uniform p^+ implantation and forms parallel electrodes with respect to the n^+ pixel implants.

5.2.1.1 Typical auxiliary sensor structures

There are several additional structures implemented in the planar pixel sensor design, which can improve the performance of the sensors and expand their testing capabilities. The layout of the sensor surface with pixel implants and their biasing structure is shown in Figure 5.4.
In the production sensors are cut from larger circular silicon wafers using a diamond saw. This leaves many physical defects in the lattice, making the edges of the sensor conductive, so it

electrically links a grounded front side with a backside at high potential. If the depleted region reaches the cutting edge, the electric field causes a sudden increase of the leakage current that leads to the breakdown of the junction. To prevent this concentric ring implants, called **Guard rings** (GR) are implemented in between the pixel matrix and the sensor border, as shown in Figure 5.4. They allows smooth potential gradient from the ground at pixel area to the region, where the high voltage is applied. Higher number of GRs leads to smaller potential steps between the rings, hence the smoother and lower the electric field and so the better breakdown behavior of the sensor. On the other hand, adding more guard rings leads to extension of the inactive area of the sensor. Usual width of the inactive surface under the GRs is from about 50 μm to about 1 mm. The guard ring structure is implemented on the p-n junction side, so for n^+-in-n sensors they are located on a backside, but for n^+-in-p case on the pixel side.

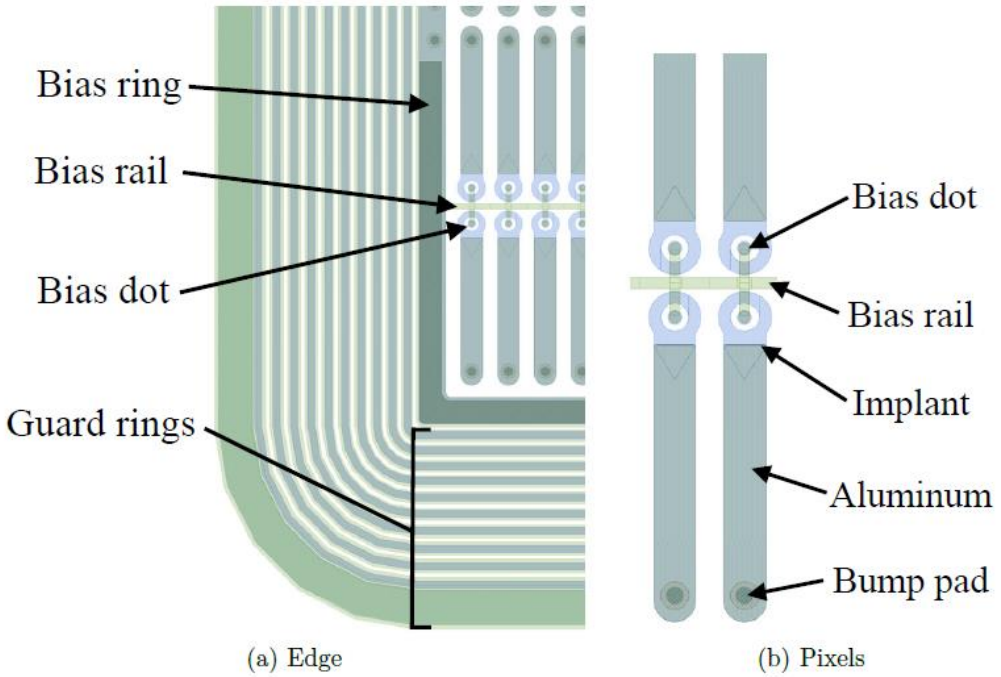

Figure 5.4 - Standard layout of a silicon pixel sensor. The edge of the sensor is shown in (a), while (b) shows the structure of the pixel cells in detail. The guard rings and the biasing structures are indicated as well as other main structures of the pixel cell.

When the GRs are on the front side there is a risk of sparks that can damage permanently the detector in the small space between the sensor edge and the grounded readout chip. To prevent these sparks an insulating coating layer of Benzo Cyclo Butene (BCB) is deposited on top of the sensor. The BCB is applied during the sensor manufacturing in relatively thick layers of typically around 3 μm. However, a remaining problem is that the cutting area and the vertical sides are not covered by BCB. For a complete protection, a layer of parylene can be deposited on the whole structure after module assembly. The high mobility of the gaseous parylene during its application ensures coverage of all surfaces even between sensor and readout chip while the high dielectric strength guarantees high voltage protection beyond 1000 V. The disadvantage of using parylene is that the deposition has to be done in a separate step after module assembly and that all contacts to the module have to be reliably protected not to be insulated as well [75].

The inner guard ring, when it is grounded, with a space-saving purpose, can be employed for biasing of the entire sensor and then it is called **bias ring**. Bias ring provides a potential around

the pixel matrix and connected to aluminum **bias rails**, which runs between the pixel columns and distribute the potential to the pixel implants. The pixel implant itself derives its potential from the bias rail through a circular implant, the **bias dot**, which is implemented in two ways: the "standard" bias dot implemented inside an opening of the pixel implant or the "common" bias dot implemented externally to the pixel implant at the corner of four neighboring pixel cells. There are two ways the pixels are connected to the bias dot: the bias resistors [95], typically polysilicon, and the "punch-through" mechanism [91]. The disadvantage of the first approach is that the resistance scales with the length of the resistor limited by the pixel size.

In the standard manufacture process the sensors cannot be tested before interconnection to a readout chip. However, it is important to check the sensors at such level, because the hybridisation is the most expensive step in module production. And the above described bias structure allows the measurements of the electrical properties of sensors before bump-bonding to readout chip. On the other hand it has been observed, that the biasing structure induces efficiency losses near the punch-through bias dots after irradiation to high fluences. These results are discussed in the section 6.4.

5.2.1.2 ADVACAM active planar sensor design

During my thesis, a set of silicon pixel planar sensors of different designs was tested. These sensor's designs was developed by ATLAS group at the Max-Plank-Institute as a baseline for the new ATLAS Inner Tracker (ITk). The designs were realized in production with active edge technologies by ADVACAM Company.

ADVACAM comprises two technology spin-off companies from Institute of Experimental and Applied Physics of Czech Technical University in Prague and VTT Technical Research Centre of Finland. The company's offering covers pixel, micro strip and diode sensors fabricated on 6" (150 mm) and 8" (200 mm) high resistivity silicon wafers having thickness from 200 μm to 1 mm. Planar Si sensor with any polarities, such as p-in-n, n-in-n, n-in-p and p-in-p can be fabricated. Both p-stop and p-spray technologies are available for the electrical isolation of the anode electrodes [107]. The sensor processes provide low leakage currents and high breakdown voltages that are typically many times higher than the depletion voltage. For example the 50 μm thick sensors show a depletion voltage at around 5 V. The company doesn't only provide the wafer processing service, but also takes the process all the way through the under bump metallization (UBM) and flip chip bonding steps.

ADVACAM has specialized in the fabrication of edgeless pixel sensors. The process technology provides inactive regions of less than 1 μm. The edgeless sensors are fabricated on 6" (150 mm) wafers with FZ silicon active bulk with high resistivity of 20-23 kΩ·cm. They provide compatible edgeless sensors to FE-I4 readout chip geometries in the thickness 50 μm, 100 μm and 150 μm. To achieve such low thicknesses the processing steps at the back side had then to be done with a thin and fragile wafer, a procedure which is obviously extremely difficult and cost-intensive. Therefore the fabrication requires the employment of a special thinning process. The one which is used by ADVACAM for the production of the active edge sensors is shown in Figure 5.5. For this an additional handle wafer is used to serve as a mechanical support to ensure the rigidity of the structure for the subsequent processing steps [108].

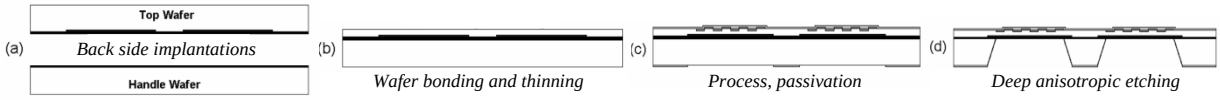

Figure 5.5 - The process sequence for production of thin silicon sensors with electrically active back side implant for the sensor devices and handle wafer (a). After direct wafer bonding, the top wafer is thinned and polished to the desired thickness (b). The processing of the devices on the top side of the wafer; the openings in the back side passivation define the areas where the bulk of the handle wafer will be removed (c). The bulk of the handle wafer is removed by deep anisotropic wet etching. The etch process stops at the silicon oxide interface between the two wafers (d).

After the finishing of the front side processing, using Deep Reactive Ion Etching (DRIE) [109] technique trenches are realized along the sensor's perimeter and so the mechanical support is provided only by the handle wafer as shown in Figure 5.6. The trench is then doped with boron and filled with polysilicon. The cut realized through DRIE produces an edge region much less damaged than the one resulting from a standard diamond-saw cut. It makes a cutting edge less conductive and implies lower leakage current generated at the borders. Since the electric field is extended to the side implantation, the entire edge is fully active, so the charge created by passing particle in the edge region can be collected by the first pixel column. In the meanwhile, the edge doping prevents the extension of the depletion region to the physical walls of the trench, Therefore, the carriers created at the cutting edge do not experience an electric field and simply recombine, without making a significant contribution to the leakage current of the device.

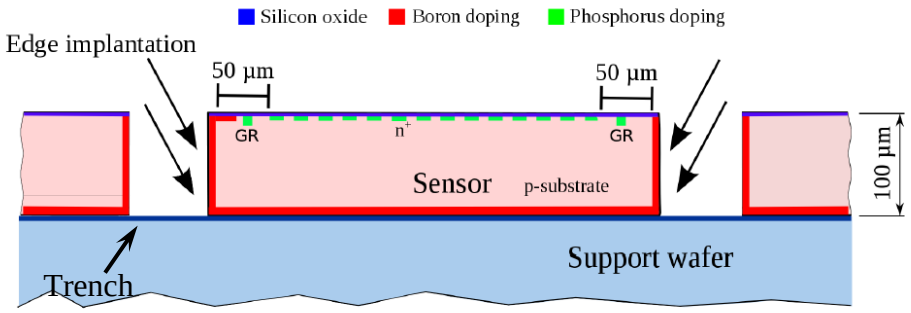

Figure 5.6 – Schematic view of the sensor processing at ADVACAM with a four-quadrant Boron ion implantation, extending the p^+ implant of the back-side to the edges [110].

After the wafer processing and UBM deposition, the handle wafer is fully removed and the sensors are interconnected to FE-I4 chips with solder bump bonding. Then the modules are coated with parylene at IZM to prevent from sparks between the readout chip and the sensor surface.

Two edge designs have been implemented in the ADVACAM production: a slim edge and an active edge, differing in the distance d_e from the last pixel column to the end of the sensor. The diversity of the sensor designs characterized during the current thesis work is schematically shown in Figure 5.7.

The active edge design as shown in Figure 5.7 (a) does not implement any grounded biasing ring, thus allows for extending the active volume to the sensor border. The active edge design

implements one floating guard ring which results in an edge width of d_e =50 µm. The slim edge design with standard punch-through structure, one guard ring and a grounded bias ring is shown in Figure 5.7 (b). The punch-through dots are implanted within the pixel implants and connected via the biasing rail. The additional guard ring allows for a smoother transition of the electric field from the last pixel implant to the edge of the sensor. A similar design with no implemented guard ring is shown in Figure 5.7 (c). The slim edge sensor with common punch-through dots as shown in Figure 5.7 (d) employs a grounded biasing ring with no guard rings implemented. All slim edge designs are characterized by an edge distance of d_e =100 µm.

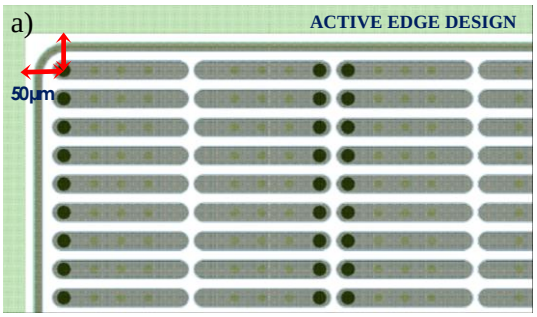

The design 1: FE-I4 with 50 µm edge, one GR, no punch-through structure

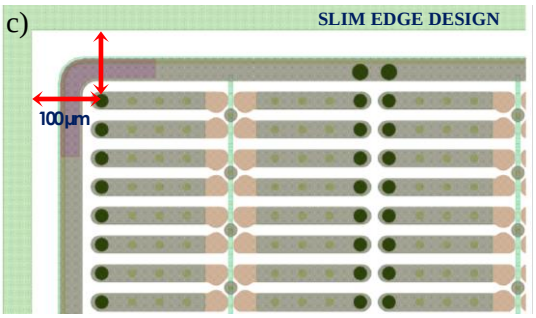

The design 2: FE-I4 with 100 µm edge, one BR, external punch-through

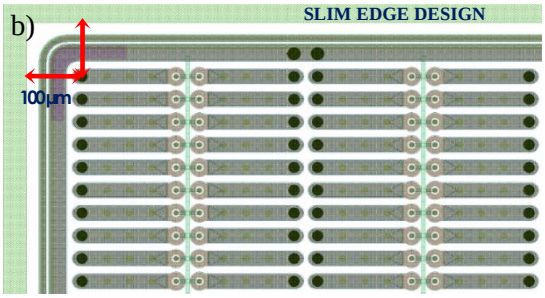

The design 3: FE-I4 with 100 µm edge, BR+GR, standard punch-through structure

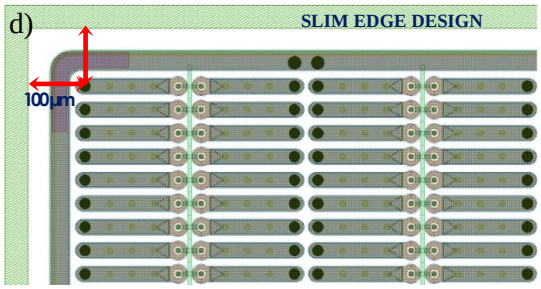

The design 4: FE-I4 with 100 µm edge, one BR, standard punch-through

Figure 5.7 – The designs of the n-in-p sensors of the ADVACAM SOI production: the active edge design with an edge width d_e = 50 µm, one GR and no p-t structure (a), the slim edge design with d_e = 100 µm, one grounded BR and the common p-t structure (c), the slim edge design with one BR and GR and the single p-t design (b) and the slim edge design with only one BR and the single p-t structure (d).

5.2.2 3D pixel sensors

Three-dimensional (3D) silicon pixel sensors were proposed in 1997 by Kenny and Parker [82] as an alternative to planar detectors. The 3D sensors are featuring columnar electrode implants of both doping types, which are penetrated into the silicon bulk substrate perpendicular to the sensor surface instead of parallel, as in the case of planar sensors. This is done through the etching of narrow deep holes in the wafer followed by doping implantation on the surface of the holes, forming p-type and n-type columns (Figure 5.8). Then the hollows are filled with a conductive material to form the anodes and the cathodes.

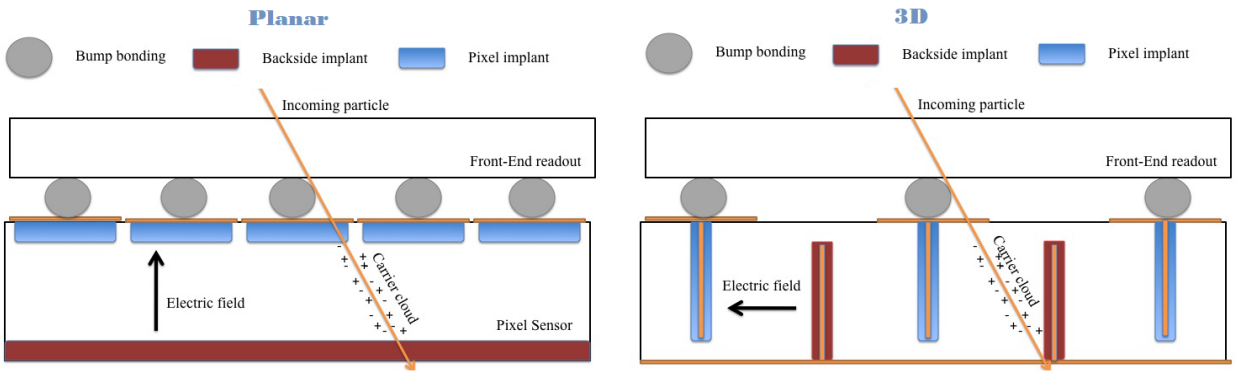

Figure 5.8 – The schematic comparison of the planar pixel sensor (left) and 3D pixel sensor (right) technologies for hybrid detector concept.

The bias voltage is applied between the n and p-type columns to generate an electric field, guiding the electrons and holes produced by the ionizing particle to the respective collection electrodes in the direction parallel to the wafer surface. This is the main feature of 3D design, when the charge collection distance is decoupled from the ionization thickness of sensors. The charge generated for an identical MIP passing through the sensitive volume for both planar and 3D technologies would be the same if the wafer thickness is not differ. But, the small (may be less than 50 μm) distance between the oppositely doped column electrodes, which defines the charge collection distance in 3D sensors, leads to a faster signal and smaller depletion voltage and, moreover, results in an increased radiation tolerance due to a reduced trapping probability during charge drift before collection.

Within the IBL detector 3D sensors have been shown to meet all the requirements and operate demonstrating high performance during the experiment. The IBL 3D sensors were produced using the double-sided processes, but for the HL-LHC upgrade the single-sided is preferred providing cost benefits.

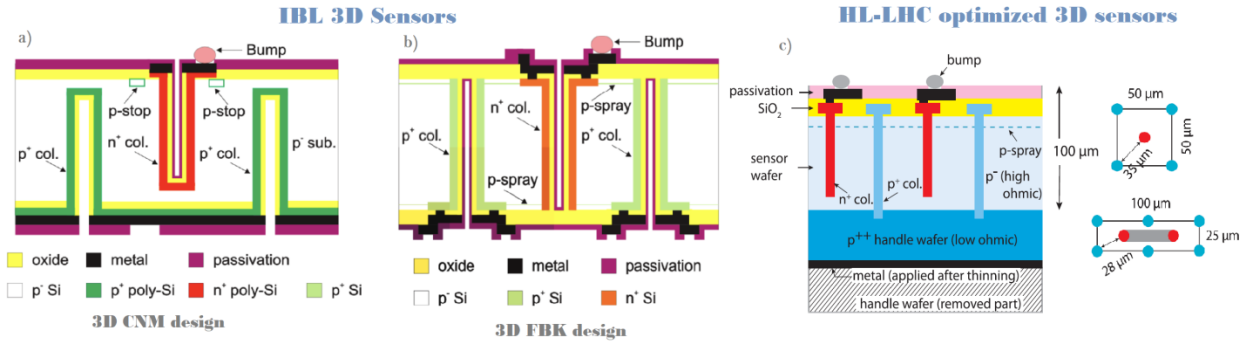

Figure 5.9 – The 3D sensor designs implemented in IBL [84]: (a) with columns, partially passing through the bulk (CNM design) and (b) with full-through column implants (FBK design) and the design optimized for the HL-LHC (c) with two top view sketches for 50×50 μm^2 and 25×100 μm^2 pixel sizes[85].

As shown in Figure 5.9, there are two different sensor designs, compatible with the FE-I4 pixel cell size of 50×250 μm^2, having a 230 μm thick p-type silicon bulk and charge collection distance of 67 μm, were developed by CNM [86] and FBK [87] to be employed in IBL. The difference between the two designs is in the process of columns. In the FBK processing column electrodes pass all through the wafer, but in CNM design the columns stop at about 20 μm from

the surface of the opposite side. These designs are known as full-through and partial-through respectively. The partially-through column design results in slightly higher charge sharing, since the generated charge can be collected on several columns. The difference in electrode depth affects the electric field at the tip of the partially-through columns and, as a drawback, introduces a lower electric field after irradiation [88]. The additional design difference is in the surface isolation between junction columns which is ensured by a p-spray layer on both sides for FBK sensors and while for CNM sensor this is done by p-stop.

The main disadvantage of 3D technology is the complexity of the process and the low production yield, making it unlikely to cover large areas. Therefore, despite their advantages, the 3D sensors will instrument only the innermost layer of the ITk for the HL-LHC.

5.3 Monolithic Active Pixel Sensors

Among the many advantages the hybrid pixel detector concept faces some serious drawbacks, as a high material budget, laborious and high-cost assembly of the hybrid modules. In contrast to hybrid pixel detectors concept, there is another so-called Monolithic Active Pixel Sensors (MAPS) concept, which is based on the approach, that pixel sensor and readout chip can be processed on the same silicon wafer. MAPSs are built on a single high resistivity silicon wafer where a low resistivity silicon layer has been grown by epitaxy. The detection diodes create local depletion regions in the high resistivity buried silicon layer, while the CMOS electronics is embedded in the low resistivity bulk, forming the readout electronics of the diode, as shown in Figure 5.10.

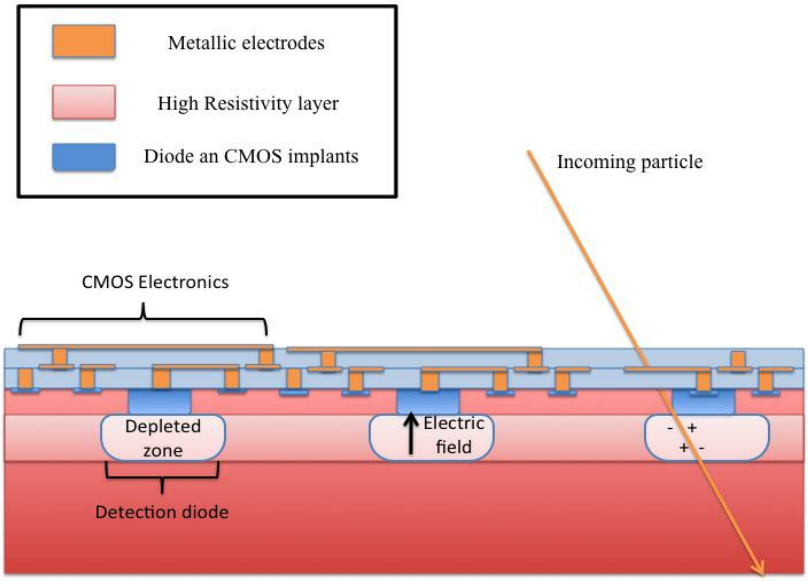

Figure 5.10 – Schematics of the High Resistivity Monolithic active pixel sensor (MAPS) [68]

A small electric field is present in the depleted region and a small signal is generated in the detection diode. The signal is then amplified and digitized on the same wafer by the readout electronics. The presence of the amplifier so close to the detection diode allows low noise operation even with the small signal produced by the passage of a particle.

Monolithic detectors employing CMOS technology were developed in 1990s and traditionally they use charge collection by diffusion, which makes them not suited for certain HEP applications in terms of speed and radiation tolerance. But the new CMOS sensor designs make possible to apply reverse bias voltage to achieve full depletion, improve the radiation tolerance and increase charge collection speed.

Integrated CMOS pixel sensors with a small collection electrode offer a small sensor capacitance, a favorable signal-to-noise ratio and power consumption, and the potential for excellent spatial and timing resolution. Such sensors have been developed and adopted for the ALICE ITS upgrade using a standard 0.18 μm CMOS imaging sensor process on a high resistivity epitaxial layer [89]. MAPS are perspective sensor technology, but for the moment in terms of rate and radiation tolerance it inferiors to hybrid pixel modules, since the CMOS active sensors are an option in the ITk only for the outer layer (L4), with low occupancy and low irradiation level.

5.4 Using TCAD tool for pixel sensor design optimization

The term Technology Computer-Aided Design (TCAD) refers to the use of computer-aided simulations with physics models to develop and optimize semiconductor processing technologies and all kinds of devices in a precise and defined computer environment. The TCAD simulation offers the advantage to predict the device performance before it is being manufactured.

This section contains the results of TCAD simulation studies on increase the performance of silicon pixel sensors. The main idea is the sensor process optimization to receive more robust sensors in terms of the breakdown voltage in particular before irradiation.

The mechanism of the breakdown needs to be understood to improve the breakdown behavior of a sensor. The breakdown of a sensor occurs if the electrical field within the sensor exceeds a critical value. The electrical field depends on the gradient of the doping concentration and the potential difference between anode and cathode. Thus, the critical region is the transition between n^+ pixel implant and p-spray layer, as it contains the largest doping concentration gradient [136]

5.4.1 TCAD Synopsys

The TCAD tools are employed in the electronic design automation aiming at modelling both semiconductor device manufacturing and operation. Solving physical partial differential equations, such as diffusion and transport equations the TCAD models the structural properties and reproduces the expected electrical characteristics of real semiconductor devices. The profound insight into fundamental physics quantities provided by TCAD gives predictive accuracy for a broad range of technologies. Therefore, when developing and characterizing a new semiconductor device or technology, it is possible to use TCAD simulations instead of costly and time-consuming test wafer runs.

The key benefits of the TCAD simulations are:

- Explore new device structures to select viable process and device development pathways.

- Use TCAD to optimize process modules and integration by fully exploring the process parameter space while reducing the number of experimental wafers and development cycles.
- Apply TCAD to capture and analyze the impact of process variation on device performance, and to increase process capability, robustness and yield. [137]

There are many TCAD software packages, grouping several elements and algorithms from different fields. Two main of them are SILVACO TCAD [144] and SYNOPSYS Sentaurus [145] frameworks, both grouping the main elements for Monte Carlo simulation, finite element solution algorithms, electrical field calculations, geometry generation and active domain simulations. The latter simulation package was used to perform the current simulation study.

Sentaurus TCAD is a commercial package offered by Synopsys Inc. for the semiconductor device simulation in 1D, 2D and 3D for various applications. The devices are approximated with a mesh of connected vertices. The vertices are the space points on which the finite element simulation is carried out to extract observables like a current for a given applied potential, an electrical field, a charge carrier's concentration, an occupancy status of various traps.

There are many tools included in Synopsys TCAD as well as the physics and radiation damage models used in the simulation. Mainly two of them were used for the simulation in the present work: process simulation (sProcess) and device simulation (sDevice).

sProcess is a way to simulate the fabrication process of silicon device. We can use it to generate a sensor structure. sProcess mimics the performing of the production steps by the foundry, for example, the dopant introduction, lithography masks and layer deposition, annealing, etching processes, etc. In the simulation, for instance, to grow the oxide layer on a silicon substrate, the full process chain is described with all details. This includes for example the duration of the growth in the oven, including the applied temperature and the details of the temperature ramp needed to reach that value, together with the description of the exact composition and flux of the gas flowing through the oven. Also, layers of photoresist can be deposited, patterned or stripped to enable the deposition of different materials or the implantation with dopants. For the implantation, the dopant material and the energy with which the dopant is shot under a certain angle on the structure together with the total dose has to be known. This level of detail is usually confidential to the foundry and hard to determine from the accessible data. Therefore, to create accurate representation of the device we wish simulate, these parameters can be obtained through experimental methods, for example, the active dopant profile can be resolve from the TLM method, which was approved during the work, described in section 5.5.

sDevice performs the device, or also called functional/electrical, simulation. It is used after the creation and meshing of the structure in every simulation. It performs all electrical characterizations by providing different possibilities to ramp up static voltages, perform AC measurements or simulate the crossing of charged particles. The steering file for sDevice simulation includes a physics section with all defined models to be used. It also includes details about the numerical models, its parameters and boundary conditions, defined by applied potential at fixed points. For the ramp of the voltage, the simulator uses a quasi-static approach in which the voltage is increased in small steps after which the Poisson equation is solved again

for the new situation. To arrive at a typical use case in HEP applications of bias voltages of a few hundred volts, several hundred steps can be necessary. During the ramping, the complete set of characteristics of the device, like electrical current, charge carrier densities or electrical field, can be saved into a file. Once the target voltage is reached, or a predefined termination condition is met, the next step is executed. The transient simulation of the device before and after the incidence can be performed as well. Also in Synopsys TCAD, bulk damage is simulated by the introduction of acceptor and donor type traps with certain cross-sections for electrons and holes as well as an introduction rate being the ratio of defect concentration to fluence for each trap.

5.4.2 Improving pixel robustness by p-spray concentration adjustment

The model of four adjacent pixels with a cell size of 50×50 μm^2 as required by ITk detector was simulated. The pixels structure consists of a 100 μm thick silicon bulk with different doping concentrations of p-spray insulation layer, which was implanted in various dose of Boron from 2.7×10^{12} cm^{-2} to 3.6×10^{12} cm^{-2} at 100 keV. A 250 nm thick oxide layer is grown on the top surface of the wafer. The pixel n^+ implantation is realized by Phosphorous ions with a total dose of 1×10^{15} cm^{-2} at energy of 160 keV. The backside was implanted by Boron ions with a dose of 1×10^{18} cm^{-2} at 60 keV.

Then the implantations are annealed at 900^0C for 3 hours. To establish an electrical contact the oxide layer was removed by etching from the top of pixels implants and aluminum of 2 μm thickness was deposited. The same was done from the back side beyond to create a backside electrode. The bias rail of the punch-through structure was also simulated.

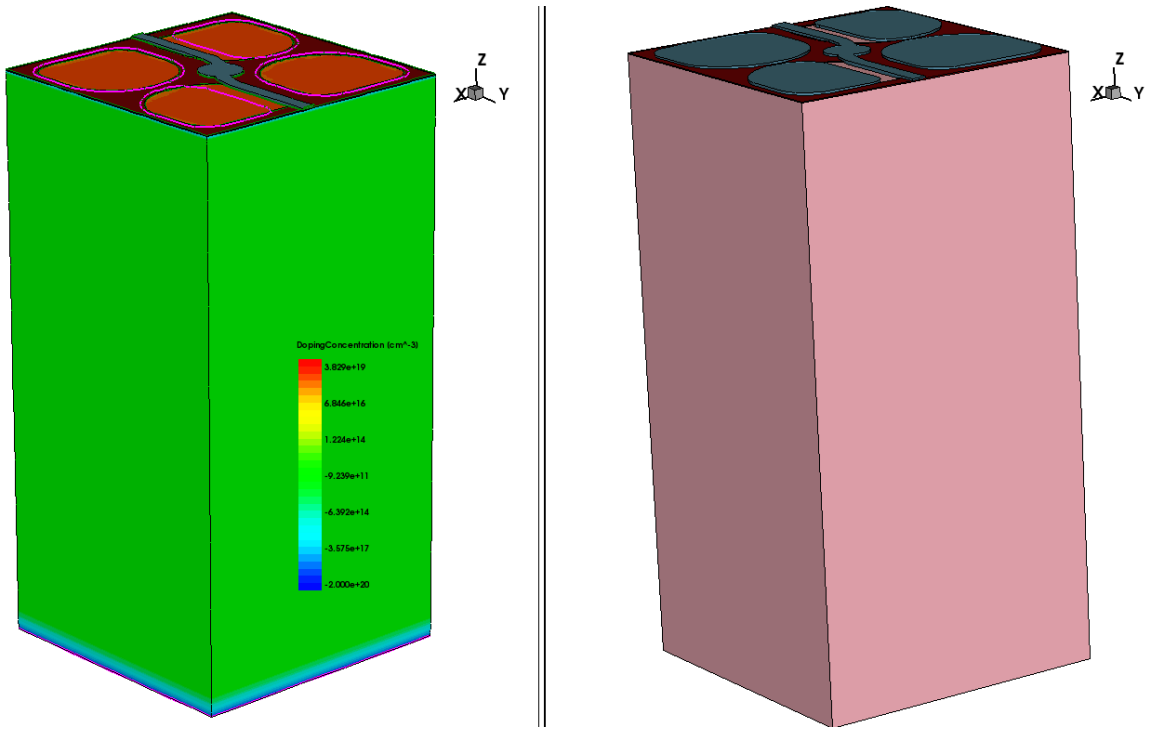

Figure 5.11 – Illustration of the geometry and doping concentration of the structure (on the left). The light red colour is a Silicon bulk, the dark red is an oxide layer. The grey colour represents the aluminium metallization.

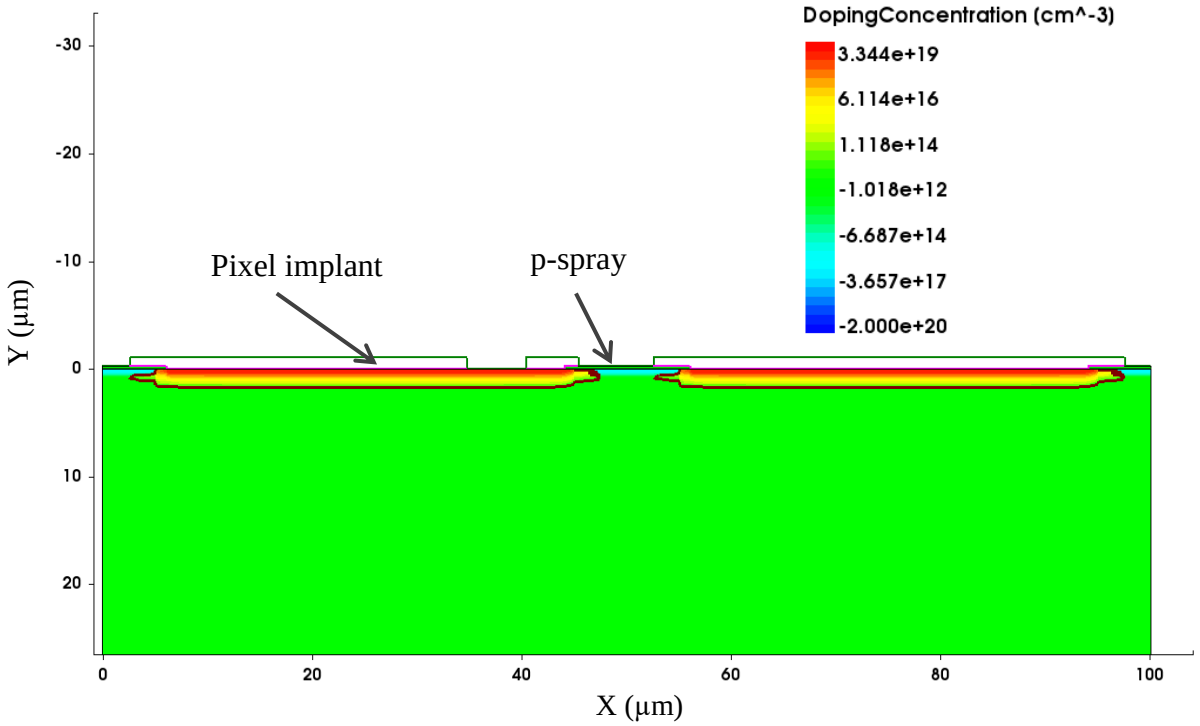

Figure 5.12 – The analytical doping profile of p-spray and pixel implants is shown. The dark-red line beneath the pixel implants shows the positon of the p-n junction

5.4.3 Results

The idea of simulation was to check the breakdown behavior of the sensors depending on the peak concentration of the p-spray implant. The understanding of the behavior can give an idea how to increase the breakdown voltage.

The plots for the current density and electric field values were simulated for different p-spray doses at several bias voltage points. The results are shown in Figure 5.13.

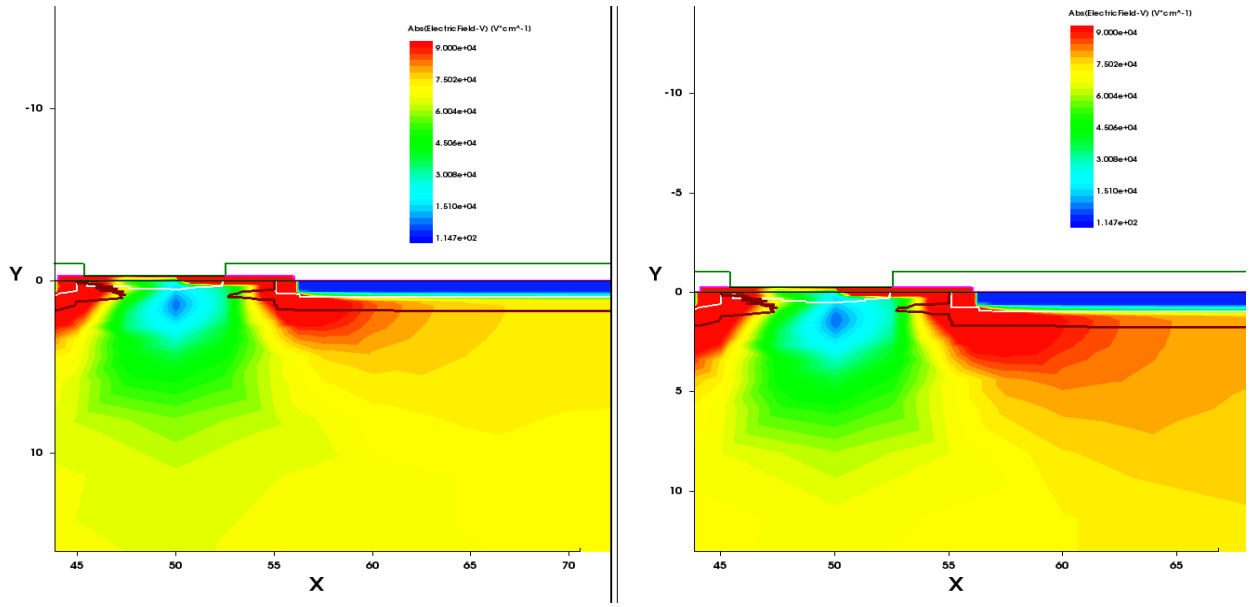

Figure 5.13 (a) – The hole-current density for the pixels with the 3.0×10^{12} cm^{-2} (left) at 350 V and for 3.3×10^{12} cm^{-2} (right).

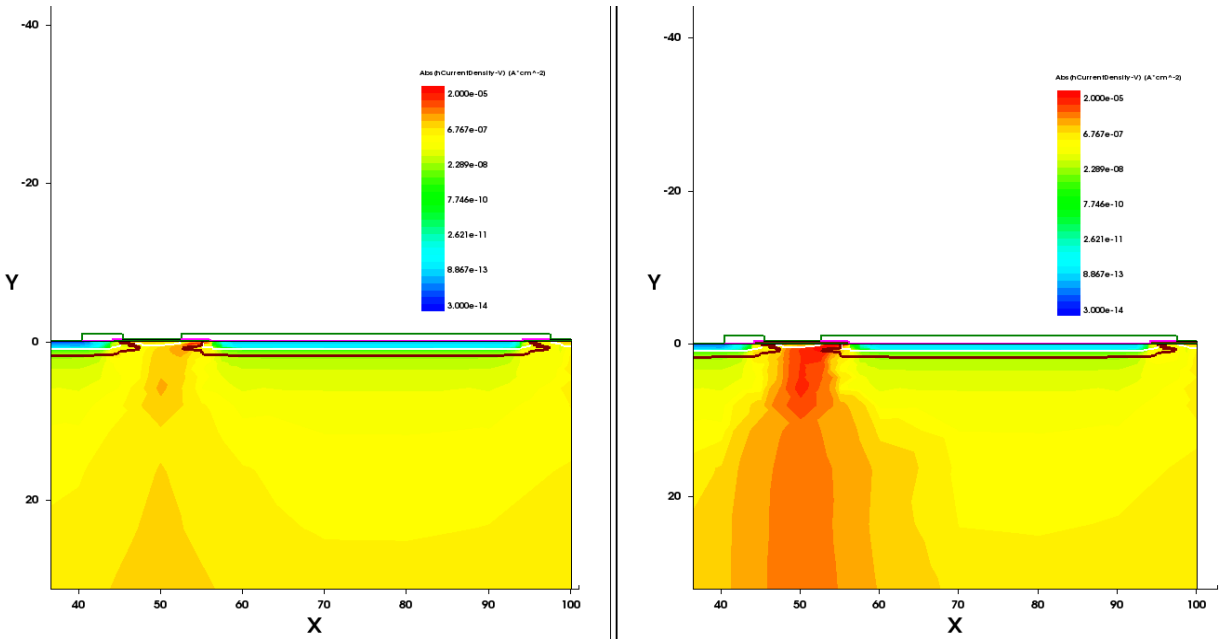

Figure 5.13 (b) – Absolute value of the electrical field for the pixels with the 3.0×10^{12} cm^{-2} (left) and for 3.3×10^{12} cm^{-2} (right) at bias voltage of 350 V.

Maximum electric field occurs at the point of transition between the n and p type material and can easily reach 10^{5}-10^{6} V/m.

To determine the breakdown voltage the IV-measurement procedure was simulated, the pixels were grounded while the sensor backside is ramped to a negative potential until current reach the defined by user maximum current, which in a given case was 10^{-7} A. The obtained IV curves are plotted in Figure 5.14.

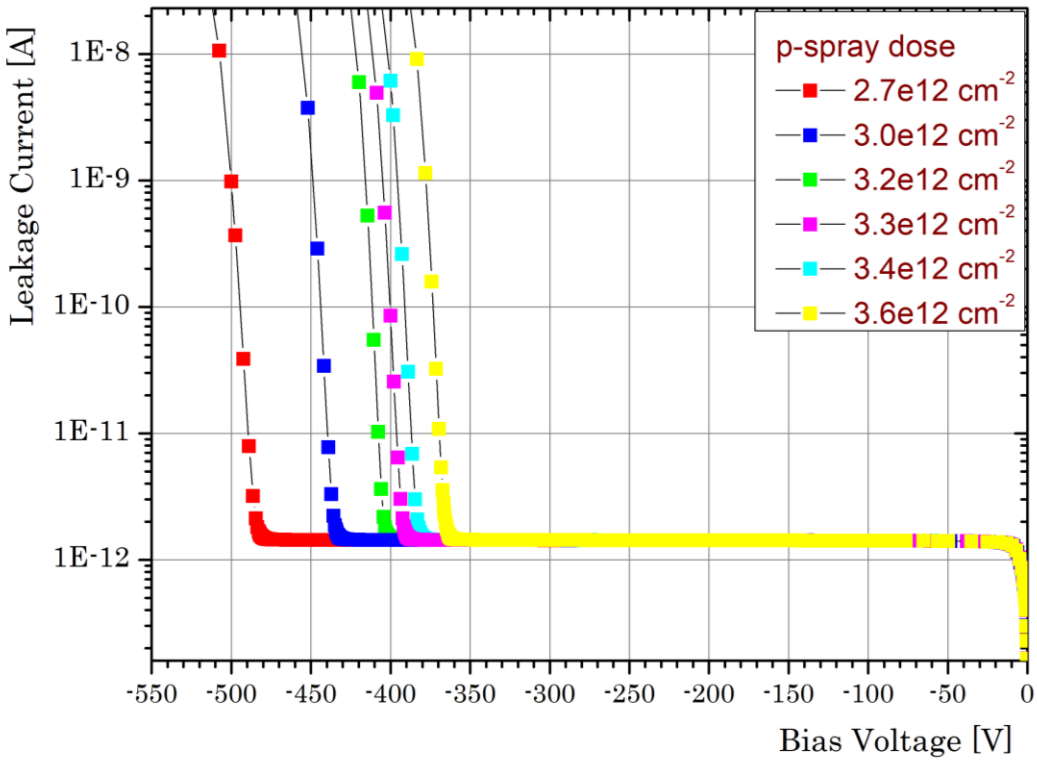

Figure 5.14 – Simulated IV curves showing a breakdown voltage for different p-spray doses.

One can notice that the breakdown voltage is clearly increased for decreasing p-spray peak concentrations. This TCAD simulation can give some hints on design optimization to increase robustness of the detectors. The obtained about the breakdown voltage depending on p-spray concentration values should be checked with experimental measurements. For this the sensor production with several pixel designs with different p-spay concentration value. This study is very important for optimizing pixel design in the future for any pixel pitch. The potential future work could be development of more advanced 3D simulation model with different p-spray concentrations and test sensor production according to the simulation results and thus the comparison of the results of the real prototypes measurements with simulations.

5.5 A new method to measure active doping profile

The study of radiation effects, which cause degradation of silicon sensor performance, is extremely necessary due to the expected high radiation exposure during operation within the ITk at the HL-LHC. The development of the methods for the measurements of the active dopant concentration in silicon sensors is important to understand how much the quantity of electrically active carriers is decreasing during irradiation and how this loss affects the performance of the detectors. The work presented in this section addresses the developing of a new method of active dopant profile measurements, called the Transmission Line Matrix method (TLM). More details about this work can be found in the [79] and [100]. In this section I will give an overview of the TLM and present my contribution in the developing of the method to determine an active doping profile in the silicon sensors by the TLM.

The TLM technique was never applied in the HEP domain, but it is widely using in semiconductor engineering, in integrated circuits and photovoltaic applications to extract the measure of contact resistance of metal-semiconductor interface

5.5.1 Basics of TLM method

Consider the TLM test structure based on the geometry displayed in Figure 5.15. It consists of embedded into silicon metallic pads of the same geometry with length (L) and width (W) and contact area A_c. The contacts are separated from each other by unequal spacing distance x_i. The TLM involves current voltage measurements on adjacent contacts to infer the resistance.

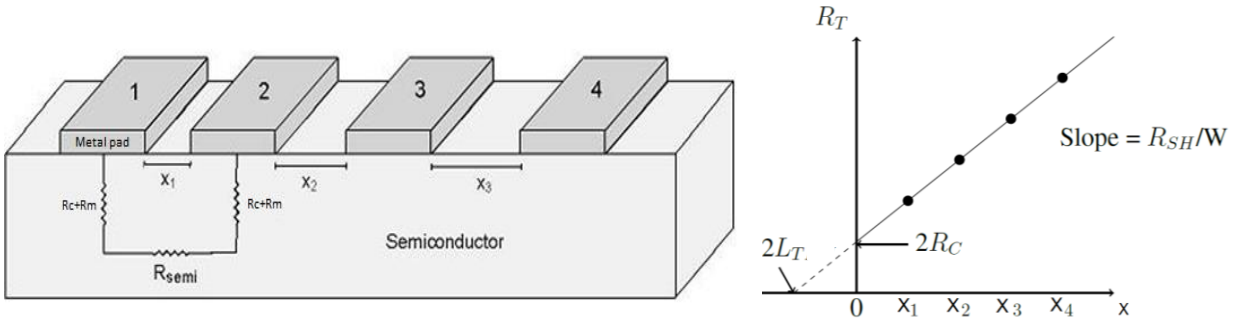

Figure 5.15 – (Left) The test structure for the TLM measurements. (Right) Resistance versus contact separation, obtained from TLM measurements. Both the sheet resistance as well as the contact resistance can be determined using this technique.

Assuming the similar contact resistance for each contact, the measured total resistance will contain several components:

$$R_T = R_{semi} + 2R_c + 2R_m \tag{5.1}$$

where R_m is the resistance due to the contact metal, R_c is associated with the metal/semiconductor interface, and R_{semi} is the usual semiconductor resistance. The resistance of a single contact is $R_m + R_c$. However, the resistivity of the metal in the contact is so low that $R_m << R_c$, and so R_m can be ignored.

The semiconductor resistance R_{semi} could be expressed using the semiconductor resistivity ρ_s:

$$R_{semi} = \rho_s \frac{X}{A_c} = \rho_s \frac{X}{Wt} \tag{5.2}$$

where X is spacing between two contacts with the cross-section area A_c. For the rectangular contact $A_c = Wt$, where W - is width and t – thickness of the contact.

The resistivity can be linked to the dopant concentration N_D

$$N_D = \frac{1}{e\mu_e\rho_s} \tag{5.3}$$

where e is the elementary charge and μ_e is the carrier mobility.

For semiconductors doped through diffusion or surface peaked ion implantation with junction depth d_j, we define the sheet resistance R_{sh} using the average resistivity $\bar{\rho} = \frac{1}{\bar{\sigma}}$, where $\bar{\sigma}$ - is the material conductivity:

$$R_{sh} = \frac{\bar{\rho}}{d_j} = \frac{1}{\int_0^{d_j} d_j \sigma(z) dz} \tag{5.4}$$

which in materials with majority-carrier properties can be approximated by (neglecting intrinsic charge carriers):

$$R_{sh} = \frac{1}{\int_0^{d_j} d_j \mu e N_D(z) dz} \tag{5.5}$$

The total resistance R_T between any two contacts (of length L and width W) separated by a distance x_i could be measured and plotted as a function of x (as in Figure 5.15). The resulting

function of $R_T(x)$ can be used to obtain transfer length L_T, measured from the intersection of the resistance curve for R_T = 0 and contact resistance values R_C.

5.5.2 TLM measurements and the results

The silicon samples (see Figure 5.19) with the special contact layout on top, as illustrated in Figure 5.16 have been produced to carry out the TLM measurements. We had four types of samples differ by the dopant type and its concentration (see Table 5.1). To create the n-type and p-type dopant region the ion implantation technique was used.

Wafer №	Implantation ion (type)	Implantation Energy	Implantation Dose [atom/cm^2]	Expected peak concentration [atom/cm^3]
Wafer 1	Phosphorus (p-type)	130keV	10^{14}	1.5×10^{18}
Wafer 2			10^{15}	1.5×10^{19}
Wafer 3	Boron (n-type)	60keV	10^{14}	1.3×10^{18}
Wafer 4			10^{15}	1.3×10^{19}

Table 5.1 – Main characteristics of the wafers with sample production for the TLM.

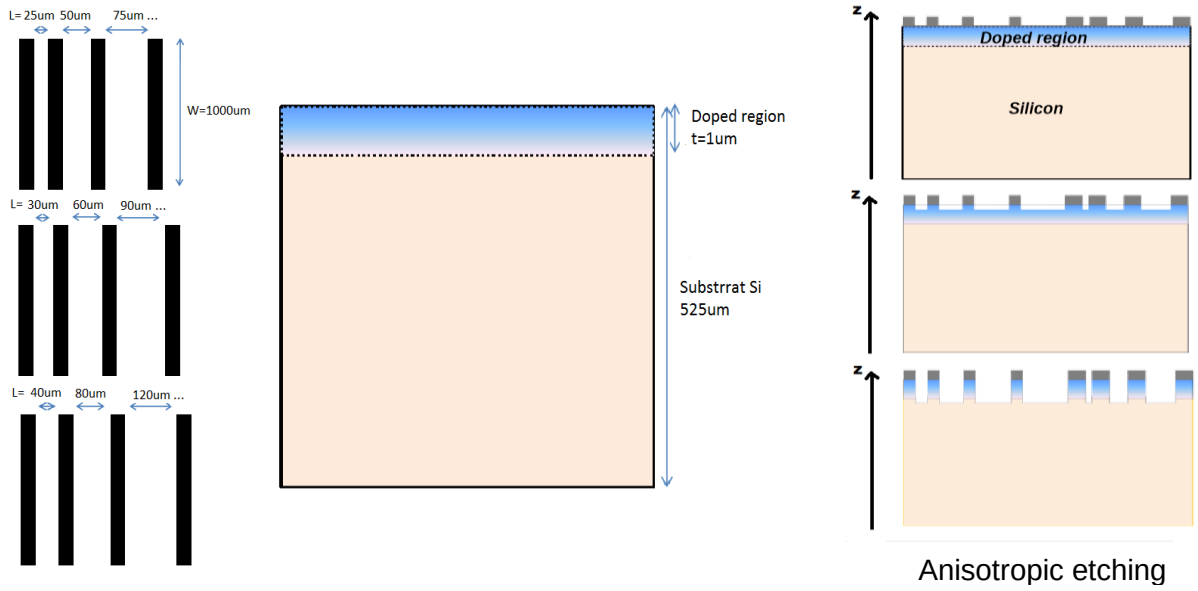

Figure 5.16 – (Left) The sample seen from above and from the side. The aluminum contacts are represented by black rectangles. The blue zone is the doped region. (Right) Cross-section of the sample, illustrating anisotropic etching process of the doped layer until reaching the silicon substrate.

To study the influence of irradiation on the electrically active dopant concentration the samples have been irradiated with neutrons with fluences of $2\times10^{15}\,n_{eq}/cm^2$ and $2\times10^{16}\,n_{eq}/cm^2$.

The procedure for the TLM measurements contains three main operational steps, which were performed repetitively in the following order:

- The **IV measurements** of the samples were performed using a probe station shown in Figure 5.18. The two probes are placed on two adjacent Al contacts as in Figure 5.19. The voltage range was chosen 0 - 0.5 V to assure the linier IV behavior. Then the

resistance between each pair of the contacts was calculated using the IV curves. Considering different distances between the contacts, ultimately we get the resistance as a function of the contact spacing see Figure 5.15(b) This function should be linear, by fitting of the result with the linear function the sheet resistance R_{sh} and the contact resistance R_c can be obtained, considering the slope is the sheet resistance divided by the contact width, and the intercept of the function with the y-axis is twice the value of the contact resistance.

- Since our interest is to measure the doping concentration as a function of depth, the **Reactive Ion Etching (RIE)** allows getting inside the silicon material to extract the resistivity depth profile. The Advanced Vacuum-Vision 320 RIE machine has been used to perform anisotropic etching, which means that the etching is performed only in Z direction as shown in Figure 5.16. The etching process using the CHF3 and SF6 gases was performed during 3 minutes, having etched about 100 nm each time. After each etching the resistance on each layer is measured until reaching the substrate, in the end allowing to find the full doped profile

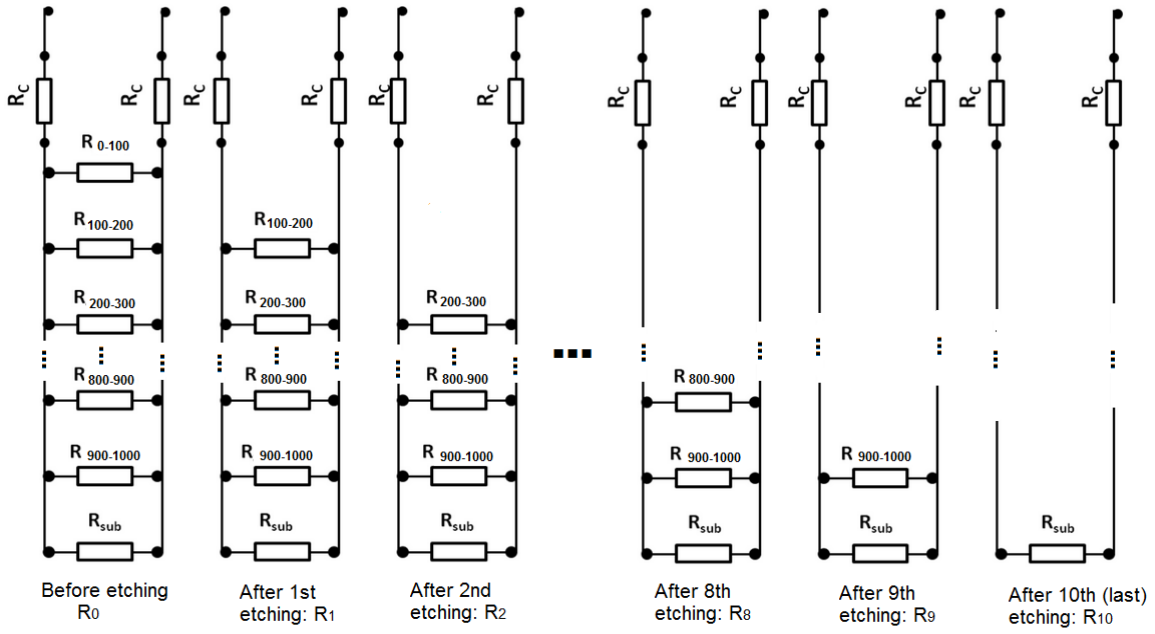

Figure 5.17 – Schematic view of the resistance in-depth measurements in the TLM method.

As we can see from Figure 5.17. the resistivity ρ_{sub} of the substrate would simply be

$$\rho_{sub} = (R_{10} - 2R_c)\frac{t_{sub}W}{X} \tag{5.6}$$

X – is the spacing, W – contact length and t_{sub} is the thickness of the substrate.

However, to calculate it for the previous layers we need to take into account that these are resistances in parallel. Therefore by having calculated the resistance for the last layer it is possible to calculate it for the previous ones. For example, the next resistivity would be

$$\rho_9 = R_9 \frac{t_9 W}{X} \tag{5.7}$$

But R_9 is not directly measured. The total resistance R_T measured in each step is the equivalent resistance of R_C R_{Sub} R_9:

$$R_T = 2R_c + \frac{1}{R_{sub}} - \frac{1}{R_9} = 2R_c + \frac{R_{sub}R_9}{R_{sub} - R_9} \tag{5.8}$$

$$R_9 = \frac{R_{sub}(R_T - 2R_c)}{R_{sub} - (R_T - 2R_c)} \tag{5.9}$$

$$\rho_9 = \frac{R_{sub}(R_T - 2R_c)}{R_{sub} - (R_T - 2R_c)} \frac{Wt_9}{X} \tag{5.10}$$

Therefore, by using Ohm's Law and measuring the resistance between the contacts, it is possible to find the resistivity of a sample's layer which leads to the active carriers dopant concentration in that layer.

- **Profile measurements** with scanning profilometer are then used after each etching in order to measure the depth of the etched layer.

This process is repeated ten times in order to obtain the full profile of the active doping concentration in the doped region.

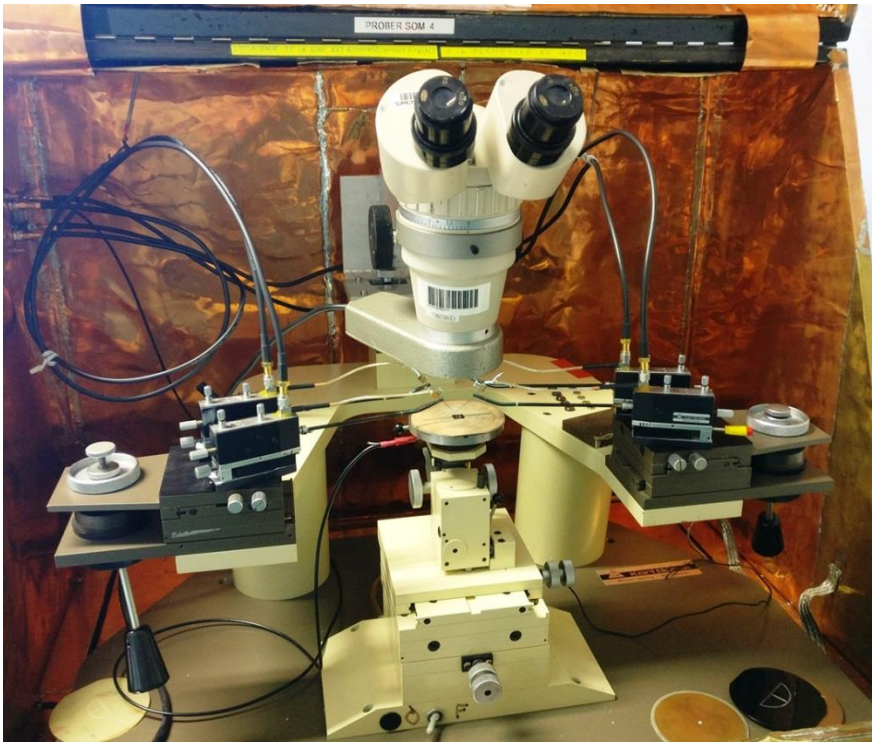

Figure 5.18 – The probe station set-up used for four probes method measurements.

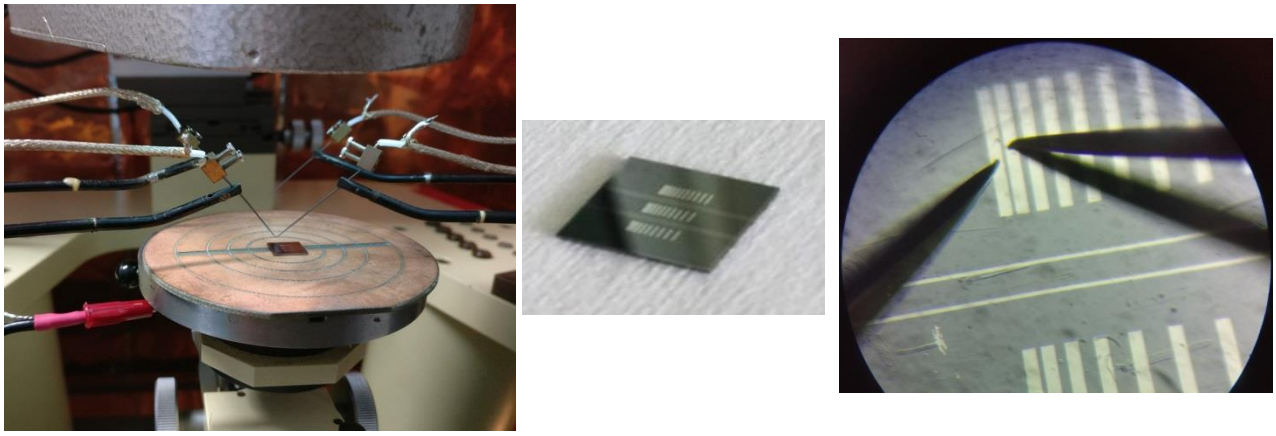

Figure 5.19 – The sample under measurement. A picture of the sample. A zoomed image of the sample with a visible TLM structure and two probes.

5.5.3 Results of TLM measurements

Using the TLM method the active carrier concentration for non-irradiated and irradiated silicon samples has been calculated. The obtained results, which in details are presented in the article [100], show that the TLM method is promising technique to measure the variation of active doping concentration in silicon after irradiation. In order to confirm the reliability of the results, the two cross-checking approaches were applied. The first is consists in using the SIMS (Secondary ion mass spectrometry) – is a standard scan method to find total doping profile and a second way is a comparison of the results with the doping profiles simulated using Sentaurus TCAD simulation tool [101].

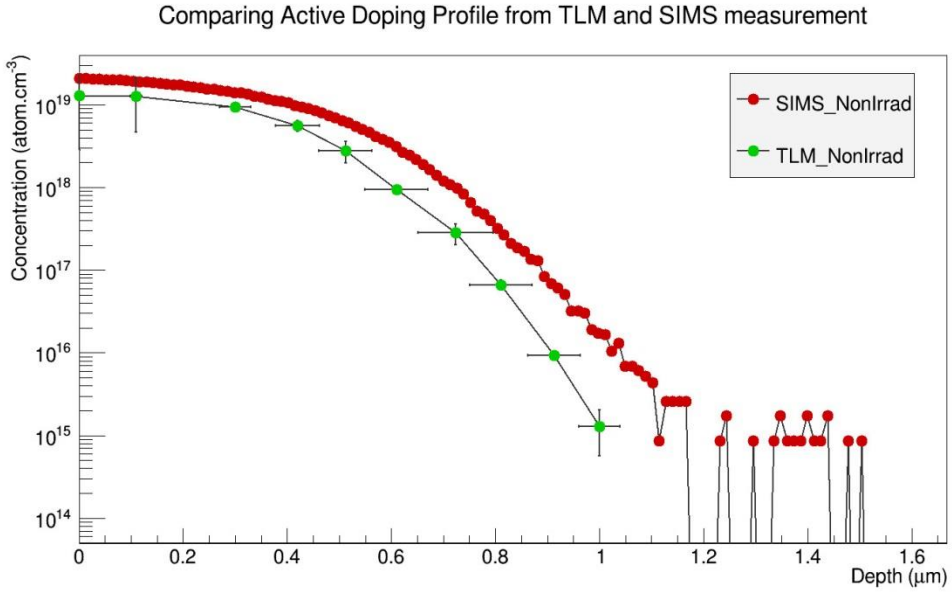

Figure 5.20 – TLM measurements (green curve) of the active carrier concentration as a function of depth for non-irradiated sample compared to SIMS measurements (red curve) of total dopant concentration [79].

The Figure 5.20 shows the TLM and the SIMS results for non-irradiated Boron doped sample. The discrepancy observed between two methods is explained by the fact that the SIMS measures the total dopant concentration, but the TLM is sensitive only to electrically active dopants. The

plot shows that the measured peak concentration was found to be of order of 10^{19} atom/cm^3, which is in a good agreement with expected value provided by manufacturer.

Using TCAD simulation the doping profiles for three different implantation energies: 240 keV, 130 keV and 60 keV, were obtained and compared to the doping profiles calculated with TLM method (see Figure 5.21). Considering that the simulation gives information about the total dopant concentration, good compatibility, among the three simulated doping profiles, is observed between the TLM results and simulated for 60 keV doping profile. This corresponds to the parameters stated by the manufacturer.

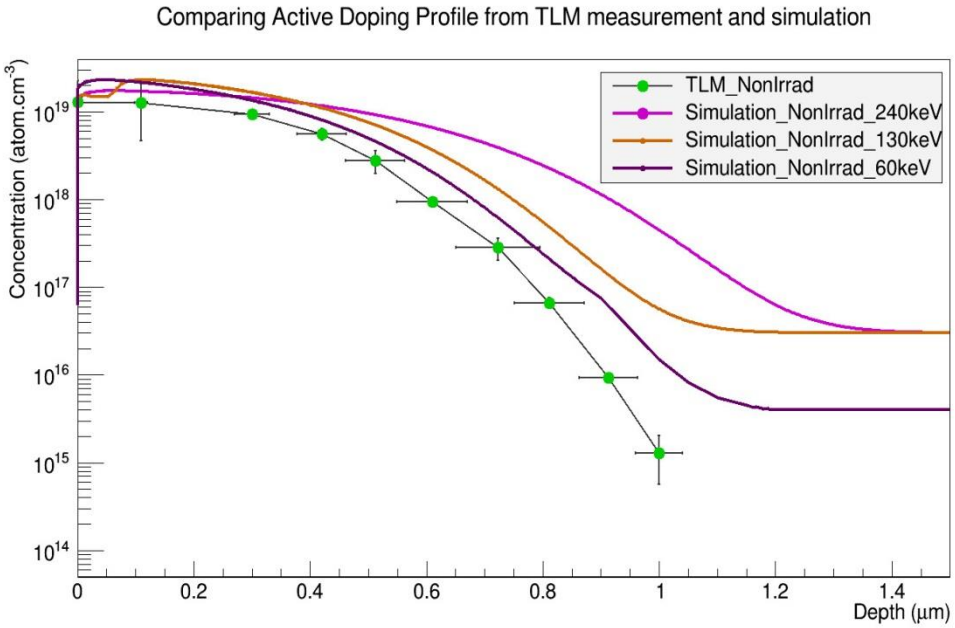

Figure 5.21 – TLM measurements (green) of the active carrier concentration as a function of depth for non-irradiated sample compared to the simulated doping profiles corresponding to three implantation energies: 240 keV, 130 keV and 60 keV [79].

Understanding the structure of the silicon detectors by measuring the doping profiles is important step in the development of the advanced radiation hard pixel detectors. The doping profile explains the operational behavior of the device and can be a quality control method of the detector production. The total doping profile of a silicon detector can be measured by very precise SIMS method, but it doesn't provide information about the active doping concentration. The TLM method is an alternative technique can measure the electrically active doping profile of silicon sensors, which may be used as inputs to simulation in order to get precise results and can tune the irradiation models to predict the behavior of silicon detectors after irradiation.

Chapter 6

High energy particle beam to evaluate innovative pixel sensor designs

Contents

The important step in the R&D of the new pixel detector modules is their characterization and tests to determine how well they function in an environment similar to that they will be used in. For this purpose the modules can be installed within the beam of high energy particles to read out them in various conditions while the relativistic particles passing through their sensitive area. These kind of experimental tests are called test beams. In this chapter the test beam facilities and the setups, which were used in this work are described. The details on the track reconstruction and analysis are discussed.

During the work described in this part of the thesis, the pixel detectors with innovative active and slim edge designs were tested in the test beams. The performance of the sensors of both designs with different thicknesses: 50 μm, 100 μm and 150 μm, before and after irradiation with the fluence of $1\text{-}2\times10^{15}$ n_{eq}/cm^2, was evaluated. The spatial resolution of the sensors has been estimated. The overall hit efficiency and in-pixel efficiency has been calculated for each sensor design for normal and inclined particle tracks incidence. The edge region of sensors with an active edge design shows the efficiency higher than 97 % up to 20 μm from the last pixel column, which gives to this design an advantage in choosing sensors to instrument the ITk Pixel detector.

6.1 Beam facilities

The test beams are the most effective reliable way to test and characterize pixel detector prototypes. In principle, they can be used to test properties of all kinds of detectors from trackers to calorimeters. The test beams are much preferable to manipulation a radioactive source since the higher statistics and possibility of charged particles tracking by using a set of well understood pixelated detectors known as a beam telescope. These tracks can be reconstructed offline to determine the interaction position. The number of tracks within the readout time of the detector system may only be slightly greater than one. The energy loss of the crossing particle can be neglected with respect to the total energy of the particle, which in turn means that the particle's trajectory will not be affected when crossing the sensors. By this definition a reconstruction can be done to obtain particle trajectories from hit pixels in the sensors. Then the reconstructed tracks can be analyzed and the detector properties are evaluated.

The test beam results presented in this chapter are based on data taken at two facilities: at CERN North Area and DESY-II. At both sites the EUDET type of telescopes [112] are installed to perform the pixel detector tests with a particle beam, providing a high spatial hit resolution.

6.1.1 CERN SPS

The Super Proton Synchrotron (SPS) at CERN is the final accelerator in the injection chain for the LHC and is primarily required to accelerate protons to 450 GeV. However, the proton beam is also extracted from the SPS before injection and directed towards three targets (T2, T4 and T6), producing in hadronic interactions beams of pions $\pi^{\pm}$ for the CERN North Area beamlines (H2, H4, H6, H8). A spectrometer magnet filters out the particles of the specific energy. Further on, the beamline contains plenty of magnets for bending and focusing the beam. Beam absorbers and collimators can be used to filter out particles of other kinds that had been created at the same time. Wire chambers are installed along the beamline to determine the position of the beam. The main user for each beam line has control over the momentum of the particles from 10 – 400 GeV/c (at H2, H4, H8) and from 5 – 205 GeV/c (at H6). A particle rate at the beam line H6, where we have tested our sensors, was approximately of 400 to 500 Hz.

Figure 6.1 – Photo of the H6A beam line zone at the CERN North Area.

Due to the multiple extractions of particles from the SPS, the beam arrives in spills. The max particle intensity is 2×10^{8} particles per spill. The spill length and frequency depend on number of users require beam extraction. Generally each spill is of the 4.8 –9.6 seconds length, with a new spill every 14–48 seconds.

6.1.2 DESY

The DESY-II electron/positron synchrotron at the DESY (Deutsches Elektronen-Synchrotron) site in Hamburg has a circumference of 292.8 m and is mainly used as an injector for the PETRA-III storage ring. However, it also supplies beam to three test beam experimental halls.

The DESY-II synchrotron is equipped with movable carbon fibers which when placed in the e^+ or e^- beam produce through bremsstrahlung radiation mechanism photons, escaping the beam line tangentially. The schematic layout of beam production is shown in Figure 6.3.

Subsequently, the photons are converted to e^-/e^+ pairs on a secondary metal target (converter). Their energy distribution reaches up to 6 GeV. A dipole magnet spreads the secondary beam out as a function of the sign and energy. The beam is subsequently directed into one of three beam areas with an achievable rate of electrons or positrons are approximately 1000 s^{-1} cm^{-2}. Each beamline is fully controlled by user, the rates or the desired beam energy within the range of 1–6 GeV/c can be adjusted by collimator and convertor target settings. The higher energy electron beam results in low rate due to Bremsstrahlung spectrum 1/*E*-dependence. A compromise between sufficient rate and an acceptable energy is obtained by selecting 4 GeV electrons. At these energies, the multiple scattering [113] is the spatial resolution dominant effect.

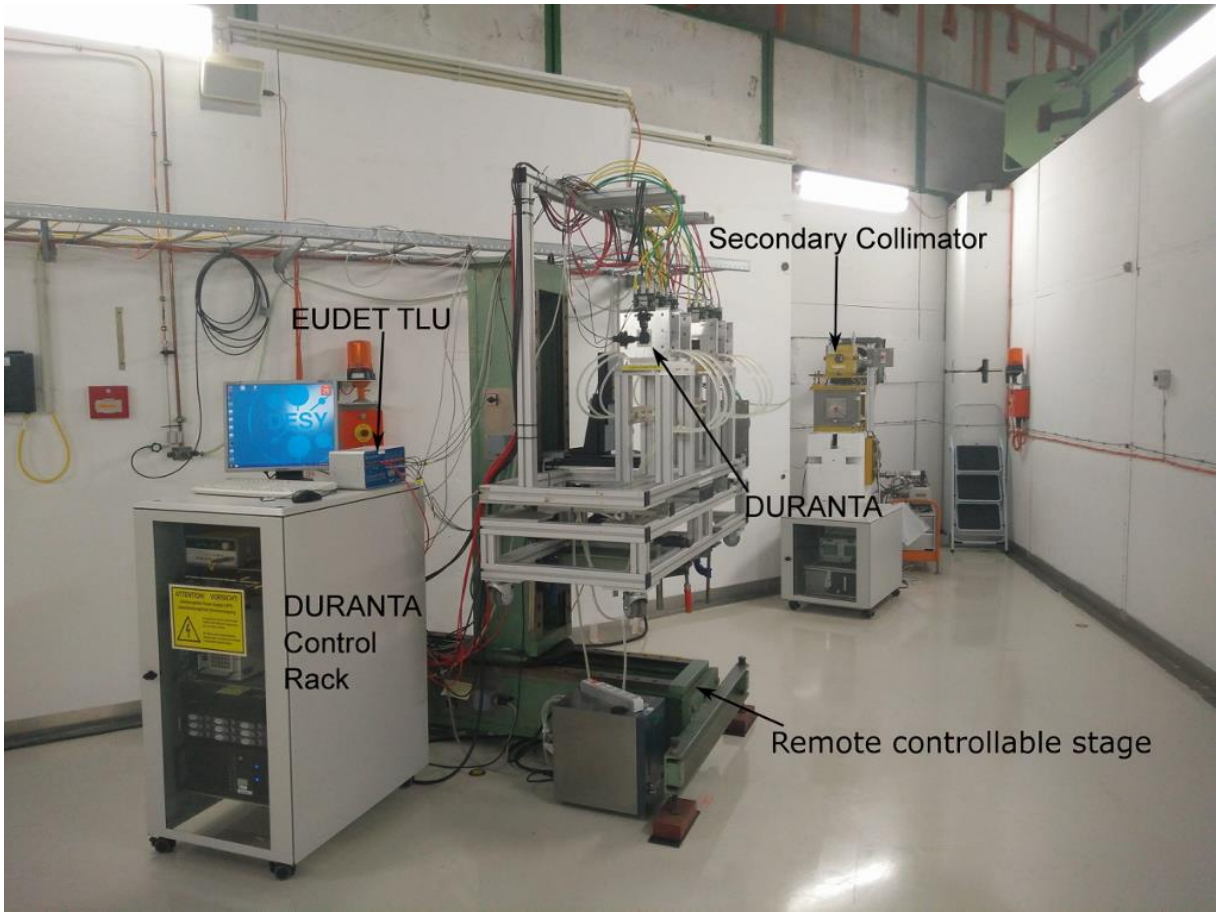

Figure 6.2 – A photo of the test beam area T22 at DESY [115].

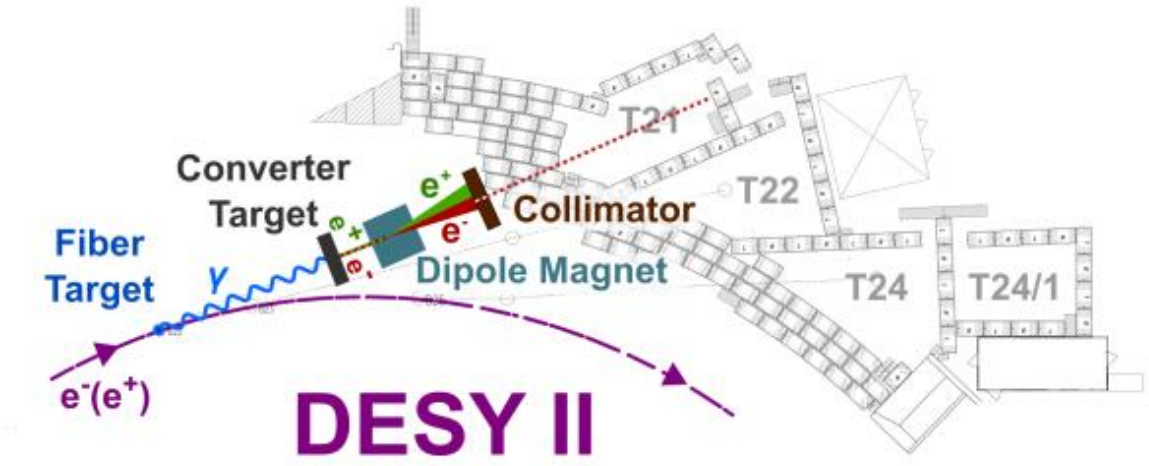

Figure 6.3 - Schematic Layout of beam production for a Test Beam at DESY [114].

6.2 Beam test setup

A common setup used in the test beams is called a test beam telescope. It is a very useful tool for testing and determining properties of the position sensitive particle detection sensors. Typically, a beam telescope is split into two arms with a testing area in the middle as shown in Figure 6.4. The whole construction of the beam telescope is based on a mechanical frame made of prefabricated aluminum profiles. This frame is mounted on a massive X-Y table that can be controlled remotely. By moving the frame on the table perpendicular to the beam in both directions, the user can align the beam spot into the middle of the telescope's sensors, which are fixed on the tables on top of the upper part of the aluminum frame. These two tables are called arms and hold three sensors each. By using a dovetail guide, the top of the two sensor tables can be moved along the beam axis. This allows an easy access to the devices that are usually attached between the telescope's arms. The position of the sensors on their arms can be set individually. The sensors of the telescope are mounted inside aluminum frames that guarantee an exact alignment of the sensors along the beam axis. The mechanics was built to be very sturdy and stable over time.

Typically the detectors which are going to be tested, also known as Device under Test (DUT) are attached in between the both telescope arms to obtain the maximum tracking resolution. The DUTs usually are mounted by telescope’s users, so their mechanical connection to the frame must have a flexible solution. All devices being tested are fixed onto a L-shaped aluminum mount which then screwed into the breadboard plate, typically placed into the cooling box (see section 6.2.2), based on a precise motorized X-Y table, which is used to move the DUTs through the active area of the telescope between its arms. To prevent short-circuiting and avoid any parasitic signal the kapton tape, which is electrically insulating and stable at low temperatures, is used to cover the L-shaped mounts.

For the test beam measurements discussed in this chapter the EUDET-type telescopes were used. The original EUDET telescope was developed within the EUDET project (2006-2010). Responding to the increasing demand of the sensor R&D community, several replicas, collectively called EUDET-type beam telescopes, have been built since then: ACONITE for the ATLAS group, which is also operated at the beamline H6, ANEMONE at ELSA (University of

Bonn), the copy for the Carlton University called CALADIUM, and two copies, DATURA and DURANTA, which are operated at DESY.

The heart of the beam telescope is the sensor. The EUDET telescope equipped with six highly granular and thin MIMOSA-26 sensors. These sensors are so called MAPS (Monolithic active pixel sensors) are manufactured in standard single side 350 nm CMOS process. The MIMOSA-26 sensor covers an active region of 21.2×10.6 mm^2. The pixel matrix is organised in 576 rows and 1152 columns with a pitch of 18.4 μm. Therefore, one sensor is covered by 663 552 pixels. At the bottom of the pixel array, each column is connected to an offset compensated discriminator to perform the analogue to digital conversion. Zero-suppression is then used to reduce the data rate. MIMOSA-26 is a fully digital sensor with binary readout. This architecture allows a fast readout frequency of ~10k frames/s. Sensors with high-resistivity epitaxial layer were thinned from the back side down to 50 μm.

The single point resolution for a MIMOSA-26 sensor depends on the sensor threshold settings. High values of the threshold lead to smaller size clusters formed by charged particles passing through the sensor. For single pixel clusters the sensor intrinsic resolution can be estimated using formula: $\frac{d}{\sqrt{12}}$, where d - is the sensor pixel pitch, and gives 5.3 μm for MIMOSA-26. Lower threshold values lead to larger clusters and improve the intrinsic resolution. Intrinsic resolution values better than 4 μm have been observed for MIMOSA-26 sensors which are operated at low threshold settings.

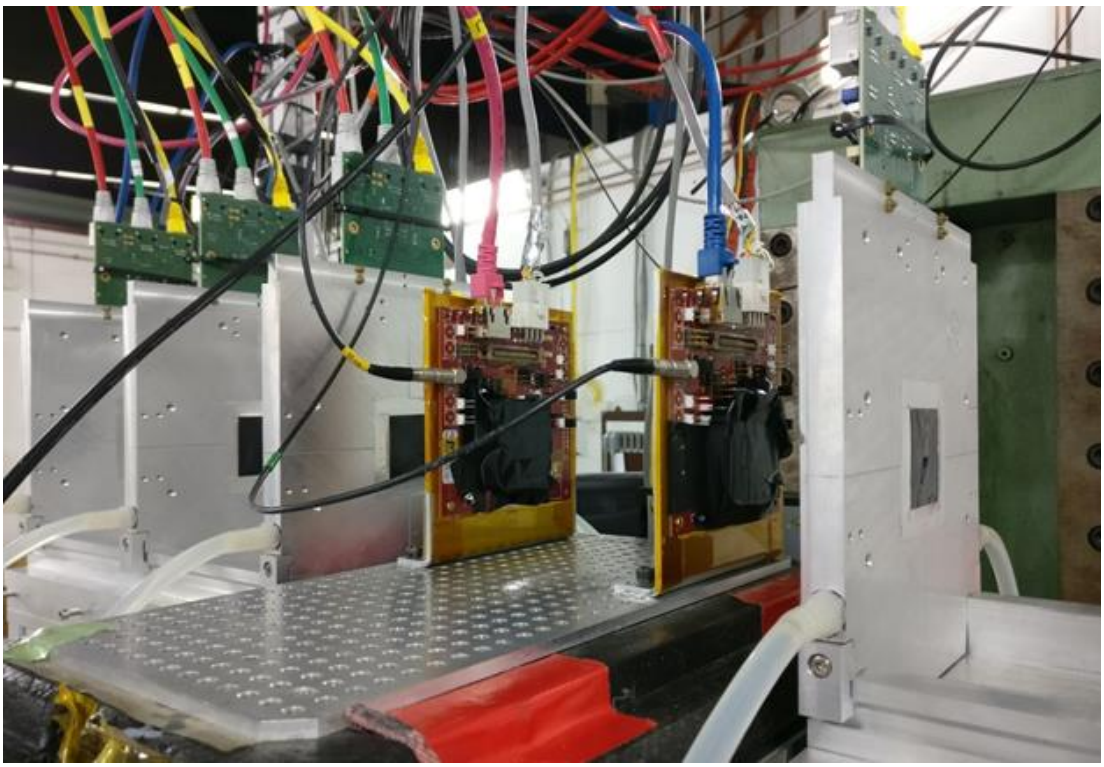

Figure 6.4 – A picture of EUDET telescope. The two DUTs and telescope planes enclosed in aluminum frames are shown. The attached rubber tubes are used for pumping cooling water though the frames. On top of the frames one can see the readout boards At the bottom an aluminum board with a grid of M5 threaded holes with 1 cm pitch is provided for mounting the DUTs by using L-shaped metallic holders.

As was mentioned before every pixel sensor is mounted within an aluminium jig (thickness of 20 mm). The jigs feature a beam window around the position of the sensor location, minimising the material budget. Lightproof Kapton foils of 25 µm thickness protect the sensors on each side. The overall material of the beam telescope thus amounts to 300 µm of silicon and 300 µm of Kapton. Furthermore, the jigs are cooled keeping the MIMOSA-26 sensors at a constant temperature of typically 18°C for stable operation. The chosen design meets most user requirements in terms of easy integration capabilities, spatial resolution, and trigger rates. The telescope planes are designed and built to keep the material budget as low as possible in order to achieve an excellent track resolution.

6.2.1 Devices under Test

The detectors to be investigated in a test beam are called DUTs. To study properties of the detector's sensor at test beams, an assembly made of sensor and read-out electronics is necessary. The sensor assembly is attached to a PCB called SCC (single chip card). The assembly is glued to the board with the sensor on top. The connections to the FE electronics and the sensor's bias pad are implemented by wire-bonds. The circuits on the board contain mainly LVDS drivers which are used to amplify the signals from and to the FE. Furthermore, decoupling capacitors are attached.

In order to readout and power the FE module some connectors need to interface the PCB (4-pin Molex connectors, and 8-pin). A RJ-45 connector is used to connect the FE readout to the DAQ system for FE-I4 chip module and DisplayPort connector for high speed data for RD53A. The bias voltage connection is made via Lemo Connector.

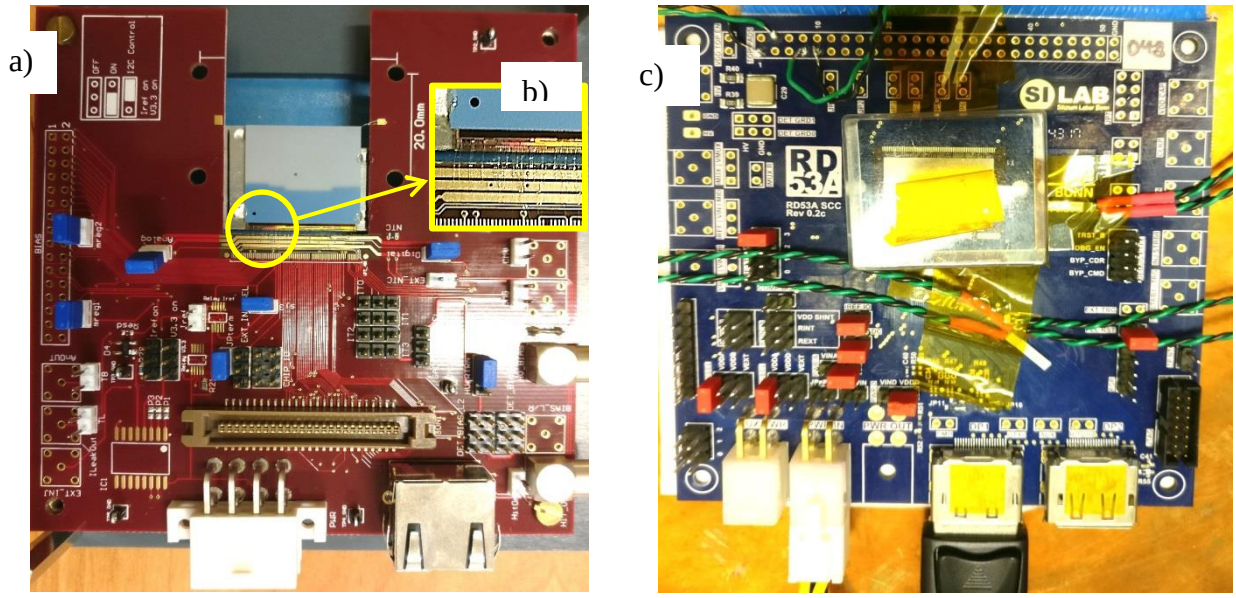

Figure 6.5- A picture of DUT single chip card (SCC): (a) shows a SCC with FE-I4 single chip assembly used for IBL Upgrade; (b) shows the assembly attached to the PCB by wire-bonding; (c) a SCC with RD53A chip, which is a large scale demonstrator for a hybrid pixel detector readout chip in a 65 nm process, common ATLAS and CMS effort.

6.2.2 Cooling

As was mentioned before the silicon sensors are sensitive to the visible light, so they should be enclosed in the light tight environment. Moreover, after irradiation, due to the radiation damage, the leakage current increases and this makes it impossible to test sensors at room temperature. There is a dependence that the leakage current doubles for every 8.5 ˚C degree Celsius raise in temperature. For these purpose was designed a few types of light-tight thermally insulated cooling boxes, shown in Figure 6.6, which we used for putting irradiated detectors to test.

One cooling box was designed at the University of Dortmund to have a low material budget and provide insulation from external temperature changes. It was made of PPE (Poly Phenylene Ether) foam, and consists of two parts separated by a thin aluminum wall. One part of the box is used to put DUTs inside, and another part can be loaded by blocks of dry ice (frozen carbon dioxide), which sublimate at -78.5˚C and used to cool down sensors to about -50˚C. The material choice of the DUT supports allows for a transfer of heat away from the sensors since the aluminium plate is in contact with the loaded dry ice.

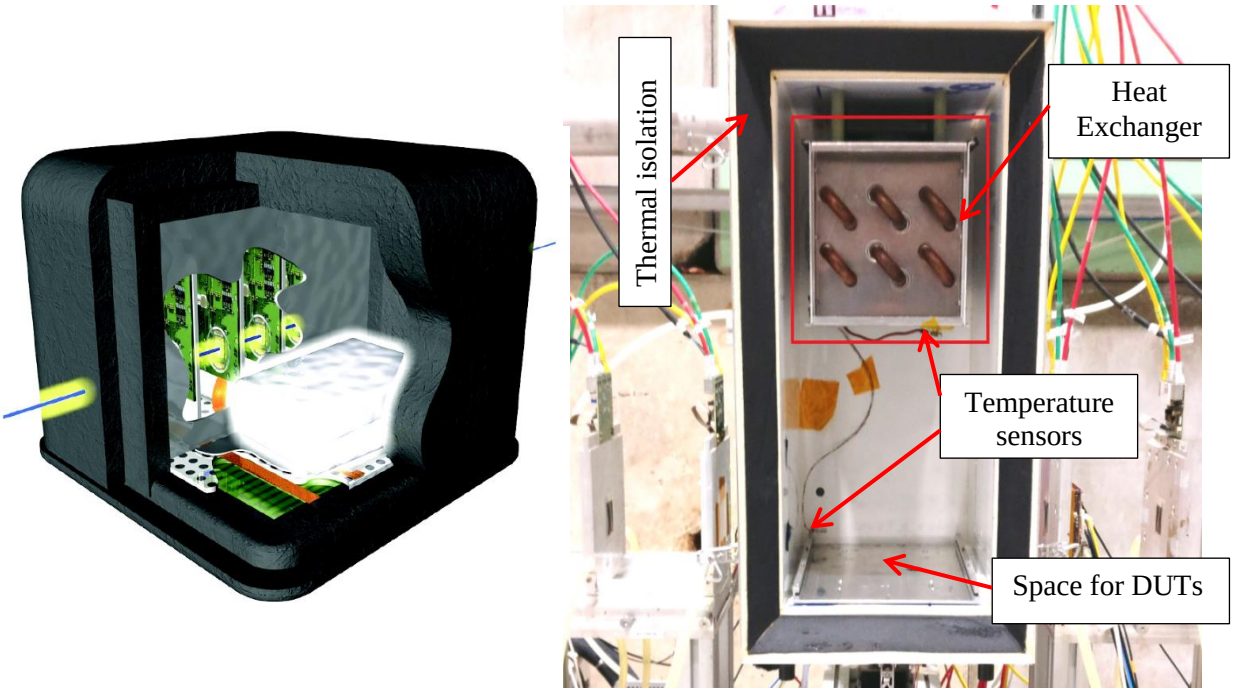

Figure 6.6 – (Left) An image of the cooling box mounted on telescope and loaded with the dry ice. (Right) A photograph of the cooling box in the centre of the two telescope arms at H6A area.

In order to avoid condensation of air, induced by cooling the environment inside the box needs to be flushed either with dry air or Nitrogen. The gas is piped into the box to reduce condensation and ice forming on the sensors which could cause damage through short-circuiting or possibly through the expansion of ice on the delicate wire-bonding. Such type of the cooling box is mounted at DESY and H6B area.

Another cooling box was designed and built at Max Planck Institute for Physics (Munich). This cooling box is easy to use and provides a stable temperature during the measurements. The target temperature can be set by user in the range up to -50 ^{o}C. It equipped with sensors to monitor the temperature inside. The box is built of aluminum to reduce the weight and scattering effect,

thermal isolation is made of 25 mm thick Armaflex. The nitrogen gas enters the box, flows in the heat exchanger where it is cooled. The heat exchanger itself is cooled by the silicon oil from the chiller. This box currently is installed at H6A area at CERN-SPS.

6.2.3 Data acquisition software

The data acquisition system of the EUDET telescope setup is a combination of dedicated hardware and software which has been designed and developed to serve as flexible and simple-to-use for data taking for the EUDET-type beam telescopes, allowing for easy integration of other devices. The data acquisition flow is sketched in the fig.: the pixel sensors are read out by custom made data reduction boards and then sent to VME CPU. The data are then packaged and sent over Gigabit Ethernet to the main DAQ PC where the events are built and written to RAW file, which contains all of the information from each telescope plane and DUT such as hit positions and time over threshold for individual events.

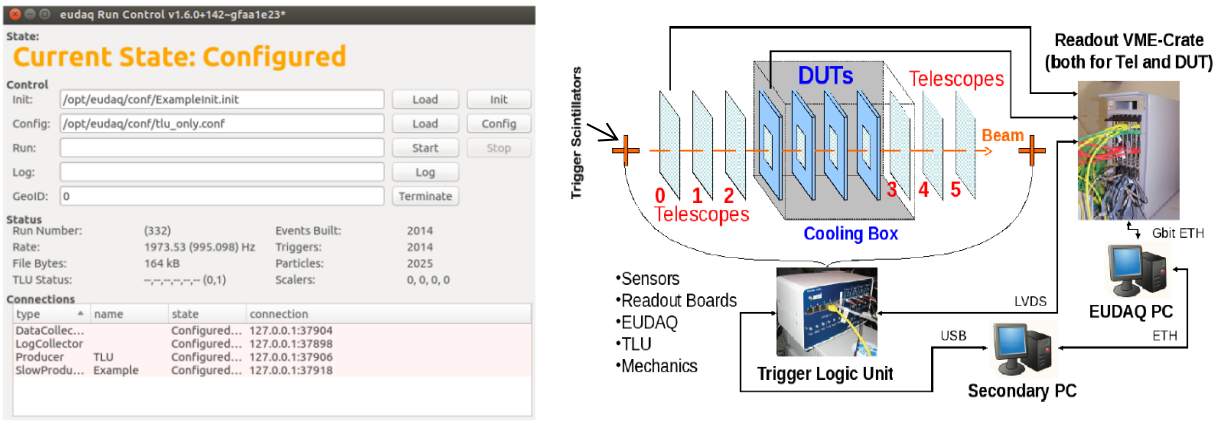

Figure 6.7 - (Left) The Run Control graphical user interface. (Right) The EUDET telescope Data Acquisition scheme.

Triggering is controlled by a custom Trigger Logic Unit (TLU). The TLU receives signals from scintillators in front of and behind the telescope, and generates triggers that it distributes to the telescope and any DUT. The four scintillators inputs can be combined in an arbitrary fashion (AND, OR, VETO) to generate the trigger signal, and there is also an internal trigger generator for testing and pedestal runs. For each generated trigger a trigger counter is incremented, and a timestamp is stored in an internal buffer that may be read out over USB by a PC. The DUTs have the option to read out the trigger number via the DUT interface in order to ensure proper synchronization of triggers. Up to six devices (including the DUT and the telescope) may be controlled by the TLU via the RJ45 connectors using LVDS.

The DAQ system is requiring one event per trigger per attached subdetector system before building the global event. Thus, the trigger rate is always limited by the slowest device.

The software, called EUDAQ [116], is a modular cross-platform data acquisition framework. The central interaction point for users with the framework is the Run Control and its graphical user interface (GUI). All other modules connect to the Run Control (see Figure 6.7) at startup and receive additional information from there during operation such as the commands for starting and stopping a DAQ run. The GUI provides all controls necessary to the user on shift.

Online monitoring

It is necessary to perform data quality control for each single run during data taking at test beam measurements to ensure that data is not corrupted. For this purpose the Online Monitor tool is available in the EUDAQ. The Online monitor connects to the Data Collector tool, which is responsible for the event building, requesting a fixed fraction of the recorded events (e.g. one out of a hundred) to fully decode all subdetector data and build basic plots (see Figure 6.8).

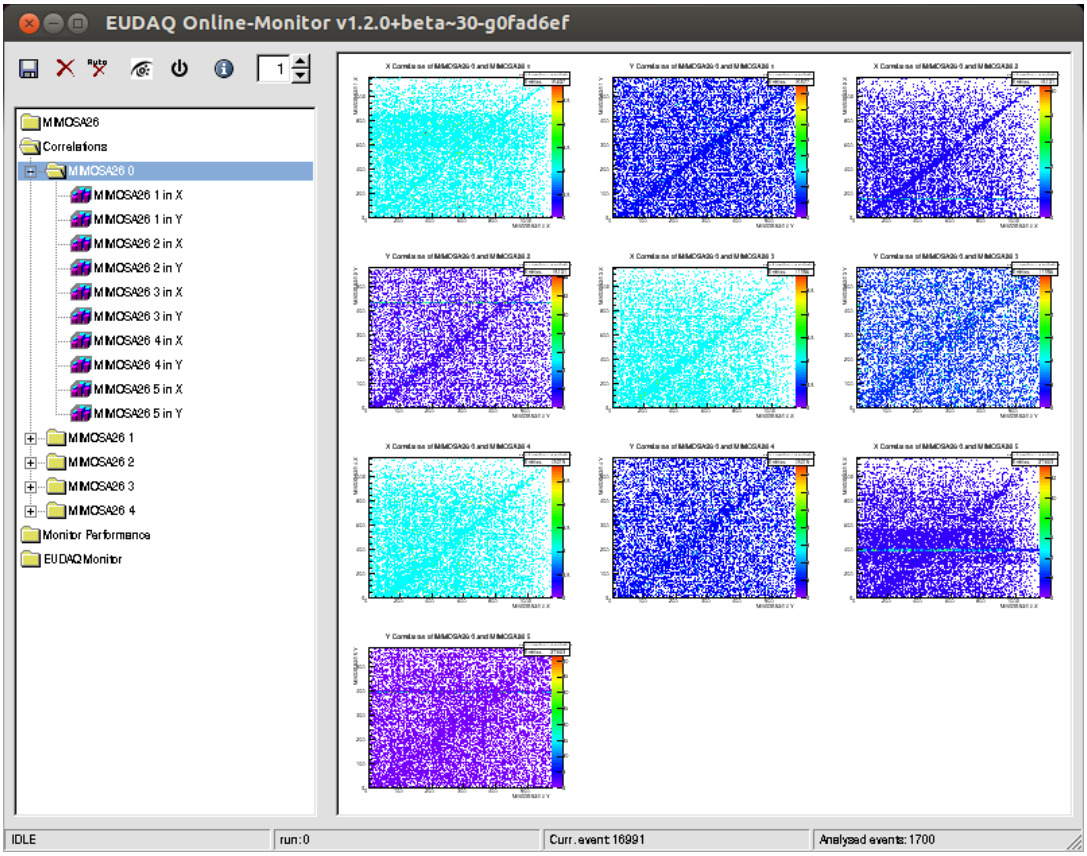

Figure 6.8 - An example of online data monitoring plots of the plane correlations provided by the EUDET Telescope Online Monitor.

For each DUT and telescope plane it provides the two dimensional hitmaps for the raw and clustered data as well as the cluster size ToT and Lvl1 distribution. With help of which it is possible to verify that the different devices are synchronized in time and all within the geometrical trigger acceptance. A histogram of hot pixels gives an indication of how noisy the sensor is; masking noisy pixels or increasing the threshold could reduce problems with data analysis later.

This online monitor does not need to be configured. The program obtains all necessary information from the data stream and will adapt its views based on the information sent.

The Online Monitor also provides correlation plots. A two-dimensional plot of the position of a hit in x or y for one device compared to the hit position on the same axis for another is known as a correlation plot provided in the Online Monitor as shown in Figure 6.8. They indicate whether two sensors overlap in the beam and allow the shifter to check that one device has not fallen out of sync with the other. Ideally for two well aligned sensors of the same dimensions and rotation,

the hits on the correlation plots will start at the bottom left corner at zero, and extend at a 45^0 degrees angle to the top right. Hits due multiple scattering or those that are out of time will not be on this line. Straight lines in the horizontal or vertical direction are generally due to noisy or 'stuck' pixels.

6.3 Test beam data analysis chain

For the detailed analysis of the data from the test beam, particle tracks through the setup must be offline reconstructed. Reconstruction means that the potential trajectories of the particles are calculated from the sensor hit positions. This is performed with the EUTelescope software, written in C++ within the ILC framework. The framework is built modularly. The modules are called MARLIN (Modular Analysis & Reconstruction for the LINear Collider) processors. To become such a processor a class in an application needs to inherit from a processor base class. Some abstract functions have to be implemented so that the MARLIN interface knows how to handle in different situations. The processors can be activated and parametrized with an XML (EXtensible Markup Language) steering file.

The software requires a description of the position of each device in the telescope frame of reference. This is described in a GEAR file, which details not only the positions but sizes of each telescope and tested device in the setup. Further information such as pixel pitch, shifts in X and Y, rotations (the relative orientation of one sensor in the global coordinate system) using Euler angles, thickness and radiation length of each device is also entered by the user. A unique device ID is assigned to distinguish detectors. Traditionally, telescopes are given an ID number between 0 and 9, FE-I3 detectors between 10 and 19, and FE-I4 detectors between 20 and 29.

6.3.1 Data reconstruction flow

The raw data collected during the test beam campaign is then offline analyzed in five main steps presented in Figure 6.9.

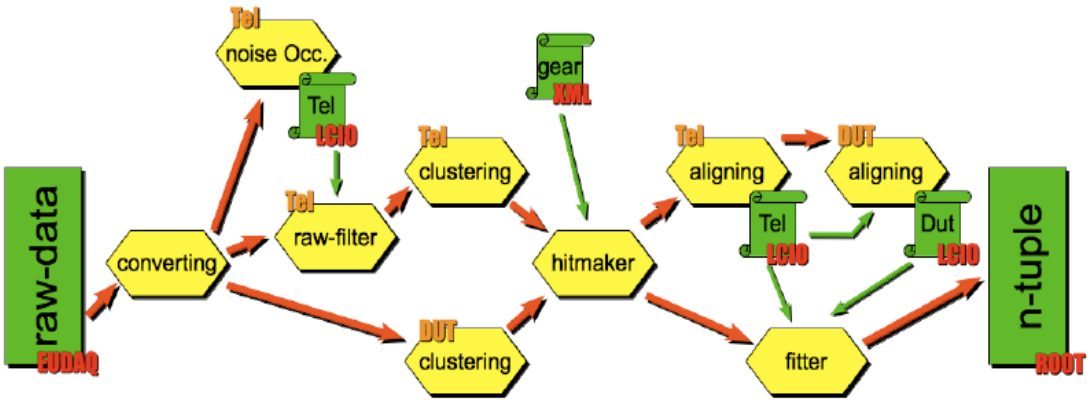

Figure 6.9 - Program flow of Eutelescope the reconstruction chain in a simplified way. On the left hand side of the figure there is an input file written out by EUDAQ and on the right hand side the output file which is in the root file format.

Converter

The converter is the first processor in the Eutelescope reconstruction chain. In this step the native EUDAQ format data is converting into the internal ILCSoft lcio (Linear Collider In/Out) data format. In this format all information from a single trigger is stored as one event:

- The column number of the recorded hit pixel ([0-79] for FE-I4, [0-400] for RD53a);
- The row number of the recorded hit pixel ([0-335] for FE-I4, [0-198] for RD53a);
- The TOT value is between ([0 – 15] for FE-I4 and RD53a);
- The time the hit was registered within the Level 1 Trigger window ([0-16] for FE-I4 and [0-32] for RD53a);
- Readout Identification number (the origin of the identified readout board).

After conversion from RAW data to the LCIO data format, a hot pixel search is performed marking pixels with firing frequencies above a certain threshold. The standard setting for the threshold probability is 0.01. This means that if a pixel was hit more than once in 100 events it is dismissed. Clusters are formed from fired, adjacent pixels and translated from two-dimensional entities on the individual telescope planes into hits in a global three-dimensional reference frame. Clusters containing at least one hot pixel are removed from the analysis.

Clustering

The charge collected from a single particle track may be registered in multiple cells within one device. This is due to charge sharing between neighboring pixels and tilting of the sensor. These hits from multiple pixels must be grouped together into a cluster in order to reduce the number of the hit positions. There are many algorithms designed for clustering data, the two main ones used for track reconstruction are Cluster Weighted Centre and Cluster Charge Weighted Centre.

Cluster Weighted Centre
The X and Y coordinates are averaged separately to give a value for the cluster centre. This algorithm is used for the telescope planes since only the location of the hit for each position in the cluster is known, therefore each hit has an equal weighting in determining the centre of the cluster position.

Cluster Charge Weighted Centre
Using the Time over Threshold (ToT) information from the DUT as a weight, the "centre of mass" for the cluster can be calculated.

Hitmaker

The local 2-dimensional coordinate system (column and row) of each sensor is translating into space points in one global coordinate system of the telescope in this step. This is a right-handed cartesian coordinate system, with positions in the *x*, *y* and *z*-axes. The *z*-axis is the beam direction which is always perpendicular to the telescope planes for beam tests described here, and is ideally centred close to x = y = 0. This stage requires a steering file created by the user called a GEAR file. Based on these coordinates and the resulting correlations between the devices, a coarse pre-alignment is done with a precision which not exceed 100 μm [124]. With

this, the pre-alignment corrects for any global misalignment and is used for the subsequent alignment step.

Alignment

There are two stages to the alignment procedure. The first one performed in hitmaker is the pre-alignment. The "pre-alignment" constants for all sensors are calculated in respect to the first upstream sensor (the first telescope plane is always fixed in its orientation and position to allow for a fixed starting point of the particle trajectory.) They can be used as correction factors for the sensor positions or as input parameters for the second "fine" stage of the alignment step.

The second stage is based on an exact matrix equation solution formalised in Millepede II package [117]. It calculates the alignment constants in order to reduce the bias and the uncertainty of the fitted track parameters and to minimize the χ^2 of the tracks. Tracks with a high value of χ^2 are excluded from further track processing. For a rigid body, six parameters are required for describing translations and rotations in space: three sensor shifts coordinates *dX*, *dY*, *dZ* and three Euler rigid body rotation angles.

Fitting

After the sensor positions are corrected, Eutelescope performs the final step is the track fitting. This step is affected by false track candidates. Due to the higher integration time of the telescope, several tracks will be recognized by the telescope but cannot be seen by the DUTs. Therefore, one can demand a number of hits in the DUTs to reduce the number of tracks which are not in time in the DUTs and the telescope. Therefore, it is essential for track reconstruction that track fitting algorithms allow for autonomous filtering of false track candidates. To overcome these difficulties, the deterministic annealing fitter (DAF) [119], which is based on a Kalman filter [120] is used.

The actual path of the particle through the setup is not a straight line, but kinked due to multiple scattering. The fitting algorithm takes these kinks into account when deciding upon the fitted track. The following assumptions [125] are made when fitting tracks:

- The telescope planes are parallel, and at normal incidence to the particle beam;
- The angular spread of the particle beam is small and scattering angles are also minimal;
- Material thicknesses are much less than the separation between planes;
- There is a negligible beam energy loss as the beam crosses each telescope plane.

The track reconstruction is completed by finally fitting the tracks with the track model of the general broken lines [121] including effect of the multiple scattering in the initial particle trajectory.

6.3.2 Analysis of the reconstructed tracks

The reconstruction process ends with the writing of the reconstructed tracks data as well as information on the telescope planes and DUTs into a final output root file. Then the output files (one file per run) reprocessed in TBmon2 [122]. This is software for the offline analysis

developed by the ATLAS pixel collaboration to study beam test data. Written in C++ and including ROOT classes, TBmon2 reads in the .root file and allows the user to cluster the DUT data, fine-tune alignment and analyze the efficiency, charge sharing and other features of the sensor depending on the analysis class selected. The standard pre-analysis steps are as follows:

- Hotpixel finder;
- Check alignment;
- Eta correction;
- Check alignment.

The check alignment analysis class is run a second time, with the results from the eta correction class applied and the results from the first iteration of alignment corrections removed.

TBmon2 allows a detailed analysis of the DUTs with their specific types of geometries, for a set of runs, which were taken under the same condition. It produces histograms such as: hit and charge sharing efficiency, ToT and cluster distributions. All the results presented in this section were produced by TBmon2.

Cluster size

Normally, the charge generated in the sensor is collected in multiple, adjacent pixels when charge sharing occurs or the track of the particle passing with the angle to the sensor surface. These multiple hits within close proximity in space and time must be grouped together as a cluster. The number of hit pixels in a cluster, which is defined as a cluster size, increases with the beam incidence angle. The length of a cluster in either pixel direction is referred to as cluster width. The local point, where the particle crosses the sensor, is defined as the geometrical center of the pixel cell.

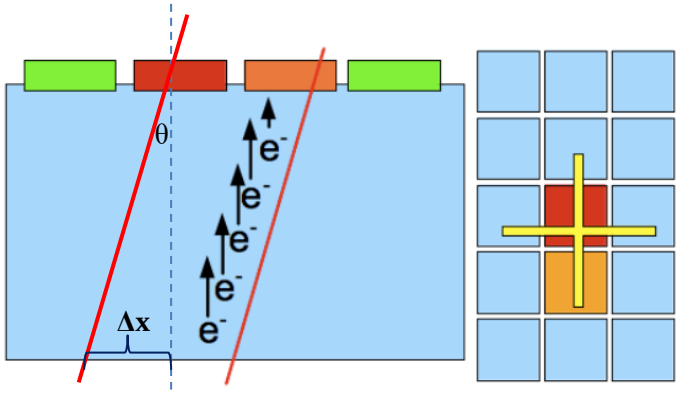

Figure 6.10 - A cross section through a sensor with a traversing particle track

The cluster size is further increased in case particles enter the detector surface with a higher incidence angle (see Figure 6.10). In this case, the seeding point is deduced from averaging the center position by weighting the collected charge in the single clusters. In addition to the dependence of the cluster size on the entering point of the particle in the detector, the cluster size is dependent on the length of the pixel cell side as well as a sensor thickness. Two-hit clusters are mostly originating from the short pixel side, where the adjacent pixels below and above the seed pixel have a higher probability to record a signal. The total number of clusters in both pixel directions is obtained from the outputs of the EUTelescope software. The clusters from a perpendicular beam incidence are interpreted as single-hit clusters. During the test beam

campaign some of the DUTs were measured at inclined beam incidence at 27^0 and 45^0 degrees. The average cluster size per hit was calculated and the distribution of obtained cluster size value is shown in the Figure 6.11 for each angle. The module at 27^0 degrees was measured in different conditions with another threshold value.

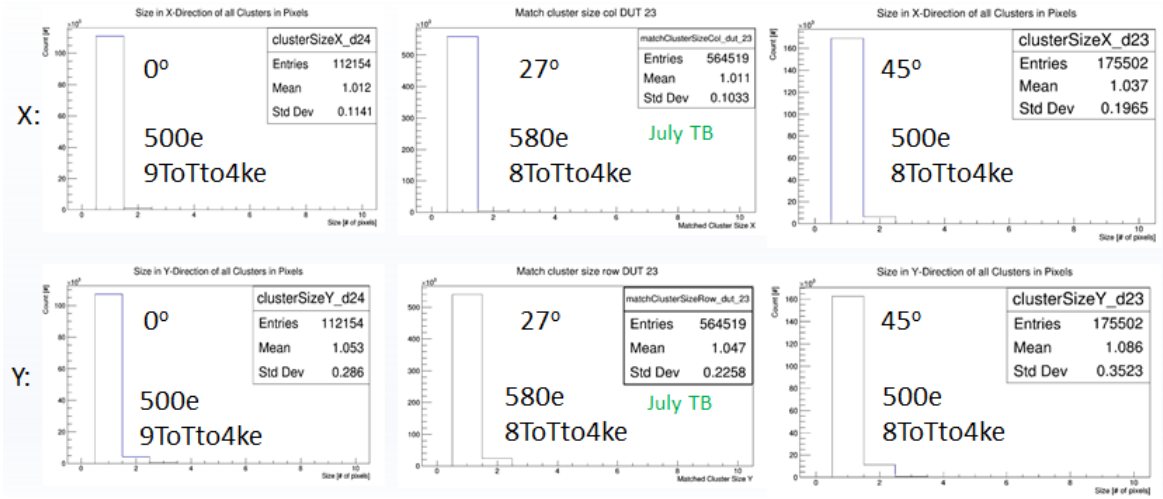

Figure 6.11 – The cluster width for X and Y for sensor thickness 50 µm is calculated for different beam incidence angles.

Residuals

The residuals are calculated separately for *x* and *y*, given the rectangular shape of pixels, and are the difference between the position of the reconstructed track and the position of the cluster centre.

Hence, the residual in *x* is given by: $\Delta x = \Delta x_{track} - \Delta x_{hit}$ and for the residual in y accordingly.

The spatial resolution of a detector is defined as the width of the unbiased residual distributions. The term *unbiased* in this case means that these detectors are not taken into account for track fitting. The width of the residual, and hence the spatial resolution, is obtained by the RMS of the residual distribution. If the reconstruction has gone well, the residual is a Gaussian distribution centred at zero with a base width approximately equal to the pixel pitch. However, this would be wider for results from DESY ($\mathbf{e}^-$ (4 GeV)) where there is increased multiple scattering, as shown in Figure 6.12.

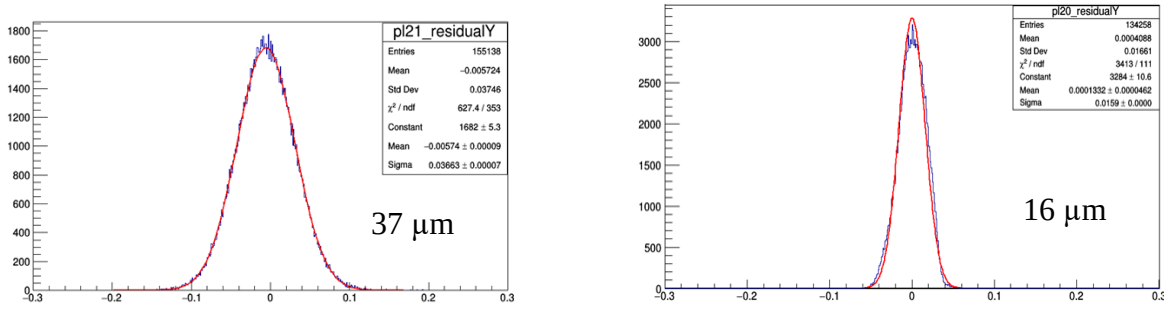

Figure 6.12 – The residual distributions in a short pixel direction (Left) from DESY test beam and (Right) CERN-SPS test beam.

The Gaussian shape is due to charge sharing at the edge of the pixels. The intrinsic spatial resolution of planar pixel sensor readout in binary mode is obtained by dividing its pitch by

$\sqrt{12}$. In the simplest case of single-hit clusters, the intrinsic spatial resolution for an FE-I4 pixel cell of 50×250 μm^2 pixel size are calculated to be $\sigma_{\text{int:X}}$=72 μm and $\sigma_{\text{int:Y}}$ =14 μm. The width of the residual distribution in the results shown in the Figure 6.12 is a little bit wider than expected $\sigma_{\text{int:X}}$ and $\sigma_{\text{int:Y}}$. It is because the pointing resolution of the telescope introduces smearing at the edges of the residuals.

In addition, to obtain the intrinsic spatial resolution of a sensor, one has to consider the contribution from clusters, the pointing resolution of the telescope and the multiple scattering contributions.

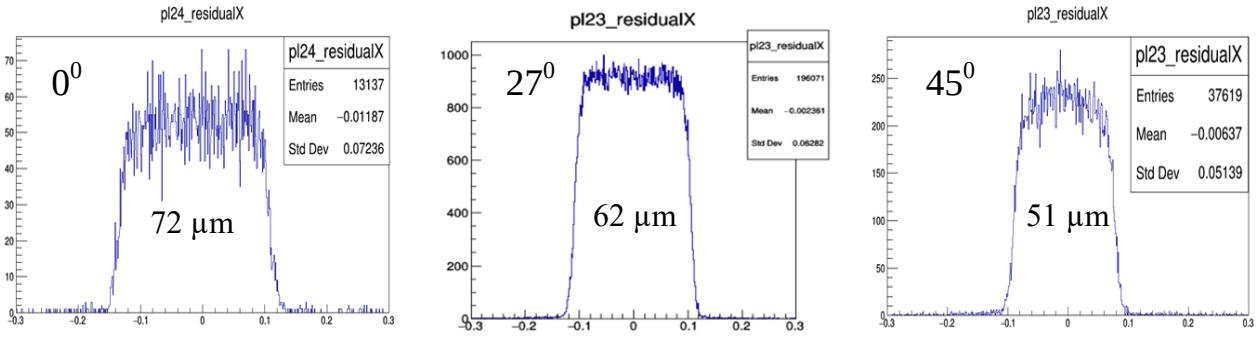

Figure 6.13 – Residual distribution of an FE-I4 module with a 50×250 μm pixel cell in the long pixel side direction depending on an incidence beam angle. Beam test measurements performed at CERN with π^+ (120 GeV).

With the increased angle of incidence beam the spatial resolution is improved. The main reason is of course the presence of clusters formed by multiple pixels.

6.4 Test beam results of active and slim edge thin sensors

One of the most interesting properties of a tracking device in test beam measurements is a hit efficiency of the device. In the current work I have tested n$^+$-in-p planar sensors of thicknesses of 50 μm, 100 μm and 150 μm with active and slim edge designs in various conditions such as irradiation, bias voltages, and inclination.

Pixel hit efficiency

The hit efficiency of the DUTs is defined as the ratio of the number of reconstructed tracks with matching hits in the DUT to the total number of reconstructed tracks passing through the DUT:

$$\text{Efficiency} = \frac{N_{\text{Matched}}}{N_{\text{Total}}} \tag{6.1}$$

For all obtained hit efficiency results, an absolute systematic uncertainty is derived. The systematic uncertainty is arising from three sources: the trajectory reconstruction, the subsequent DUT analysis and the fluctuations on the resulting efficiencies during the measurement time. The total systematic uncertainty on all obtained hit efficiency values is calculated to be 0.3 % [110]. The statistical uncertainty usually is small compared to the systematic one due to the high event rate in the test beam.

Analysis of 50 µm sensors

A hit efficiency of a non-irradiated module employing a 50 µm thick sensor with implemented active edge design has been studied at different sensor sides. The results of threshold characterization show that a real threshold value is higher on the left side than on the right side of the module. This fact should have an effect on pixel efficiency: a lower efficiency level is observed on the left side.

A pair of sensors of both active and slim edge designs before (50-3-1D and 50-3-3A) and after irradiation (50-3-1A and 50-3-3B) were taken to be characterized with a particle beam. The modules have been measured at about the same tuned threshold value in the range of 500 e^- - 600 e^- and with a charge calibration of 8 ToT for 4000 e^-.

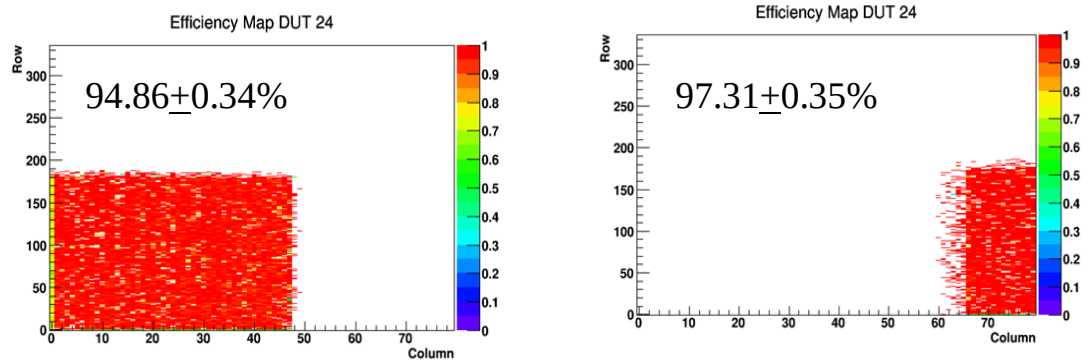

Figure 6.14 – The efficiencies for an active edge sensor at 50 V are observed to be different between one side the another. The part of the beam limited by scintillator crossing is shown.

At 50 V the active edge sensor with no punch-through implemented reaches an overall hit efficiency of 94.86±0.34% and 97.21 ±0.35% for the left and the right side correspondingly. The efficiency maps, showing the efficiency value for each of the pixels bounded by the beam profile, are shown in Figure 6.14.

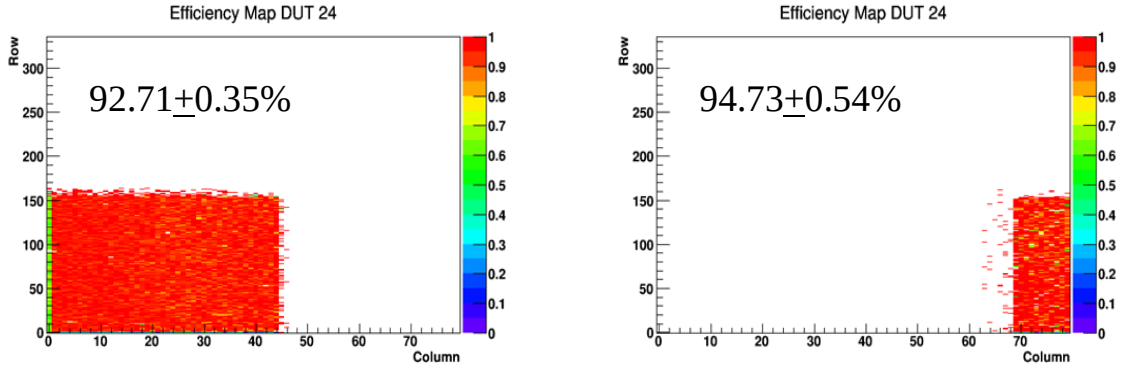

Figure 6.15 – The efficiencies for a slim edge sensor at 50 V are observed to be different between one side the another. The part of the beam limited by scintillator crossing is shown.

The slim edge with bias rail, one guard ring and standard p-t structure implemented, as shown in Figure 5.7 (c), shows an efficiency of 92.71±0.35% and 94.73±0.54% on the left and the right sides respectively.

Considering the in-pixel efficiency maps for both designs one can see the reasons of loss of efficiency for the both designs (Figure 6.16). For the active edge design inefficiencies are due to the charge sharing between the pixels. This is mainly visible at the corners of a pixel cell, where

the charge is shared among the four adjacent pixels, while at the long side of the pixel the charge signal is shared only by two adjacent pixels. The hit efficiency of the slim edge sensor is reduced primary due to the punch-through dots and secondary to the charge sharing between pixels.

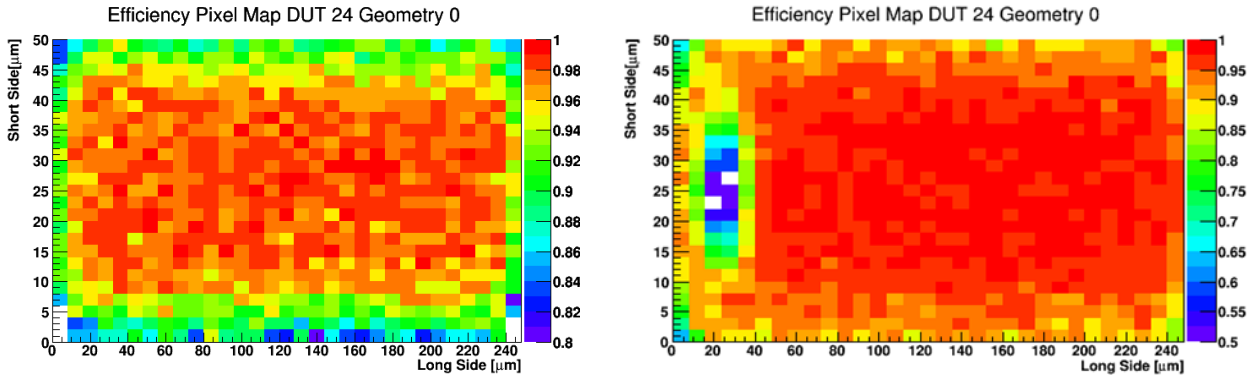

Figure 6.16 – In-pixel hit efficiency plots for an active (left) and a slim edge (right) sensor.

The full depletion for non-irradiated 50 µm sensors reaches at about 5 V as we can see from the results in Figure 6.17. The plots show the evolution of the hit efficiencies before and after full depletion of the sensor.

After irradiation, the hit efficiency is reduced due to the radiation damage. The trapped charge carriers decrease the hit efficiency given a higher probability for the signal to be below threshold.

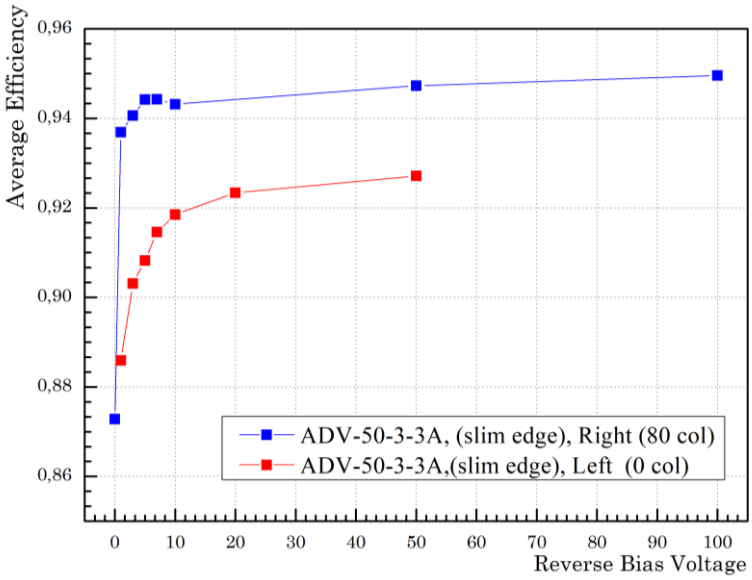

Figure 6.17– Efficiency vs bias voltage for the non-irradiated sensor

The Figure 6.18 shows the in-pixel efficiency maps for the left side of a module employing a 50 µm thick active edge and slim edge sensors irradiated to 10^{15} n_{eq} cm^{-2} at the Birmingham cyclotron facility. The maps at 50 V and 120 V demonstrate how the hit efficiency recovers with increasing of the bias voltage.

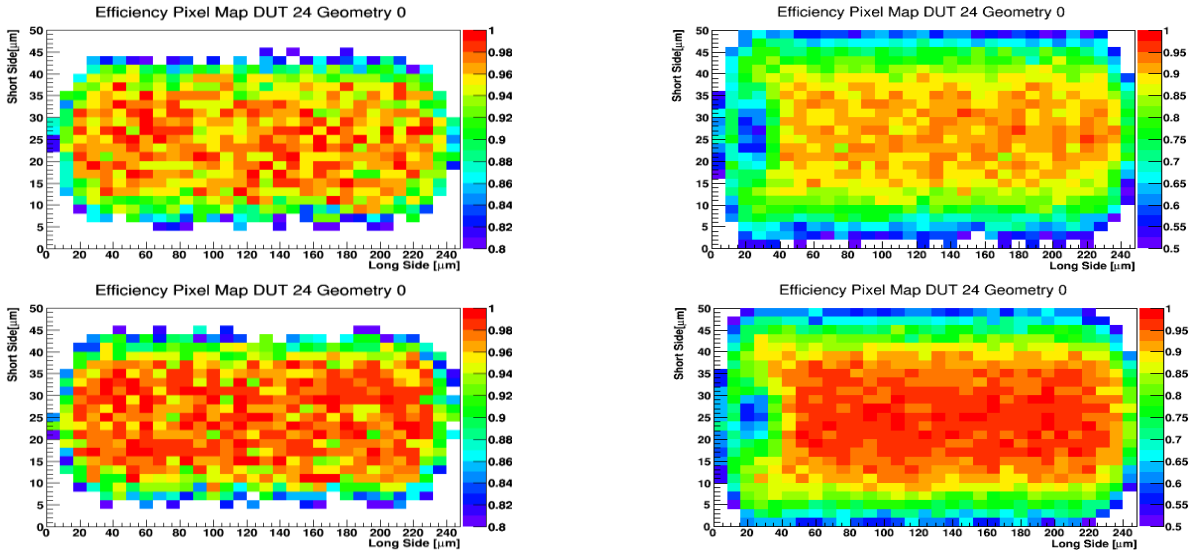

Figure 6.18 – In-pixel efficiency plots after irradiation for an active (right) and a slim edge (left) design sensors at 50 V (top) and 120 V (bottom).

At 120 V the active edge sensor with no punch-through structure reaches an overall efficiency of 89,27±0.3%. Comparing the hit efficiency of the sensors with the same design before irradiation, the increased effect of charge sharing after irradiation is clear at the corners of the pixels and hence a lower overall efficiency is obtained.

The slim edge sensor with punch-through reaches a maximum overall hit efficiency of 84,33±0.3% at 120 V. It shows a lower hit efficiency due to the irradiation and the presence of a biasing structure.

To compare the performance of the irradiated active and slim edge sensors, the overall hit efficiencies as a function of the bias voltage on the left side for both sensors are summarized in Figure 6.19.

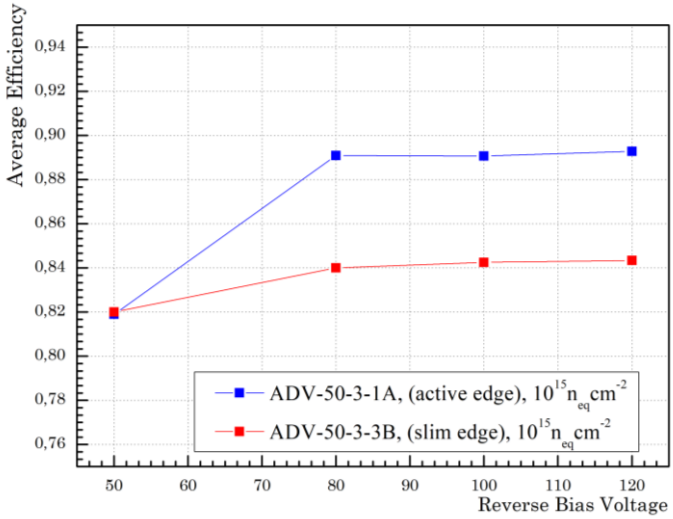

Figure 6.19 – A comparison between the hit efficiencies as a function of the bias voltage for the active (no PT) and slim edge (PT) irradiated sensors.

The slim edge sensor shows about 10 % less efficiency than the active edge sensor at the highest voltage point of 120 V. Both sensors show a constant efficiency after 80 V, the flat plateau is interpreted as full sensor depletion.

Efficiency at the inclined tracks

At the real tracking system of ATLAS the particles will traverse at some angles to the surface of the sensors. At the test beam the module was rotated in respect to the incident beam to investigate the hit efficiency and compare to the perpendicular beam.

The test has been done with 50 µm thick active edge module at 27˚ and 45˚ degrees. According to the results hit efficiency was improved and reached 95 % at 80 V bias voltage at 45˚ degree beam incidence. The results are summarized in Figure 6.20.

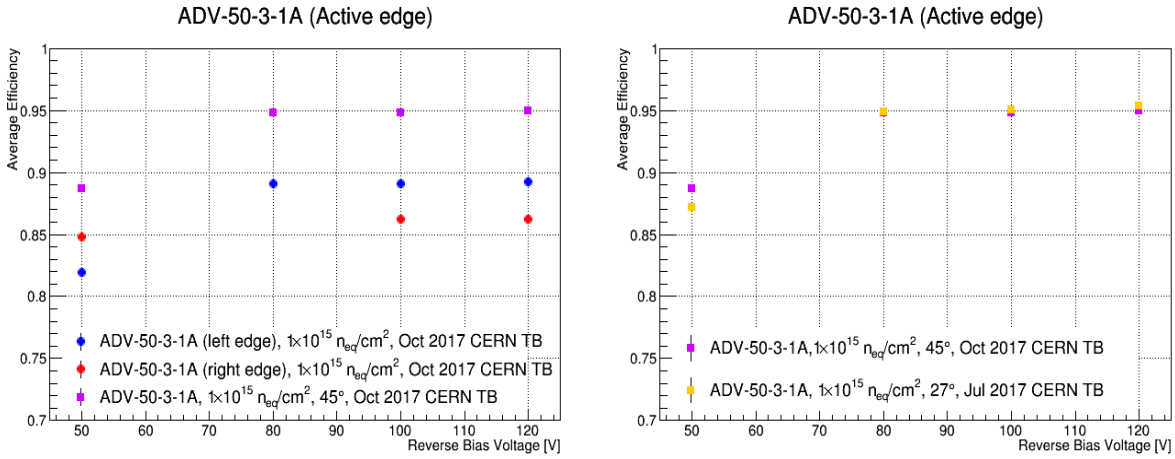

Figure 6.20 – A comparison between the hit efficiencies at different angles (0˚, 27˚, 45˚) as a function of the bias voltage.

The performance is very similar to the performance of the same sample tilted at 27˚, but it could be explained that the module was measured at different conditions; particularly the temperature was not monitored.

Edge efficiency

The edge characteristics of the active and slim edge sensors from the ADVACAM production are particularly interesting due to their production process with the side activation. Sensors with reduced inactive edge area are the most important in use close to the interaction point in a detector to achieve high tracking efficiency. Both left and right edges of each module are measured separately with the beam centered on each edge. Due to the fact that the analysis is performed only at the edge column, longer beam time is needed to obtain the required statistics. The pixel efficiencies beyond the last pixel column are discussed in this section.

The hit efficiencies at the edges of a non-irradiated 50 µm thick active edge sensor measured at CERN SPS are shown in Figure 6.21 for the left and right edges.

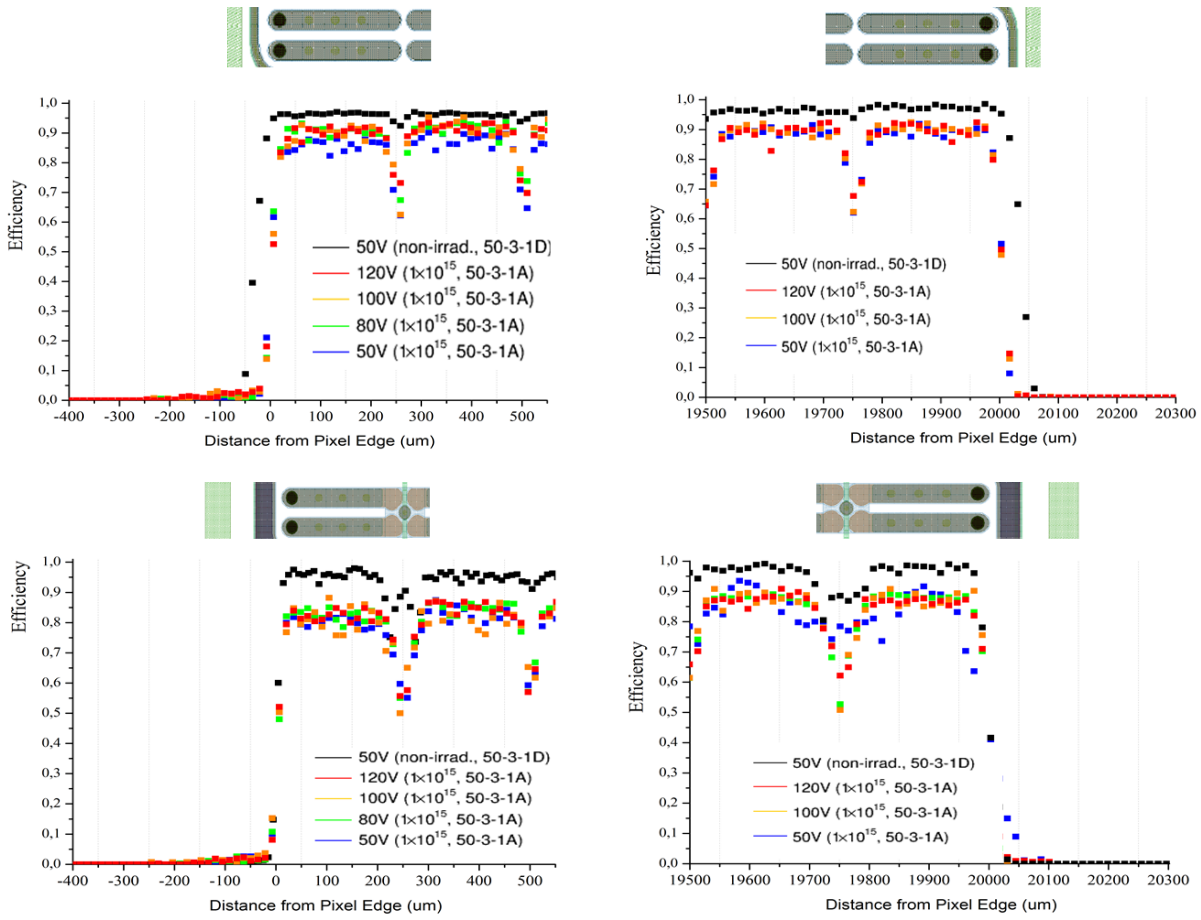

Figure 6.21 – Hit efficiencies as a function of the bias voltage at the edges of 50 µm thick sensors irradiated to 10^{15} $n_{eq}cm^{-2}$. For an active edge sensor with the beam positioned at (a) the left edge and (b) the right edge. Slim edge sensor with beam positioned at (c) the left edge and (d) the right edge.

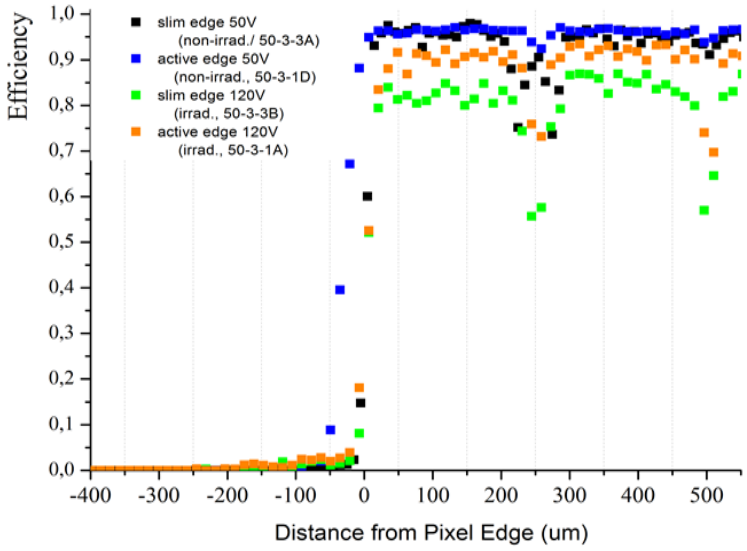

Figure 6.22 – Comparison of the edge efficiency for the sensors of the slim and active edge designs.

The active edge employs an edge distance d_e =50 µm with one floating guard ring and no biasing ring implemented. This allows the electric field to extend to the edges of the sensor. The

decrease of the hit efficiency at the beginning of the pixel column at *X*=250 μm is due to charge sharing. Moreover, the decrease of efficiency is higher in the slim edge design due to the implemented standard punch through structure shown by the overlaid design. The punch-through dot implanted within the pixel implant acts like a collecting implant and attracts the charge carriers that go in this way undetected hence the lower efficiency.

The irradiation increases the limit of the bias voltage needed to achieve constant hit efficiency over the pixel implants. Therefore, measurements at higher voltages up to 120 V are performed to reach efficiencies as high as possible. For the active edge sensor at the highest voltage of 120 V, the efficient area at the edge decreased to about 25 μm for both edges. Moreover, for the slim edge sensor the edge efficiencies as a function of the bias voltage are shown in Figure 6.21 (c) and (d) for the left and right edge respectively. The slim edge sensor shows efficiency after irradiation up to 20 μm beyond the last pixel column.

A comparison of the edge efficiencies for both active and slim edge sensors before and after irradiation is shown in Figure 6.22. Both active and slim edge modules achieve lower edge efficiencies within a smaller active area beyond the last pixel implant after irradiation, which could be explained by dominance of charge trapping effects.

100μm and 150μm thickness sensors

The 150 μm thick active edge sensors and 100 μm slim edge sensor were measured before and after irradiation at CERN-PS irradiation facility with 24 GeV protons to the level of $2\times10^{15} n_{eq} cm^{-2}$.
These are thicker and more reliable sensors compared to 50 μm described above, and are selected as the baseline for the future ITk ATLAS upgrade.

Hit efficiency

For the non-irradiated active edge module with one floated guard ring the hit efficiency reaches 97,8+0,3% at 50 V. The slim edge design with only bias rail at the edge and external punch-through structure implemented, hit efficiency is 96,9+0,3%.

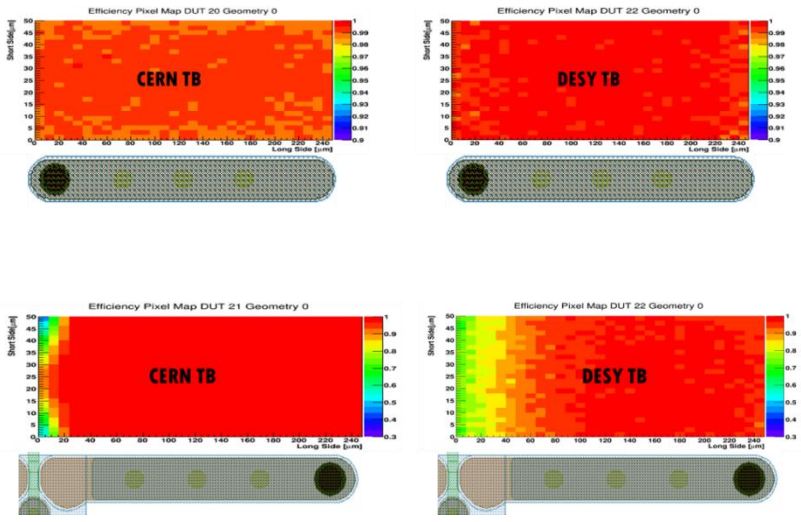

Figure 6.23– In-pixel efficiency of the active (top) and slim edge (bottom) sensors at 50 V obtained from CERN SpS (left) and DESY (right) test beams.

The sensors before irradiation were measured at both CERN and DESY facilities, so we can compare the efficiency and observe the smearing in the pixel map due to low spatial resolution in the reconstruction, because of the multiple scattering effects.

If we consider the in-pixel efficiency maps for both designs we can see the reasons of loss of efficiency in both designs (Figure 6.23). For the active edge design inefficiencies are due to the charge sharing between the pixels. This is mainly visible at the corners of a pixel cell where the charge is shared among the four adjacent pixels, while at the long side of the pixel the charge signal is shared only by two adjacent pixels. The hit efficiency of the slim edge sensor is reduced primary due to the punch-through dots and secondary to the charge sharing between pixels.

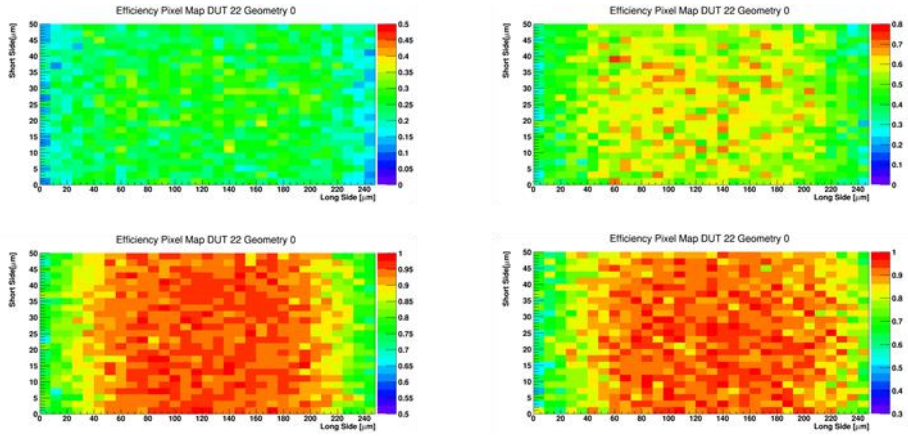

Figure 6.24 – In-pixel efficiency after irradiation for an active (right) and a slim (left) edge sensors at 50 V (top) and 180 V (bottom).

After irradiation the sensors were measured at DESY facility. The in-pixel efficiency results are shown in the Figure 6.24. At 200 V the active edge sensor reaches an overall efficiency of 92,46±0.3%. The slim edge sensor with punch-through reaches an overall hit efficiency of 89.55±0.3% at 180 V.

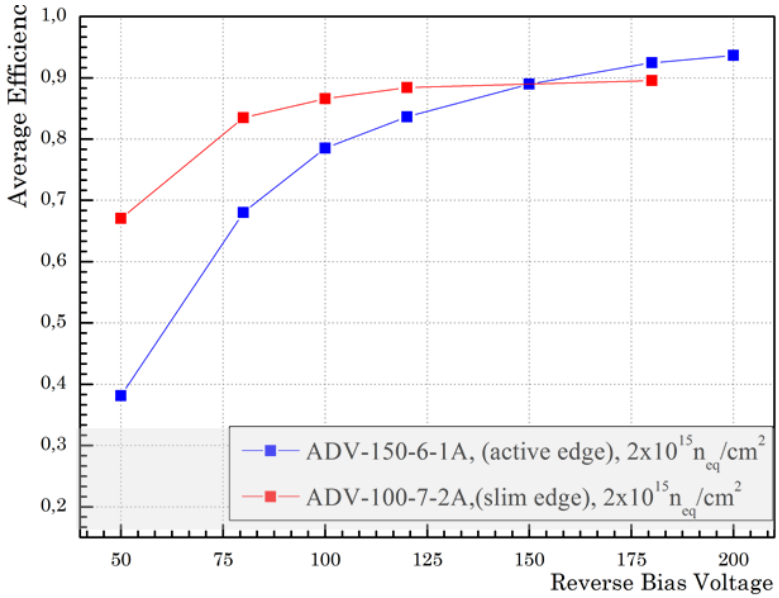

Figure 6.25 - Comparison of the global hit efficiency vs bias voltage for active and slim edge designs.

The modules were measured at several bias voltage points up to the breakdown voltage, which is starting early around 200 V for these sensors, because of the thin edge. The comparison and the results are presented in the Figure 6.24.

Thicker sensors show better results than the thin 50 µm sensors. This fact can be explained that the threshold level of FE-I4 readout chip is definitely high for using with very thin sensors. It has an offset and cannot be tuned to lower values in order to increase the hit efficiency after irradiation.

Edge efficiency

The active edge design employs an edge distance d_e =50 µm with one floating guard ring and no biasing ring implemented. This allows the electric field to extend to the edges of the sensor. The decrease of the hit efficiency at the beginning of the pixel column at x=250 µm is due to charge sharing.

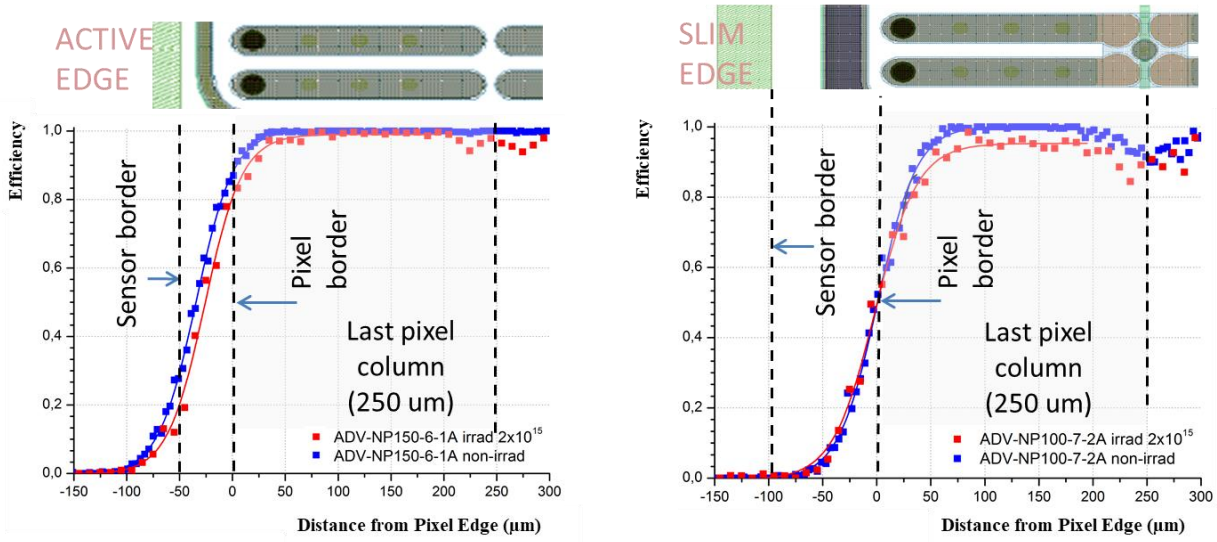

Figure 6.26 - Hit efficiency plot at the sensor edge of the 150 µm thin sensor (a) with 50 µm active edge and (b) 100 µm thin sensor with slim edge design 100 µm wide edge. Comparison before and after irradiation. The pixel cell has an FE-I4 cell size of 50×250 μm^2 and the hit efficiency is evaluated as a function of the distance from the last pixel column to the edge region.

A comparison of the edge efficiencies for both active and slim edge sensors before and after irradiation is shown in Figure 6.26. Both active and slim edge modules achieve lower edge efficiencies within a smaller active area beyond the last pixel implant after irradiation. The presented results are smeared due to the multiple scattering effects of the electrons, which were used to estimate sensor efficiency at DESY test beam. This effect increases the spatial resolution of the telescope up to 20-30 µm.

6.5 Conclusions

The tested in this work designs for thin planar sensors are prototypes of the possible options for the ITk Pixel detector. The new sensor technology with a reduced inactive area at the edges has two different designs, an active edge and a slim edge design that have been investigated before

and after irradiation. The active and slim edge sensors have an edge width of 50 μm and 100 μm respectively with a pixel cell size of 50×250 μm^2.

A novel aspect of this work is the study of the performance of 50 μm thick sensors with an active and a slim edge designs interconnected to FE-I4 read-out chip. The hit efficiency measurements of the sensors have been carried out using particle beams before and after irradiation to a fluence of 10^{15} n_{eq} cm^{-2}. The active edge sensors without any biasing structure implemented show better overall and edge efficiency compared to the slim edge sensors. But due to the lack of biasing structures, it is not possible to test the functionality of the pixel cells before interconnection. Furthermore, after bump bonding the pixels are only grounded via the connection to the chip. A disconnected channel will cause a local modification of the electric field, which may lead to a lower breakdown voltage.

Both designs show good hit efficiencies beyond the last pixel implants. Before irradiation, the edge efficiency for the active edge sensor extends to 50 μm beyond the last pixel column up to the end of the sensor. In the case of the slim edge sensor, the edge efficiency extends up to 25 μm beyond the last pixel column corresponding to the position of the bias ring that collects the signals from the edge area. After irradiation, the edge efficiency for both designs is reduced.

These results on 50 μm thick sensors shape an outlook for future designs for the ITk. A performance can be improved using a new RD53A read-out chip, which is able to achieve lower real threshold values down to 600 e^-. Thinning down the sensor allows mitigating the charge trapping effect caused by radiation. But the very thin sensors are mechanically fragile and delicate in the operation. The performance of 50 μm thick sensors is still to be investigated at higher fluences with a new generation of the readout chip.

Besides these results, in the work more thick sensors ranging between 100 - 150 μm of the same designs were investigated. The edgeless design by ADVACAM has demonstrated good radiation hardness at the ITk fluences. The design could be improved by increasing the breakdown voltage for these sensors, as well as the other options for the biasing structure should be investigated, including the option of the removable metallization.

Chapter 7

Front-end electronics for Phase-2 Pixel detectors

Contents

This part of the current thesis will introduce the working principles and tuning procedures for the front-end electronics, which is used to process signals from the pixel sensors. A new generation of readout electronics for Phase-2 LHC upgrade is going to be used in hybrid pixel detectors. The discussed readout chip, called RD53A, is a joined prototype of ATLAS and CMS experiments implemented in 65 nm CMOS technology. It was designed to find the best analog and digital design in terms of radiation hardness, power consumption and readout performance.

In this chapter my contribution to RD53A chip testing is described. It contains the study of the frequency of ring oscillators embedded in the chip to perform radiation damage monitoring and beam test characterization of RD53A pixel sensor modules. The dependencies of the ring oscillator frequency on temperature, supplied voltage and irradiation were measured and are presented in the following sections, as well as the results on test beam measurements to determine spatial resolution and hit efficiency of RD53A module in various conditions.

7.1 Pixel detector front-end electronics

In hybrid detectors the sensor is bump bonded to the front-end chip to read out signals created by particle tracks. The front-end chip is a first stage of the signal processing from the charge collected in the sensor to the digital data stored on PC. Although the existing pixel chips use different geometries, readout philosophies, and analog circuits, several building blocks and properties are common to the major part of the designs [96].

As shown in Figure 7.1, the front-end chip is divided into an active area, containing a repetitive matrix of nearly identical pixel cells, and chip periphery from where the active part is controlled, global functions and variables common to all pixels are stored and data is buffered and then transmitted.

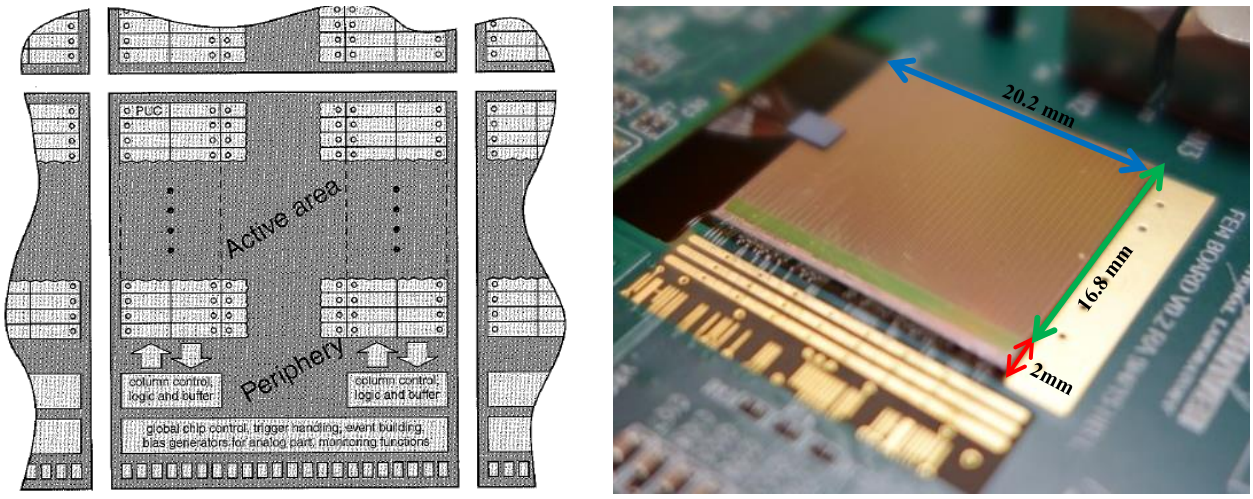

Figure 7.1 – (Left) Schematics of the arrangement of several adjacent chips on a module [96]. (Right) The FE-I4B chip with the small HV-CMOS pixel sensor glued on [97]. The wire bond pads usually located on the one side at the lower edge, so the chips can be abutted side by side on a module.

The pixel unit cell (PUC) is electrically connected one-to-one with the corresponded pixel on a sensor through the bump bonds, it is a very sensitive node and care must be taken in the layout to shield it toward the underlying circuitry and the substrate. A PUC contains an analog and a digital block. To operate the analog and the digital circuit have separate voltage supply, for FE-I4 an analog part requires 1.5 V, while a digital part operates at 1.2 V. The two stage layout implemented in the analog part allows better optimization in terms of charge collection efficiency, signal rise time and power consumption [98]. In the analog integrated circuit (shown in Figure 7.2) a small (about μA) and short (a few ns) signal from the sensor is amplified by a charge sensitive amplifier (CSA), which sends out a signal relative to the charge accumulated on its input. The preamplifier is one of the most crucial parts in the PUC. It must provide an inverting gain of well above 100 with a sufficient bandwidth and minimized both the frequency-independent (thermal and shot noise) as well as the 1/f noise. The power consumption must be kept very low in order to limit the heat dissipation in the active area.

Each pulse of signal from the detector, which is typically modeled as constant current source, causes the output of the CSA to step. A feedback capacitor C_f between the input and output of amplifier stores the charge from the detector. The gain of the CSA in the ideal case is $1/C_f$ [102], and the output voltage step is:

$$U_{out} = -\frac{Q_{coll}}{C_f} \tag{7.1}$$

where Q_{coll} is collected charge. The C_f value is a compromise between gain, input impedance, speed and stability.

To compensate a significant fraction of the leakage current from the sensor a DC feedback scheme is implemented. It is necessary because the leakage current of 10 nA on the feedback resistor of about 100 MOhm can introduce ~ 1 V, a value which may bring out the typical electronic circuits.

After each single pulse the feedback capacitor C_f is being charged for a continuous reset either a resistor or a constant current source has to be placed parallel to the C_f. This is realized by a NMOS feedback transistor, controlled by a Digital-to-Analog Converter (DAC) voltage which can be controlled via the FDAC value [98]. Behind the two amplification stages the signal is passed through a discriminator to distinguish signal from noise. This is the second stage of an analog part of the detector front-end electronics, the discriminator retains signals above the adjustable threshold and outputs the analog signal into a digital square wave. The programmable trimming registers GDAC (global) and TDAC (individual for each pixel) change the reference voltage of the discriminator to which incoming signals are compared to. The typical step width per DAC count allows uniform threshold settings with a precision of few tens of e^-.

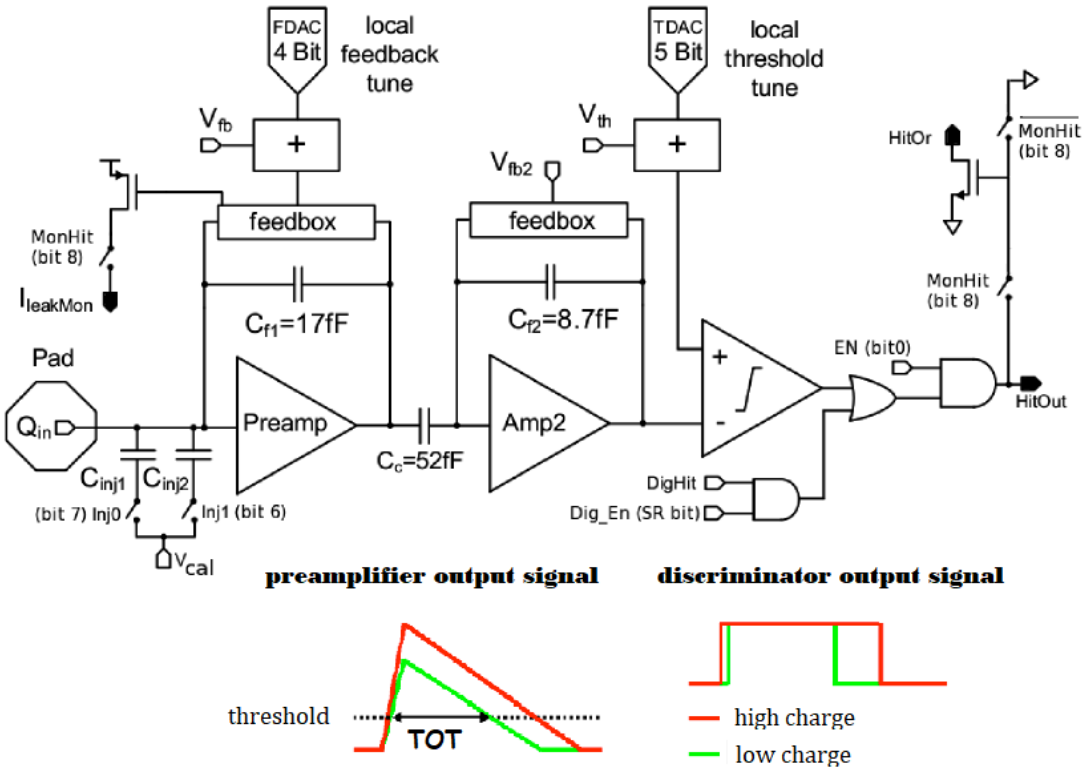

Figure 7.2 – Schematics of an analog part of the FE-I4 chip. It shows charge signals before and after the discriminator stage and visualizes how the output signal depends on a charge. [99]

The output of the discriminator is a step function that equals to a digital 1 when the compared signal is above threshold and equals 0 when the signal is below threshold. Changing the feedback current by changing the FDAC value the shape of the signal can be changed

individually for each pixel, so the time the signal is over threshold can be adjusted and in principle used for the evaluation of to the amount of deposited charge. Technically, if a signal is above the threshold, as shown in Figure 7.2, the discriminator output signal is logical 1 and it gets a timestamp so the time between rising and falling edge of the discriminator output signal is calculated. This time is called Time over Threshold (ToT). In Figure 7.2 one can see that the ToT is a function of the injected charge.

The digital part of the FE chip holds the logic for data processing. It includes an Analog-to-Digital Converter (ADC) which digitizes the signal and converts it into amplitude information of the ToT. The ToT length is measured in a 4-bit resolution using an external clock frequency of 40 MHz. A ToT with code of 0 corresponds to the time of 25 ns over the threshold, then code of 1 is 50 ns. This behavior is valid for ToT code values up to 13, the code of 14 is an overflow bin and 15 means no hit. Then the digital information is further processed by circuitry in the pixel and at then at chip periphery. All incoming hit information, including hit pixel address, timestamp and ToT value are buffered there for a short time interval until retrieved by a trigger signal to be transmitted serially out of the chip in the same order as the trigger arrival. When a hit time becomes longer than the latency of the L1 trigger (approximately 3.2 μs) and no trigger signal is recorded, the hit information is automatically discarded.

The PUCs are often grouped in columns; i.e., power, bias, and control signals and the output data flow are routed vertically and only very few signals run horizontally [96]. Two columns are often grouped together to form a “column pair” in order to share circuitry between pixels, usually the pixel pair has a common digital and separate analog parts. It is done to minimize digital crosstalk between circuits, which can happen through the bulk material of the chip. The pixel columns end by the region at the periphery, named End-Of-Column (EOC), which stores all the hit information and is responsible for the communication with the outside world. Once the information from the FE-pixels reaches the EOC buffers, it is erased from the FE-pixels making them ready to detect a new hit. Then, as was already discussed, the trigger signal initializes the readout to the Module Controller Chip (MCC) from the corresponding EOC buffers.

The ionisation particles generating a charge signal in a sensor may cause ionisation in the FE electronic. These charges can change the state of a sensitive node in the FE, which is called single event upset (SEU). It is a not permanent damage of the electronics but it can result in a bit flip. In order to create a SEU tolerant FE electronic, all registers are set up in a redundant way.

7.1.1 Tuning procedure of the Front-end electronics

Due to production variations over the chip surface, the intrinsic differences in the electronics of each pixel occur. Prior to the pixel module operation or test, the FE-chip has to be properly tuned to compensate the electronics mismatches in the individual pixels and to make the pixel output as uniform as possible. For this reason the tunings to set the threshold value and the gain between charge and ToT value are performed. Both threshold and ToT tunings have two steps: a global and a local tuning, which respectively set the DAC values for all the pixels at the same time and for the individual pixel response to reach the target values of the threshold and ToT. After finishing of the tuning procedure, all the DAC settings of the FE-chip are written to the configuration file, which can be loaded to the chip later to set specific parameters.

To test the functionality of the pixel electronics in the FE-chip a charge injection circuitry for characterization and tuning is implemented. The FE-I4 chip has a programmable pulse generator, which is called *PlsrDAC* that is used to inject signals into the analog circuitry of each pixel. As shown in Figure 7.2, the analog injection circuitry has two injection capacitors connected in parallel. The two capacitors together with the calibration voltage V_{cal} determine the injection charge Q_{inj}. For accurate measurements of the ToT and threshold values, the injected charge Q_{inj} must be known with good precision.

The standard tuning procedure used for the laboratory or the test beam module characterization is described below.

Current-voltage (IV) measurements

Before using the detector it is important to determine an optimal bias voltage for the best performance. At the too low bias voltage, the sensor will be under-depleted, but if the biasing is excessive, an avalanche break-down can occur possibly damaging the device. The optimum voltage can be determined by recording the current as a function of the input voltage, known as an IV curve. Also, the IV measurements may be a way to test a device for any technical problems.

To perform the IV measurements of flip chipped pixel sensors, the special application has been developed using the LabVIEW software [104]. The program, the user interface is shown in Figure 7.3, automatically performs the IV measurements, providing a high accuracy and saving a time. The idea of the program is to control the source meter Keithley 2410, which able to measure the current and apply a stable DC voltage. The program allows for safe manipulation with the pixel module during the measurements, it limits the maximum currents and voltages and provides the smooth change in voltage, preventing the damage of sample. In the end the results are recorded as a function of current versus the bias voltage into the text file for further processing.

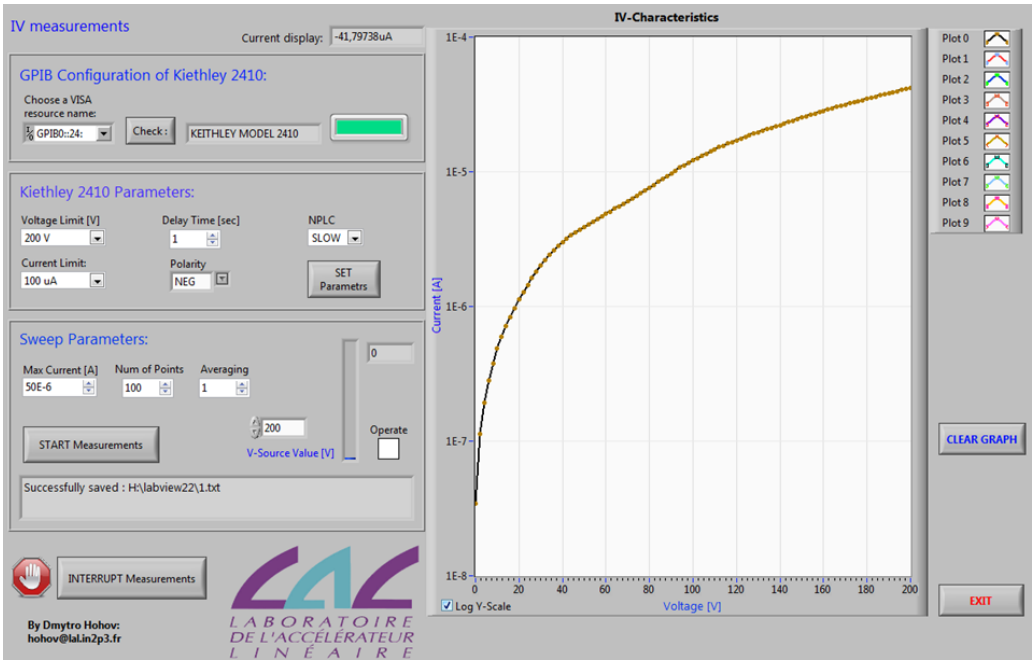

Figure 7.3 - The screenshot of the program for IV-measurements of sensors bump-bonded to an FE I4 readout card.

Analog and digital scans

Using an external charge injection circuit a defined charge can be injected several times directly into the discriminator “digital scan” or in the analog circuitry before the preamplifier “analog scan” of each pixel. The example of the analog and digital scan of the FE-I4 chip performed by using STControl software [111] is shown in Figure 7.4

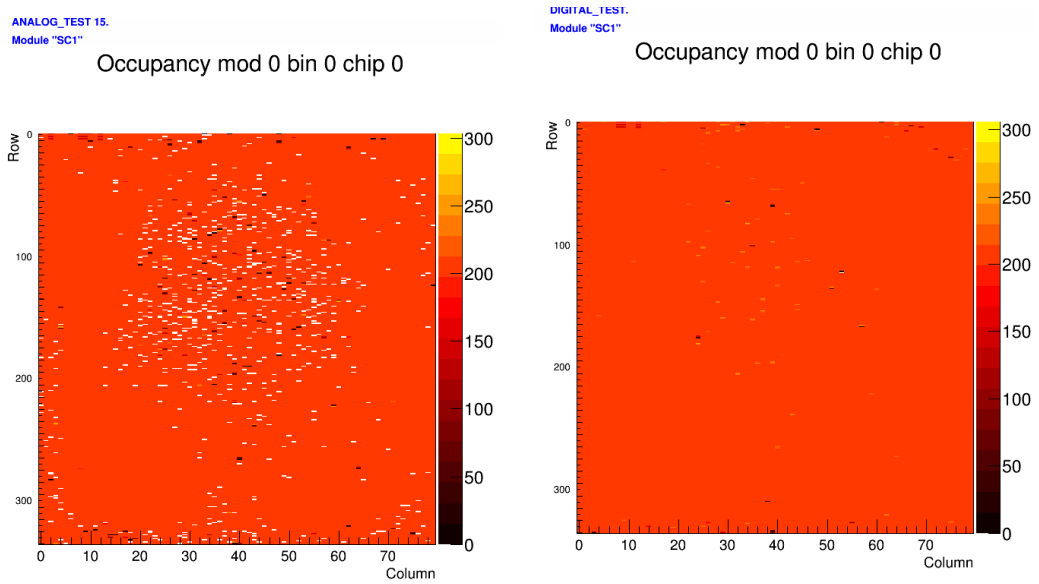

Figure 7.4 - Analog scan (left) and digital scan (right) for FE-I4 front-end card, the charge was injected 200 times for every pixel. It can be noticed that the under test chip has a big number of faulty pixels. One can see the noisy pixels in yellow, black pixels with the very high threshold and disabled pixels in white.

These are the fundamental tests show if the analog and the digital part of a pixel cell work as expected. A fixed charge, which exceeds most threshold settings, is injected subsequently into each pixel according to a mask pattern. The read-out of each pixel should report the number of registered hits which is the same as the number of injected pulses in case of full functioning. If the pixel register more hits than the number of injections, it would be consider as a noisy pixel, the dead pixels will not have any hits or just a few. Such non-working pixels can be masked using the results of an analog scan, which means that they are not considering and will not affect the results.

Threshold tuning

The threshold is a crucial parameter of the FE-chip for the detection efficiency. In principle, it should be set as low as possible in order to maximize the number of detected hits, but at the same time it should be low to keep the rate of fake hits caused by electronics at the acceptable level. The aim of a threshold tuning is to set the same value of the threshold for each pixel to have a uniform response over the entire module surface. In practice, the threshold may differ in different parts of the chip, which was demonstrated analyzing the hit efficiency on different sides of the module, the results is discussed in Chapter 6.

In order to determine the threshold charge Q_{th}, a scan is performed by injecting a defined charge into the preamplifier via the injection capacitance C_{inj} in the analog circuit. The response of each pixel to the multiple injections of different charges is recorded. The charge value that is above

the discriminator threshold results into a hit. The discriminator has a 0 and 1 response that develops a digital square wave function (step function). Because of noise, charges near the threshold sometimes trigger, sometimes they do not, the resultant response of the discriminator forms a step function convoluted with a Gaussian distribution (this is fitted with a convolution of a step function and a Gaussian distribution which describes the probability of having a signal p for a certain injected charge Q as). This behavior results in the creation of the following s-curve function, shown in Figure 7.5.

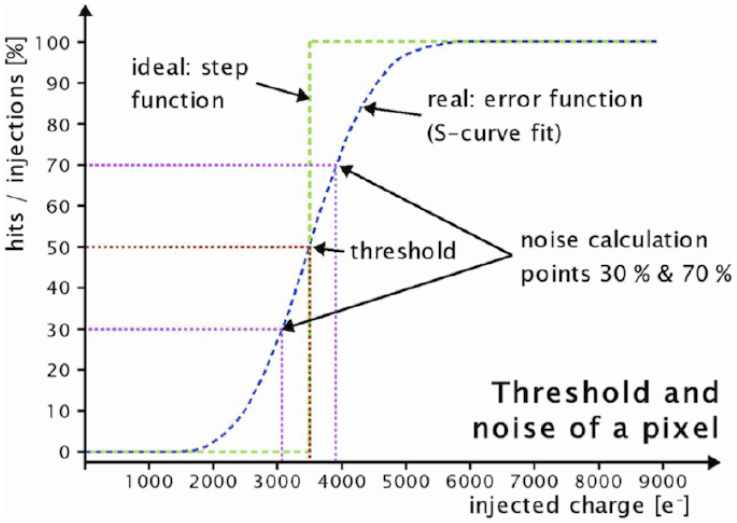

Figure 7.5 – Schematics of an analog part of the FE-I4 chip. It shows charge signals before and after the discriminator stage and visualizes how the output signal depends on a charge. [99]

From the S-curve the actual threshold value Q_{th} is defined as an amount of charge that is registered in 50% of the cases. The probability p_{hit} to register a hit of charge Q depends on the threshold as well as the average noise level noise as σ_{noise}:

$$p_{hit} = 0.5 \cdot \mathrm{erfc}\left(\frac{Q_{th} - Q}{\sqrt{2} \cdot \sigma_{noise}}\right) \tag{7.2}$$

where Q – is injected charge, the $\mathrm{erfc}()$ is the statistical complementary error function which is defined as:

$$\mathrm{erfc}(x) = 1 - \mathrm{erf}(x) = 1 - \int_{-x}^{x} \frac{e^{-y^2}}{\sqrt{\pi}} dy \tag{7.3}$$

where $\mathrm{erfc}()$ – is the error function that describes the probability of a random variable x with a mean value 0 and variance 0.5 falling in the range $[-x, x]$.

The σ_{noise} is a noise level, which is usually less than 200 electrons for the non-irradiated samples. There are three main sources of noise in the electronics:

- **Shot noise** arises because of the discrete nature of the charges carried by charge carriers, electrons or holes. In electronics it is generated by unavoidable random statistical fluctuations of the electric current in an electrical conductor and occurs when a voltage is applied.

- **Thermal noise** is caused by the random thermal motion of charge carriers inside an electrical conductor, which happens regardless of any applied voltage. Its power spectral density is nearly equal throughout the frequency spectrum.
- **1/**f **noise** occurs in almost all electronic devices and results from a variety of the effects, though always related to a direct current. Unlike shot and thermal noise the 1/*f* noise is a signal or process with a frequency spectrum that falls off steadily into the higher frequencies.

The threshold is adjusted globally by the GDAC register, which controls the discriminator stage of the chip by setting a common value for all pixels. The threshold value achieved by performing of the GDAC tune is an average value to the target threshold over the entire module. Typically at this stage a threshold dispersion normally is around 600-700 e^-. To reduce this dispersion the local tuning is used to adjust the threshold value for each pixel independently using the TDAC register. The TDAC tune command performs a scan over a range of injected charges and calculates the threshold of each pixel. During the scan procedure if the threshold of the pixel is recorded lower than the target value, the TDAC is increased by one defined step. In contrast, if the threshold of the pixel is recorded higher than the target value, the TDAC is decreased by one defined step. This procedure does not change the mean value of the threshold achieved by the GDAC and minimizes the threshold dispersion down to 60 e^-.

A successful tuning of the threshold is achieved by producing a narrow and symmetrical distribution of the threshold around the target value as shown in Figure 7.6.

Time over Threshold

Once a threshold is set, a ToT to charge tuning has to be performed to adjust the ToT value response to a certain amount of charge. Usually it aims to match the most probable value of ToT and the expected charge deposited by MIP in the sensor. This approach minimizes the risk of overflow and results in an intensional ToT distribution. For example, in 100 μm thick sensors, a MIP is expected to produce about 8000 electrons, so this charge should correspond of about the center of the ToT distribution between 0 and 13.

The tuning algorithm for the ToT operates in a similar way as for the threshold. The global ToT setting is adjusted by the *PrmpVbpf* register which controls the feedback current responsible for the discharge speed of an incoming signal of the preamplifier of each pixel. The local setting for the ToT is adjusted by the FDAC register, which configures the feedback current of all pixels. The adjustment of the local ToT register is done via the FDAC tune scan command. It probes all possible FDAC values for all pixels and choses the value resulting in the best fit to the required ToT response. Lower FDAC parameters correspond to lower feedback currents and thus longer discharge times and higher ToT. If an injected charge signal is shared exactly between two pixel cells, the ToT value theoretically lowers to half correspondingly. Therefore, the ToT is used to derive the deposited charge

The ToT response of each pixel on a certain amount of the injected charge is shown in Figure 7.6. A good tuning corresponds to the narrow ToT code distribution around the target value.

Usually, after the finishing of the ToT tuning the threshold fine tuning has to be run for a second time, because the threshold is being altered by the change in ToT. If needed, the TDAC and FDAC tunes can be performed until results are satisfactory.

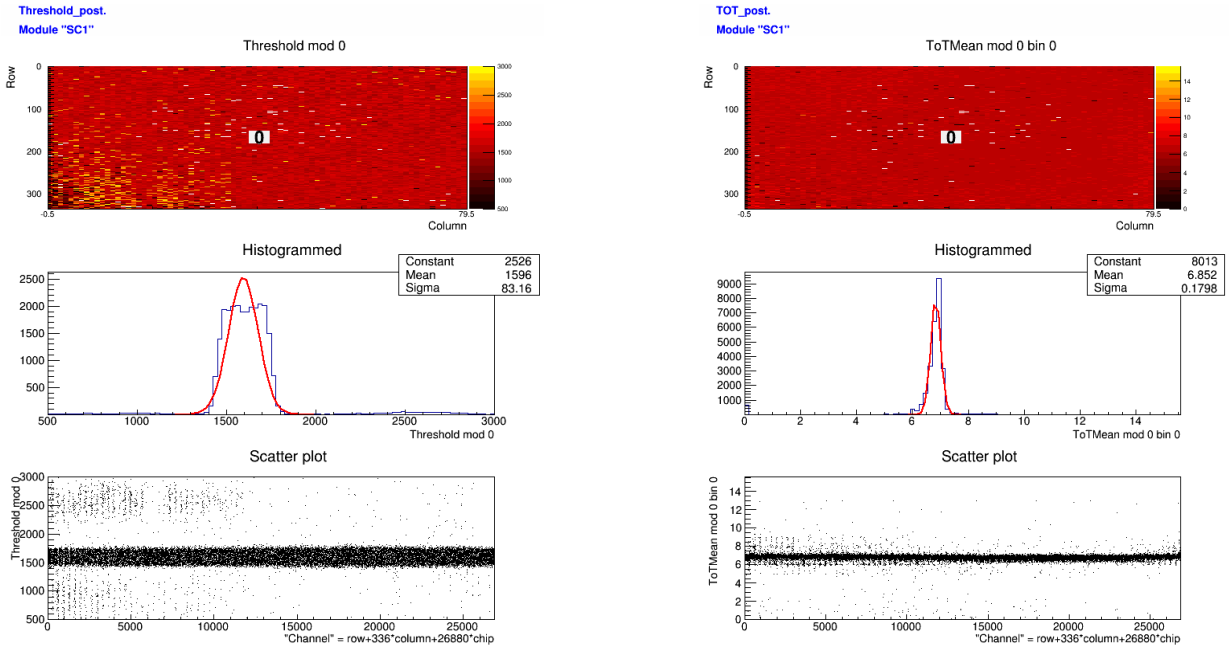

Figure 7.6 - Threshold scan (left) and ToT scan (right). The top part shows the analysed value in a colour-coded pixel map. In the middle the values for all pixels are histogramed and the bottom figure shows a scatter plot, which contains the value against an identification number defined by channel=row+336*column+26880*chip.

7.2 Usage possibility of RD53 chip to monitor effective radiation damage

The new generation of the readout chip for the ITk upgrade will be exposed to large radiation dose during operation. It will cause the radiation damage and detector performance degradation. To maintain performance at high level the operation conditions and configuration of the chip has to be changed with the radiation dose. It will be useful to have a possibility for monitoring radiation damage in the chip to compensate the loss of performance and to estimate the radiation dose. For example, the threshold and ToT tunings can be adjusted during the operation time to be more effective in particle detection.

7.2.1 RD53 CERN collaboration

The RD53 CERN collaboration is arranged to design the next generation of hybrid pixel readout chips, needed for the High Luminosity LHC upgrades of ATLAS and CMS detectors. The collaboration consists of 24 institutes from Europe and USA and more than 100 members. The work of the scientists specifically is focused on the development of the pixel readout chip capable to effectively operate in the high event rate conditions and under harsh radiation levels expected in ATLAS and CMS detectors after LHC Phase II upgrade. The RD53 collaboration activity will be based on the following aspects:

- Radiation qualification and characterization of 65nm technology to very high radiation levels;

- Development of tools and methodologies to design efficiently large, complex pixel chips;
- Development and characterization of circuits and building blocks needed for pixel chips [126].

The current LHC experiments are primarily based on a 250 nm CMOS technology and on-going developments for Phase I upgrades have to a large extent moved to a 130 nm technology. The 65 nm CMOS technology node has been identified as a particular promising technology for long term Phase II developments [126]. Tolerance to the high radiation level is one of the prime drivers, but the 65 nm technology must meet several other specific requirements:

- Appropriate for highly integrated mixed analog/digital signal designs;
- Sufficient circuit density for both analog and digital functions;
- Low power consumption;
- Well defined and well supported design kit for complex modern technology;
- Flexible access by the HEP community;
- Affordable for small prototype circuits and for the very large final pixel chips;
- Long term availability from multiple vendors, as the qualification, design, prototyping, testing, and final production will stretch over a relatively long period of 5-10 years.

Such a large and complex chip should be fabricated with a minimum number of design iterations given the high cost of such production.

7.2.2 RD53A chip specifications

The RD53A chip is intended to demonstrate in a large format IC the suitability of the chosen 65 nm CMOS technology for HL-LHC upgrades of ATLAS and CMS, including radiation tolerance, stable low threshold operation, and high hit and trigger rate capabilities. RD53A is not intended to be a final production IC for use by the experiments, and will contain design variations for testing purposes, making the pixel matrix non-uniform as shown in Figure 7.7 [127]. The chip size is 20.0 mm by 11.6 mm, for cost reasons it has been made half height of final pixel.

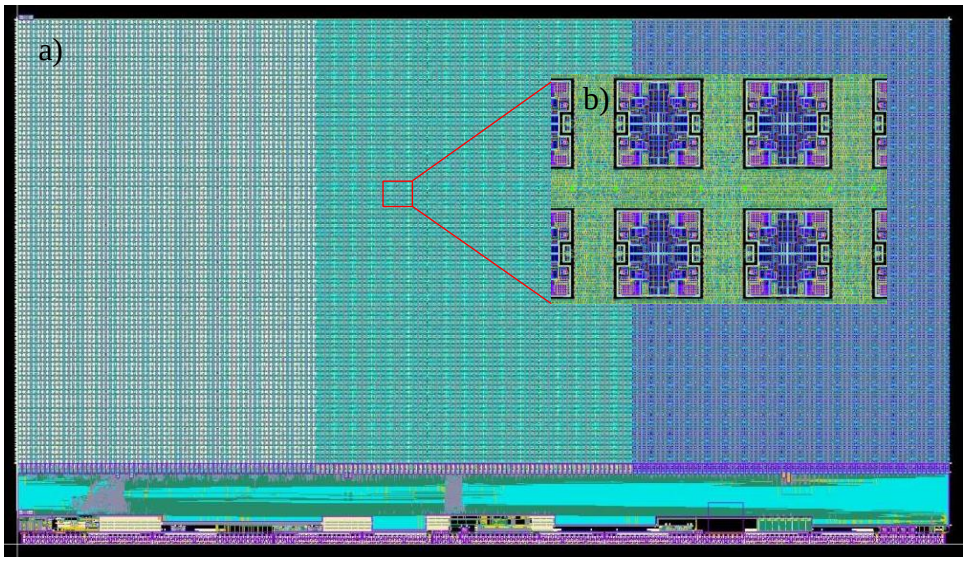

Figure 7.7 - a) Layout of RD53A demonstrator pixel chip. The inclusions of 3 different analogue front-ends are visible as slight colour differences between the 3 parts of the pixel array. b) Layout of analog island concept.

RD53A integrated circuit is a prototype developed by the BONN group for further testing in order to improve and develop the future RD53B prototype. It is a prototype that has flexibility for different measurements and tests. RD53A single chip card presented in Figure 6.5.

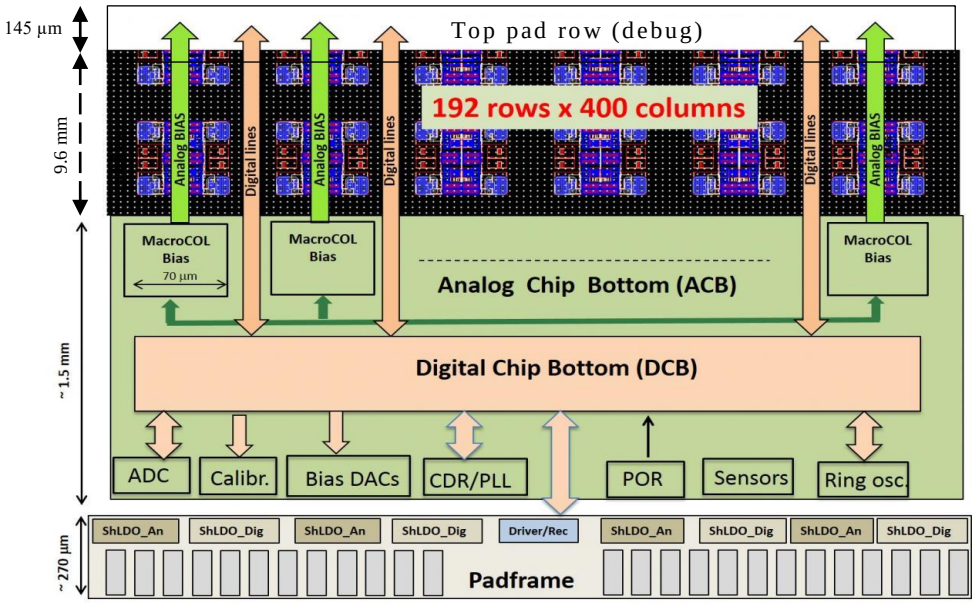

Figure 7.8 - RD53A floorplan Functional overview of RD53A pixel chip.

In Figure 7.8 the layout and functional view of RD53A floorplan are shown. The sensitive area of the chip is placed at the top of the chip and is arranged as a matrix of 192 x 400 pixels of 50 µm x 50 µm. At the top is a row of test pads for debugging purposes, which should be removed in a production chip. The peripheral circuitry is placed at the bottom of the chip and contains all global analog and digital circuitry needed to bias, configure, monitor and readout the chip. The wire bonding pads are organized as a single row at the bottom chip edge and are separated from the first row of bumps by 1.7 mm in order to allow for wire bonding after sensor flip-chip.

The pixel matrix is built up of 8 by 8 pixel cores. The 64 front ends within a core are placed as 16 so-called analog islands with 4 fronts-ends each, which are embedded in a flat digital synthesized “sea” as shown in Figure 7.7(b). Prototype tests have shown that, within the digital/analog isolation scheme used, this approach does not introduce any visible systematic differences between islands [127].

Parameter	Typ.	Max.
Core direct supply voltage	1.2 V	1.32 V
ShuLDO input voltage	1.5 V	2.0 V
Per pixel analog current	4 µA	8 µA
Per pixel digital current	4 µA	6 µA
RD53A Periphery analog current	30 mA	60 mA
RD53A Periphery digital current	30 mA	60 mA
Output drivers (each)	20 mA	30 mA
Total RD53A current (4 outputs)	0.7 A	1.3 A

Table 7.1 : RD53A power supply limits

For single supply serial powered operation RD53A is designed with connections from the bottom of chip only. However, because it is a prototype that must have flexibility for a variety of measurements, it is also be possible to power the chip by directly supplying the internal rail voltages, bypassing the regulation. The chip includes two internal voltage rails for powering the chip core, analog (VDDA) and digital (VDDD). Table 7.1 gives the power supply limits.

RD53A chip contains three different front end (FE) designs as shown in the Figure 7.9. This allows detailed performance comparisons for each type of front end called Differential, Linear and Synchronous. These are not small variants of one common design, but substantially different ground-up designs [127].

The Differential front end is a pure analog circuit. It contains no memory latches, flip-flops or counters. Static configuration values are provided by the digital core, which receives only the comparator out signal from the analog part. The ADC function is implemented entirely in the digital core by digitizing the Time-over-Threshold (ToT) of the comparator pulse. The Differential front end uses a differential gain stage in front of the discriminator and implements a threshold by unbalancing the two branches. The global threshold is adjustable through two distributed voltages (VTH1 and VTH2) which introduce an offset between the two branches of the pre-comparator. Differential threshold circuit is optimized for low threshold and low noise operation.

The Linear front end has classical FE architecture: linear pulse amplification in front of the lower power discriminator, which compares the pulse to a threshold voltage. It has a single amplification stage for minimum power consumption. The readout chain includes a charge sensitive amplifier (CSA) featuring a Krummenacher feedback complying with the expected large leakage current after irradiation. The signal from the CSA is fed to a high-speed, low power current comparator that, combined with the ToT counter, is exploited for time-to-digital conversion.

The Synchronous front end features a single stage CSA with a Krummenacher feedback AC coupled to a synchronous discriminator composed of a Differential Amplifier (DA) and a positive feedback latch. Due to transistor mismatch effects, considerably relevant in deep submicron technologies like 65nm, the output baseline of the first stage is subject to quite large fluctuations (tens of mV) between different channels. Usually to handle with these mismatches, which results in an offset of the DA output voltage between pixels, the digital-to-analog converter (DAC) trimming is used. But in the Synchronous FE to compensate offsets a baseline "auto-zeroing" mechanism is implemented. This requires acquisition of a baseline every 100 μs or less. The baseline acquisition takes 100 ns and is intended to take place during LHC abort gaps. During collisions, the difference signal (signal minus stored baseline) is fed into the positive feedback latch, which performs the comparison and generates the discriminator output. This stage has been designed to minimize mismatch effects causing a dynamic offset resulting in additional threshold dispersion. The efficient self-calibration can be performed according to online machine operations. Furthermore, the latch can be turned into a local oscillator up to 800 MHz using an asynchronous logic feedback loop, and so used to perform a fast ToT counting.

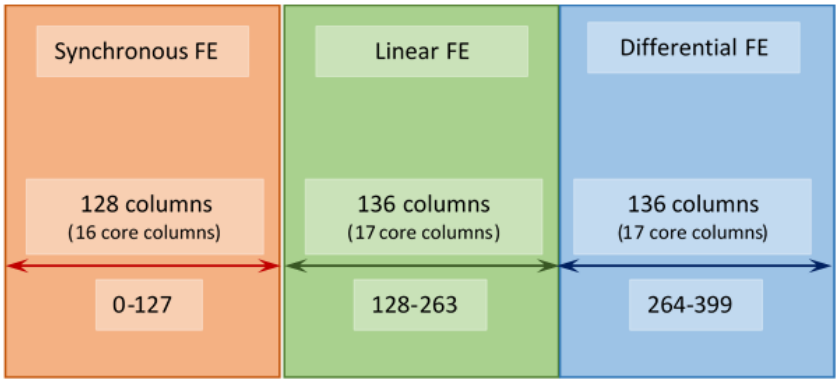

Figure 7.9 - Arrangement of front end flavors in RD53A. The pixel column number range of each flavor is shown.

The RD53A chip is fully controlled with a single serial input stream. All data, messages, and configuration read-back are output on a high speed serial port. This consists of 4 Current mode logic (CML) outputs sending encoded data at 1.28 Gbps nominal bandwidth. The encoding used is Aurora 64b/66b. All clocks needed for operation are derived from the 160 Mbps input [128].

All output that is not hit data looks to the user as readback of a random access memory with 16-bit content and 10-bit extended address space. This content includes configuration data, monitoring values, errors and warnings, and test structures. All information types use the same format of 10-bit extended address plus 16-bit value, collectively known as global registers. All registers are synthesized in the digital bottom of chip. The implementation of the registers varies according to their function. There are different register implementations [128]:

- Global Configuration (R/W)
- Pixel Configuration Portal (R/W)
- Diagnostic Counters (R/W)
- Ring Oscillator Counters (R-only)
- Monitoring ADC (R-only)
- SEU-soft Dummy Registers (R/W)

7.2.3 Ring oscillators

Ring oscillator is a device which comprises an odd number of inverters (NOT gates) located in a ring. Typical ring oscillator scheme are shown in Figure 7.10. Output of inverters oscillates between two voltage levels, representing true and false. Inverters are attached in a chain and the output of the last inverter is fed back into the first. Ring oscillator contains the multiplexer that selects mode of work. There are three modes: clocked mode, blocked mode or free-run mode, which are activated by using pulse.

For radiation testing RD53A chip contains eight different ring oscillators. The ring oscillators are located near the bottom right corner of the chip bottom, between wire bond pads 197 and 198. Each ring oscillators is built with using a different logic cell for testing to choose better flavor for the next versions of RD53 chip.

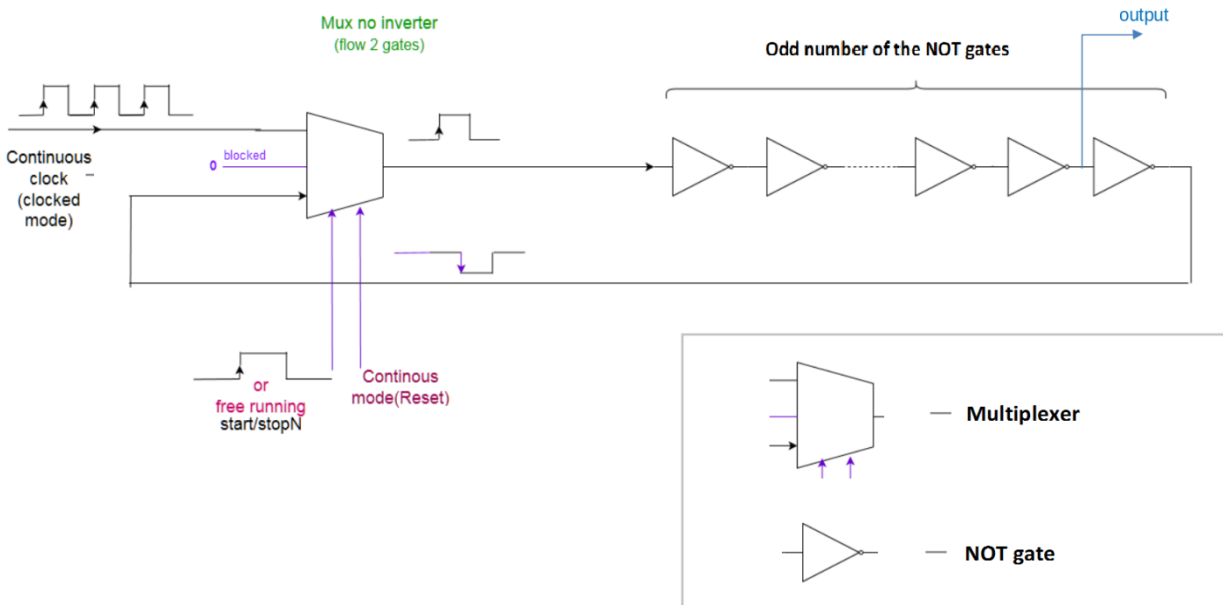

Figure 7.10 – Ring oscillator scheme.

Table 7.2 shows ring oscillator flavors and the length (in number of gates) for each type of ring oscillator. The number of gates in each ring was chosen to have a simulated frequency close to 1 GHz before irradiation at 1.2 V *VDDD*.

Address	Ring oscillator flavor	Length (number of gates)
110	strength 0 inv. clock driver	55
111	strength 4 inv. clock driver	51
112	strength 0 inv.	55
113	strength 4 inv.	51
114	strength 0 4-input NAND	19
115	strength 4 4-input NAND	19
116	strength 0 4-input NOR	19
117	strength 4 4-input NOR	19

Table 7.2 : Ring oscillator flavors and lengths (in number of gates)

Each ring oscillator corresponds to a 16-bit read-only register consists of a 4-bit counter [F:C] which counts start/stop cycles (the counters will count while start/stop is high) and a 12-bit counter [B:0] which counts ring oscillator clock cycles (see Figure 7.11). The counters can be reset by writing to the corresponding register address.

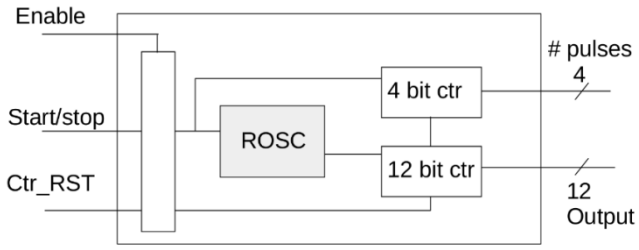

Figure 7.11 – Diagram of a ring oscillator block. There are 8 such blocks differing only in the number and type of the ring oscillator logic cells [128].

Since the ring oscillator frequency depends on voltage and temperature differently from radiation for each logic cell used, with suitable calibration the ring oscillators could be used to measure temperature and *VDDD* voltage as well as radiation [128]. The next section will show the results of measuring of such dependencies.

7.2.4 Laboratory tests of RD53A chip

To provide measurements with RD53A chip one need to use a special readout system. There are two most commonly used readout systems: YARR [129] and BDAQ53 readout boards. Both of them are available and used for RD53A testing in the lab.

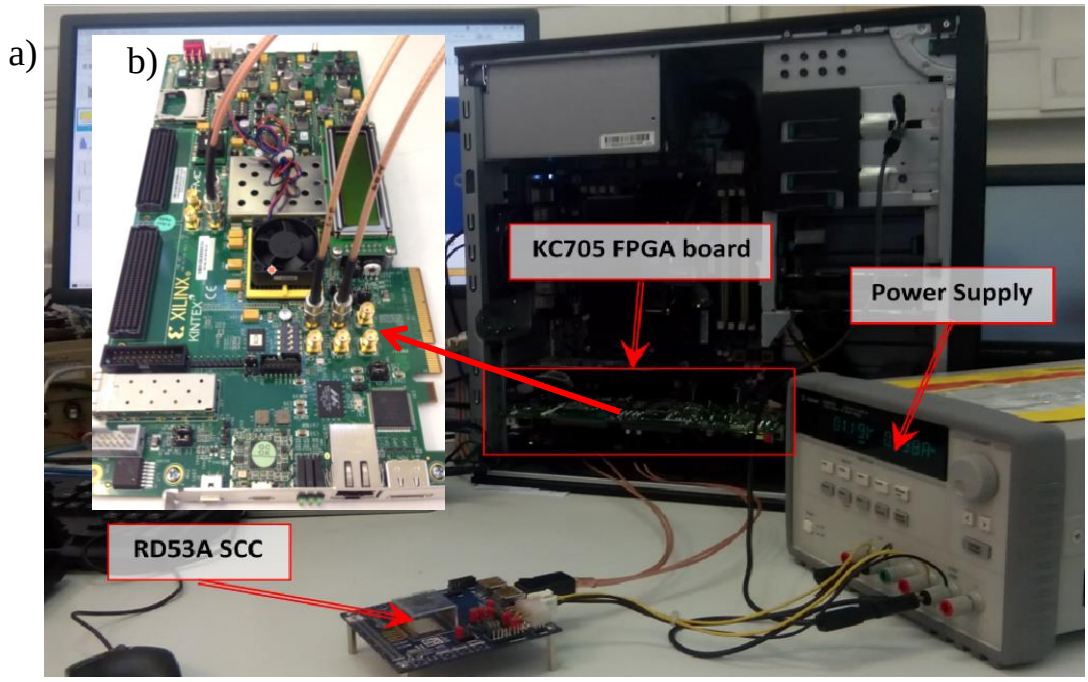

Figure 7.12 – a) BDAQ + RD53A SCC (Single Chip Card) system at LAL; b) KC705 FPGA board for data taking.

The Yet Another Rapid Readout (YARR) system, developed by LBL Berkeley Lab, is a DAQ system designed for the readout of current generation ATLAS Pixel FE-I4 and next generation chip which is currently being developed by the RD53 collaboration. A new generation of YARR system has increased from 160 Mbps to 5 Gbps bandwidth, achievable by using a new PCIe bus card with a faster FPGA, Xilinx Series 7.

BDAQ53 readout system is developed by Si-Lab group from Bonn University. It is based on two platforms KC705 [130] and BDAQ53 + KX2 [131] (uses Mercury KX2 FPGA module). They are both equipped with Xilinx Kintex-7 FPGA. The BDAQ53 is intended as a lab test system for desk-characterization, irradiation and test beam setups and other supervised measurements of RD53A bare chips as well as flip-chipped modules. The software part of the readout system is written in Python and is based on the open source data acquisition and system testing modular framework Basil [132].The software contains specific methods to read and write to the RD53A configuration registers and routines to process and store the received data. The Python scripts can be easily understandable and modifiable for various chip tunings and scans.

The BDAQ readout system which is installed in our lab and we used for the tests, results of which are presented in this section, is composed of: FPGA KC705 board, DisplayPort-SMA adapter (has to be used to interface the RD53A SCC to the readout boards, which don't support direct connection via DisplayPort), PC with CentOS operating system, communicated with readout board via 1 Gb Ethernet interface.

7.2.4.1 Ring oscillator frequency measurements

This section demonstrates the results of testing the ring oscillator contained in RD53A chip. As was mention in the description of ring oscillators, there is a register which contains the number of start/stop pulses. In principle, by knowing the number of counts and pulse duration one can calculate ring oscillator frequency. For the frequency measurements the python script was successfully written. This script gives possibility to enable ring oscillator, reset using the global pulse signal, and data taking from each counter. Global pulse signal can be sent with different duration, the possible pulse duration values: *6.4, 12.8, 25.6, 51.2, 102.4, 204.8, 409.6, 819.2, 1638.4* and *3276.8 ns*.

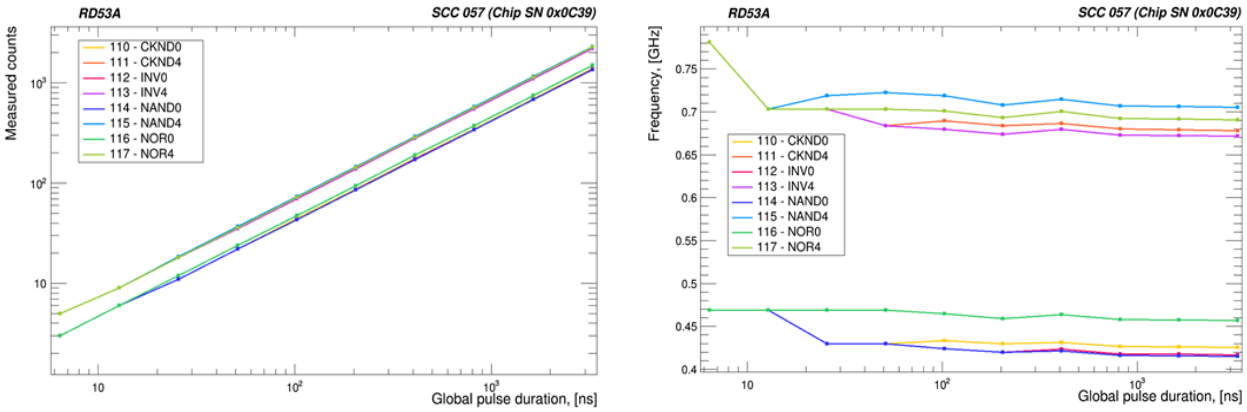

Figure 7.13 – RD53A ring oscillator linearity. Number of counts *vs* global pulse duration (left). Frequency *vs* global pulse duration (right).

The typical output of the script execution is a number of counts for each ring oscillator flavor depending on the global pulse duration. The plot of the output is shown in the Figure 7.13. From the results we can observe a good enough linearity starting from the pulse duration of *204.8* ns. For the smaller durations the number of counts in the ring oscillator is very small, so we are going to have a large uncertainty without good statistics. So, as expected, we can observe a stable ring oscillator frequency that for the global pulse duration > *200 ns.*

The ring oscillator frequency depends on chip powering voltage, temperature and radiation dose for each ring oscillator flavor differently. Measurements of these dependencies are presented in the next section.

7.2.4.2 Measurement of the voltage and temperature dependencies

For the voltage dependence measurements the direct chip powering mode was used. The observed behavior was linear as expected (see Figure 7.14).

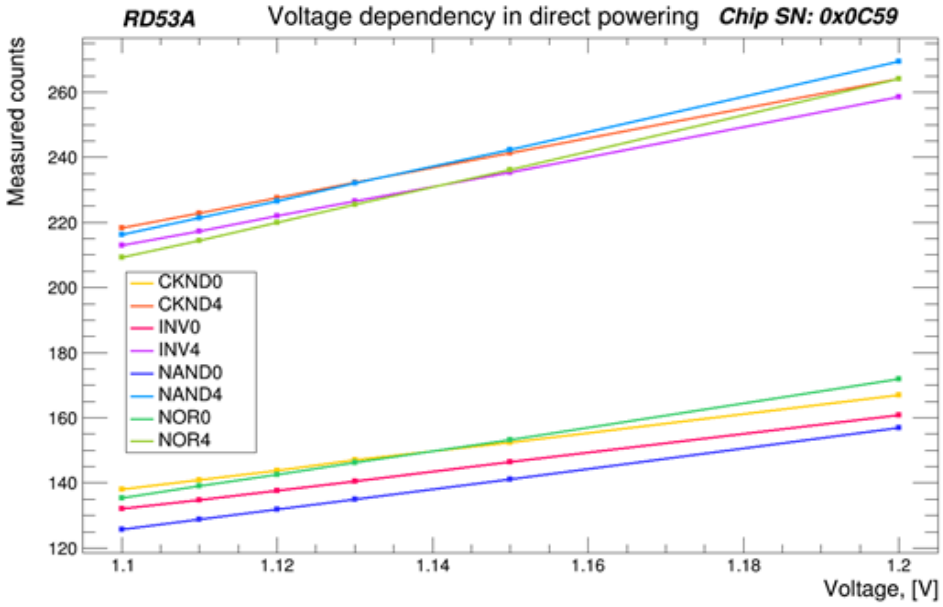

Figure 7.14 – RD53A ring oscillator voltage dependence

For the temperature dependence measurements the climatic chamber (Heraeus HT4020, located in CERN) was used. To change temperature we put the climate chamber T^{o}C set point, but the actual temperature of the chip differs from the ambience, because of chip heating during the operation.

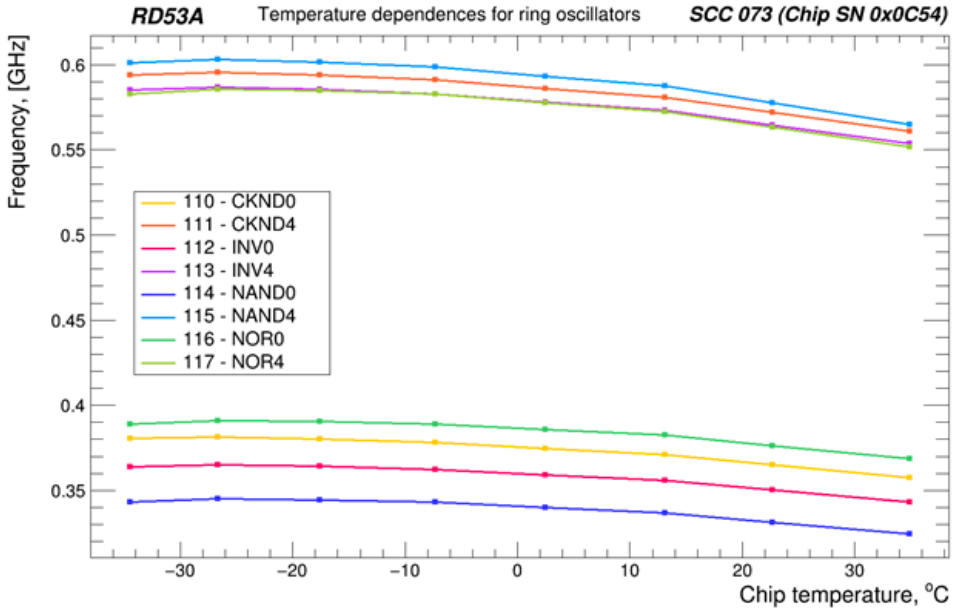

Figure 7.15 – The ring oscillators Frequency vs Temperature. The temperature was measured on the chip surface. In the climate chamber the temperature was changed from -40 to 30 ^{o}C.

The temperature logging was done by using a simple thermometer probe connected directly to the chip bottom. A typical difference between the temperatures was about (3 - 8) ^{o}C. Corresponding temperature dependencies for the ring oscillator are shown in the Figure 7.15.

The observed temperature dependence in the range from -40 to +30 ^{o}C is not quite linear, but as expected, we can observe a decreasing of the oscillator frequency with increasing of temperature. It can be concluded that after performing the preliminary calibration, it is possible to use the ring oscillator to evaluate the temperature of the chip.

7.2.4.3 Irradiation test

The irradiation testing campaigns were done at CERN using Precision X-Ray machine X-RAD iR160 (at ATLAS Pixel group). The machine is composed of an irradiation chamber, a control panel display, a HV system and a cooling box (Figure 7.16).

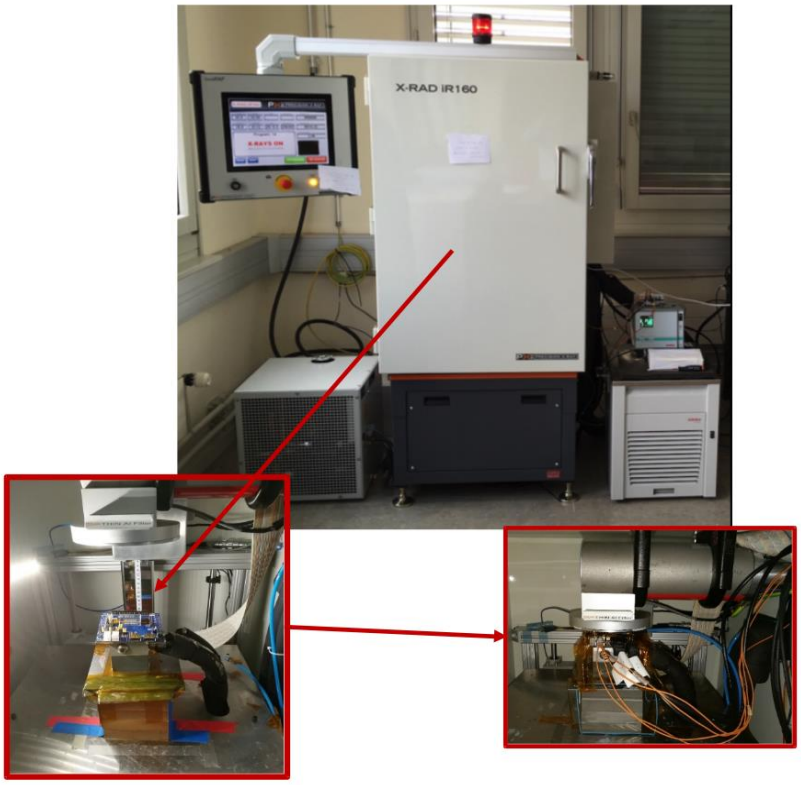

Figure 7.16 – X-RAD iR160 machine for cell irradiation and biological research.

The irradiator is calibrated with a silicon sensor up to a dose rate of 3.75 Mrad/h at a minimum distance to the source of 10 cm. This allows the study of irradiation effects on pixel detectors, imitating as much as possible the variable, low dose irradiation over long periods of time of the ATLAS experiment. The chips can be placed inside the machine at different heights and exposed to different dose rates using a formula: $D(x[\mathrm{cm}]) = \frac{375}{x[\mathrm{cm}]^2}[\frac{\mathrm{MRad}}{\mathrm{h}}]$. Beam energy is within range: 15 - 160 keV [133].

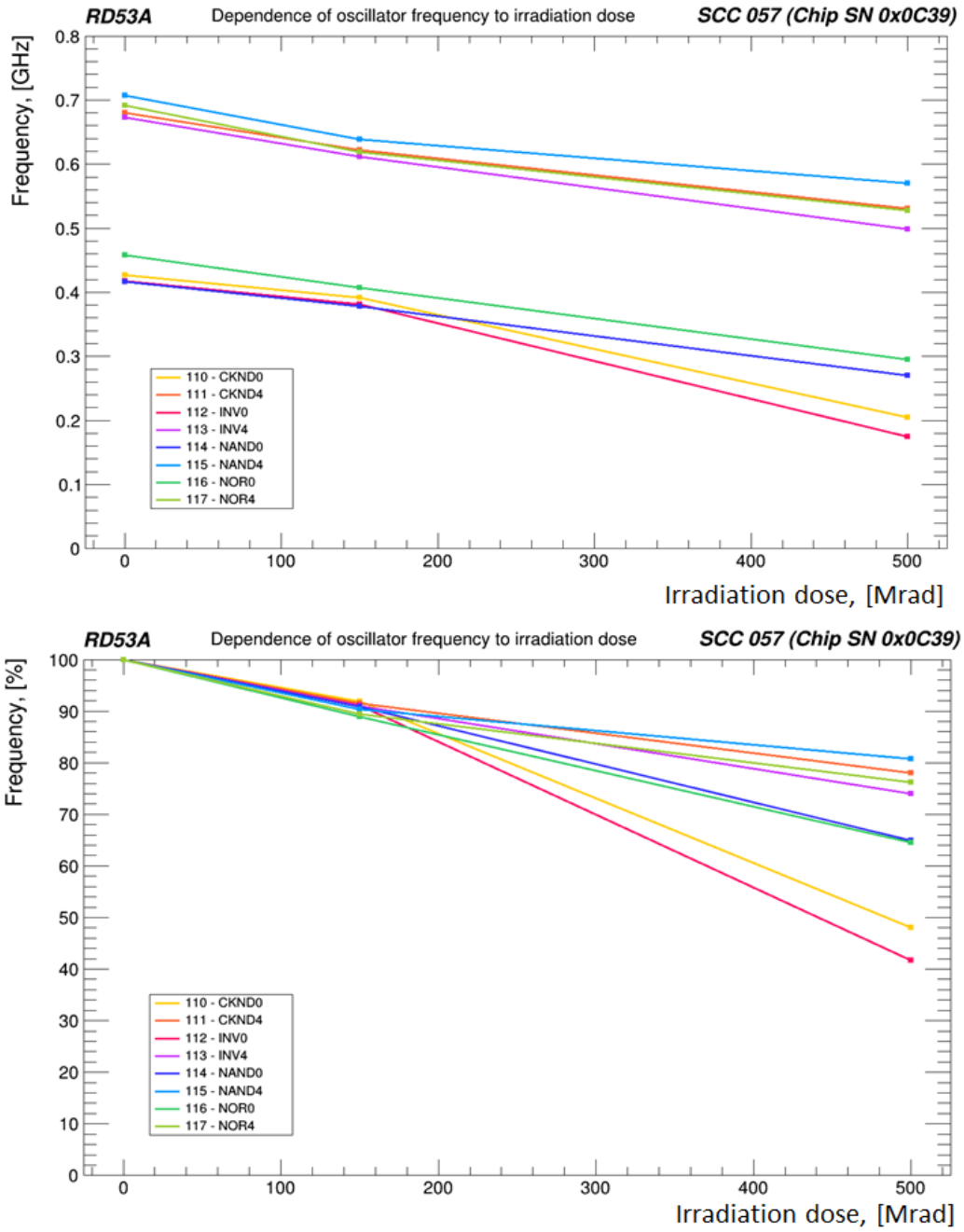

Figure 7.17 – Dependence of the ring oscillator frequency on irradiation in absolute units of frequency [GHz] (top) and relative units [%] (bottom). For 100 % - the frequency is taken before irradiation.

The tests aimed to measure the dependence of the ring oscillator frequency on irradiation dose in the range up to 500 Mrad, the minimum total dose the RD53A chip was designed to be radiation tolerant.

The main goal of the first irradiation campaign was to test the radiation effects on a unbiased RD53A chip at room temperature, as these are the normal conditions when sensor testing.

During the irradiation the maximum achievable dose rate was about 3.9 Mrad/h. The chip was placed at a distance of around 10 - 11 cm and the beam was uniform inside an aperture of 37^{o}, so the whole RD53A chip was irradiated uniformly. The chip was unbiased (non-powered) and at the room temperature. The ring oscillator measurements (the chip was powered for this) were

taken at three points: before irradiation, at 150 Mrad and at 500 Mrad. The obtained dependence of the ring oscillator frequency on irradiation dose is shown in Figure 7.17.

We can observe the degradation of the ring oscillator performance by irradiation. The frequency decreased by 25 – 50 % depending on the ring oscillator cell configuration. During the tests the chip was powered with: *VDDD - 1.2 V, VDDA – (1.2 -1.3) V*. The global pulse length – *1.6 μs*

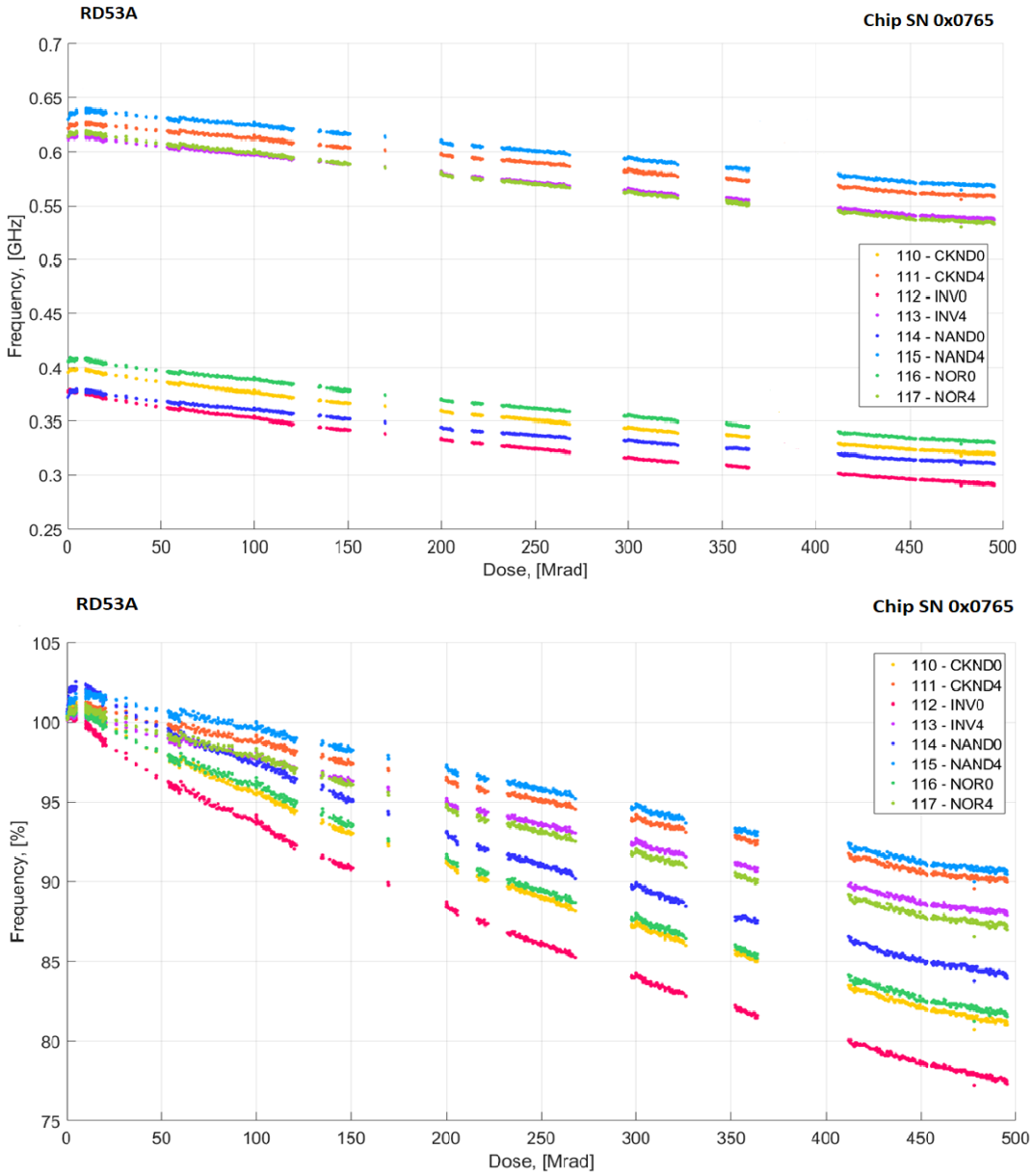

Figure 7.18 – Dependence of the ring oscillator frequency on irradiation in absolute units of frequency (top) and relative units (bottom). Chip was at -6 - 9 ^{o}C.

The first irradiation campaign was held for the preliminary testing to get a first feeling of the behavior of the chip after irradiation, whereas the second campaign was dedicated for detail tests. During the second campaign the measurements have been carried out while the chip was being irradiated in real time. Chip was cooled down up to - *6 – 9 ^{o}C* and was kept in this condition during measurements. The chip was powered during irradiation up to 500 Mrad with VDDD – *(1.13-1.15) V*. Measurement was done for 1.6 μs duration of the global pulse.

The result of the measurements is shown in Figure 7.18. Considering the results from both campaigns one can conclude that radiation effects are larger when irradiation is performed at room temperature. In the case when the chip was cooled down the degradation of the ring oscillator frequency at 500 Mrad was in the range from 10 to 25 % depending on the oscillator flavor. The dependence of frequency on radiation dose is quite linear. Applying a linear fit to the results a frequency reduction coefficient for all flavors of ring oscillators was obtained: 0.167 ± 0.015 [MHz/Mrad].

7.2.4.4 Annealing effect

After the end of irradiation, the chip was kept in the same condition i.e. powered and cooled down and data taking continued for few days to study the annealing effect (see section 4.4.1) for ring oscillators. The obtained results are shown in Figure 7.19.

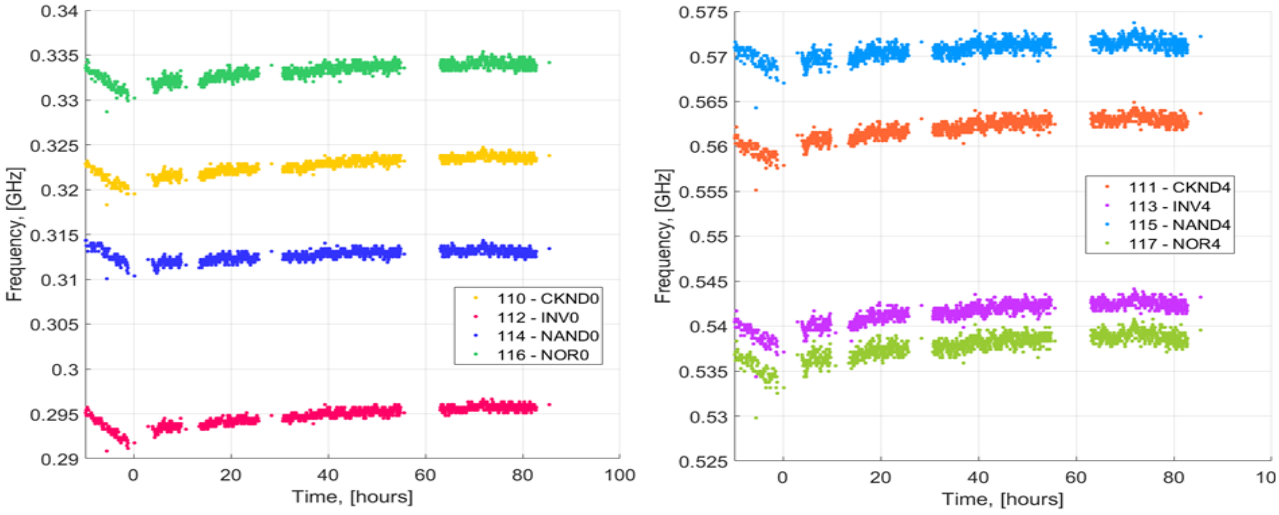

Figure 7.19 – Annealing effect for ring oscillators. Zero point corresponds to the finish of irradiation and start of annealing.

The properties of the silicon don't remain constant after irradiation, but start changing as a function of time and temperature. This is called annealing effect, it causes the restoration of the chip properties, so called beneficial annealing [134]. In case of ring oscillator the frequency increases, but it doesn't restore to the initial value. From the plots we can observe an increase in the frequency with time, but after a few tens of hours an effect of annealing is almost stopped and the frequency becomes stable.

7.3 Hit efficiency study of new 50×50 µm granular pixel generation

This section presents the results of the one of the very first test beam campaigns for characterization of non-irradiated and irradiated RD53A chip pixel modules. The presented results are obtained by the analysis of the data collected in a test beam setup at DESY facility with the beam crossing the module surface perpendicularly. The e^- particle beam with an energy of 4 GeV was used to characterize the hit efficiencies and the spatial resolution of the detector which is beyond the capabilities of the laboratory setup.

The hit efficiency of the detector is one of the most important parameters needed to design the reliable and highly performing tracking system. A low hit efficiency affects the precision of the track reconstruction and decrease overall particle detection efficiency. The key parameters causing the loss of efficiency of the pixel detectors are charge trapping and charge sharing among the neighbor pixels in the sensor. But not only sensor related parameters affect detector efficiency, also a threshold setting in the front-end chip has an influence. The performance of the analog and digital parts of the chip must be as high as possible, the threshold set value must be well known, low enough and uniform throughout the chip. If the value of threshold is out of the given range or cannot be well measured, the charge generated by particle crossing the sensor volume may not be registered, being below the threshold in one of the pixel cells, which may bias the hit position determination, and hence affects the track resolution.

The study in this section is mainly focused not on the analysis of the sensor performance as in the previous chapter, but on the RD53A chip design features. The hit efficiency and the spatial resolution are determined for the different RD53A front-end flavors and pixel cell size before and after irradiation.

7.3.1 Efficiency performance of non-irradiated modules

To compare the hit efficiency performance of the each of the RD53A analog front-end flavors (Synchronous, Linea and Differential as discussed in 7.2.2), the non-irradiated module with 100 µm thick sensor and 25×100 μm^2 pixel cell size was tested. The data was taken separately for each of the three analog parts of the chip. For each measurement the beam was directed to cover by the beam profile a particular part of the module surface. We can see the areas of the beam incidence on the sensor surface on the efficiency map shown in Figure 7.20. The threshold value has been tuned to be more or less the same value for the each front-end: Synchronous – 1100 e^-, Linear – 1060 e^- and Differential 1160 e^-.

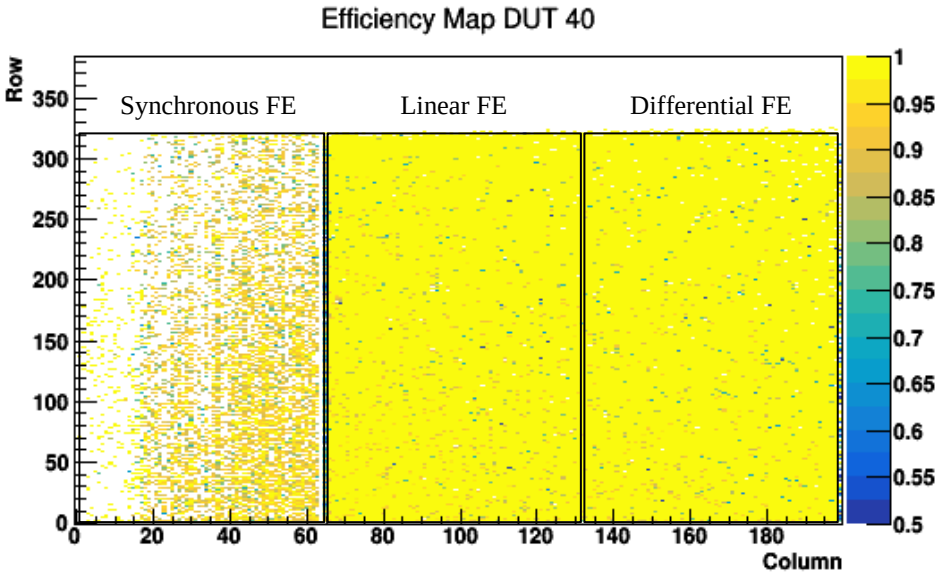

Figure 7.20 – The two dimensional map showing the efficiency values calculated for the pixel cells. The analog front-end parts of the RD53A chip are separated. The white pixels are masked pixels or not illuminated by the beam.

Using the reconstruction Eutelescope software and TBmon2 tool for the analysis the efficiencies have been calculated for each front-end independently. The 2D map with the hit efficiency value for each pixel is shown in Figure 7.20. At this stage of development the Synchronous FE is difficult to tune uniformly. Therefore many pixel cells, which are noisy at low threshold values, were masked before performing the measurement.

Also the hit efficiency as a function of the bias voltage is investigated for this module. For this reason the measurements were performed at different bias voltage points from 5 V to 25 V. The obtained results are plotted in Figure 7.21.

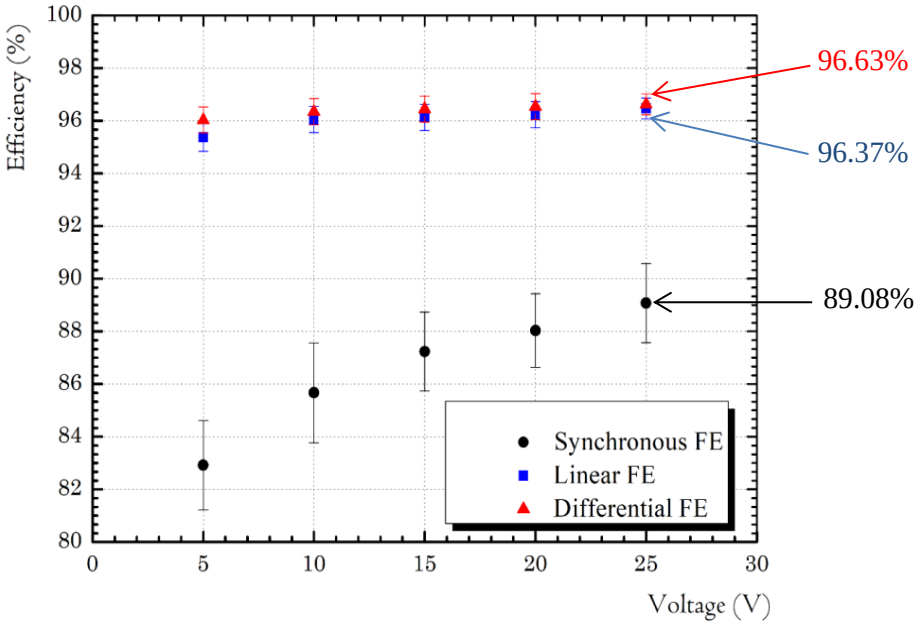

Figure 7.21 – Hit efficiencies of each FE flavor of RD53A chip as a function of bias voltage of a non-irradiated 100 µm thick sensor with 25×100 µm^2 pixel cell.

Over all hit efficiencies obtained for the linear and differential FE are about 96 % at 25 V and compatible with ITK requirements. The synchronous FE shows about 10 % lower over-all efficiency value, partially due to higher than for other FE flavors pixel dead time and buffering overflow.

Also, to check the charge collected by the pixels with different analog part, the ToT value for the pixel clusters with matched hits are built depending on the applied bias voltage. These ToT distributions are plotted for the bias voltage points and are shown for 5 V, 15 V and 25 V in Figure 7.22. The collected charge is increased with voltage and repeats the shape of the Landau distribution. For the RD53A the ToT value cannot be tuned to a certain amount of charge by user and ToT tinning is done automatically depending on the threshold.

Investigating the cluster ToT distribution behavior for linear and differential FE, the latter has higher TOT value with the same tuned threshold. At higher voltages for the synchronous and differential FE in the ToT distribution the second peak appears. This behavior is subject for further investigation.

From the plot in Figure 7.21 the efficiency for the differential and linear FE saturates at about 10 V, for synchronous this value is higher. The plots in Figure 7.22 indicate the slowing down the increase in collected charge with voltage and saturation at about 20 V.

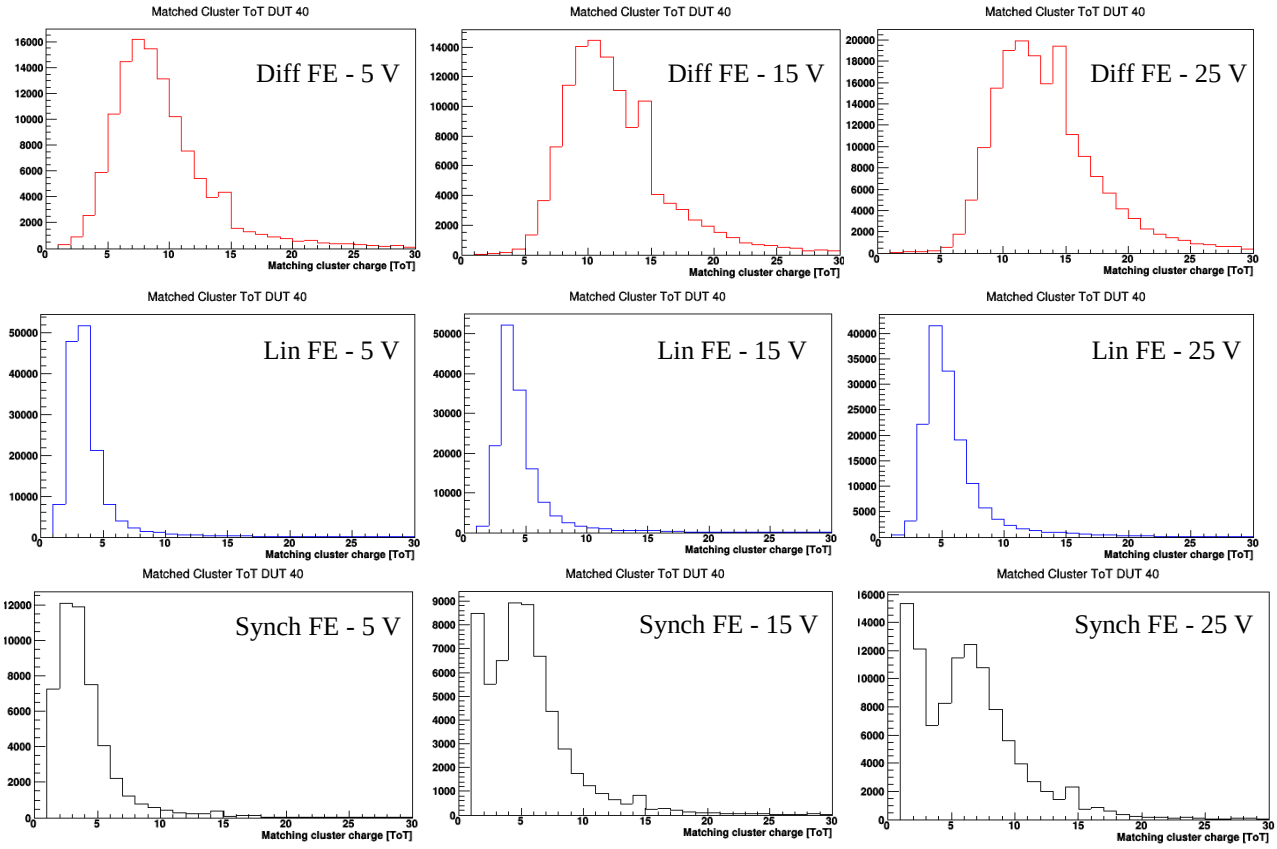

Figure 7.22 – The ToT distribution for clusters with matching tracks, calculated for each front-end flavor depending on a bias voltage.

7.3.2 Efficiency performance of irradiated modules

Two modules with 130 μm thick sensors have been irradiated CERN PS facility to 5×10^{15} n_{eq}/cm fluence, comparable to the expected at the HL-LHC. One module has a square pixel cell of 50×50 μm^2 and another has 25×100 μm^2 pixel geometry.

The modules are measured with a tuned threshold of 1250 e^- for Linear FE and Differential FE in module with 25×100 μm^2 pixel pitch and with a threshold of 1180 e^- for Linear FE for the module with 50×50 μm^2 sensor.

For these two different sensor geometries the spatial resolution has been obtained from the residual distribution. A residual is the difference between the crossing position measured in a certain plane and the reconstructed impact point of the closest fitted track associated to it. Due to the rectangular shape of the pixel cells the residuals are calculated separately in both directions according to the coordinate systems. Due to the uniform particle flux, for single pixel clusters the residual distributions are expected to be box shaped, with a smearing at the edges, given by the pointing resolution of the telescope. For clusters with higher pixel multiplicity the resolution is improved with the charge information and the distribution is expected to have a Gaussian shape.

The spatial resolution at DESY test beam facilities with a beam of electrons with a momentum of 4 GeV/c is much affected by the multiple scattering. In the track reconstruction process wider residuals are obtained and plotted in Figure 7.23. The smearing effect due to the multiple scattering is about 20 μm, which is larger than an intrinsic resolution of the simple pixel, which

is for 25 μm pixel side size about 7.2 μm. The value for the resolution obtained as a width of residual distribution is about 26 μm, considering very strict cutting parameters applied to diminish smearing in the resolution.

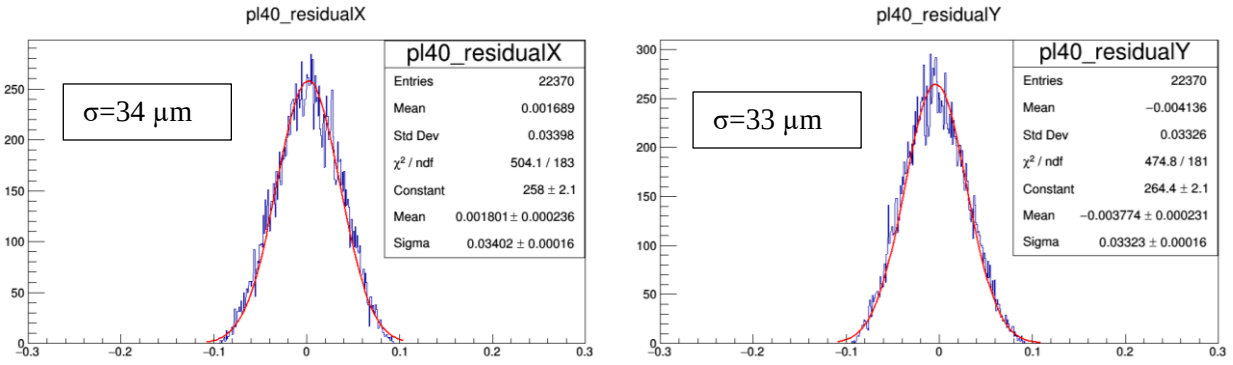

Figure 7.23 – Histograms show the residual distributions of a RD53A module with a 50×50 μm^2 pixel cell (left) in the X direction and (right) in the Y pixel direction.

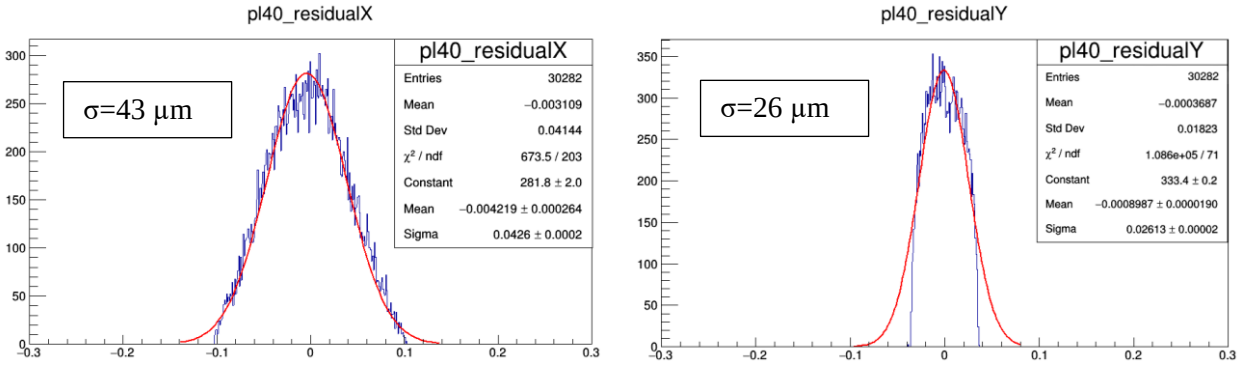

Figure 7.24 – Histograms show the residual distributions of a RD53A module with a 25×100vμm^2 pixel cell (left) in the long pixel side direction and (right) in the short pixel direction.

After irradiation, the hit efficiency is reduced due to the radiation damage. The trapped charge carriers decrease the hit efficiency given a higher probability for the signal to be below threshold. To recover the efficiency the sensor is biased to higher voltages. The modules during the measurements were kept in the cooling box with dry ice at the temperature about -40 ^{o}C. The global hit efficiency has been calculated for both modules at different bias voltage points. The comparison of these dependencies as a function of the bias voltage is summarized in Figure 7.25.

In the test beam the beam was directed to cover the differential and linear front-ends at once. The analysis has been done for each front-end separately. The synchronous part was not considered as it was difficult to tune after irradiation.

The differential FE shows about 3 % higher efficiency in comparison to the linear FE at the same threshold tuning. It also can be explained by the inhomogeneous irradiation profile provided by the CERN PS facility, the exact radiation fluence is lower for the periphery part of the module.

The hit efficiency saturates in between 400 V and 500 V. For the 25×100 μm^2 pixel geometry it shows within 0.3% uncertainty 98.3 % in the differential FE and 95 % in the linear part at 500 V.

The 50×50 μm^2 option has about 94.4 % of overall efficiency at the same voltage. The efficiency of 25×100 μm^2 pixel pitch shows about 1 % higher efficiency compared to the standard pixel cell, this can be related that the pixel cell is double the size along the long pixel direction and has a less effect of the biasing structure.

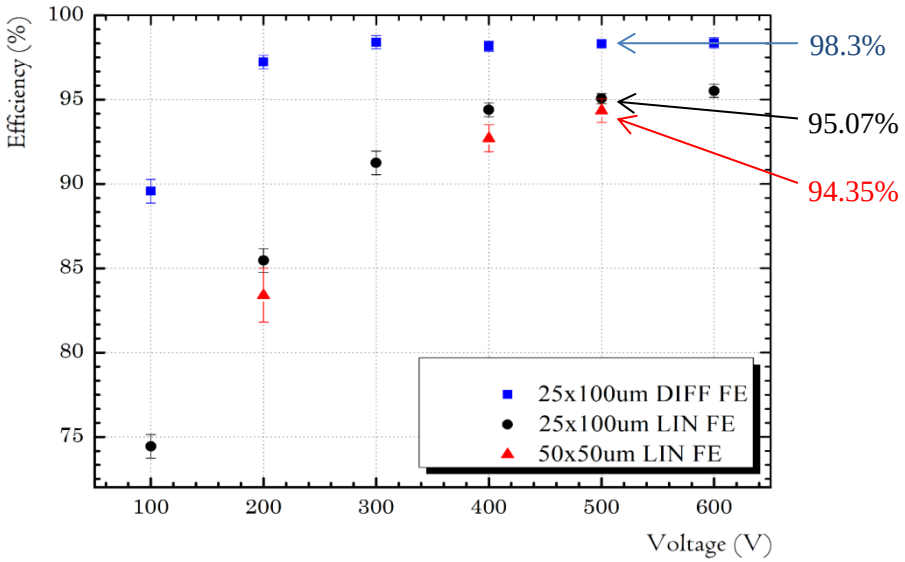

Figure 7.25 – A comparison between the hit efficiencies as a function of the bias voltage for the different front-end flavors and pixel cell geometry after irradiated to 5×10^{15} n_{eq} $cm^{-2.}$.

The Figure 7.26 shows the in-pixel efficiency map for the module employing 25×100 μm^2 pixel geometry. In the map 4-pixel cells are visualized. The hit efficiency is dependent on the collected charge. The loss of hit efficiency for the both geometry designs is due to the charge sharing between the neighbor pixels and the effect of bias voltage structure implemented in between pixel columns. This is mainly visible at the corners of a pixel cell where the charge is shared among the four adjacent pixels; at the long side of the pixel it is less noticeable, because the charge signal is shared only by two adjacent pixels. The same 4-pixel efficiency map was built for the module with 50×50 μm^2 pixel pitch sensor and is shown in Figure 7.27.

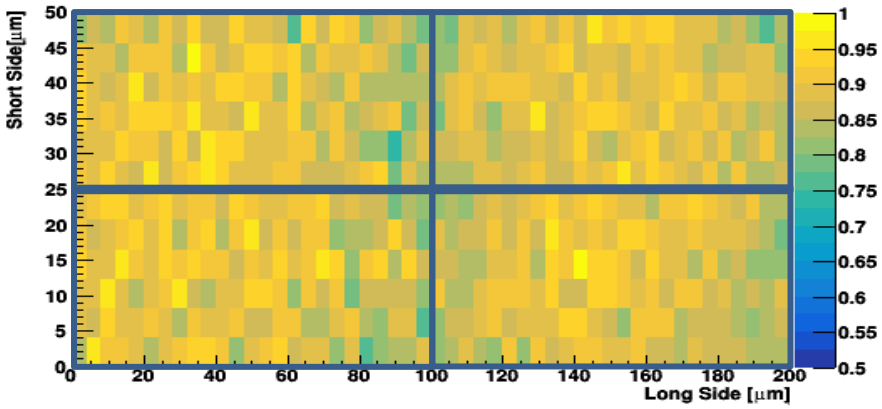

Figure 7.26 – In-pixel hit efficiency of 4 pixel cells of 25×100 μm^2 size at 500 V bias voltage after irradiation to a fluence of 5×10^{15} n_{eq} cm^{-2}.

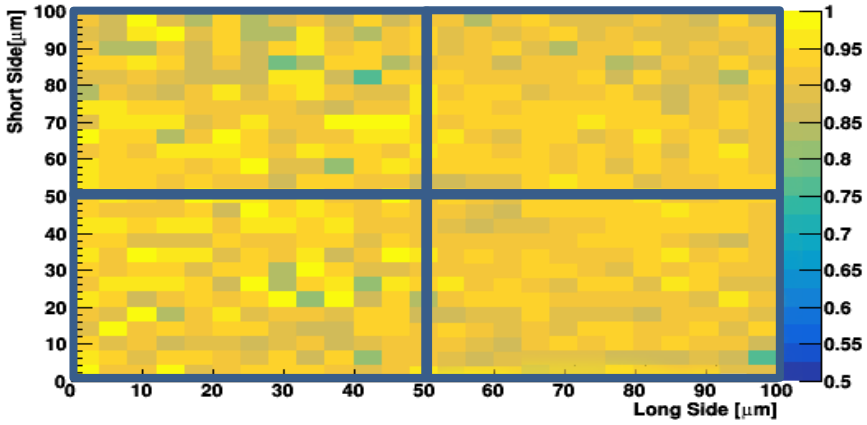

Figure 7.27– In-pixel hit efficiency of 4 pixel cells of 50×50 μm^2 size at 500 V bias voltage after irradiation to a fluence of 5×10^{15} n_{eq} cm^{-2}.

7.4 Conclusions

The RD53A laboratory tests were successfully done to study the behavior of the frequency of different ring oscillator flavors implemented in RD53A chip after irradiation. The obtained plots that show the decreasing of ring oscillator frequency demonstrate how much the digital transitions are slowed down by irradiation. It can help to evaluate how well the radiation models describe the degradation of performance, so that the digital design can be implemented in future with more robust cells.

The important point was to check the feasibility of using ring oscillators for monitoring the received radiation dose. And it looks possible with pre-calibration to employ ring oscillators as a radiation monitor and temperature sensor. Moreover by having different flavors of oscillators the measurements of dose and temperature can be refined to achieve high precision.

The results obtained were presented in RD53 collaboration. Using these results, one can compare the behavior of various ring oscillators with irradiation and choose the best of them for the next chip generations.

The hit efficiency measurements of the RD53A modules employing different sensor geometries 50×50 μm^2 and 25×100 μm^2 have been carried out using particle beams before and after irradiation to a fluence of 5×10^{15} n_{eq}cm^{-2}. The hit efficiencies of the pixel modules with different front-end analog flavors implemented in the chip were compared.

Chapter 8

Developing an accurate and robust tool for pixel module characterization

Contents

The presence of a compact, affordable and robust instrument for the characterization of the silicon pixel detectors is desirable, because it gives a possibility to test in situ pixel detectors before test beam. The test bench based on an infrared laser allows for high precision charge injection into the silicon pixel sensor. The position and area of the charge injection, as well as an amount of injected charge are well-known and can be adjusted with a high accuracy. With this tool it is possible to study the effects which appear at the edge of a pixel or the sensor edges. The laser pulse rate can be regulated and to be at high frequency up to 1 MHz, which allows to reach a large number of charge injections in a very short time.

During my thesis work the laser test bench setup based on an infrared laser has been built at LAL for performance studies of the silicon pixel detector prototypes. This chapter describes the principle of the testing method, the detailed scheme of the setup, the control software, the adjustment procedure and the results of the performed tests.

8.1 Motivation of the developing of a new tool for pixel module characterization

After the module assembly and wire-bonding the properties of the detector prototypes has to be tested prior to the detector large scale production and installation in the experiment. The first characterization of the pixel detectors can be done in the laboratory. The IV measurements and chip tunings, as described in section 7.1.1, have to be performed and then, as a final step, the characterization of the modules on a particle beam, it is so called source scan tests. The availability and accessibility of the relativistic particle beams used for the detector tests, discussed in the Chapter 6, is limited, because the beam time is shared between many different projects and research groups. The time slot for the beam using at the dedicated beam facilities has to be paid and agreed in advance. To be more flexible in the detector testing, there are several other options, which could be realized to characterize pixel detectors in conditions close to real working environment. For this purpose one needs to simulate the MIP interaction behavior in the silicon bulk, for the reason that the most of the particles created in the high energy particle collisions are MIPs and, moreover, it is the worst case in terms of the amount of generated charge in the sensor volume.

The relativistic particle beams produced at accelerators are typically used to characterize silicon pixel detectors. The size, momentum and other spatial and time information about the particle beam propagating through the detector under the test are well known. However it is not always convenient to use particle beams due to time constraints at test beam facilities. Also, the hit position, the space point where the particle crossed the detector, has to be reconstructed.

One of the possibilities is to use β-radioactive sources or cosmic rays. This method and the results obtained using the ^{90}Sr radioactive source will be discussed further in the section 8.5. But the energy of the β-spectrum is broad and low energy particle deposit more energy than MIPs along the trajectory. Furthermore the interaction point position cannot be determined. And, of course, the particle rate from the small laboratory radioactive source or cosmic rays is low and so the statistics is worse comparing to the accelerated particle beams.

Another method, which will be discussed in this section, is usage of a laser beam to generate a signal in the silicon sensor to mimic the MIP crossing. The laser allows for flexible charge injection with the well-known hit position and area, where the charge is injected, since the laser beam spot and its diameter are well defined. The injection depth is varied by the wavelength of the laser light and the amount of charge can be modified easily by variation of the laser pulse intensity using attenuators to reduce the laser output power. Since the repeatability of the pulses can be set to kHz or MHz frequency, it is possible to reach a large number of charge injections in a very short time.

Usually, for this purpose, infra-red lasers are used, due to the specific light interaction with silicon in this wavelength range. The photon energy of the laser beam with wavelength $\lambda = 1060$ nm is 1.17 eV, which is slightly above the energy gap of silicon at room temperature. It makes possible the photon absorption primarily due to a photoelectric effect. Thus, the ionization density is nearly uniform along the laser beam path through the sensor. The intensity of the light penetrating through silicon drops exponentially:

$$I = E_0 e^{-\frac{\kappa}{Z}} \tag{8.1}$$

where Z – the light penetration depth and κ is weakening coefficient, which depends on wavelength λ:

$$\kappa = \frac{\mu\lambda}{4\pi} \tag{8.2}$$

where μ is absorption coefficient in μm. Using (8.1) it is possible to find the penetration depth of the laser light. The Figure 8.1 shows the experimental dependence of the penetration depth on the photon wavelength in the visible and close infrared range for silicon.

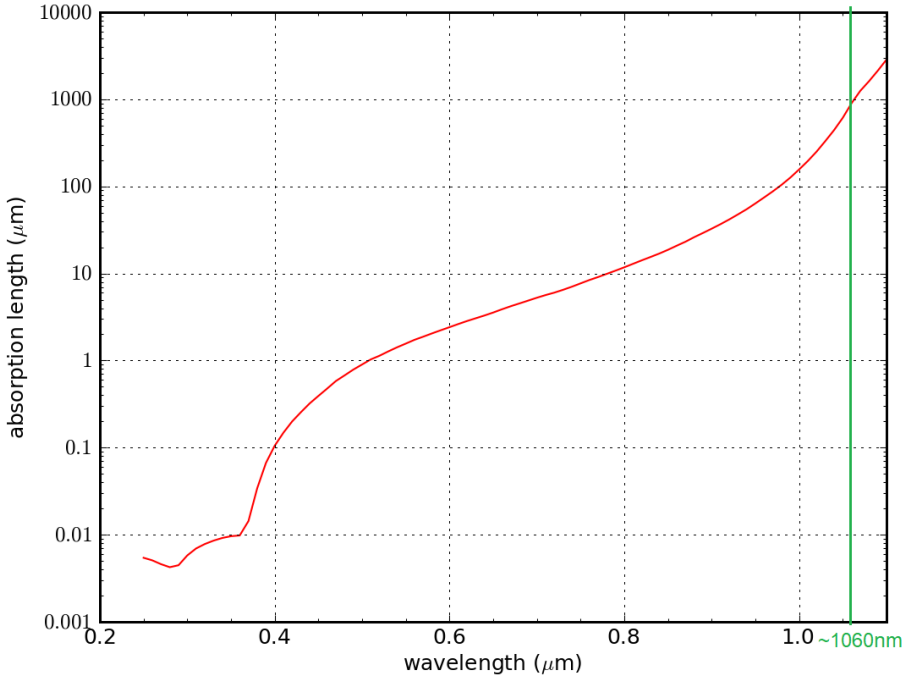

Figure 8.1 –The penetration depth in silicon versus the wavelength. [148]

The photon with a wavelength of 1060 nm can go about 850 μm in depth into the silicon material. This means that a pulse of the collimated laser light of this wavelength can easily traverse a 230 μm thick silicon sensor bulk, producing a column of uniformly distributed charge, which is actually simulates MIP charge generation.

The sensor production process involves aluminum layer deposition on a backside to create an electrical contact to provide the sensor biasing. The infrared light cannot penetrate the aluminum and about 95 % of the incident light reflects from its surface. For laser illumination to perform the tests, the rectangular openings on top of each pixel were designed. The picture of the sensor with openings arrangement is presented in Figure 8.2. The size of not covered pixel surface is 30 x 70 μm^2. The module used in the work described in this part of the thesis is the FE-I4 chip based. The pixel size is 50 x 250 μm^2.

Figure 8.2 – The sensor design with openings in backside metallization. The aluminum layer, which can prevent almost completely the infrared photons penetration through the bulk, is partially removed. Each pixel has a rectangular opening as shown on the left picture.

Such a table-top laser test bench setup would be of a great help in pixel detector characterization, complementary to the particle beam tests, described before in the Chapter 6. Using this tool it is possible to test pixel modules before going to beam tests, thanks to the high spatial precision, it would be feasible to study the effects, which appear at the edge of a pixel or at the edge of the whole sensor with high statistics and without secondary ionization. The focusing of the laser beam to the small spot size close to diffraction limits makes the system more challenging for realization. The effect of reflection from an aluminum surface and oxide-Si boundaries as well as the beam refraction makes it difficult to calculate precisely the amount and the position of injected charge. Moreover, the laser light interaction mechanism, as was discussed in section 4.1.2, is different from the particle interaction, and must be thoroughly studied to achieve the reliable information on the effects connected to this.

8.2 Laser test bench setup

During my thesis, the laser test bench setup has been developed in the clean room conditions, which are required during pixel detector characterization. This tool was designed and constructed to provide reliable and high precision laser scan measurements. The block diagram of the developed setup is sketched in Figure 8.3.

In the setup scheme, the laser pulse from a semiconductor laser is generated after receiving a trigger signal, provided by a function generator. The rise time of a laser pulse and an electrical pulse from a function generator is typically not more than 5 ns. Then the light is guided by single mode optical fibres. There is an optical splitter introduced into the system, which divide the optical power with a ratio of 25:75. One of the branches is used to lead the light to a focusing system, which need to target the laser beam on a pixel detector surface. And another branch contains optical power meter to monitor laser output power. The single chip card (SCC) with the pixel module under test is mounted on a rotation mechanical stage, which in turns is fixed on a high precision motorized X-Y table with a minimum motion step of 0.1 μm. The sensor of the detector under the test is biased using a high voltage power supply via LEMO cable. The module is powered by a low voltage power supply connected by Molex 8 power cable to the SCC. The

data readout is occured via RJ-45 cable which connected to the USBPix system, also powered by a low voltage supply. The USBPix readout system is triggered by TTL pulse, guided by coaxial cable and synchronized with function generator pulse, which initiates a laser beam generation. The whole setup is placed in a light tight box that provides a dark environment for the tests performing, as external photons increase the noise signal in the sensor. The temperature and humidity are monitored in the box.

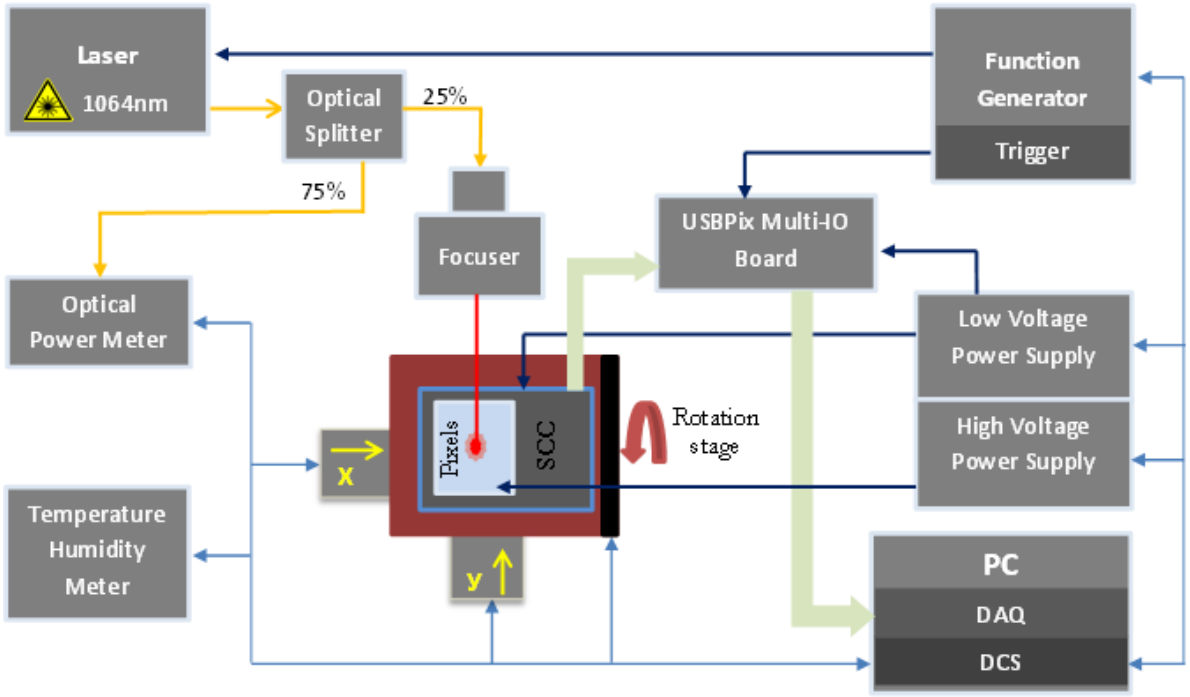

Figure 8.3 – A schematic illustration of the developed laser test setup.

The measured data are collected by USBPix system and then transferred via USB to a PC. The setup is controlled via GPIB and USB interface by a PC with the LabVIEW software developed for this system. The software will be discussed in the section 8.3.

8.2.1 The mechanics

To make accurate measurements by given laser test bench possible, a special attention was paid to the development of the mechanical part of the setup. The black box, a patch panel and mechanical supports have been designed and partially manufactured at LAL.

The whole setup is shown in Figure 8.4. It consists of dedicated devices, discussed in the previous section, which are arranged in the rack and the mechanical moving tables, supports as well as the optical focusing system, enclosed in the black box. The cable and optical fiber connections are realized through the wall mounted patch panel. The patch panel contains all needed connectors for controlling, electrical and optical signal transmission and data acquisition, as well as spare connections, especially for the optical fibers, which may get dirty, introducing attenuation.

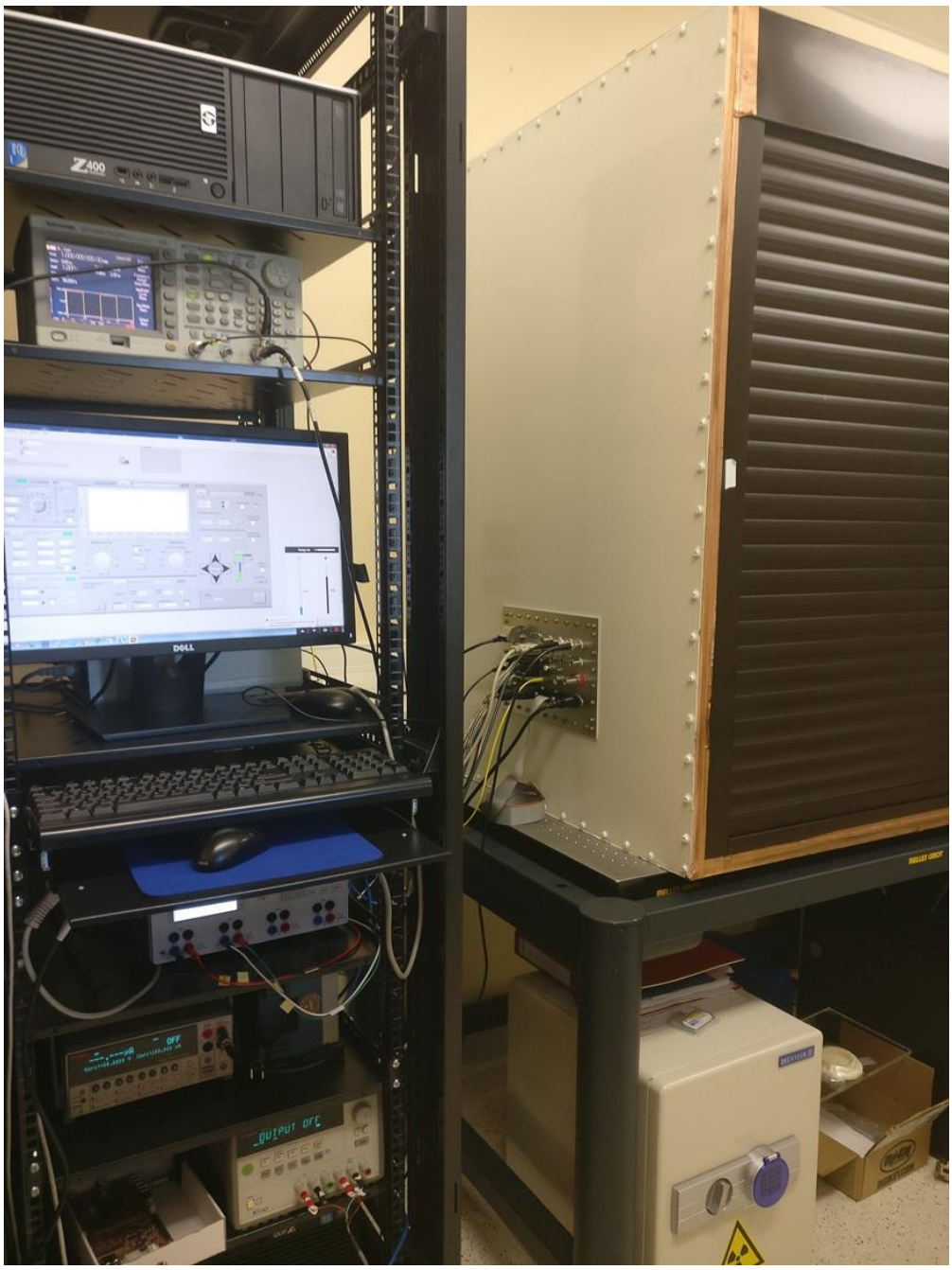

Figure 8.4 – The rack with the devices and a PC used for the laser system and the black box containing the test bench are shown. The cable connections are realized using a patch panel mounted in the wall of the box.

All the mechanical components of the setup are fixed on an aluminum bread board of the 30 x 70 cm^2 size and with M4 threaded holes. The X-Y table and optical posts are fixed by bolts to the bread board as shown in Figure 8.7. On the X-Y table an L-shaped aluminum support is mounted to hold up the rotation stage needed to tilt the pixel detector module for the inclined tracks measurements. To attach the SCC containing a pixel module to the rotation stage the special support was designed and made of high quality plastic on a 3D printer.

The design of the plastic support, shown in Figure 8.5, is done to keep on it the SCC and the scintillator with a photomultiplier (PMT) underneath. The scintillator is needed to provide a trigger signal during the measurements with a radioactive source, which will be discussed in the

section 8.5. The plastic support has an opening underneath the pixel module to allow for a free particle crossing in the path to a scintillator.

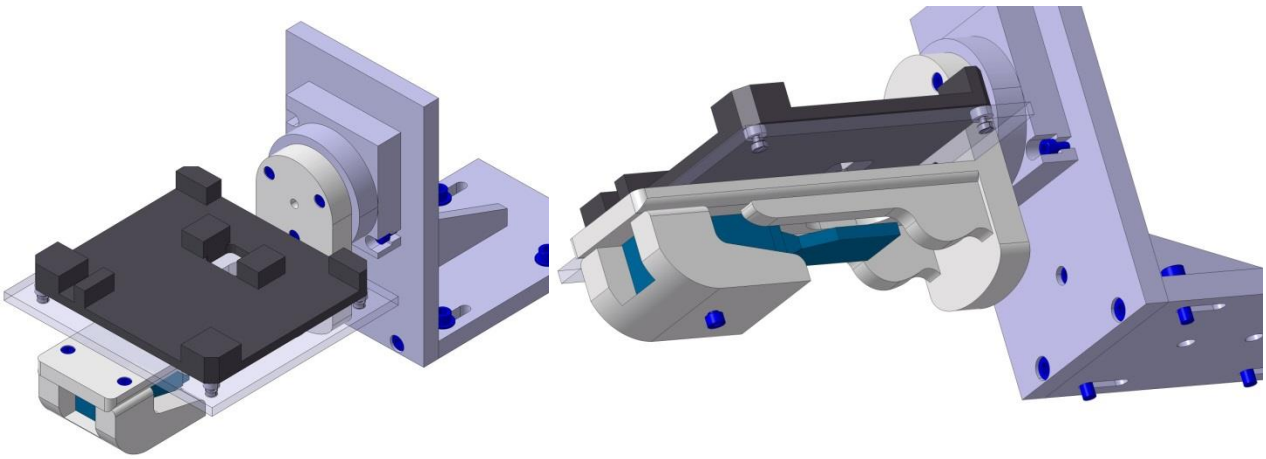

Figure 8.5 – A model of a 3D printed plastic holder to support a SCC with the pixel module and a scintillator.

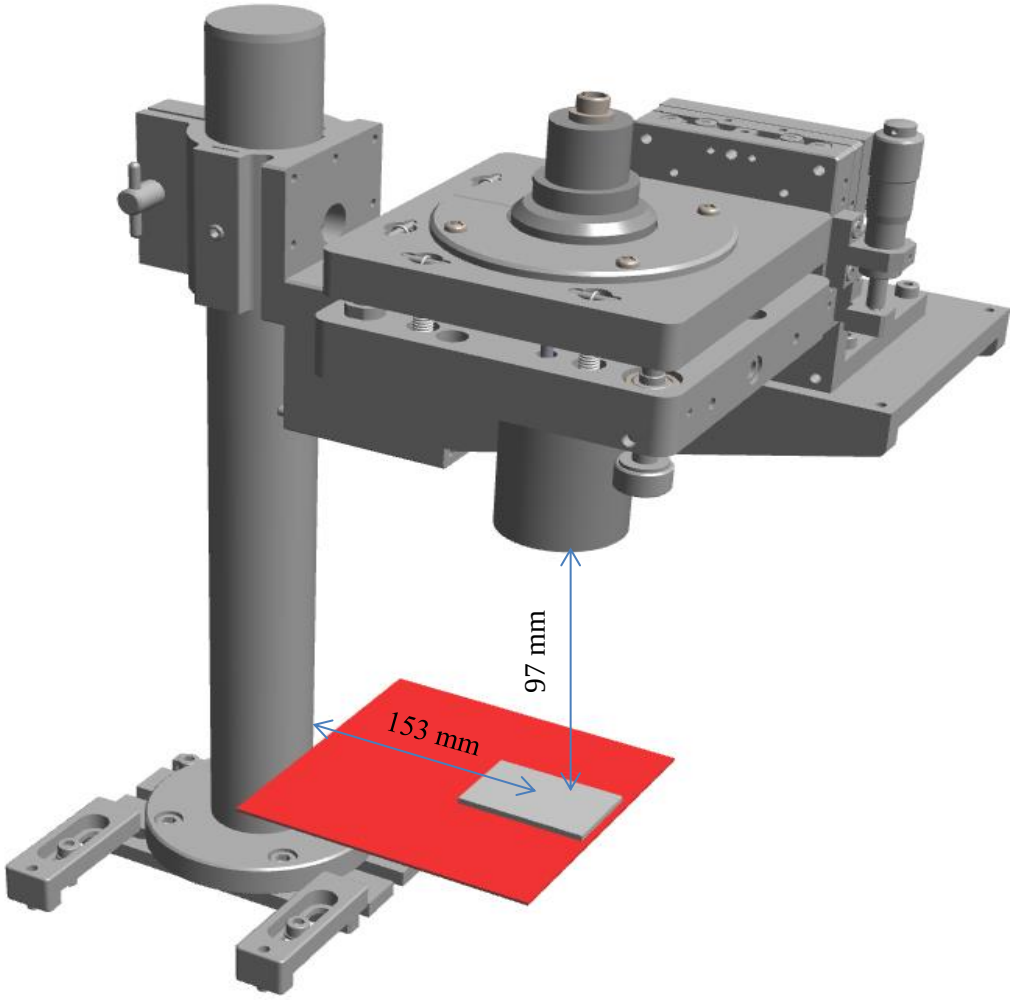

Figure 8.6 – A model of the support for the optical focusing system. The SCC and the distances from the module to the lens and the post are shown.

There are a few aluminum posts fixed by bolts to the bread board in the setup. One is needed to carry the optical focusing system, the design of it is shown in Figure 8.6, and the other supports a CCD camera for laser beam measurements.

The flexibility of the mechanical construction allows for using of the focusing systems with different working distances, which was approved during the system development, as well as additional optical components, for example pinholes to collimate a beam. Also, the addition aluminum support can be quickly and easily installed to prepare the setup for the radioactive sources scan measurements. The support is used to hold up the source over the pixel sensor. The position of the source can be aligned with respect to the pixel module using a red laser.

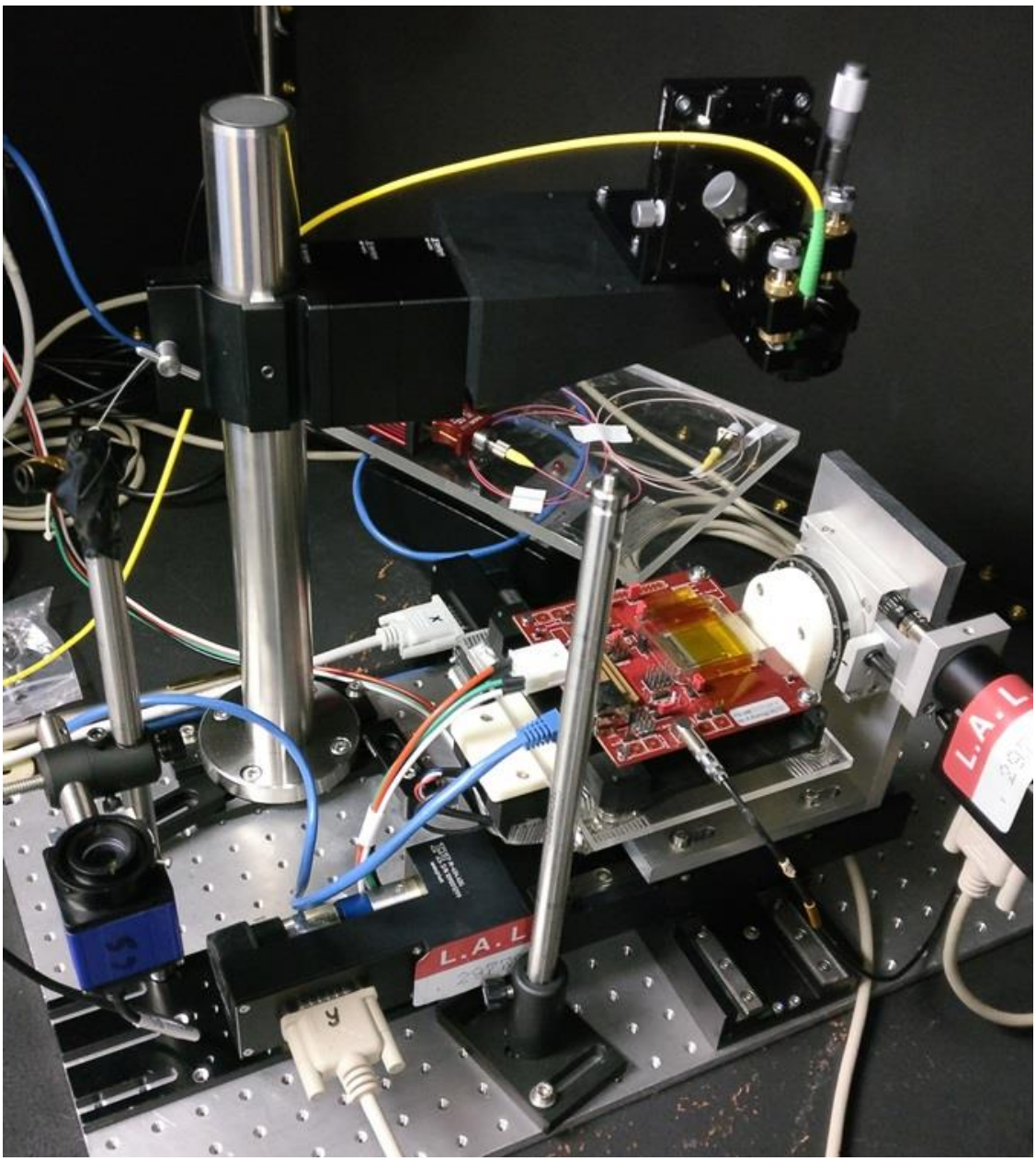

Figure 8.7 – Photograph of the laser test bench. The SCC with a pixel module attached to the rotation stage, which is mounted on the X-Y table. The massive post holds a focuser. The blue CCD camera is fixed at the same level as a pixel module for the beam characterization.

8.2.2 Lasers and optical components

Lasers

The setup can use two lasers: an infra-red laser and a red laser, which is used for the alignment, because unlike the infrared one, it is visible for human eye, and also for the pixel module characterization, when a charge generation at the sensor surface is needed.

An infra-red laser with a center wavelength of 1064 nm and spectral width of 2 nm is used to illuminate the pixel sensors in the setup. It is a class III, single mode Fabry Perot laser, based on Gallium Arsenide (GaAs) diode produced by QPHOTONICS. The laser can operate in a continuous wave (CW) or pulsed mode with 0.5 ns rise time. The wavelength temperature is coefficient 0.3 nm/^{o}C.

Another one is a class I laser with 635 nm wavelength produced by Advanced Laser Diode Systems. It is a pulsed mode laser with pulse duration of 45 ps and 600 mW of peak power. The laser pulse rate is controlled by the function generator and synchronized with the pixel detector readout electronics.

Power measurements

The laser pulse power is tunable and depends on amplitude of an electrical signal sent by function generator on an input of laser driver. The system has an optical power meter, which can measure a laser power. By power variation it is possible to make the energy deposition in the silicon equivalent to that created by MIP traversing the sensor. The high energy particle creates about 80 electron hole pairs per 1 μm of the path in silicon. For a one single pair creation in silicon the energy deposition of $W_{silicon}$ = 3.62 eV is required. To generate the same number of electron hole pairs, as a MIP in 230 μm thick silicon bulk only 10 fJ has to be delivered by laser beam in a pulse. Knowing the pulse length it is possible to find the output laser power needed to mimic charge generation of MIP particles. But not all the beam energy is delivered to the pixel sensor. The system has losses which are difficult to calculate due to beam intensity attenuation on optical components (fibers, lenses) and reflection effects on an aluminum and silicon oxide surfaces.

The laser output power was measured and calibrated depending on an input voltage. The measured dependence is shown in Figure 8.8. From the plot we can see that the sufficient loss is introduced when optical fibers are attached. It was observed that power attenuated not in the fibers, but rather on a fiber connection and a cleanliness of the connector surface is very important to ensure efficient transmission. Repeatedly connecting and disconnecting optical fibers the connector becomes dirty due to dust and grease. The dirt from connectors can be removed by using isopropyl alcohol with lint-free cloths and then dry air spraying. When the connector is not too dirty the special tool, called One Click Cleaner, can be applied. The result of the cleaning procedure is shown in Figure 8.9. To look at the connector surface to inspect it, the camera of an optical reflectometer embedded in EXFO FTB-200 compact modular platform with tips adapted to the type of connectors was employed.

The temperature has an effect on the output of the semiconductor lasers. When the temperature increases then significant power losses occurs within the laser. The cooling is important,

sometimes they cooled by liquid cooling systems or operate in pulsed mode only. Therefore, the changes of power have to be monitored during the accurate measurements. Also, the diode temperature can rise up to the nominal operation value after turning it on. The laser power was measured just after turning on and after the device warming up, during 30 minutes to measure the effect. The result is shown in Figure 8.7.

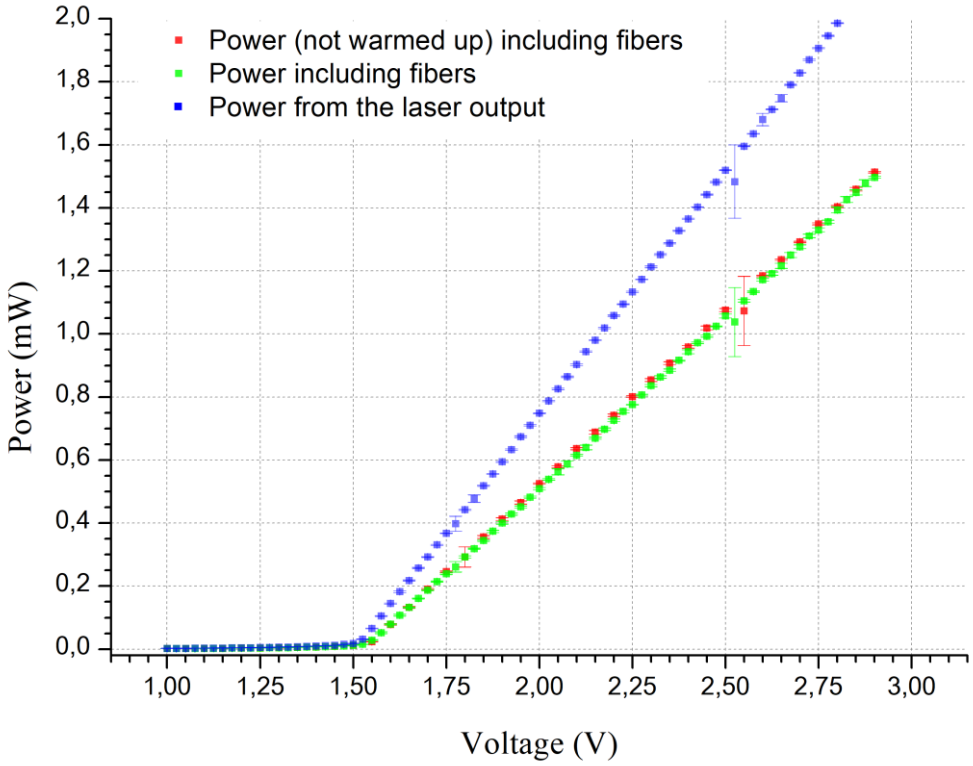

Figure 8.8. – The output laser power depending on amplitude of the input signal. The blue curve is a power measured just after the laser driver. The red curve is a power measured after an optical splitter. The green curve is measured at the same place after 30 minutes of warming-up. The green and red curves show about 2 % difference. The laser generation mode is starting from 1.5 V of biasing.

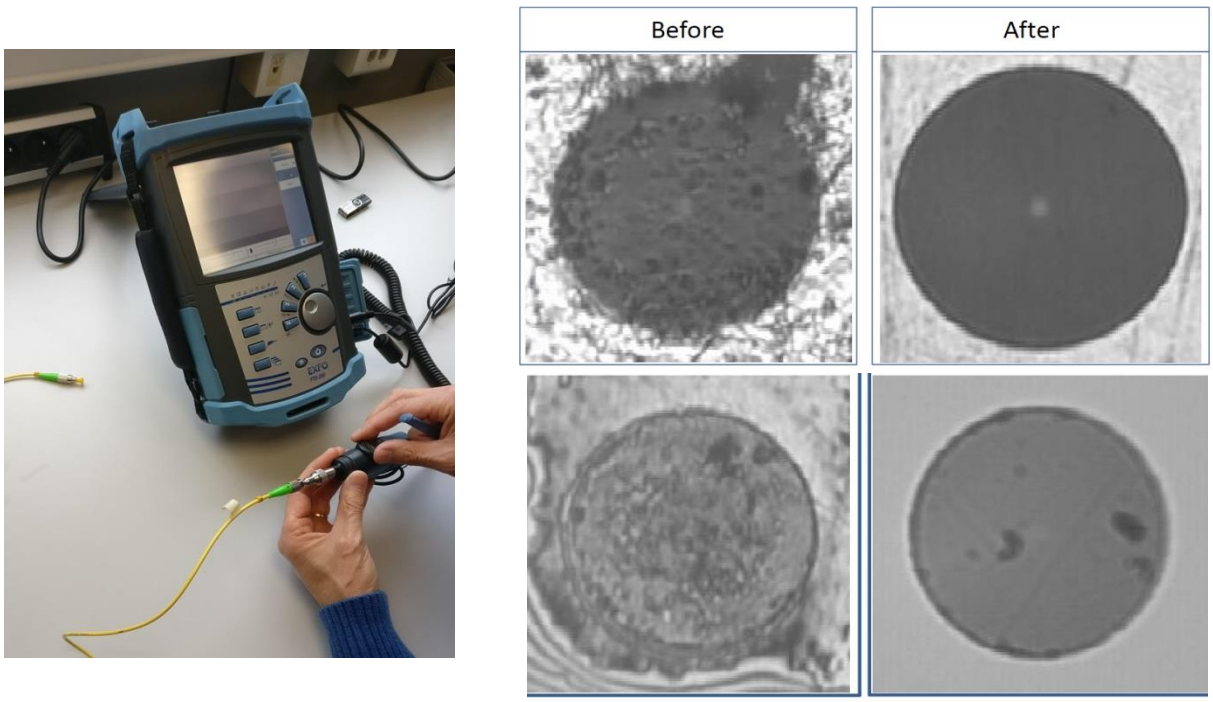

Figure 8.9. – The fiber connector cleaning process using one-click cleaner. The results of the cleaning visualized using a camera and an optical reflectometer are shown (Right).

8.2.3 Focusing

The most common intensity profile of the laser beams is a Gaussian. All real laser beams have some deviation from an ideal Gaussian and to describe this deviation the M^2 – beam quality factor is used. A diffraction-limited beam has $M^2 = 1$, and is a Gaussian beam and smaller than 1 values of M^2 are physically not possible. The most of information reported below are taken from the resources [135].

The Gaussian beam has the irradiance profile that follows a Gaussian distribution. This means that intensity decreases as a function of a distance from the center of the beam:

$$I(r) = I_0 \exp(\frac{-2r^2}{w(z)^2}) = \frac{2P}{\pi w(z)^2} \exp(\frac{-2r^2}{w(z)^2}) \tag{8.3}$$

where I_0 is the peak intensity at the center of the beam, r is the radial distance away from the axis, $w(z)$ is the radius of the laser beam where the irradiance is $1/e^2$ (13.5%) of I_0, z is the beam propagation distance, and P is the total power. Hence there is a dependence of $w(z)$ on z, which means the profile does not stay constant as the beam propagates through space. Due to diffraction, a Gaussian beam will converge and diverge from an area called the *beam waist* w_0, which is the place where the beam diameter reaches a minimum value. The beam converges and diverges equally on both sides of the beam waist by the divergence angle θ (Figure 8.10). The beam waist and divergence angle are both measured from the axis and their relationship can be written as:

$$w_0 = \frac{\lambda}{\pi\theta} \tag{8.4}$$

Considering a real beam with a quality factor M^2:

$$w_0 = M^2 \frac{\lambda}{\pi\theta}; \quad \theta = \frac{M^2\lambda}{\pi w_0} \tag{8.5}$$

where λ is the wavelength of the laser. As seen from *(8.5)*, a small beam waist results in a larger divergence angle, while a large beam waist results in a smaller divergence angle (or a more collimated beam). This explains the principle of beam expanders which reduce beam divergence by increasing beam diameter.

Variation of the beam diameter in the beam waist region is defined by:

$$w(z) = w_0\sqrt{1+\left(\frac{\lambda z}{\pi w_0^2}\right)^2} \tag{8.6}$$

The Rayleigh range of a Gaussian beam is defined as a function of z where the cross-sectional area of the beam is doubled. This occurs when $w(z)$ has increased to $\sqrt{2}w_0$. Using *(8.6)*, the Rayleigh range z_R, which is important characteristic of the beam, can be expressed as:

$$Z_R = \frac{\pi w_0^2}{\lambda} \tag{8.7}$$

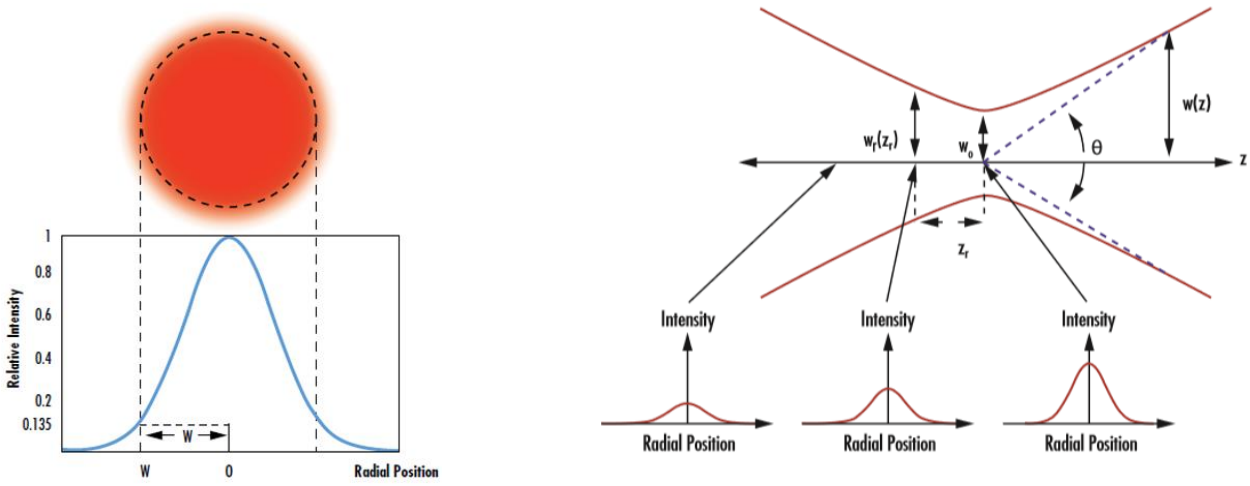

Figure 8.10 – The waist of a Gaussian beam is defined as the location where the irradiance is $1/e^2$ (13.5%) of its maximum value. Gaussian beams are defined by their beam waist (w_0), Rayleigh range (z_R), and divergence angle (θ) [135].

In many applications it is important to focus a laser beam down to the smallest spot possible to maximize intensity and minimize the exposed area. This may be done using optical components such as lenses, mirrors, prisms, etc. The behavior of an ideal thin lens can be described using the following equation:

$$\frac{1}{s'} = \frac{1}{s} + \frac{1}{f} \tag{8.8}$$

s' is the distance from the lens to the image, s is the distance from the lens to the object, and f is the focal length of the lens. If the object and image are at opposite sides of the lens, s is a

negative value and s' is a positive value. This equation ignores the thickness of a real lens and is therefore only a simple approximation of real behavior.

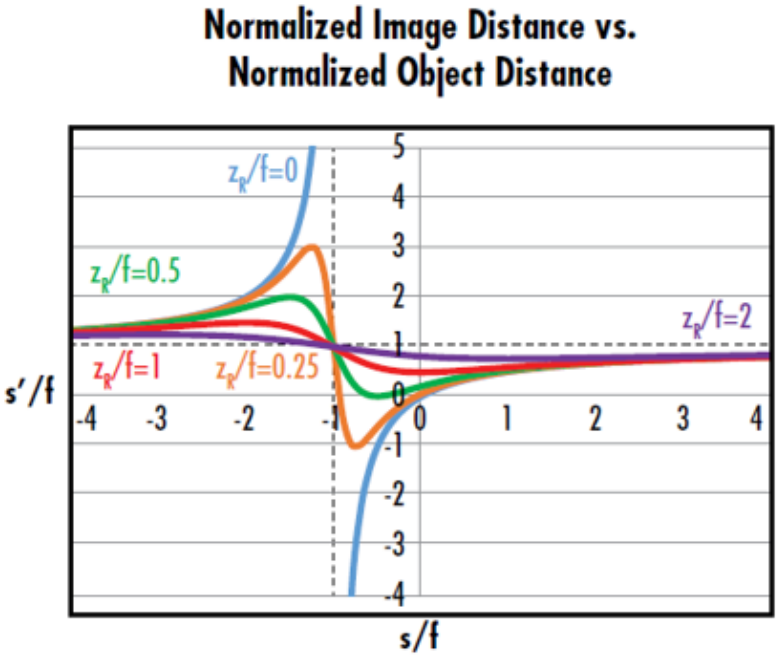

Figure 8.11 – The curve where $Z_R/f=0$ corresponds to the conventional thin lens equation. The curves where $Z_R/f>0$ show that Gaussian imaging has minimum and maximum image distances defined by the Rayleigh range [135].

In addition to describing imaging applications, the thin lens equation is applicable to the focusing of a Gaussian beam by treating the waist of the input beam as the object and the waist of the output beam as the image. Gaussian beams remain Gaussian after passing through an ideal lens with no aberrations. In 1983, Sidney Self developed a version of the thin lens equation that took Gaussian propagation into account:

$$\frac{1}{s'} = \frac{1}{s + \frac{Z_R^2}{(s+f)}} + \frac{1}{f} \tag{8.9}$$

A plot of the normalized image distance $\frac{s'}{f}$ versus the normalized object distance $\frac{s}{f}$ shows the possible output waist locations at a given normalized Rayleigh range $\frac{Z_R}{f}$ (Figure 8.11). This plot shows that Gaussian beams focused through a lens have a few key differences when compared to conventional thin lens imaging. Gaussian beam imaging has both minimum and maximum possible image distances, while conventional thin lens imaging does not. The maximum image distance of a refocused Gaussian beam occurs at an object distance of $-(f + Z_R)$ as opposed to $-f$. The point on the plot where $\frac{s}{f} = -1$ and $\frac{s'}{f} = 1$ indicates that the

output waist will be at the back focal point of the lens if the input is at the front focal point of a positive lens.

In order to understand the beam waist and Rayleigh range after the beam travels through the lens, it is necessary to know the magnification of the system α, given by:

$$\alpha = \frac{w_0'}{w_0} = \frac{1}{\sqrt{1-(\frac{s}{f})^2+(\frac{Z_R}{f})^2}} \tag{8.10}$$

where w_0 is beam waist before the lens and w_0' is the beam waist after the lens. The inverse of the squared magnification constant can be used to relate the beam waist sizes and locations [135]:

$$\frac{1}{\alpha^2} = \frac{|s|-f}{s'-f} = (\frac{w_0}{w_0'})^2 \tag{8.11}$$

The goal of focusing is to minimize w_0'. Solving (8.11) for w_0' results in:

$$w_0' = w_0 \frac{f}{\sqrt{(|s|-f)^2+Z_R^2}} = \alpha w_0; \quad \alpha = \frac{f}{\sqrt{(|s|-f)^2+Z_R^2}} \tag{8.12}$$

From this equations we can see that the focused beam waist can be minimized by reducing the focal length of the lens and $(|s|-f)$.

There are two limiting cases which further simplify the calculations of the output beam waist size and location: when s is much less than Z_R or much greater than Z_R.

The second case when the lens is far outside of the Rayleigh range and $s >> Z_R$, which is the case for our focusing system, the (8.12) simplifies to

$$\alpha = \frac{f}{|s|} \tag{8.13}$$

And finally the output beam waist diameter:

$$w_0' = \frac{f}{|s|} w \tag{8.16}$$

In this case also the distance from the lens to the focused spot equals the focal length $f \approx s'$.

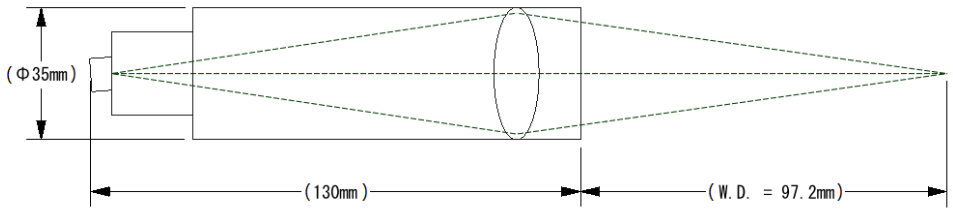

Figure 8.12 – A simplified design scheme of the focuser with a working distance around 97 mm.

The working distance, another useful parameter, is the distance between object and the lens front edge. For a single lens in above considered case, the working distance would be the focal length, but for compound lenses it is not.

For the developed laser test bench setup, the working distance is one of the crucial parameters, which defined the design of the focusing system (see Figure 8.12). It is a distance between the lens and the pixel sensor surface and to not damage both of these components it is important to separate them by as large as possible spacing. Moreover, a study when the module is tilted is foreseen, which means that rotating the detector one side of it rises and may touch the lens in case of using the focuser with a short working distance as shown in Figure 8.14.

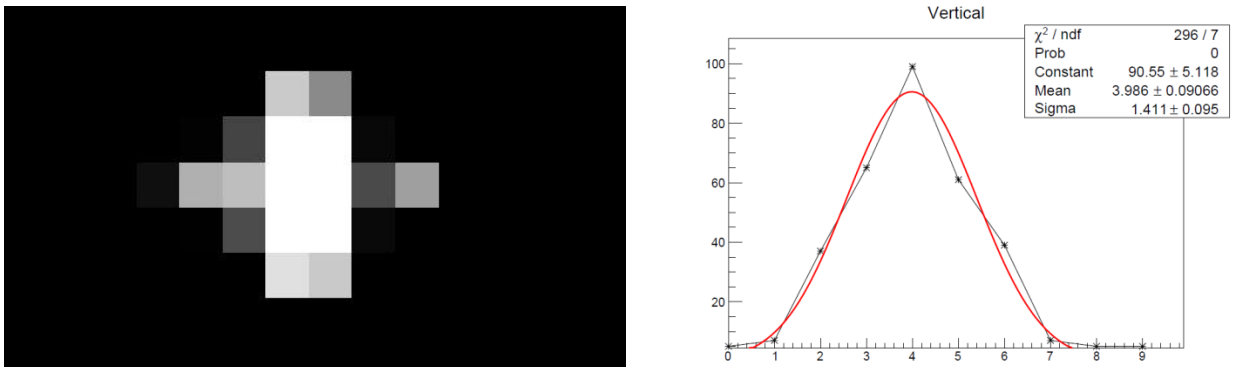

Figure 8.13 – The results of a beam spot measurements. (Left) the image if the spot on a CCD camera. (Right) The intensity plot fitted my Gaussian. The size is specified in pixel units.

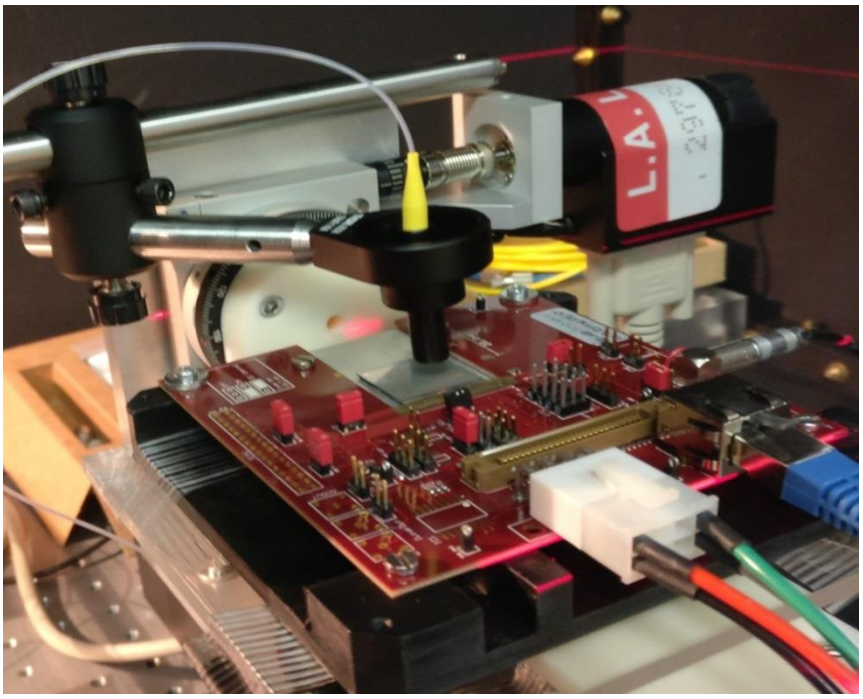

Figure 8.14 – The pixel module and the optical focuser with a working distance of 4.8 mm used to focus the IR laser beam to less than 10 μm size.

The beam spot size has been measured using a CCD camera 640 x 480 resolution and 5.6 μm pixel size. The size of the spot, shown in Figure 8.13, is about 15 μm, using the relationship between the FWHM and the $1/e^2$ intensity point, which is $w \approx 0.85 \cdot FWHM \approx 0.85 \cdot 2.35 \cdot \sigma$

The working distance decreases as you increase magnification. So, to have a very small beam spot at a large working distance the optical systems becomes more complex. For example, there are two focusing systems used in the current laser setup, one with the small about 5 mm working distance is shown in Figure 8.14 and another with working distance of 97 mm, shown in Figure 8.16.

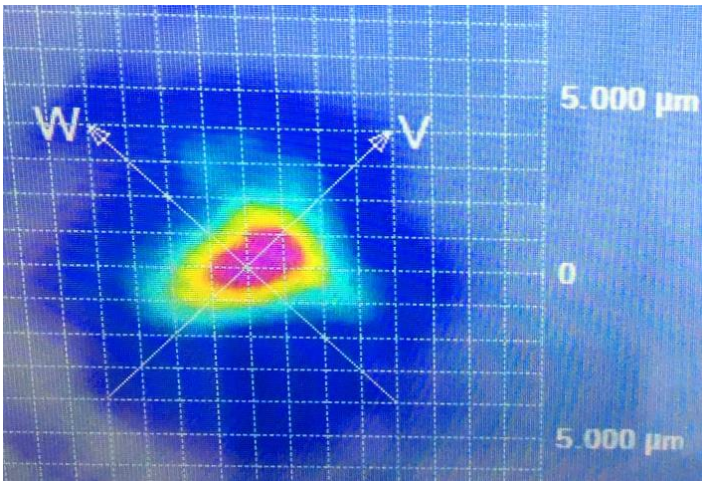

Figure 8.15 – The laser beam spot intensity, shown on a monitor of a beam profiler.

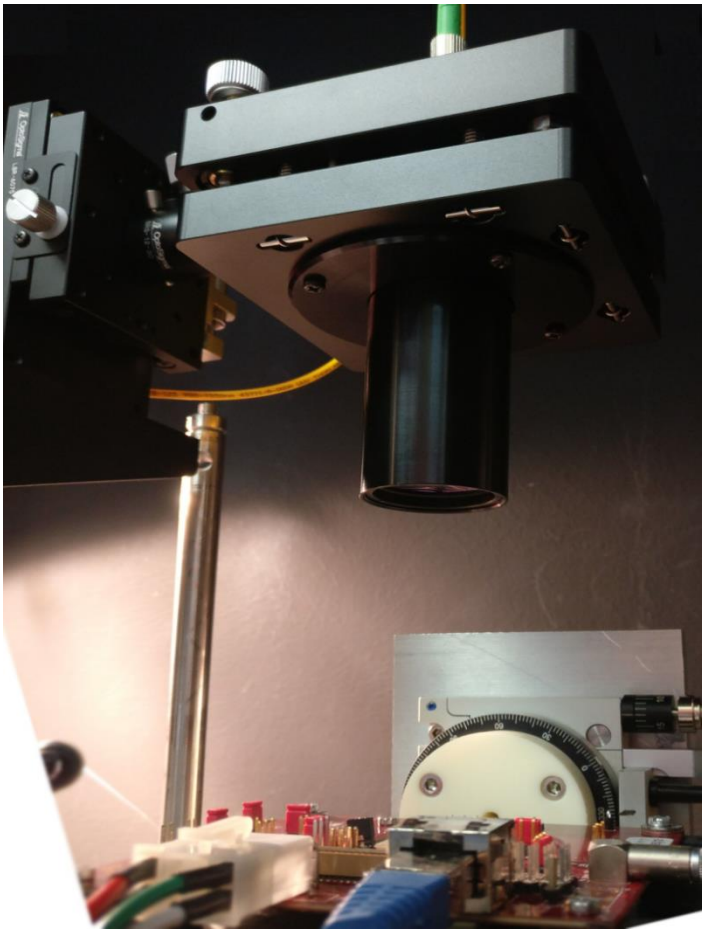

Figure 8.16 – A picture of the focuser located on a working distance of about 97 mm over the pixel module under the test.

The results of a beam spot measurements with the system with higher working distance, which will be used in the final version of the laser test bench is shown in Figure 8.15. It gives the size at the $1/e^2$ (13.5%) intensity point about 10 µm. The 80% of the beam intensity is concentrated in 2 µm size spot.

8.2.4 DAQ system

To read out and tune the FE-I4 module tested in the laser system the DAQ system called USBPix was used. The compact USBpix read-out system [106] employs adapter cards, for different types of modules: FE-I3 and FE-I4 chips. The hardware and software components have a modular structure in order to provide large flexibility.

The USBPix Board, shown in Figure , contains a multi-purpose Xilinx Spartan3 FPGA (Field Programmable Gate Array) card with a USB2.0 interface, 8051 microcontroller (µC) and and 2 MB of onboard memory (SRAM). The micro controller handles the scan routines. The FPGA controls all signals going to the FE, like configuration commands, and stores data coming from the FE in the memory. Thus, standard scan routines can be executed without communication to the PC, saving processing time. An Adapter Card is connected to the Multi-IO board, which is dedicated to the specific flavor of the read-out chip. The card for the FE-I4 contains voltage regulators to power the front end. The output of the regulators can be set by the user. Via a flat ribbon cable or RJ45 cable, that routes all data and power lines, the Adapter Card is connected to the Single Chip Card (SCC).

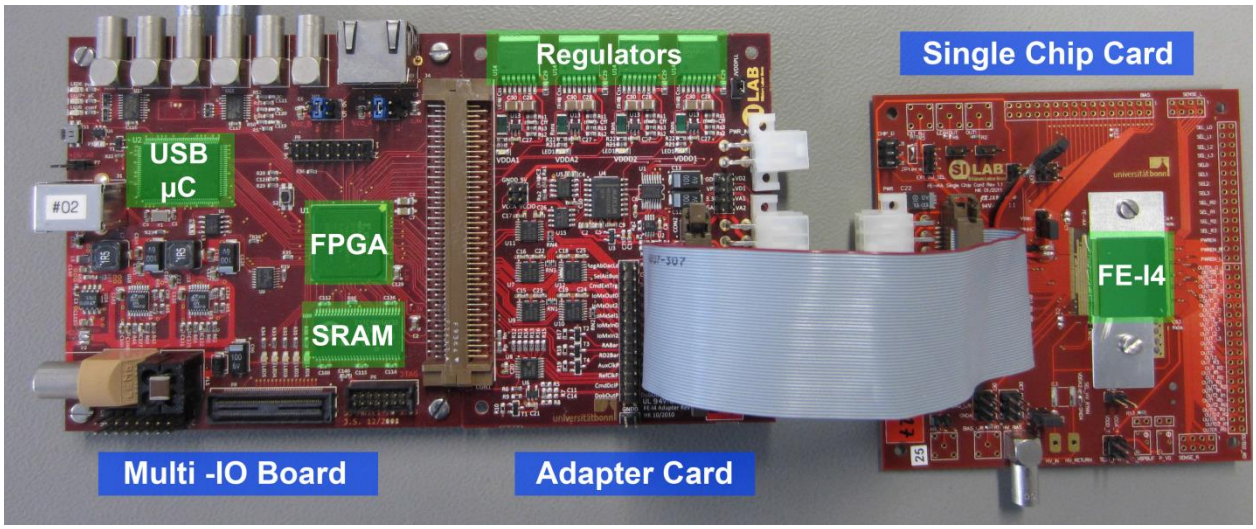

Figure 8.17 – Picture of a USBpix read-out system with Multi-IO board, Adapter Card and Single Chip Card with FE-I4.[105]

The communication between the USBPix board and user occurs via the STControl software running on a standard PC. It is the graphical user interface, based on ROOT and Qt, which allows for configuration and operation of the connected module assembly. STcontrol is a collection of C++ classes based on the ATLAS PixLib package, controlling scans and measurements. By changing of the C++ code the application software can be modified. STcontrol provides the loading of chip configurations, includes different test and measurement

routines and has a data analysis tool called Module Analysis, which completes the software package.

8.3 Software for the setup controlling

The above described laser system has many component nodes to manage. In order to control them and to simplify the process of adjustment and operation of the setup, the software has been developed. The software is written using visual programming environment LabVIEW (Laboratory Virtual Instrument Environment Workbench) [146]. The graphical programming language «G» employed in the LabVIEW package is based on the architecture of data streams. The sequence of operators in such languages is not determined by their order, as in imperative programming languages, and the availability of data on the inputs of these operators. Operators are not related to data, are executed in parallel in any order. The programming code in LabVIEW is represented in the form of graphical objects - function-nodes, which perform operations on variables that are propagated by wires connected to nodes terminals. The example of the part of a code used in the software is pictured in Figure 8.19.

The developed program allows for connection to all the devices containing in the setup, in order to regulate the parameters, obtain data and status and control measurement process to avoid any damages to the detector under the test. The communication to devices ensue through the standardized SCPI commands (Standard Commands for Programmable Instruments), which are sent via the I/O interface Virtual Instrument Software Architecture (VISA) [147]. The SCPI defines a standard for syntax and commands to use in controlling programmable test and measurement devices.

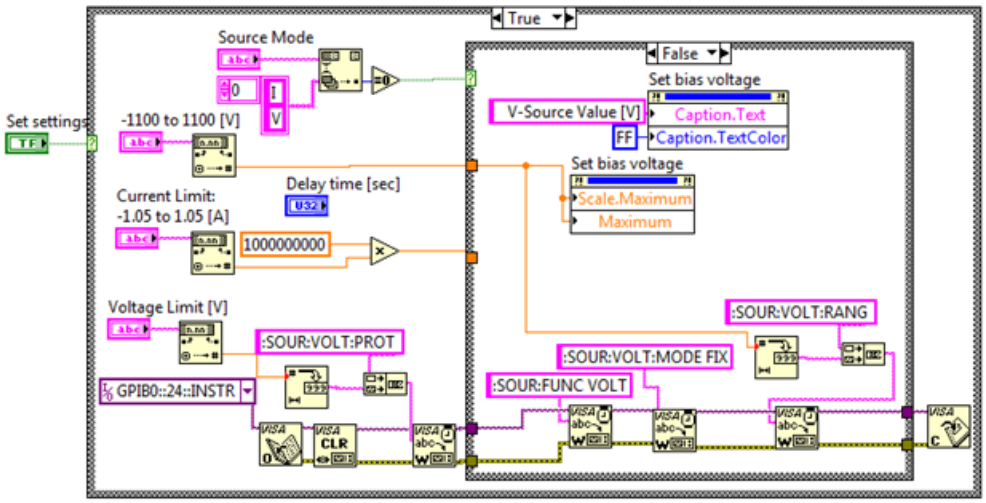

Figure 8.19 – The part of the program source code in LabVIEW. It sets the parameters for the Keithley sourcemeter.

The program structure as a program interface, shown in Figure 8.20, is divided on an individual blocks for each instrument providing ease of use and modification. Looking to the interface, on the top left, one can find the control block for Keithley Source Meter. It allows user to set voltage and current limits, a current compliance value, which is the range of current over which the load regulation is within specified limits. It is needed to prevent the damage to the module through the breakdown. Also, it is possible to set a value for the bias voltage and to choose the

voltage polarity. The algorithm provides smooth ramping up in voltage, because a sharp increase in voltage may damage the sensor structure. So, the voltage step value and the delay in seconds between them can be specified by user. The voltage drop occurs in the same way. The increasing in biasing voltage is displayed in the progress bar on the front panel; user may observe it as well the leakage current value and, if it is needed, can interrupt the process. There is a protection in the program, which always decreases the biasing voltage step by step, even if user turns of the output status. Also there is an indicator, implemented on the front panel, which shows the level of leakage current in the detector during the operation.

The next down block is dedicated to a pulse generator device control, needed to trigger the laser pulse generation and to initiate DAQ read out. In this part, it is possible to change for each channel individually a signal shape (rectangular, sinusoidal and pulse mode with a varied duty cycle) and other pulse signal characteristics as frequency, amplitude, phase, duration and polarity. The output amplitude of generator is programmatically limited at 3 V and it is always kept in positive range, which is an essential requirement for safe operation of the laser diode. It is possible to change the load impedance of a function generator output terminal from 50 Ohm for a laser input to a high Z (1 MOhm) when it is connected to the oscilloscope. There is possibility to regulate duty cycle or pulse duration from ns to ms in the pulse mode.

The two parts on the bottom of the interface panel are implemented to control power supplies, needed for a low voltage supply of the USBPix system board and for a supplying of a digital and an analog part of front-end chip of the pixel detector module. The user can set output current and voltage limits and the voltage values needed to the dedicated devices. One of the power supplies feeds through the two channels a USBPix board that requires a value of 2 V on both channels. From another supply the voltage applies to the pixel module. An analog part needs 1.5 V, while a digital one – 1.2 V. The current consumption of the module must be monitored and keep at proper values for the FE-I4 module, which is about 100 mA for the digital part, and 300 mA for the analog at these voltage levels. The deviations of these values from the norm affect the module performance.

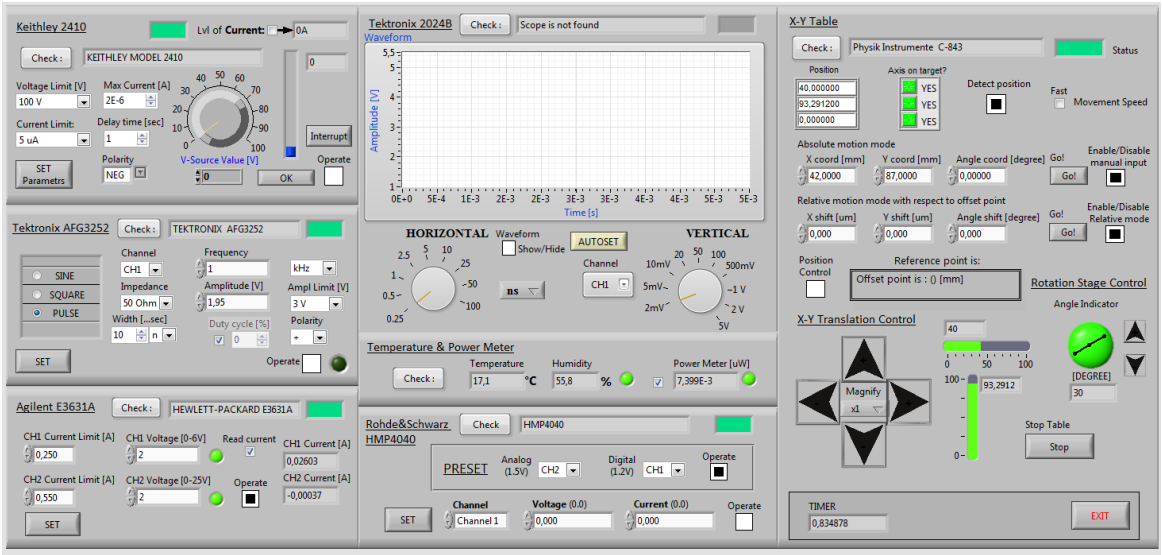

Figure 8.20 - The screenshot of the program interface for the control of the laser test bench setup is represented.

In the middle one can find an oscilloscope control block. In the setup oscilloscope can be used to monitor the output laser pulse using an optical-to-electrical converter. The waveform shape from the scope can be visualized in a program interface window. The waveform acquisition time has been sufficiently reduced by using the binary code for the data transfer instead of ASCII format. The vertical and horizontal sweep of the oscilloscope can be adjusted. Some other options like Autoset that will measure the input signals that are fed into the oscilloscope and will find some range that the signal falls into and then display it on the oscilloscope.

Also, the temperature and humidity, important parameters during the measurements of silicon pixel detectors, are monitored in this software. The indication of the measured power of the laser pulse by the optical power meter is shown in the program.

On the left part, the block for controlling of the translation and rotation mechanical stages is implemented. It has the handy buttons and indicators for the manipulation of the X-Y table and the rotation stage. They can be moved manually by single button press or continuously while the button is pressed. In addition, the movement can be established by setting the absolute or relative (the reference point should be chosen) coordinates. Current position and the motion status of the motorized tables are indicated in the program. The speed of movement can be increased when it shifts in a long distances. The space range for moving without obstacles was measured and limits are set in the program.

8.4 Results

In this section the results obtained using the laser test bench during the measuring an FE-I4 pixel module. The chip has been tuned before measurements to a threshold value of 2000 e^- and ToT was tuned to correspond to the charge of 16 ke^- at 8 ToT. The noise pixel mask is applied.

8.4.1 Beam characterization and alignment

Before starting the measurements the laser beam has to be well aligned and focused. The alignment in this case means that the beam has to penetrate the silicon sensor perpendicularly. Any deviation from the perpendicularity will complicate the focusing process, because it may distort the result.

The preliminary alignment of the system is done using the laser level. The focuser, pixel detector under the test and CCD camera using for a beam focusing and alignment must be parallel to each other. Moreover, the detector and CCD camera are fixed at about the same level. Then to refine an alignment the CCD camera is used to adjust and to check the beam perpendicularity. For this, the position of the beam spot on a CCD matrix is measured at the lowest possible location of the focusing lens over the camera. Then the focuser base raises along the post without any movement in the perpendicular plane, it can be ensured by adding another post, so two points of the base are fixed. And if during the lifting it up, the spot is moving, that means that a focuser is fixed with some angle. By special adjusting screws we can change the tilting angle of a focuser in two directions. The procedure continuous until the spot will stay at the same position on a matrix while the focusing system is moving up or down.

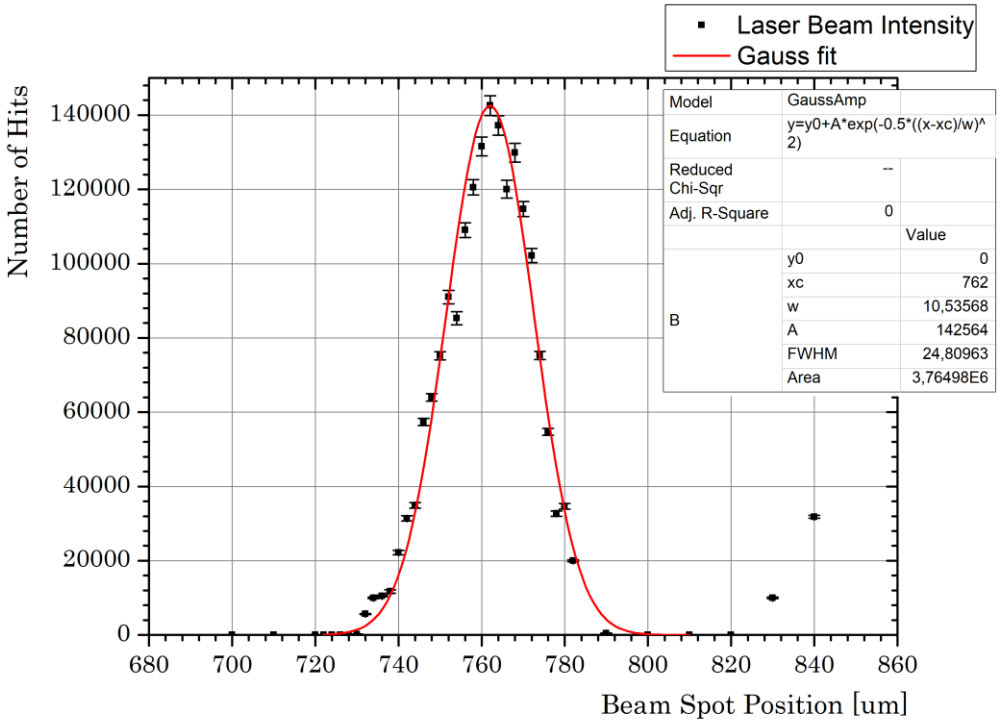

Figure 8.21 – The number of registered hits by the detector, when the laser spot moves over the pixel sensor in one direction. The result is fitted by Gaussian function.

The focusing at first is done with using of a CCD camera fixed at the same level as a pixel module. Then the base of the focuser is moving from the position over the camera to the positon over the pixel sensor. And then the iterative measurements with the pixel detector are performing. By changing the focusing distance using the manual micrometric stage one can try to get the smallest beam spot.

Given the fact that on the pixel sensor surface we have openings in aluminum, and it is possible do not observe any intensity, when the beam is focused on an aluminum surface and have a maximum intensity when the spot is in a middle of the pixel. The width of the beam waist at the sensor level has been estimated by looking at the variation of the charge or the number of hits collected by the module as the laser spot moves over the pixel sensor surface with openings in an aluminum layer. An example of such a scan is shown in Figure 8.21 which shows the number of registered hits by the pixels around the beam spot versus the beam position relative to the pixel.

8.4.2 Laser scan

To make measurements with the pixel detector illuminated by a laser beam, a standard procedure, called Source scan, is performing. This scan is included in STControl software, and provides us with hitmaps histograms and ascii-files with raw data, the example of which is shown in Figure 8.22. Every external trigger is marked with the letters TD (green box) and every data header (DH) contains a new bunch-crossing identifier (BCID) to synchronise with the other detectors. The hit information is transmitted in the data record (DR, red box). After the DR there is the hit information of column and row and the ToT Code for pixel (col, row) and a second ToT Code for the pixel (col, row+1) [105].

To initiate the readout the trigger signal synchronized with laser pulse is coming to the USBPix board. To compensate the mismatch of the trigger signal and the laser pulse introduced by a signal rising and propagation time, and the timewalk effect, the STControl allows to set a delay time for the readout. Observing the Lvl1 distribution, which shows the time window, when hits arrive in the module, we can adjust this delay to register all the hits correctly.

```
4   0xf84000
5   0x000001
6   TD 2 0 1
7   0xe9563a
8   DH 0 86 58
9   0xe9563b
10  DH 0 86 59
11  0xe9563c
12  DH 0 86 60
13  0xe9563d
14  DH 0 86 61
15  0xe9563e
16  DH 0 86 62
17  0xe9563f
18  DH 0 86 63
19  0x2d0d2f
20  DR 22 269 2 15
21  0xe95640
22  DH 0 86 64
23  0xe95641
24  DH 0 86 65
25  0xe95642
26  DH 0 86 66
27  0xe95643
28  DH 0 86 67
29  0xe95644
30  DH 0 86 68
31  0xe95645
32  DH 0 86 69
33  0xe95646
34  DH 0 86 70
35  0xe95647
36  DH 0 86 71
37  0xe95648
38  DH 0 86 72
39  0xe95649
40  DH 0 86 73
```

Figure 8.22 - Snapshot of the output raw date file of a Source Scan for one external trigger (TD, green box) with one hit (DR, red box) in pixel (22,269) with ToTCode=2 at BCID=6 [105].

The example of the hitmaps measured with the laser is shown in Figure 8.23. The two cases when only one pixel fired and several pixels fired by a laser beam are considered. Depending on laser power we can have a cluster of several pixels that register hits. It happens through the charge sharing mechanism and perhaps due to reflection from the front side metallization.

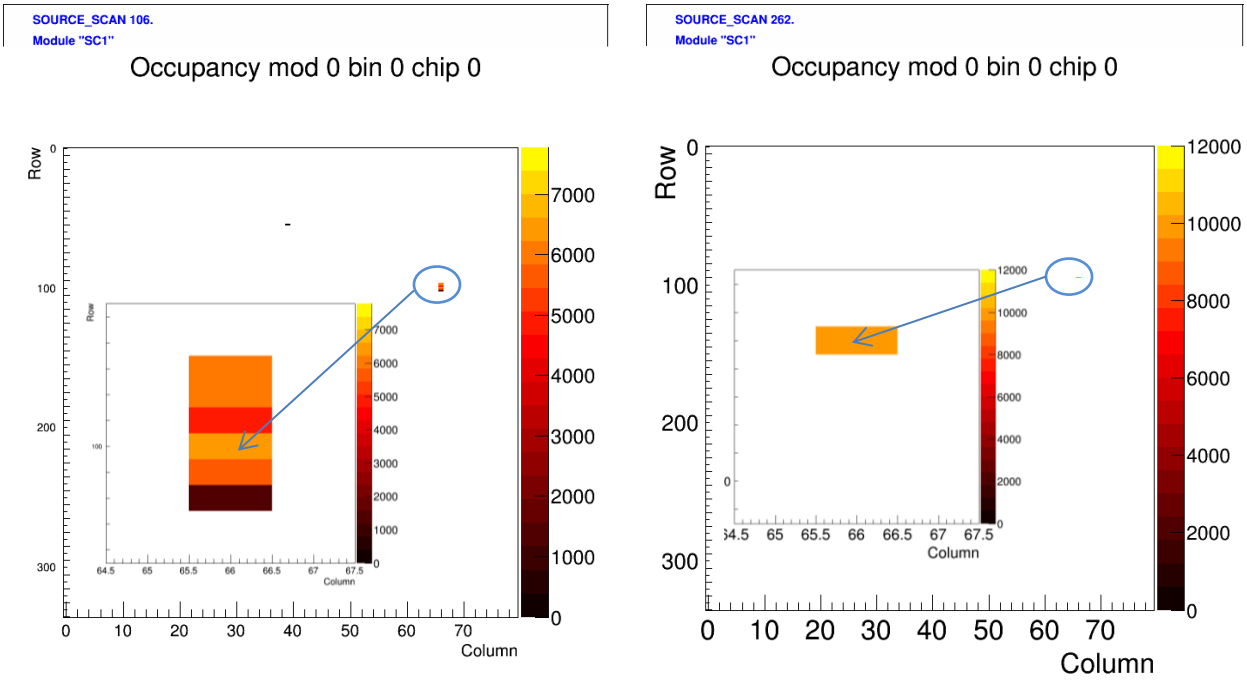

Figure 8.23 – The laser scans hitmaps. The whole sensor matrix is shown, as well as a zoomed image of the laser beam spot. The beam spot is seen in several pixels (Left) and in only one pixel (Right).

The Lvl1 distribution and ToT distribution, which is used to recover the deposited charge, are plotted in Figure 8.24 and Figure 8.25 for the both cases discussed above. The ToT distribution for the case, when generated charge is collected in one pixel, is represented by a peak, the most hits are in one bin and others in a few much smaller. Such behavior could be explained by a charge deposition of a laser beam of such wavelength mainly through a photoelectric effect, so the full energy of photons is transferred to Silicon atoms. The Compton Effect is minor in this

energy range. When the laser beam is registered in several pixels, the total generated charge is shared between them, so it results in a ToT distribution that is much spread.

The Lvl1 distribution for the both cases has a peak shape, which assures that almost no noise is registered. In the case when charge is shared between adjacent pixels the Lvl1 distribution may contain a fraction of a late hits delayed because of a time of charge diffusion.

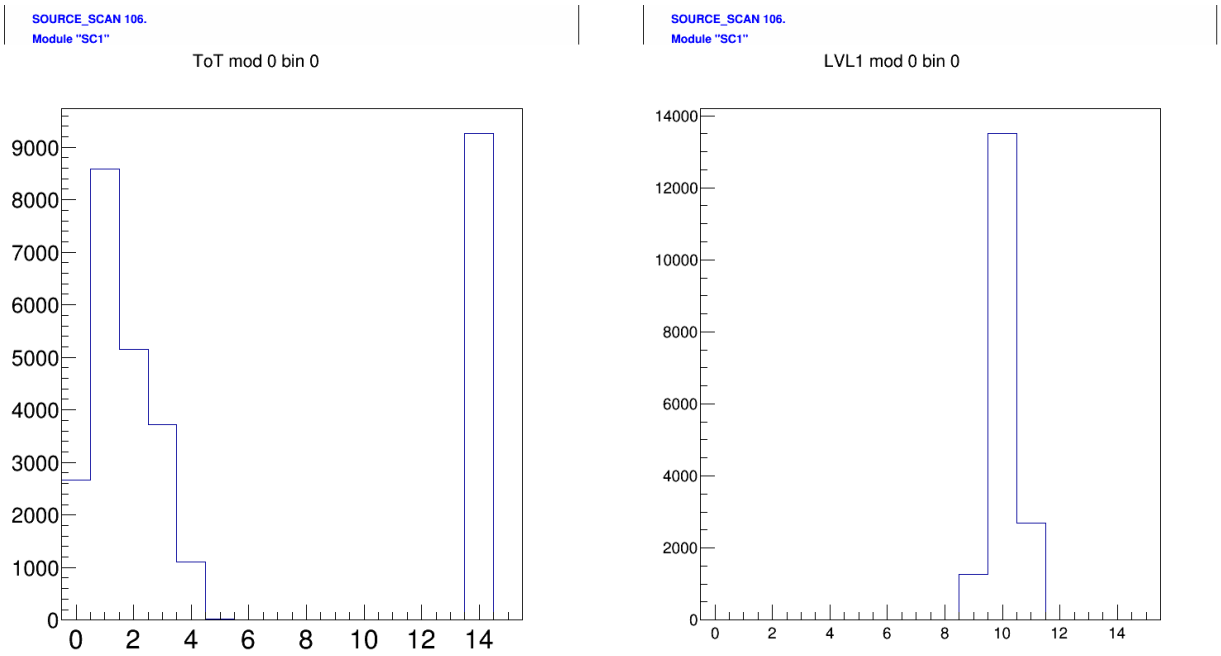

Figure 8.24 – The TOT distribution (Left) and Lvl1 distribution (Right). For the case when the charge generated by a laser beam is collected by several pixels.

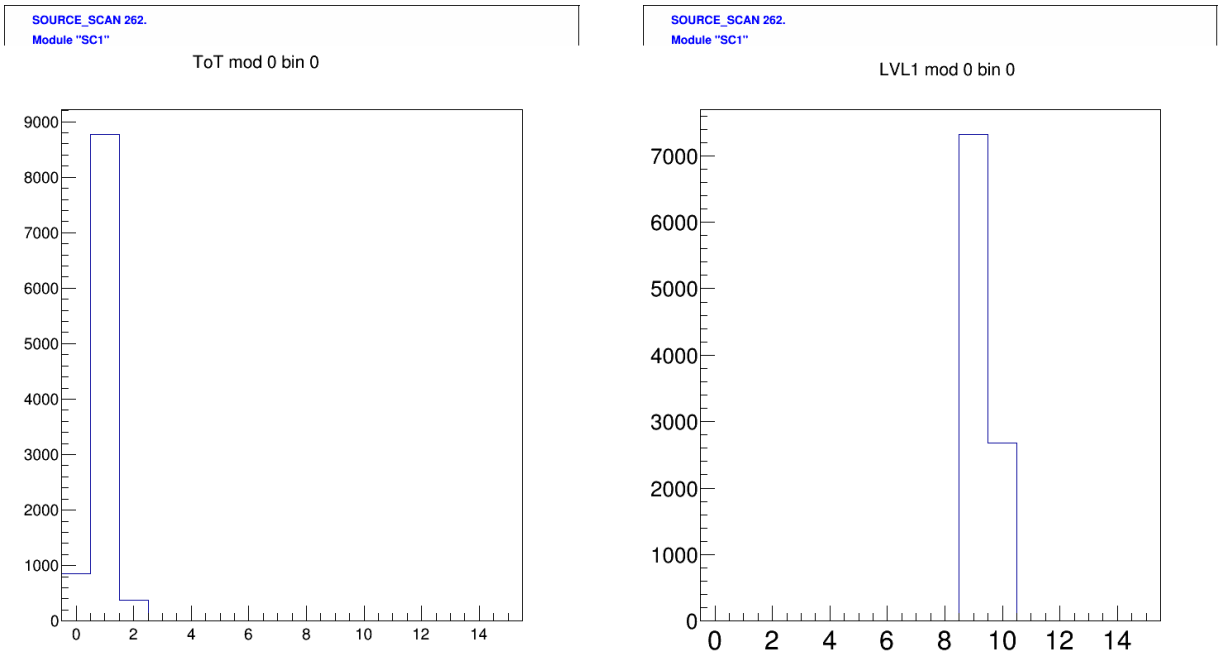

Figure 8.25 – The TOT distribution (Left) and Lvl1 distribution (Right). For the case when the charge generated by a laser beam is collected by only one pixel.

8.4.3 Charge to ToT calibration

The time over threshold (TOT) is the time (measured in clock cycles of 25 ns) that the analog signal, induced by the charged particles, has spent over the threshold. This digital information is proportional to the charge release, itself depending on the particles charge and energy. At fixed charge injection, the ToT depends on the threshold value and on the charge conversion. High ToT values will correspond also to higher processing time, so that the conversion has to be properly tuned. The ToT analysis verifies that a ToT tuning succeeded and that a given charge corresponds to the expected ToT value for all the pixels within a module.

The charge to ToT relation is not linear. To estimate which charge value corresponds to which ToT values, a charge to ToT calibration scan has to be performed. The FEI4 chip produces a range of signal amplitudes using the voltage injector Vcal. For each injected charge signal, an equivalent ToT signal is registered. The response of each pixels can be different especially after irradiation of the chip. Once this scan has been performed, one can extract parameters describing a second order polynomial function which gives the correspondence between the charge and the ToT.

The relation between the range of injected charge into the preamplifier and the ToT is measured during the ToT calibration. Although a homogenous nominal ToT tuning is achieved over the entire chip, the ToT calibration measurement shows a difference in the pixel-to-pixel response to a fixed injected charge. The ToT values exhibit a non-linear relation with the injected charge. Therefore, a correlation between the ToT-charge values is obtained for every pixel. This correlation reduces the uncertainty of the direct conversion from ToT values to real charge values. In contrast to the ToT tuning, where only a fixed amount of charge is injected, the ToT calibration aims to cover a charge range as large as possible. The ToT calibration measurement is done by scanning the ToT values against a range of injected charge with the same mechanism performed in the tuning procedure. The ToT-to-charge relation is calibrated by the fit parameters of the ToT. The calibrated charge function is defined by:

$$Q = \mathrm{Par\_A} + \mathrm{Par\_B} \cdot \mathrm{ToT} + \mathrm{Par\_C} \cdot \mathrm{ToT}^2 \tag{8.17}$$

where Par_A, Par_B and Par_C are the fit parameters per pixel. These parameters are used to convert the ToT values from the charge collection measurements into charge values. The example of thise parameters are shown in Figure 8.26 by histograms containing the value for each pixel.

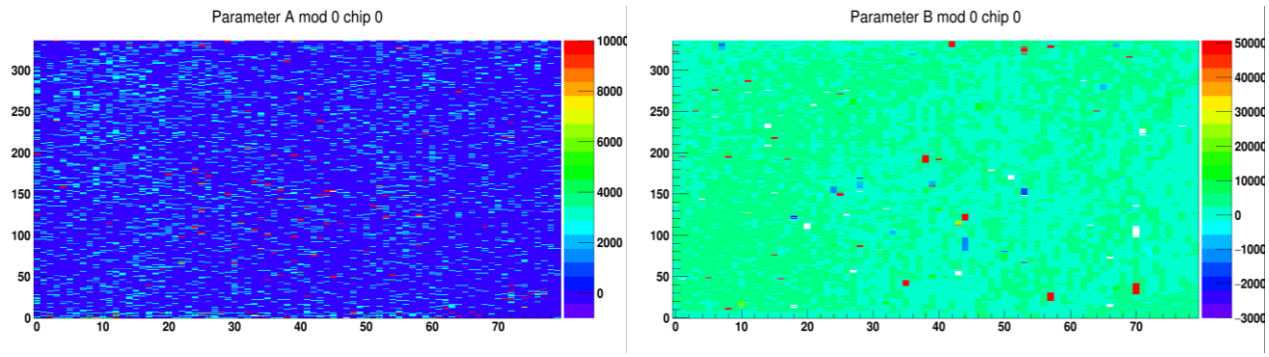

Figure 8.26 – Example of a histogram with a parameter value for the each pixel. The example of Par_A (Left) and Par_B (Right) are shown. The histograms are the result of the ToT Calibration Scan.

The resulted ToT to charge calibration curve calculated by (8.17) for a one pixel is shown in Figure 8.27.

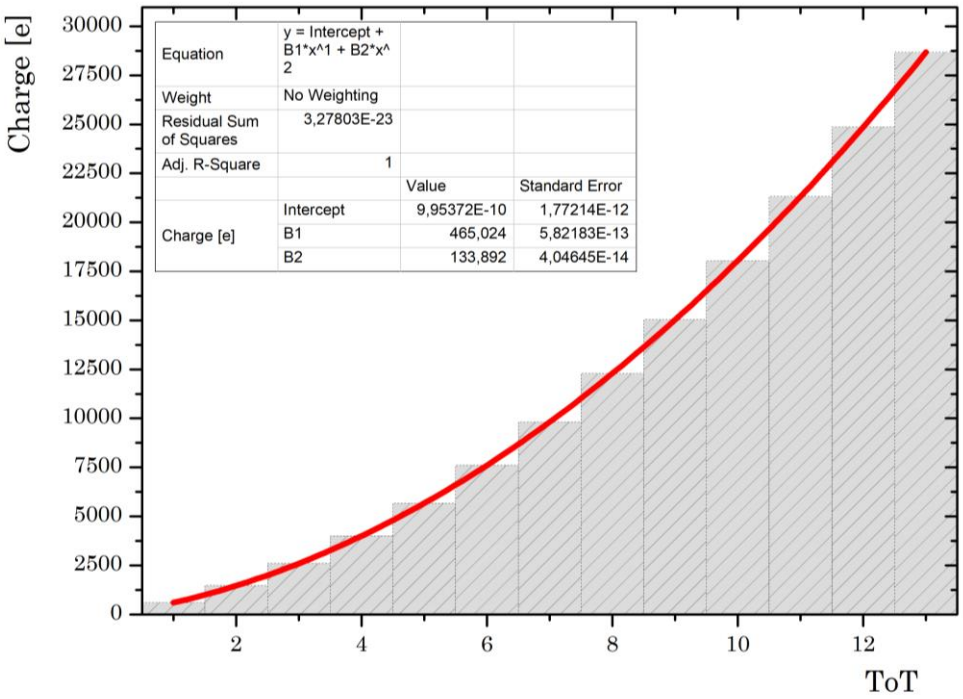

Figure 8.27 – Dependence of mean deposited charge on ToT value for one pixel. The histogram is fitted with a second order polynomial function.

8.4.4 Depletion voltage measurements

The full depletion voltage is one of the most important parameters can be determined by using a laser system. The IV curves, as was discussed in section 4.4, are not always clear way to determine the full depletion.

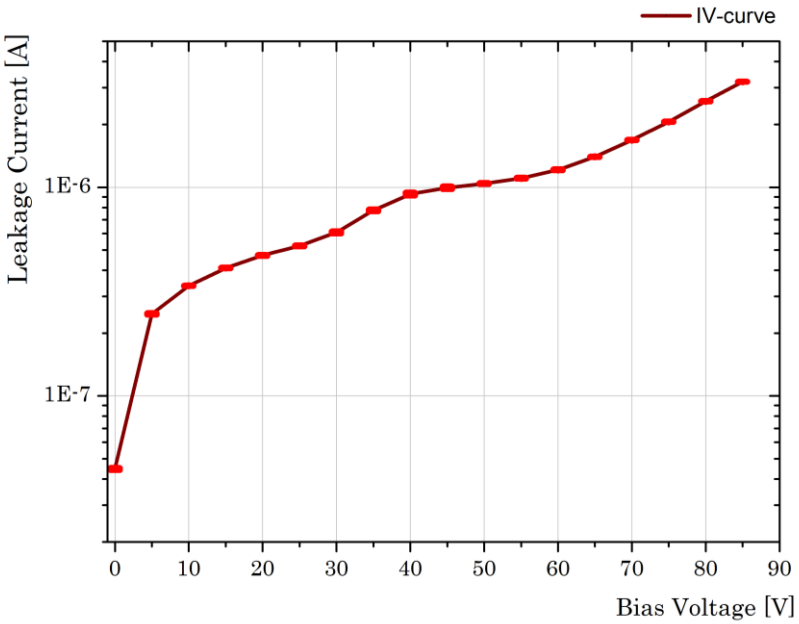

Figure 8.28 – The leakage current of the pixel sensor versus applied bias voltage.

The IV measurement of the pixel module, which was tested with the laser test bench, is shown in Figure 8.28, and the full depletion is not clearly seen.

The collected charge at full depletion shows saturation. Plotting the mean ToT value of the registered during the laser illumination hits versus the bias voltage one can find the turning point when the mean ToT value becomes plateau. Using this point, the full depletion voltage could be determined unambiguously. The curve, shown in Figure 8.29, measured for the same module as the IV-measurement was done. From the plot one can conclude that the full depletion voltage is about 70 V.

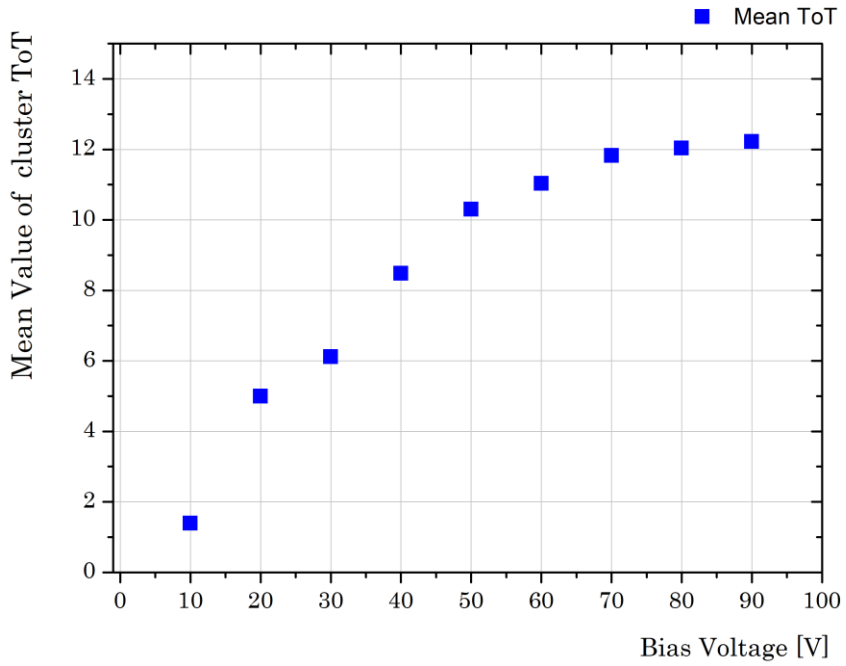

Figure 8.29 – The charge signal amplitude of the seed pixel versus the applied bias voltage.

8.5. Source scan

There are two types of radioactive sources which are used for different purposes in the process of pixel module characterization. The first type is γ-sources, which emit γ-quants with known energy spectrum. These sources are used as reference for the collected charge. The second type is β-sources, which radiate the electrons, and if the energy of electrons is high enough (to interact as a MIP particles (see section 4.1.1), they can be used to study charge collection efficiency.

For the source tests performing in this section we have used the 37 MBq activity of ^{90}Sr isotope source encapsulated in stainless steel support with round window (see Figure 8.30), emitting electrons spectrum by β-decay:

$$\begin{aligned} {}^{90}Sr &\rightarrow e^{-} + \overline{\nu}_e + {}^{90}Y \quad t_{half} = 28.8y \quad E_{\max} = 0.55MeV \\ {}^{90}Y &\rightarrow e^{-} + \overline{\nu}_e + {}^{90}Zr \quad t_{half} = 2.67d \quad E_{\max} = 2.28MeV \end{aligned} \tag{8.18}$$

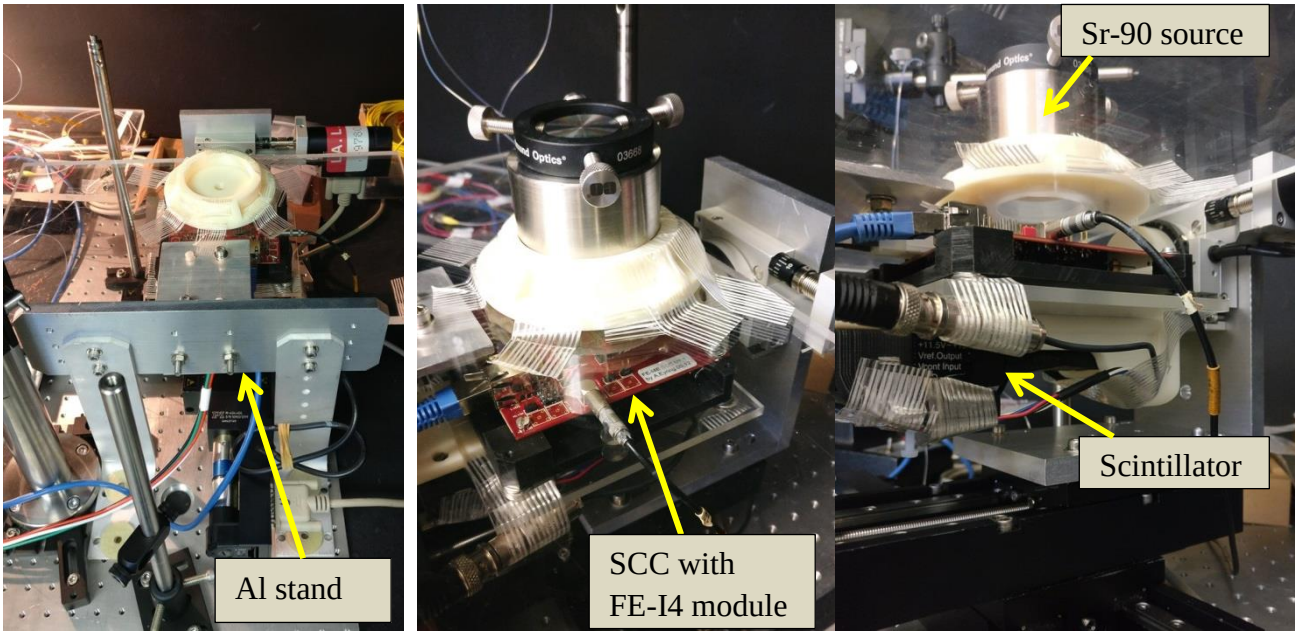

Figure 8.30 – Setup to perform source measurements with an under test pixel module. The module is placed in between a source, which emits the particles, and a scintillator for triggering the readout. The aluminum stand is additionally installed to the laser setup to support radioactive source for the source measurements.

The developed laser test bench setup can be easily transformed for radioactive source or cosmic rays measurements. For this purpose the source is placed on the additionally installed aluminum stand (shown in Figure 8.30) with a plexiglas plate and a plastic support on it for the simple positioning of the source over the pixel sensor. There are two ways for triggering the readout of the pixel detector. First, an external trigger signal from a scintillator below the assembly. The scintillator output can be shaped with an external discriminator, so that only hits above a certain noise level cause a trigger signal. Second, the trigger signal can be generated by the hitbus, which forms a coincidence of the discriminator output of all pixels. Thus, it indicates a hit anywhere on the chip. Noisy and stuck pixels, which disable the hitbus, have to be masked in order not to use them for triggering. This way is called internal trigger. Mostly used for the γ-source, where the photons release all their energy at once when they interacting with the atoms in silicon and then can't reach the scintillator. An external trigger signal can be used to assure that the hit was caused by a high energy particle (MIP) passing the sample and scintillator. After a presence of trigger, the event information is readout and in the end is written into an ascii-file, referred to as raw data file, which can be analyzed.

For a possibility of an external triggering in our setup, the rotating holder dedicated to support the SCC with the pixel module during the tests, shown in Figure 8.5, contains the space for a scintillator and a PMT (photomultiplier tube) and a large opening under the sensitive pixel matrix to not prevent the particles passage.

The source measurement was done for a non-irradiated FE-I4 module tuned to a threshold of 2500 e^- and to ToT gain to correspond 20 000 e^- to 8 ToT. The noisy and stuck pixels were masked. The measurement is performed via a "source scan" command from STcontrol software using the USBPix readout board. The result is presented in Figure 8.31.

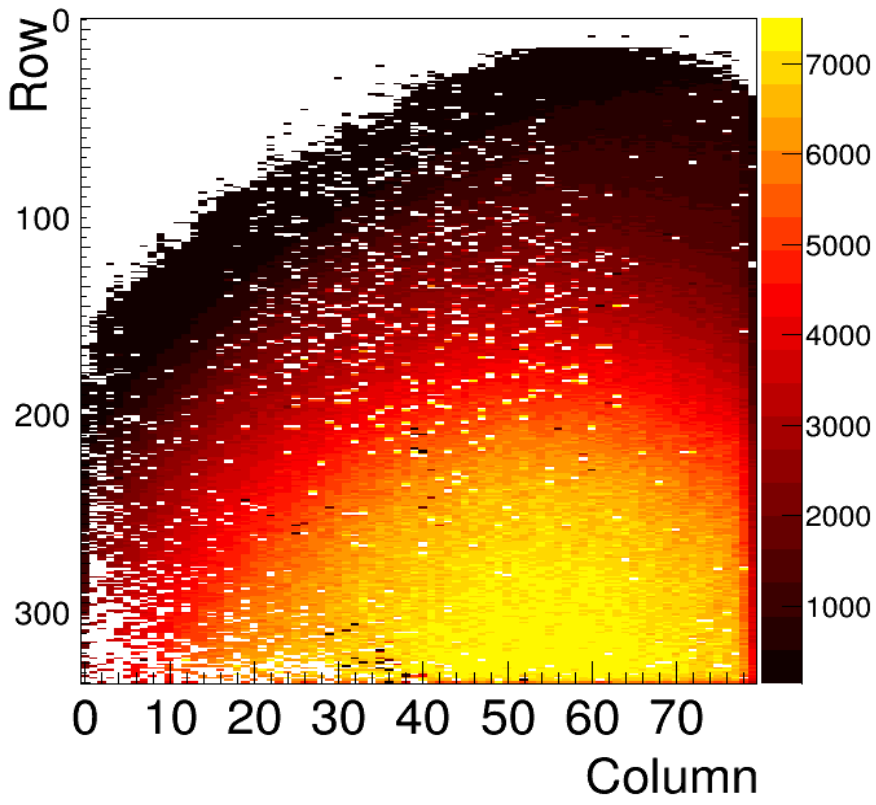

Figure 8.31 – A two dimensional hitmap taken during a source scan with external trigger. The source placed in the position above the corner of the pixel matrix. Comparing the results from this source scan with the chip analog scan (Figure 7.4) of the same module, one can see a group of "white" pixels with disconnected bump bonds in left bottom and right up corner. The device was biased to -70 V and 20^0C temperature.

8.6 Conclusions

A test system based on an infra-red laser has been built in order to test the silicon pixel detector assemblies. This setup is easy to prepare and flexible in using, with different laser wavelengths (we used 635 nm and 1064 nm) it is possible to inject charges only on the surface of the sensor or throughout the whole sensor thickness. The small beam spot size and accurate positioning make it possible in future to make in-pixel efficiency scans over the whole pixel sensor surface including the edges. To analyze the data, any track reconstruction is not needed.

Such a table-top laser test bench setup would be of a great help in pixel detector characterization, complementary to the particle beam tests. In the future this laser setup will be integrated with other instruments such as probe station to further enhance the laboratory in-house test capabilities for the pre-production and production phases towards the construction of ATLAS ITk pixel detector.

Chapter 9

Conclusion and Outlook

A large-scale upgrade of the LHC accelerator complex and the detector systems is planned to operate in HL-LHC phase to explore new high-energy physics frontiers. The tracking detector of the ATLAS experiment will be replaced by the ATLAS Inner Tracker (ITk), which is currently in preparation to maintain, but in many aspects to improve the tracking performance comparing to the present ATLAS Inner Detector despite the increased demand posed by operating at the HL-LHC. A high radiation damage and increased track density will be most challenging for the detectors. The new pixel sensor and pixel detector technologies were developed to address the requirements coming from this harsh environment. Some of them, for example, the thin planar n-in-p sensors with active edge design and new pixel detector readout chip made in 65 nm CMOS technology, were tested and presented in this thesis. They have proven to be a reliable detector component, with high performance before and after irradiation.

In the thesis I have shown my contribution to R&D activities aiming to develop efficient planar pixel sensors for the ITk upgrade and the robust tool for pixel module characterization, as well as a contribution to a pixel barrel stave prototype construction for a Demonstrator phase.

Knowledge on a pixel module assembly process has been acquired using a modern clean room experimental infrastructure and specific low noise instrumentation, contributing to the ATLAS Outer Barrel Demonstrator project. The work done in this regard is presented in Chapter 3.

Using the TCAD simulation tool it was shown that planar pixel sensors design could be optimized for a better robustness. The obtained results, discussed in Chapter 5, verify that the breakdown voltage increases with the decreased p-spray concentration dose during the sensor production process. Several pixel sensor designs with different p-spray concentration values could be produced according to simulation outcome in order to compare the obtained results with experimental measurements and in future to optimize pixel sensor design for any pixel pitch.

A better understanding of radiation damage of the silicon planar pixel sensors could be achieved thanks to a novel TLM method to study the active doping profile of heavily irradiated sensors. My contribution and the first results on active doping profile measurements in the silicon samples before and after irradiation are presented in Chapter 5.

The major achievements are made in understanding the performance of planar pixel sensors before and after irradiation. This target has been achieved by laboratory electrical characterization and by using relativistic particle beams. The charge collection and hit efficiency performance of the ADVACAM active and slim edge pixel detectors have been investigated and presented in Chapter 6. The study was performed for the sensors with different thicknesses of 50 μm, 100 μm and 150 μm before and after irradiation with fluence of $1 - 2\times10^{15}$ n_{eq}/cm^2 with regard to the HL-LHC requirements. The tested sensor designs prove high hit efficiency at the sensor edges beyond the pixel matrix. An active edge sensor design shows the efficiency higher than 97 % up to 20 μm from the last pixel column, which gives to this design an advantage in choosing sensors to instrument the ITk Pixel detector. The thin planar pixel sensors after

irradiation demonstrate hit efficiency of 93,4+0,3% for the active edge and 89,5+0,3% for the slim edge design starting from a voltage of 200 V. The slim edge design shows a lower overall efficiency mainly caused by losses appeared in the areas near bias dots and bias rail. To cope with this problem the option with the addition of a temporary metal for biasing structures implementation, called "Removable Bias Grid" designing now by FBK company, can be implemented. This will allow for the measurements of the sensor electrical properties by shorting all pixels before flip chipping. And then the biasing structure can be removed before further processing.

For the ITk construction for the HL-LHC, which requires more granular thin pixel sensors with faster and radiation hard front-end electronics, the performance study of the pixel detectors employing different sensor geometries 50×50 μm^2 and alternative 25×100 μm^2 and equipped with a novel RD53A chip have been carried out using particle beams. The spatial resolution of the different pixel geometry was estimated. The hit efficiency before and after irradiation to the fluence of 5×10^{15} $n_{eq}cm^{-2}$ of the pixel modules with different front-end analog flavors implemented in the chip has been evaluated and compared.

The Ring Oscillators (RO) embedded in RD53A chip meant to monitor irradiation at the HL-LHC have been evaluated and reported in the thesis in Chapter 7. The obtained results show the linearity in the dependence of the RO frequency on the irradiation dose and temperature. This make possible to use the RD53A chip to measure radiation dose and temperature in the ITk Pixel detector. Moreover, the different flavors of the RO implemented in the chip, has a different slope in the measured dependencies, so by analysis of the results from each of them the calculated dose and temperature can be refined to achieve high precision.

An important contribution to the PhD project has been devoted to build a new specific test bench setup based on an infra-red laser beam that "mimic" MIP particles crossing in a silicon substrate. This is a cost effective solution to characterize pixel module prior the test beam campaigns to validate any new or existing sensor designs. The setup allows a study of charge collection efficiency of pixel detector with well-defined timing, position and energy deposition. The developed test bench setup, described in Chapter 8, is compact and versatile; it can be used for the measurements with a laser, radioactive source and cosmic rays. This work will be submitted to publication for the community. Using this setup the illumination scan of a single pixel has been carried out and the full depletion voltage of the pixel module has been determined. The laser test bench will be integrated with other instruments such as probe station to further to enhance the laboratory in-house test capabilities for the pre-production and production phases towards the construction of ATLAS ITk pixel detector.

In future to improve the pixel sensor design technology and testing infrastructure the following activities have to be done:

- The production of different in total p-spray dose wafer runs with 50×50 μm^2 pixel sensor geometry to test and verify simulation;

- Improving of radiation damage study methods in Silicon pixels by developing alternative methods to TLM, like Terahertz Method (to be investigated in the future). Getting a better understanding of irradiated sensor performance in terms of charge collection and

electric field distributions sensors using a laser system for the edge transient current technique [149].

- Increase expertise and knowledge on system design to build a large number of modules for the construction phase and RD53 electronics tests in the lab.

- Improving the laser test bench to be able to test more granular modules with different readout electronics. Performing the study not only with X-Y position resolution, but also with inclined position resolution.

The work done will be very useful for the new ATLAS tracker development and building, in particular for a Paris cluster's laboratories collaboration during the pixel modules construction and testing for the ITK.

Acknowledgements

These pages at the end are devoted to people, who supported and helped me during the whole period of my thesis. Without your assistance and encouragement the successful finalization of this work would not have been possible. I would like to use this opportunity to express my sincere gratitude to all of you. There are too many names to mention all of them here, so I apologize to anyone not listed, please know your support was greatly appreciated!

Initially, I would like to express my special gratitude to my supervisor Abdenour Lounis, whose expertise was invaluable in the formulating of the research topic and methodology. You gave me the opportunity to join the research activities as an intern and then to perform my PhD in the ATLAS group at LAL. Your useful advises, continuous support, guidance, motivation, patience have been helping me throughout the research work and writing of my thesis. Abdenour by engaging me into new ideas, encouraging attending different conferences and meetings, has strengthened me as a researcher and my personal skills.

Also, I want to thank people without whom I would not have the opportunity to study in France. I am very grateful to my professor Oleg Bezshyyko from the University in Ukraine for the inspiration and motivation to do physics research and to Sergey Barsuk who both with Oleg introduced me to Abdenour.

I want to acknowledge my colleagues: Tasneem, Anastasia, Tobias, Maurice, Cristophe and Jimmy for your help and for having nice time together during meetings, workshops, travels and test beams. Ιδιαίτερες ευχαριστίες to Dimitris! Thanks for the lunchtime runs and JRJC;)

I would give thanks to former students of Abdenour Clara and Vagelis who met me and introduced many useful things which helped me to start working in the group when I had come for a first time to LAL. I would like to thank everyone in the ATLAS-LAL group and the students: Vasyl, Kostya, Sabrina, Yuxeu I had pleasure to work with. Merci pour tous les membres de personnel du LAL pour votre aide concernant les procédures administratives.

Many thanks to the people with whom I participated to many test beam campaigns. Grazie mille Anna Macchiolo and Marco Bomben for your support and guidance during the long test beam days and thank you for providing us with the test modules. As well, I would like to thank to all members in MPP, LPNHE and Hong Kong test beam groups: Audrey, Natascha, Julien, Reem, Kirill, Julia, Ki and others.

I want to express my deepest gratitude to Mathieu Benoit who helped me a lot with TCAD simulation.

Thanks a lot to Aboud who was always helpful. I really appreciate it, without your contribution it would be not possible to build many constructions for the laser test bench setup.

Merci beaucoup pour Stephane Trochet for your availability and for willingness to help with any technical issue and the maintenance of CAPTINNOV probe station.

I am grateful to Julian Dajczgewand for the help in the design and manufacturing of the optical focusing system and Большое спасибо to Victor Soskov for fruitful discussions and providing (so many times) the CCD camera.

I cannot express how much I appreciate your surroundings during this period of my life, Leonid and Sasha. You supported me not only academically but also otherwise. Your sport motivation, advices and conversations after work were necessary and very useful for me. Also, I would thank to other my friends, who were of great support in deliberating over any problems and findings, as well as providing happy distraction to rest my mind outside of my research.

In addition, many thanks to all the member of the jury, and special thanks to my two referees Fares Djama and Giovanni Calderini for reviewing this manuscript.

Finally, I would like to express my thankfulness to my parents for teaching me so much, for your wise counsel and strong support. Without so much love from your side, this achievement would not be possible.

Dmytro
Orsay in September 2019

Bibliography

[1] Convention for the Establishment of a European Organization for Nuclear Research, Paris, 1st July, 1953 as amended on 17 January 1971 https://council.web.cern.ch/en/content/convention-establishment-european-organization-nuclear-research

[2] L. Evans and P. Bryant (editors), LHC Machine, JINST 3 (2008) S08001.

[3] O. S. Brüning et al., LHC Design Report, CERN, (2004).

[4] C. Lefevre, *The CERN accelerator complex*, CERN-DI-0812015, Dec, 2008, https://cds.cern.ch/record/1260465.

[5] ATLAS Collaboration, The ATLAS Experiment at the CERN Large Hadron Collider, JINST 3 (2008) S08003

[6] ALICE Collaboration, The ALICE experiment at the CERN LHC, JINST 3 (2008) S08002.

[7] CMS Collaboration, The CMS experiment at the CERN LHC, JINST 3 (2008) S08004.

[8] LHCb Collaboration, The LHCb Detector at the LHC, JINST 3 (2008) S08005.

[9] https://twiki.cern.ch/twiki/bin/view/AtlasPublic/LuminosityPublicResultsRun2#Luminosity_summary_plots_for_201

[10] https://twiki.cern.ch/twiki/bin/view/AtlasPublic/LuminosityPublicResultsRun2#Pileup_Interactions_and_Data_Tak

[11] Luminosity: http://pdg.lbl.gov/2011/reviews/rpp2011-rev-accel-phys-colliders.pdf

[12] The ATLAS Collaboration. “Observation of a new particle in the search for the Standard Model Higgs boson with the ATLAS detector at the LHC” Phys.Lett. B716 (2012) 1-29

[13] The ATLAS Collaboration. “Measurements of Higgs boson production and couplings in diboson final states with the ATLAS detector at the LHC” Phys. Lett. B 726 (2013) 88 (page 15)

[14] ATLAS Collaboration (Eric Feng (CERN) for the collaboration) “Measurements of the Higgs Boson Mass and Couplings with ATLAS 13 TeV Data” PoS EPS-HEP2017 (2017) 697

[15] ATLAS Collaboration, Measurement of the Higgs boson mass in the $H \rightarrow ZZ^{*} \rightarrow 4$` and $H \rightarrow \gamma\gamma$ channels with $\sqrt{s}$=13 TeV p-p collisions using the ATLAS detector,ATLAS-CONF-2017-046(2017).

[16] ATLAS Collaboration, ATLAS Inner Detector: Technical Design Report 1, CERN, (1997), CERN-LHCC-97-016.

[17] ATLAS Collaboration, ATLAS Inner Detector: Technical Design Report 2, CERN, (1997), CERN-LHCC-97-017.

[18] ATLAS Collaboration, ATLAS Calorimeter Performance: Technical Design Report, CERN, (1996), CERN-LHCC-96-040.

[19] ATLAS Collaboration, ATLAS Liquid-Argon Calorimeter: Technical Design Report, CERN, (1996), CERN-LHCC-96-041.

[20] ATLAS Collaboration, ATLAS Tile Calorimeter: Technical Design Report, CERN, (1996), CERN-LHCC-96-042.

[21] ATLAS Collaboration, ATLAS Muon Spectrometer: Technical Design Report, CERN, (1997), CERN-LHCC-97-022.

[22] https://cds.cern.ch/record/2209070/plots

[23] The ATLAS Collaboration "The ATLAS Inner Detector commissioning and calibration" Eur.Phys.J.C70:787-821,2010, page 11

[24] G. Aad, M. Ackers, F.A. Alberti, M. Aleppo, G. Alimonti, et al. ATLAS pixel detector electronics and sensors. JINST, 3:P07007, 2008. doi: 10.1088/1748-0221/3/07/P07007.

[25] I. Peric et al., *The FEI3 readout chip for the ATLAS pixel detector*, Nucl. Instr. Meth. A 565 (2006) 178

[26] M. Garcia-Sciveres et al., *The FE-I4 pixel readout integrated circuit*, Nucl. Instr. Meth. A 636 (2011) S155

[27] E. Vianello et al., *Optimization of double-side 3D detector technology for first productions at FBK*, IEEE Nucl. Sci. Symp. Conf. Rec. (2011) 523

[28] https://www.lhc-closer.es/taking_a_closer_look_at_lhc/0.lhc_layout

[29] Y. Unno, ATLAS silicon microstrip Semiconductor Tracker (SCT), Nucl. Instr. Meth. A453 (2000) 109.

[30] F. Martin, The ATLAS transition radiation tracker (TRT) from construction to installation, Nucl. Instr. Meth. A581 (2007) 535.

[31] A. Vogel, ATLAS Transition Radiation Tracker (TRT): Straw tube gaseous detectors at high rates, Nucl. Instr. Meth. A732 (2013) 277.

[32] ATLAS Collaboration, *ATLAS liquid-argon calorimeter: Technical Design Report*. Technical Design Report ATLAS. CERN/LHCC, 1996. https://cds.cern.ch/record/331061.

[33] Arantxa Ruiz Martıınez on behalf of the ATLAS Collaboration, *The Run-2 ATLAS Trigger System*., 2016. ATLAS. ATL-DAQ-PROC-2016-003.

[34] Performance of calorimeters at the LHC To cite this article: Francesca Cavallari 2011 J. Phys.: Conf. Ser.293 012001 Page 3 - 8

[35] ATLAS Collaboration, *ATLAS liquid-argon calorimeter: Technical Design Report*, CERN, Geneva (1996), URL https://cds.cern.ch/record/331061

[36] ATLAS Collaboration, *ATLAS calorimeter performance: Technical Design Report*, CERN, Geneva (1996), URL https://cds.cern.ch/record/331059

[37] Paolo Francavilla (on behalf of the ATLAS Collaboration), The ATLAS Tile Hadronic Calorimeter performance at the LHC, Physics: Conference Series404(2012) 012007

[38] S. Palestini et al., *The muon spectrometer of the ATLAS experiment*, Nucl. Phys. B - Proceedings Supplements 125 (2003) 337

[39] C. Bini, *Study of the performance of the ATLAS Muon Spectrometer*, Nuclear Science Symposium and Medical Imaging Conference (NSS/MIC) (2011) 1265–1268.

[40] The ATLAS Tile Calorimeter A. Henriques, CERN, on behalf of the ATLAS Collaboration

[41] F. Bauer, U. Bratzler, H. Dietl, H. Kroha, T. Lagouri, et al., Construction and test of MDT chambers for the ATLAS muon spectrometer,Nucl.Instrum.Meth.A461 (2001) 17–20.

[42] T. Argyropoulos, K. A. Assamagan, B. H. Benedict, V. Chernyatin, E. Cheu, et al.,Cathodestrip chambers in ATLAS: Installation, commissioning and in situ performance,IEEETrans.Nucl.Sci.56 (2009) 1568–1574.

[43] G. Aielli, A. Aloisio, M. Alviggi, V. Aprodu, V. Bocci, et al.,The RPC first level muon triggerin the barrel of the ATLAS experiment,Nucl.Phys.Proc.Suppl.158 (2006) 11–15.

[44] S. Majewski, G. Charpak, A. Breskin, and G. Mikenberg, A Thin Multiwire Chamber Operating in the High Multiplication Mode,Nucl.Instrum.Meth.217 (1983) 265–271.

[45] The ATLAS Collaboration. Performance of the ATLAS Trigger System in 2015.Performance of the ATLAS Trigger System in 2015.Eur. Phys. J. C, 77 (CERN-EP-2016-241.5):317. 76 p, Nov 2016. URLhttps://cds.cern.ch/record/2235584. (page 61) http://atlas.web.cern.ch/Atlas/GROUPS/PHYSICS/PAPERS/TRIG-2016-01/

[46] The ATLAS collaboration Walkowiak, Wolfgang (Department Physik, Universitat Siegen) “ATLAS Plans for the High-Luminosity LHC” ATL-PHYS-PROC-2018-048

[47] ATLAS Collaboration, Einsweiler, Kevin; Pontecorvo, Ludovico Technical Design Report for the ATLAS Inner Tracker Pixel Detector CERN-LHCC-2017-021, https://cds.cern.ch/record/2285585

[48] ATLAS Collaboration, McMahon, Stephen; Pontecorvo, Ludovico, Technical Design Report for the ATLAS Inner Tracker Strip Detector CERN-LHCC-2017-005, https://cds.cern.ch/record/2257755

[49] Catrin Bernius, on behalf of the ATLAS and CMS Collaborations “HL-LHC prospects from ATLAS and CMS “, ATL-PHYS-PROC-2019-02

[50] image https://project-hl-lhc-industry.web.cern.ch/content/project-schedule

[51] ATLAS Collaboration, *ATLAS public results* (2018), URL https://twiki.cern.ch/twiki/bin/view/ AtlasPublic/LuminosityPublicResultsRun2

[52] The ATLAS collaboration Vankov, Peter (FOM - Institute SAF Nikhef and University of Amsterdam/Nikhef) "ATLAS Future Upgrade"ATL-UPGRADE-PROC-2016-003

[53] M. Capeans et al., ATLAS Insertable B-Layer Technical Design Report, Tech. Rep. CERN-LHCC-2010-013. ATLAS-TDR-19, CERN, Geneva, Sep, 2010.

[54] ATLAS Collaboration Technical Design Report for the Phase-I Upgrade of the ATLAS TDAQ System, CERN-LHCC-2013-018 ; ATLAS-TDR-023, page 11

[55] ATLAS, Collaboration, *Letter of Intent for the Phase-II Upgrade of the ATLAS Experiment*, CERN-LHCC-2012-022, Dec, 2012, http://cds.cern.ch/record/1502664.

[56] ATLAS muon spectrometer: Technical design report - ATLAS Collaboration CERN-LHCC-97-22, ATLAS-TDR-10

[57] ATLAS Collaboration, ATLAS Insertable B-Layer Technical Design Report Addendum, Tech. Rep. CERN-LHCC-2012-009. ATLAS-TDR-19-ADD-1, CERN, Geneva, May, 2012. Addendum to CERN-LHCC-2010-013, ATLAS-TDR-019. Page 9

[58] Alessandro La Rosa on behalf of ATLAS collaboration Irradiation induced effects in the FE-I4 front-endchip of the ATLAS IBL detector, arXiv:1611.00803v1 [physics.ins-det] 2 Nov 2016

[59] A. Ferrari, P. R. Sala, A. Fasso, and J. Ranft, FLUKA: A multi-particle transport code (Program version 2005).

[60] T. Sjöstrand, S. Mrenna, and P. Z. Skands, A Brief Introduction to PYTHIA 8.1, Comput.Phys.Commun. 178 (2008) 852–867, arXiv:0710.3820 [hep-ph].

[61] M. Garcia-Sciveres et al., *The RD53A Integrated Circuit*, CERN-RD53-PUB-17-001, Oct, 2017,https://cds.cern.ch/record/2287593.

[62] Podgorsak, E.B. (2010). *Radiation physics for medical physicists*. Berlin, Heidelberg, New York: Springer.

[63] G. Lutz et al., *Semiconductor radiation detectors*, vol. 40. Springer, 1999

[64] S. M. Sze "Semiconductor Devices" Physics and Technology (Wiley, New York (1985)

[65] D. Groom et al., *Review of particle physics. Particle data group*, European Physical Journal C 15 (2000) 1-4 1–878 page 399

[66] K. Roy et al., *Leakage current mechanisms and leakage reduction techniques in deep-submicrometer CMOS circuits*, Proceedings of the IEEE (Volume: 91 , Issue: 2 , Feb. 2003) 305–327.

[67] G. F. Knoll, Radiation Detection and Measurement, vol. Chapter 11. Wiley, 4th ed.,2010.

[68] Mathieu BENOIT, Étude des détecteurs planaires pixels durcis aux radiations pour la mise à jour du détecteur de vertex d'ATLAS, PhD thesis, Université Paris XI, Orsay, 2011

[69] S. Ramo, Currents Induced by Electron Motion, Proceedings of the IRE 27 (1939) 584.

[70] W. Shockley, Currents to Conductors Induced by a Moving Point Charge, Journal of Applied Physics 9 (1938) 635.

[71] M. Moll, Radiation tolerant semiconductor sensors for tracking detectors, Nucl. Instrum. Meth. A 565 no. 1, (2006) 202 – 211. http://www.sciencedirect.com/science/article/pii/S0168900206007571. PIXEL 2005.

[72] JR Srour et al., Review of displacement damage effects in silicon devices, IEEE Transactions on Nuclear Science 50 (2003) 3 653–670.

[73] P. W. Marshall and C. J. Dale, "Space Radiation Effects on Optoelectronic materials for a 1300 nm Fiber Optic Data Bus," IEEE Trans. Nucl. Sci, vol. 39, no. 6, p. 1989, 1992.

[74] V. A. J. Van Lint , R. E. Leadon and J. F. Colwell , "Energy Dependence of Displacement Effects in Semiconductors," IEEE Trans. Nucl. Sci., vol. 19, no. 6, pp. 181 185, 1972.

[75] J-C Beyer, Optimisation of Pixel Modules for the ATLAS Inner Tracker at the High-Luminosity LHC, PhD thesis München, 2019.

[76] M. Moll, Radiation damage in silicon particle detectors: microscopic defects and macroscopic properties. oai:cds.cern.ch:425274. PhD thesis, Hamburg University,1999.

[77] G. Kramberger et al., E_ective trapping time of electrons and holes in di_erent silicon materials irradiated with neutrons, protons and pions, Nucl. Instr. Meth. A481 (2002) 297.

[78] M. Moll, Radiation Damage in Silicon Particle Detectors, PhD thesis, Universitat Hamburg, (1999).

[79] Tasneem Saleem, Development of pixel detector for ATLAS Inner Tracker Upgrade at HL-LHC, PhD thesis, Universite Paris–Saclay, Orsay, 2019

[80] K. Wright, A. R. Barron, Secondary Ion Mass Spectrometry (SIMS), http://cnx.org/content/m50227/1.1

[81] C.Nellist, Characterisation and Beam Test Data Analysis of 3D Silicon Pixel Detectors for the ATLAS Upgrade, PhD thesis, the University of Manchester, 2013

[82] S. Parker, C. Kenney, and J. Segal, 3D - A proposed new architecture for solid-state radiation detectors, Nucl. Instrum. Meth. A 395 (1997) 328–343

[83] Garcia-Sciveres, MWermes, , A review of advances in pixel detectors for experiments with high rate and radiation, Reports on Progress in Physics, 81(6) , 2018, https://escholarship.org/uc/item/1zn1j5x9

[84] ATLAS IBL collaboration, *Prototype ATLAS IBL modules using the FE-I4A front-end readout chip*, JINST 7 (2012) 11 P11010.

[85] Dalla Betta G-F et al 2016 Development of a new generation of 3D pixel sensors for HL-LHC Nucl. Instrum. Methods A 824386–7

[86] Pellegrini G et al 2013 3D double sided detector fabrication at IMB-CNM Nucl. Instrum. Methods A A69927–30

[87] Giacomini G et al 2013 Development of double-sided full-passing-column 3D sensors at FBK IEEE Trans. Nucl. Sci.602357–66

[88] Savić, Natascha , Development of pixel detectors for the inner tracker upgrade of the ATLAS experiment. Dissertation, LMU München: Faculty of Physics, 2018

[89] Snoeys et al., A process modification for CMOS monolithic active pixel sensors for enhanced depletion, timing performance and radiation tolerance,NIMA871(2017) 90-96

[90] Pixel Detectors for Charged Particles - Wermes, Norbert Nucl.Instrum.Meth. A604 (2009) 370-379 arXiv:0811.4577 [physics.ins-det]

[91] ATLAS Pixel Collaboration, J. Grosse-Knetter, *The ATLAS pixel detector, Nucl. Instrum. Meth.* A568 (2006) 252–257, [https://dx.doi.org/10.1016/j.nima.2006.05.240].

[92] Garcia-Sciveres, Maurice *et al* , A review of advances in pixel detectors for experiments with high rate and radiation, Rept.Prog.Phys. 81 (2018) no.6, 066101 arXiv:1705.10150 [physics.ins-det]

[93] G. Lindström et al., *Radiation hard silicon detectors-developments by the RD48 (ROSE) collaboration*, Nucl. Instr. Meth. A 466 (2001) 2 308–326.

[94] ATLAS pixel detector electronics and sensors G Aad[11], M Ackers[2], F A Alberti[12], M Aleppo[12,13], G Alimonti[12], J Alonso[1], E C Anderssen[1], A Andreani[12,13], A Andreazza[12,13], J-F Arguin[1]Show full author list Published 24 July 2008 • Journal of Instrumentation, Volume 3, July 2008

[95] Y. Unno et al., Development of n-in-p silicon planar pixel sensors and flip-chip modules for very high radiation environments, Nucl. Instr. Meth. A 650 (2011) 129

[96] L. Rossi et al, Pixel Detectors from Fundamentals to Applications, Proceedings of the 1999 Particle Accelerator Conference, New York, 2005

[97] http://cds.cern.ch/record/2141992/plots

[98] Ulrich Koetz, Igor Rubinskiy "ATLAS FE-I4A Pixel Moduleas a Trigger Plane for the Beam Telescope" USER MANUAL, Göttingen, 2013

[99] J. Albertet al.,Prototype ATLAS IBL Modules using the FE-I4A Front-End Read-out Chip, JINST7, P11010,2012.

[100] T. Saleem-Rashid et all, Innovative method to study irradiation damage in silicon pixel detectors for HEP:TLM, NIM, 2019

[101] TCAD SYNOPSYS Inc. https://www.synopsys.com/silicon/tcad.html

[102] https://www.cremat.com/why-use-csps/

[103] Georg Troska, Development and operation of a testbeam setup for qualification studies of ATLAS Pixel Sensors, Technische Universitat Dortmund, 2012

[104] Getting Started with LabVIEW, National Instruments, 2013

[105] Julia Rieger, Comparison of Thin n- and p-type Bulk Silicon Pixel Sensors, Goettingen, 2012

[106] USBpix - USB based readout system for ATLAS FE-I3 and FE-I4 , http://icwiki.physik.uni-bonn.de/twiki/bin/view/Systems/UsbPix. website, visited on September 8th, 2012.

[107] http://advacam.com/service/sensor-manufacturing

[108] L. Andricek at al., *Processing of ultra-thin silicon sensors for future e+ e- linear collider experiments*, IEEE Trans. Nucl. Sci. 51 (2004) 1117–1120.

[109] N. C. Matthew Wasilik, *Deep reactive ion etch conditioning recipe*, vol. 5342, pp. 103–110, AA(BSAC/Univ. of California/Berkeley, USA), SPIE, 2004.

[110] N. Savic, Development of Pixel Detectors for the Inner Tracker Upgrade of the ATLAS Experiment, PhD thesis, München, 2017

[111] J. Knetter, *The usbpix system*, http://icwiki.physik.unibonn.de/twiki/bin/view/Systems/UsbPix.

[112] H. Jansen, S. Spannagel, et al. Performance of the EUDET-type beam telescopes.EPJ Techniques and Instrumentation, 3(1):7, 2016. ISSN 2195-7045.doi: 10.1140/epjti/s40485-016-0033-2. URLhttp://dx.doi.org/10.1140/epjti/s40485-016-0033-2.

[113] R. L. Gluckstern. Effect of multiple scattering on measurement of track momentum and direction. Nuclear Instruments and Methods, 56:145–147, January 1967. doi:10.1016/0029-554X(67)90271-6

[114] https://particle-physics.desy.de/e252106/e252106/e252211].

[115] The DESY II Test Beam Facility - Diener, R. *et al.* Nucl.Instrum.Meth. A922 (2019) 265-286 arXiv:1807.09328 [physics.ins-det] DESY 18-111, DESY-18-111 \

[116] EUDAQ Software Developers (2016) EUDAQ Website. http://eudaq.github.io. Accessed 21 Apr 2015

[117] “Millepede II.” Online - https://www.wiki.terascale.de/index.php/millepede_ii.

[118] V. Blobel, *Software alignment for tracking detectors*, Nucl. Instr. Meth. A 566 (2006) 1 5–13.

[119] S. Fleischmann, Track Reconstruction in the ATLAS Experiment: The deterministic annealing filter. PhD thesis, Universität Wuppertal.

[120] R. Kalman et al., A new approach to linear filtering and prediction problems, Journal of basic Engineering 82 (1960) 1 35–45.

[121] C. Kleinwort, *General Broken Lines as advanced track fitting method*, Nucl. Instr. Meth. A 673 (2012) 107–110.

[122] K. Sjøbæk, *Full simulation of a testbeam experiment including modeling of the Bonn ATLAS Telescope and ATLAS 3D pixel silicon sensors*. PhD thesis, University of Oslo, 2010. https://www.duo.uio.no/handle/10852/10980.

[123] M. George, *Testbeam Measurements with Pixel Sensors for the ATLAS Insertable b-Layer Project*. PhD thesis, Georg-August-Universitat Göttingen, 2014. https://ediss.uni-goettingen.de/handle/11858/00-1735-0000-0022-5F07-A.

[124] https://ac.els-cdn.com/S1875389212017889/1-s2.0-S1875389212017889-main.pdf?_tid=ca8a74d7-1fe5-42e3-9d52-a61b1ba23345&acdnat=1552224764_0dd097959f617a5fb9c5de67b8c0624c

[125] A. Bulgheroni, T. Klimkovich, P. Roloff, and A. Zarnecki, EUTelescope: tracking software, EUDET-Memo-2007-20 144 (2007).

[126] RD53 Collaboration, RD Collaboration Proposal: Development of pixel readout integrated circuits for extreme rate and radiation," CERN-LHCC-2013-008; LHCC-P-006 (2013).

[127] RD53 Collaboration, RD53A Integrated Circuit Specifications," CERN-RD53-PUB-15-001 (2015)

[128] RD53 Collaboration, RD53A Integrated Circuit," CERN-RD53-PUB-17-001 (2018)

[129] YARR - A PCIe based Readout Concept for Current and Future ATLAS Pixel Modules Timon Heim Lawrence Berkeley National Lab, USA

[130] https://www.xilinx.com/products/boards-and-kits/ek-k7-kc705-g.html

[131] https://www.enclustra.com/en/products/fpga-modules/mercury-kx2/

[132] https://github.com/SiLab-Bonn/basil

[133] https://ade-pixel-group.web.cern.ch/ade-pixel-group/xray/

[134] G. Lindström, M. Moll, and E. Fretwurst, “Radiation hardness of silicon detectors—A challenge from high energy physics,” Nucl. Instrum. Meth., vol. A426, pp. 1–15, 1999.

[135] https://www.edmundoptics.com/resources/application-notes/lasers/gaussian-beam-propagation/

[136] Julien-Christopher Beyer, Optimisation of Pixel Modules for the ATLAS Inner Tracker at the High-Luminosity LHC, PhD thesis, München, 2019

[137] Synopsys, Inc., URL https://www.synopsys.com/silicon/tcad.html

[138] The ROSE collaboration: Note on the fluence normalization based on the NIEL scaling hypothesis. Technical Note ROSE/TN/200-02, CERN, Geneva, Swiss (2000).

[139] T. R. Oldham, F. B. McLean, Fellow, Total Ionizing Dose Effects in MOS Oxides and Device, IEEE TRANSACTIONS ON NUCLEAR SCIENCE, VOL. 50, NO. 3, JUNE 2003

[140] Brower KL. Kinetics of H2 passivation of Pb centers at the (111) Si-SiO2 interface., Phys Rev B Condens Matter. 1988 Nov 15;38(14):9657-9666. (page 66)

[141] V.Radeka: Ann. Rev. Nucl. Part. Sci. 38, 217-277 (1988)

[142] https://www.cedesa.com.mx/pdf/keithley/keithley_ACS-BASIC_user_manual.pdf

[143] Jan M. Rabaey, Digital Integrated Circuits (2nd edition) 1999 , page 47

[144] SILVACO® Inc., 55, Blaise Pascal, 38330 Montbonnot, St. Martin, France, http://www.sil-vaco.com/products/tcad.html

[145] SYNOPSYS® Inc., 690 East Middlefield Road, Mountain View, CA 94043, http://www.syn-opsys.com/tools/tcad/Pages/default.aspx

[146] Rick Bitter et al, LabVIEW Advanced Programming Techniques, CRS Press, 2007

[147] https://www.ni.com/visa/

[148] http://www.canuckmediamonitor.org/bGlnaHRpbmcgcGVuZXRyYXRpb24gZGVwdGg/

[149] G. Kramberger, et al, Investigation of Irradiated Silicon Detectors by Edge-TCT, IEEE Trans.Nucl.Sci. 57 (2010) no.4, 2294-2302

université PARIS-SACLAY | ÉCOLE DOCTORALE PHENIICS

Titre: Avancées technologiques dans le domaine des pixels planaires pour l'expérience ATLAS Phase 2

Mots clés: Pixel granulaires, ATLAS phase 2, Technologie planaire, collisionneur HL-LHC

Résumé : Le complexe d'accélérateurs du grand collisionneur de hadrons (le Large Hadron Collider - LHC) sera mis à jour lors du long arrêt de la période LS3 en 2023-2025 pour passer à la phase de haute luminosité (HL-LHC). La luminosité instantanée sera multipliée par 5 pour atteindre 7.5×10^{34} $cm^{-2}s^{-1}$, ce qui correspond à environ 200 collisions inélastiques par croisement de paquets comparé aux 50 par croisement au LHC. Pendant le fonctionnement du HL-LHC, afin d'atteindre une haute précision dans les études des processus physiques du modèle standard et les recherches de nouvelle physique, le collisionneur à protons devra fournir une luminosité intégrée de l'ordre 400 fb^{-1} par an pendant une dizaine d'années soit 4000 fb^{-1} escomptées. Ceci représente un ordre de grandeur supérieur à l'ensemble de la période du LHC. Le détecteur interne (Inner Detector) ATLAS actuel ne sera pas en mesure de faire face efficacement à l'augmentation du taux d'événements et de la dose de rayonnement. Afin d'obtenir des performances au minimum égales ou supérieures à celles de la phase LHC, et tenant compte d'un environnement plus hostile en termes de radiations et d'empilements d'évènements, il a été décidé d'opérer le remplacement complet du trajectomètre interne ou Inner Tracker (ITk); à cette fin, une technologie tout silicium a été choisie.

Cette thèse est axée sur l'étude de nouveaux capteurs pixels planaires fins à bords très minces, basés sur le concept d'utilisation de matrices de diodes à implants dopés n sur un substrat dopé p. Ce choix est motivé par les critères de meilleure performance intrinsèque, de radio-tolérance élevée ainsi qu'un coût de production optimisé pour de grandes surfaces. Dans ce travail, des capteurs de différentes épaisseurs allant de 50 µm à 150 µm dotés de bords actifs et minces ont fait l'objet d'études approfondies notamment lors de leur fonctionnement à haut flux de particules chargées.

De nombreuses analyses minutieuses ont été menées pour déterminer leur résolution en position à l'aide d'un télescope de faisceau de haute énergie. Les régions d'impacts sur la zone active des pixels ainsi que sur la région des contours ont été scrutées avant et après leur irradiation. En effet, de nombreux résultats obtenus en faisceau de protons et électrons seront montrés, notamment. une étude comparative des différents concepts de matrices de capteurs de pixels planaires lus avec la puce de lecture « FE-I4 » en technologie CMOS 130 nm.

Préparant la phase future du LHC, nous montrerons les premiers résultats obtenus avec la nouvelle génération de pixels granulaires. Ces matrices ont été couplées à la nouvelle puce de lecture frontale récemment développée au CERN, utilisant la technologie CMOS 65 nm. Ces capteurs dotés d' une plus fine granularité de 50×50 μm^2 , ont un pas optimisé lequel est nécessaire pour maintenir un taux d'occupation aussi bas que possible dans un contexte de multiplicités de particules chargées très élevées.

Dans ce travail, une contribution personnelle à l'électronique de lecture sera détaillée, en particulier les études ont été menées sur la puce nommée «Ring-Oscillator» ou moniteur de radiations, développée au laboratoire. On décrira son comportement dynamique en fonction de la température, de la tension nominale et en conditions hautement radiatives (500 MRad).

La mise au point d'un nouvel outil de caractérisation de détecteurs pixels a fait l'objet d'un développement important. Grâce à un ensemble basé sur une excitation laser de 1060 nm, il sera possible de disposer d'un système précis et autonome capable de mesurer rapidement les caractéristiques fonctionnelles des matrices de pixels avec une excellente résolution spatiale. Les caractéristiques de cet outil fera l'objet d'une présentation exhaustive.

Title: Advanced Planar pixel technology developments for ATLAS upgrade phase 2

Keywords: Granular pixel sensors, ATLAS phase 2, Planar sensor technology, HL-LHC collider

Abstract: The Large Hadron Collider (LHC) will go through the accelerator complex upgrade during the LS3 long shutdown in 2023-2025 to move to the High Luminosity phase (HL-LHC). As a result, an instantaneous luminosity will increase sevenfold to 7.5×10^{34} $cm^{-2}s^{-1}$, corresponding to approximately 200 inelastic collisions per bunch-crossing, whereas the LHC runs resulted in up to 50 collisions per bunch-crossing. During the operation of the HL-LHC, in order to achieve high-precision in studies of Standard Model processes and searches for new physics, about 4000 fb^{-1} of integrated luminosity be collected, which is of an order of magnitude larger than over the entire LHC period. The present ATLAS Inner Detector (ID) will not be able to efficiently cope with the increased event rate and radiation dose. Due to this fact the complete replacement of the ID is foreseen with fully silicon Inner Tracker (ITk) to provide high tracking performance in harsher environment delivered by the HL-LHC.

This thesis is focused on the study of new n^{+}-in-p planar silicon sensors, as a promising option to instrument the ITk pixel layers, considering their radiation hardness and cost-effectiveness. Sensors of different thicknesses ranging from 50 µm to 150 µm of active and slim edge designs have been tested at a high energy particle beam to investigate hit efficiency performance analyzed on the pixel active area and on the edge area before and after irradiation. The test beam results and their comparison for the different designs of the pixel sensors compatible with FE-I4 readout chip are discussed.

Also, the first results on test beam characterization of the pixel modules employing a newly developed prototype of readout chip for the ITk, RD53A chip, implemented in 65 nm CMOS technology, were obtained. The sensors with the decreased to 25×100 μm^2 and 50×50 μm^2 pixel pitch to maintain the lower level of occupancy at high particle multiplicity were measured. Additionally, the tests of ring oscillators, contained in RD53A chip, which may be used as a monitor of the received radiation dose, were carried out depending on temperature, supplied voltage and irradiation level up to 500 MRad.

Finally, the test bench setup for silicon pixel detectors characterization using an infra-red laser has been the subject of an original development in this thesis. The setup was developed in the clean room at Laboratoire de l'accélérateur linéaire (LAL) and it is capable of rapidly measuring the functional characteristics, providing a flexible charge injection with well-defined hit position to characterize the silicon pixel matrixes. The software to control the setup was created using LabVIEW programming environment. The results of the measurements with the FE-I4 module implemented with openings allowing the laser beam passage on a sensor backside are presented in this thesis.

Université Paris-Saclay
Espace Technologique / Immeuble Discovery
Route de l'Orme aux Merisiers RD 128 / 91190 Saint-Aubin, France